

Doppler Ultrasound measurement of Arterial Wall Motion (AWM)

Judith A. Dineley, MSc

A thesis submitted for the degree of Doctor of Philosophy

The University of Edinburgh

December 2005



L2

Abstract

Arterial Wall Motion (AWM) is of value in evaluating the elasticity of arteries, which is associated with the degree of focal and diffuse arteriosclerosis. A new technique derives AWM using integrated velocity data generated by Tissue Doppler Imaging (TDI) ultrasound. The technique provides spatial and temporal AWM data over segments up to 35 mm long and cine loops typically 3-5 cardiac cycles long. Limited data exists in the literature quantifying accuracy and precision. The aim of this thesis was to assess technique accuracy and precision in detail, *in vivo* and in the laboratory using specially designed test objects.

A preliminary *in vivo* reproducibility study in asymptomatic carotid arteries revealed high inter-measurement variability (Limits of agreement in TDI derived maximum dilation, Mx: 159 μm) and several sources of variability. Accuracy assessment was performed in the laboratory with a device based upon a moving plate which mimicked physiological and sinusoidal motion and whose maximum displacement was known to within 3 μm . Accuracy in Mx ranging from $-3\pm 8\%$ to $-23\pm 1\%$ was obtained for sinusoidal device motion ranging in amplitude from 248 to 1190 μm . Underestimation of Mx by the TDI/AWM software was found to systematically increase with increasing sinusoid amplitude and peak velocity.

A compliant wall vascular flow phantom designed to mimic physiologic AWM and have mechanical and acoustic properties similar to *in vivo* was developed in order to assess AWM technique precision. It consisted of a 6 mm diameter uniformly elastic piece of vessel mimicking material (VMM) of wall thickness 1.73 mm set in gelatin based tissue mimicking material (TMM). Two TMM versions were devised: 'A' mimicked soft tissue attenuation for assessment of AWM precision, and 'B' maximised backscatter from the vessel. The latter was to optimise TDI/AWM technique performance during phantom characterisation measurements by maximising the signal received at the transducer. A range of realistic dilations and wall velocities were generated with pulsatile flow. AWM precision was found to

vary with vessel depth (7 ± 3 %), beam-vessel angle (22 ± 3 %), scan plane-vessel coincidence (34 ± 2 %) and transducer pressure (20 ± 3 %).

AWM accuracy and precision have been assessed for the special case of uniformly elastic vessels. Future work could investigate technique efficacy for vessels of non-uniform elasticity and geometry, in order to assess the potential for identification of plaques at risk of rupture.

Declaration

I declare that this thesis has been written by myself and that work contained within is my own. Where work has been in collaboration with other people, an acknowledgement has been made.

Judith Dineley

Date 09/12/05

Acknowledgements

This thesis would not be completed without help from many people. Thanks must go to my supervisors Pete Hoskins and Norman McDicken for their guidance and constructive feedback provided on this thesis. Steve Pye, Tamie Poepping, Bill Easson and Tom Anderson have been huge helps with ideas for my work, advice and objective perspectives. The contributions of Karen Gallagher, Sarah-Jane Johnson and Paul Allan were invaluable in conducting the work in Chapter two. I am thankful to Robin Prescott and Mandy Lee of the Medical Statistics Unit for statistics guidance. I am also grateful to Steven Hammer for not running screaming from the lab when work on the validation device in Chapter three did not run smoothly. Thanks also to Jane Blackford and Dan Higgins of mechanical engineering for access to their tensile testing rigs. To Bobby Hogg of the engineering workshop I am truly indebted for providing me with moulds, phantom housings and advice on materials. Special thanks to Nick, Dad & Andrew for help with typing in the final messy stages when my wrists had had enough of this thesis.

On a personal note many people have made the time spent on my thesis much more bearable and cheerful; my fellow lab rats (thanks especially to Mairéad for giggles and helping me out too many times to mention here, and Kate and Siobhan for tracking down random bits of information while I was in Galway), Jacinta for proof reading and guiding me through various levels of panic with patience and Katherine for encouraging me to eat more cake (like I needed it?).

Love and thanks to my family: Mum, Dad, Andrew & Katie, and my friends that I've neglected so much when the work piled up. Nick, I can't thank you enough for going way beyond the call of duty and making me smile. You deserve co-author credits...and yes I'm finished now.

Table of Contents

CHAPTER 1 CARDIOVASCULAR DISEASE AND ASSESSMENT OF DISEASE SEVERITY 1

1.1	CARDIOVASCULAR DISEASE (CVD), ATHEROSCLEROSIS AND STROKE	1
1.1.1	Introduction.....	1
1.1.2	Atherogenesis and changes in the artery wall.....	3
1.1.3	The high risk plaque	5
1.1.4	Clinical management of carotid atherosclerosis	6
1.1.5	Summary.....	6
1.2	CLINICAL IMAGING OF CAROTID ARTERY DISEASE.....	7
1.2.1	X-ray angiography	7
1.2.2	Magnetic Resonance Angiography (MRA)	8
1.2.3	Ultrasonography.....	9
1.2.4	Summary.....	12
1.3	GEOMETRIC AND MORPHOLOGICAL METHODS OF CAROTID DISEASE ASSESSMENT 13	
1.3.1	Measurement of wall thickness.....	13
1.3.2	Plaque characterisation for identification of high risk plaques.....	14
1.3.3	Summary.....	15
1.4	THE MECHANICAL PROPERTIES OF ARTERIES	16
1.4.1	The healthy artery	17
1.4.2	Effects of aging & atherosclerosis	19
1.4.3	Summary.....	25
1.5	IN VIVO MEASUREMENT OF THE ELASTIC PROPERTIES OF THE ARTERIES	26
1.5.1	Assessment by quantitative mechanical parameters.....	26
1.5.2	Assessment by Elasticity Imaging	33
1.5.3	Indirect assessment of wall elasticity.....	33
1.5.4	Summary.....	34
1.6	OUTLINE OF THESIS	35

CHAPTER 2 IN VIVO INTRA- AND INTER-OBSERVER VARIABILITY OF TDI DERIVED ARTERIAL WALL MOTION (AWM)..... 39

2.1	INTRODUCTION	39
2.1.1	Definition of AWM indices	40
2.2	METHODOLOGY	42
2.2.1	Logistics.....	42
2.2.2	Scan protocol	43
2.2.3	Data extraction & analysis.....	44
2.3	RESULTS & DISCUSSION	47
2.3.1	Sources of variability	47
2.3.2	Intra-segment variability for fixed observers and fixed acquisition sessions.....	58
2.3.3	Intra-segment agreement and variability between observers and acquisition sessions.....	59
2.4	SUMMARY AND CONCLUSIONS.....	64

CHAPTER 3 ARTERIAL WALL MOTION (AWM) TECHNIQUE ACCURACY ASSESSMENT USING A CONTROLLED VALIDATION DEVICE .67

3.1	INTRODUCTION	67
3.2	MATERIALS AND METHODOLOGY	70
3.2.1	The AWM validation device.....	70
3.2.2	AWM waveforms investigated	72
3.2.3	TDI data acquisition.....	74
3.2.4	TDI independent verification of device motion.....	74
3.2.5	TDI Data analysis	75
3.3	RESULTS AND DISCUSSION	76
3.3.1	TDI independent verification of device motion.....	76
3.3.2	Qualitative assessment of TDI derived AWM accuracy	78
3.3.3	Quantitative assessment of TDI derived AWM accuracy	84
3.3.4	Validation device limitations	88
3.4	CONCLUSIONS	89

CHAPTER 4 PHANTOM MATERIAL CHARACTERISATION..... 90

4.1	INTRODUCTION	90
4.2	CHOICE OF MATERIALS	90
4.2.1	Geometry	91
4.2.2	Mechanical properties.....	92
4.2.3	Acoustic properties	94
4.2.4	Optical transmission	95
4.2.5	Remaining properties.....	96
4.2.6	Conclusion	98
4.3	PHANTOM MATERIAL PREPARATION	100
4.3.1	Tissue mimicking material (TMM)	100
4.3.2	Vessel-mimicking material (VMM)	101
4.4	MECHANICAL CHARACTERISATION.....	103
4.4.1	Methodology.....	103
4.4.2	Results & discussion.....	107
4.5	ACOUSTIC CHARACTERISATION	114
4.5.1	Background.....	114
4.5.2	Methodology.....	114
4.5.3	Results & discussion.....	116
4.6	SUMMARY & CONCLUSION	118

CHAPTER 5 COMPLIANT WALL FLOW PHANTOM DESIGN & CHARACTERISATION 121

5.1	INTRODUCTION	121
5.2	CHOICE OF AWM PHANTOM DESIGN	122
5.3	PHANTOM DESIGN REQUIREMENTS	123

5.3.1	VMM wall thickness, h , and diameter, D	124
5.3.2	AWM dilation, velocity and acceleration magnitude	125
5.3.3	AWM rise time and cycle duration	125
5.4	PHANTOM DESIGN & FLOW GENERATION	126
5.4.1	Vessel mimicking material (VMM)	126
5.4.2	Blood-mimicking fluid (BMF)	132
5.4.3	Phantom & flow rig construction	133
5.5	VARIATIONS IN AWM WITH APPLIED FLOW WAVEFORM SHAPE: A PILOT STUDY 135	
5.5.1	Background	135
5.5.2	Methodology	136
5.5.3	Results and discussion	138
5.6	VARIATIONS IN AWM WITH CHARACTERISTICS OF A GENERIC FLOW WAVEFORM & OUTFLOW IMPEDANCE	141
5.6.1	Methodology	141
5.6.2	Results and discussion	143
5.7	SUMMARY AND CONCLUSION	158

CHAPTER 6 EVALUATION OF ARTERIAL WALL MOTION (AWM) PRECISION WITH VARYING ACQUISITION GEOMETRIES 161

6.1	INTRODUCTION	161
6.2	METHOD	162
6.2.1	Depth variation	163
6.2.2	Transducer-vessel angle variation	164
6.2.3	Scan plane variation	165
6.2.4	Transducer pressure variation	165
6.3	RESULTS & DISCUSSION	166
6.3.1	Variation in AWM precision with vessel depth	166
6.3.2	Variation in AWM precision with transducer-vessel angle	169
6.3.3	Variation in AWM precision with scan plane variation	170
6.3.4	Variation in AWM precision with exerted transducer pressure	172
6.4	SUMMARY & CONCLUSIONS	175

CHAPTER 7 CONCLUSION AND FUTURE WORK 176

APPENDICES 179

APPENDIX A	MEASURES OF ARTERIAL STIFFNESS	179
APPENDIX B	MEASURES OF ARTERIAL STIFFNESS	181
APPENDIX C	PRELIMINARY MEASUREMENTS TO DETECT STRAIN RATE DEPENDENCE OF TANGENT MODULUS OF ELASTICITY, E_T IN VMM AND TMM	182
APPENDIX D	A QUALITATIVE EXPLANATION OF PRESSURE AND FLOW PULSE PROPAGATION IN THE COMPLIANT WALL PHANTOM	183

LIST OF FIGURES

FIGURE 1.1: SITES OF ATHEROMA FORMATION IN ARTERIES SUPPLYING THE HEAD AND NECK ⁵ . REPRINTED FROM 'STROKE, A PRACTICAL GUIDE TO MANAGEMENT', 2ND EDITION, WARLOW, C.B. ET AL, COPYRIGHT (2001), WITH PERMISSION FROM THE BLACKWELL SCIENCE.	2
FIGURE 1.2: APPROXIMATE DISTRIBUTION OF CAUSE OF CEREBRAL ISCHAEMIC EVENTS (BOTH PERMANENT & TRANSIENT) IN WHITE POPULATIONS ⁶	3
FIGURE 1.3: CROSS SECTIONAL VIEW OF THE ARTERY WALL ⁹ . REPRINTED FROM NATURE, 407, LUSIS, A.J. ET AL, 'ATHEROSCLEROSIS', 233 - 241, COPYRIGHT (2000), WITH PERMISSION FROM NATURE PUBLISHING GROUP.	4
FIGURE 1.4: A COLOUR FLOW IMAGE OF A HEALTHY COMMON CAROTID ARTERY. COLOUR PIXELS REPRESENTING FLOW VELOCITY ARE SUPERIMPOSED ON A B-MODE IMAGE WHICH DEMONSTRATES TISSUE ANATOMY IN THE SCAN PLANE. 10	
FIGURE 1.5: SPECTRAL DOPPLER TRACE OF AN ASYMPTOMATIC COMMON CAROTID ARTERY.	10
FIGURE 1.6: STRESS-STRAIN BEHAVIOUR OF AN EXCISED HUMAN AORTOILIAC ARTERY. REPRINTED FROM THE JOURNAL OF BIOMEDICAL MATERIALS RESEARCH, 35, TOPOLESKI, L.D.T. ET AL, 'COMPOSITION- AND HISTORY-DEPENDENT RADIAL COMPRESSIVE BEHAVIOUR OF HUMAN ATHEROSCLEROTIC PLAQUE', 117 - 127, COPYRIGHT (1997), WITH PERMISSION FROM JOHN WILEY AND SONS INC.	18
FIGURE 1.7: VARIATIONS IN STRESS-STRAIN CURVES OBSERVED ON COMPRESSION TESTING OF ATHEROSCLEROTIC PLAQUE. REPRINTED FROM THE JOURNAL OF BIOMEDICAL MATERIALS RESEARCH, 35, TOPOLESKI, L.D.T. ET AL, 'COMPOSITION- AND HISTORY-DEPENDENT RADIAL COMPRESSIVE BEHAVIOR OF HUMAN ATHEROSCLEROTIC PLAQUE', 117 - 127, COPYRIGHT (1997), WITH PERMISSION FROM JOHN WILEY AND SONS INC.	21
FIGURE 1.8: ASCENDING AORTIC PRESSURE WAVEFORM MEASURED ON A MIDDLE-AGED SUBJECT. REPRINTED FROM AMERICAN JOURNAL OF HYPERTENSION, 15, WILKINSON, I.B. ET AL, HEART RATE DEPENDENCY OF PULSE PRESSURE AMPLIFICATION AND ARTERIAL STIFFNESS, 24 - 30, COPYRIGHT (2002), WITH PERMISSION FROM THE AMERICAN JOURNAL OF HYPERTENSION, LTD.	26
FIGURE 1.9: (A) TDI DERIVED AWM SUPERIMPOSED UPON A GREY SCALE IMAGE OF AN ASYMPTOMATIC COMMON CAROTID ARTERY AT SYSTOLE. (B) ASSOCIATED SPATIAL PLOT OF MAXIMUM DILATION.	31
FIGURE 1.10: (A) TDI DERIVED AWM SUPERIMPOSED UPON A GREY SCALE IMAGE OF A SEVERELY STENOSED CAROTID BIFURCATION AT SYSTOLE. (B) ASSOCIATED SPATIAL PLOT OF MAXIMUM DILATION.	32
FIGURE 2.1: <i>IN VIVO</i> AWM DERIVED FROM TDI DATA FROM A COMMON CAROTID ARTERY PLOTTED (A) TEMPORALLY AND (B) SPATIALLY. DILATIONS FROM ONLY 3 SCAN LINES AND 3 FRAMES ARE SHOWN FOR CLARITY.	41
FIGURE 2.2: VARIATION IN SPATIAL GRADIENT OF DILATION FOR THE AWM IN FIGURE 2.1.....	42
FIGURE 2.3: PATTERN OF TDI DATA ACQUISITION.	42
FIGURE 2.4: TDI DATA ACQUISITION LOCATIONS.	43
FIGURE 2.5: (A) A B-MODE FRAME DEMONSTRATING A REVERBERATION ARTEFACT, MARKED WITH AN ARROW (B) A COMPARISON OF SPATIAL VARIATION IN MAXIMUM DILATION FOR ONE LOOP UNAFFECTED BY THE ARTEFACT AND ANOTHER AFFECTED BY THE ARTEFACT. A TROUGH IS EVIDENT AT THE ARTEFACT SITE (VOLUNTEER 5, SESSION 1, OBSERVER 1, LOOP 1).....	49
FIGURE 2.6: AWM MASKED BY NOISE DUE TO POOR DEFINITION OF THE ARTERY WALLS (VOLUNTEER 3, LICA SESSION 2 OBSERVER 1 LOOP 1). EACH LINE	

REPRESENTS THE MEAN DILATION OF EACH SCAN LINE AVERAGED OVER SEVERAL CARDIAC CYCLES.	50
FIGURE 2.7: (A) A SEGMENTATION ERROR IN A CCA DUE TO A STRONGLY REFLECTING JUGULAR VEIN WALL (B) THE EFFECT ON AWM IS SEEN IN CYCLE-AVERAGED MINIMUM DILATION CURVES (VOLUNTEER 3, SESSION 1, OBSERVER 1, LOOP 1).50	
FIGURE 2.8: (A) TDI AND (B) AWM DATA DEMONSTRATING THE EFFECT OF INCLUSION OF BLOOD VELOCITIES WITH TISSUE VELOCITIES (VOLUNTEER 3, LICA, SESSION 2, OBSERVER 2, LOOP 1). BRIGHTNESS IN (A) IS ENHANCED IN ORDER TO VISUALISE THE TDI COLOURS.....	51
FIGURE 2.9: A SCHEMATIC DIAGRAM DEMONSTRATING THE MECHANISM RESULTING IN MISINTERPRETATION OF NON-SIMULTANEOUS DILATIONS AS SIMULTANEOUS, DUE TO A FINITE SCANNING TIME ACROSS THE COLOUR BOX LENGTH.	52
FIGURE 2.10: MAXIMUM CYCLE-AVERAGED DILATION SHOWING A LACK OF SYNCHRONISATION BETWEEN SCAN LINES (VOLUNTEER 1, LCCA, SESSION 2, OBSERVER 2, LOOP 1).....	53
FIGURE 2.11: REDUCTION IN MEAN DILATION DUE TO THE PRESENCE OF A MOTION ARTEFACT (VOLUNTEER 5, LCCA, SESSION 1, OBSERVER 2, LOOP 1).	53
FIGURE 2.12: COMPARISON OF CYCLE AND SCAN LINE AVERAGED AWM OF THE ENTIRE SCANNED SEGMENT, THE LOWER WALL ONLY AND THE UPPER WALL ONLY DEMONSTRATING THE EFFECT ON AWM SHAPE OF THE JUGULAR INDUCED MOTION (VOLUNTEER 4, LCCA, SESSION 1, OBSERVER 2, LOOP 3).	54
FIGURE 2.13: DEMONSTRATION OF THE EFFECT OF OFF-AXIS POSITIONING OF THE TRANSDUCER (A) B-MODE FRAME (B) MAXIMUM CYCLE AVERAGED DILATION VARIATION WITH POSITION (VOLUNTEER 2, LCCA, SESSION 2, OBSERVER 1, LOOP 1).....	55
FIGURE 2.14: A COMPARISON OF TWO AWM FRAMES AT SYSTOLE OF THE SAME ARTERY SEGMENT IMAGED IN THE SAME SESSION BY DIFFERENT OBSERVERS EXHIBITING (A) DILATIVE AWM AND (B) TRANSLATORY AWM (VOLUNTEER 5, RICA, SESSION 1).	57
FIGURE 2.15: AWM ARTEFACT FREQUENCY FOR A SAMPLE OF 24 SCANNING EPISODES FOR EACH ARTERY TYPE. NOTE CONTRIBUTIONS FROM DIFFERENT SOURCES OF UNCERTAINTY SUM TO MORE THAN THE SAMPLE SIZE SINCE MORE THAN ONE ARTEFACT MAY OCCUR IN A GIVEN SCANNING EPISODE. ALSO NOTE THE ABSENCE OF SOURCES 5 AND 10; THE FORMER IS PRESENT IN ALL SCANNING EPISODES AND THE EFFECT OF THE LATTER IS UNKNOWN.	58
FIGURE 2.16: A BLAND & ALTMAN PLOT OF THE DIFFERENCE IN MX OBTAINED BY THE TWO OBSERVERS VERSUS THE MEAN VALUES OF THE TWO OBSERVATIONS AVERAGED OVER BOTH DATA ACQUISITION SESSIONS. THE RANDOM NATURE OF THE DATA EXCLUDES THE SYSTEMATIC VARIATION OF THE DIFFERENCES WITH INDEX MAGNITUDE.	59
FIGURE 2.17: A HISTOGRAM DEMONSTRATING A NORMAL DISTRIBUTION OF DIFFERENCES BETWEEN PAIRED MX VALUES FOR INTER-OBSERVER VARIABILITY IN SESSION 2.	60
FIGURE 2.18: BAR CHART OF MEAN BIASES OF DIFFERENCES IN PAIRED AWM INDICES FOR GIVEN SEGMENTS OF ARTERY. LOA ARE REPRESENTED BY THE ERROR BARS ATTACHED TO THE DIFFERENCE BARS. MEAN AWM VALUES ARE PLOTTED ALONGSIDE LOA VALUES AND THEIR ERROR BARS REPRESENT ± 1 SD. Y-AXIS UNITS ARE MICRONS, WITH THE EXCEPTION OF MG WHOSE UNITS IS $\times 10^{-3}$	61
FIGURE 3.1: THE AWM VALIDATION DEVICE (A) WITH ONLY THE LOWER, MOVING TMM LAYER IN PLACE (B) WITH THE TRANSDUCER IN PLACE AND A LAYER OF TMM SECURED TO IT, ACTING AS THE NEAR ARTERY WALL (C) A CLOSE UP OF THE TRANSDUCER HOLDER.....	71
FIGURE 3.2: A RAW TDI IMAGE OF THE AWM VALIDATION DEVICE WITH THE TWO CRYOGEL LAYERS IN PLACE. 2D GAIN HAS BEEN ENHANCED IN ORDER TO VISUAL THE NEAR PVA LAYER.....	71

FIGURE 3.3: (A) SINUSOIDAL (B) PHYSIOLOGICAL DISPLACEMENT WAVEFORMS PERFORMED BY THE VALIDATION DEVICE FOR ACCURACY ASSESSMENT OF TDI/AWM SOFTWARE TECHNIQUE.	73
FIGURE 3.4: AN EXAMPLE OF PSEUDO-M-MODE IMAGE GENERATED FROM A 2 MM WIDE ROI IN THE TDI SCANNED SEGMENT OF B-MODE DATA FOR WAVEFORM B.	77
FIGURE 3.5: AN EXAMPLE OF THE DILATION PLOTS FOR WAVEFORM B MOTION GENERATED FROM B-MODE DATA FOR 2 × 2 MM WIDE ROI OF THE TDI SCANNED SEGMENT.	77
FIGURE 3.6: PERCENTAGE DIFFERENCE BETWEEN LASER VIBROMETRY AND B-MODE ESTIMATES OF MAXIMUM DILATION.	78
FIGURE 3.7: TDI DERIVED AWM FOR TYPICAL (A) SINUSOIDAL MOTION (WAVEFORM 3) (B) PHYSIOLOGICAL MOTION (WAVEFORM A) (C) PHYSIOLOGICAL MOTION (WAVEFORM B). THE SOLID BLACK LINE REPRESENTS THE ACTUAL DEVICE MOTION AS MEASURED BY LASER VIBROMETRY. 'I' DEMONSTRATES BROADENING OF DILATIONS (SEE 3.3.2.1). 'II' DEMONSTRATES SPATIAL BUNCHING OF DILATIONS (SEE 3.3.2.2).	79
FIGURE 3.8: MEAN AWM VERSUS TIME DEMONSTRATES THE VARIABILITY IN DERIVED AWM BETWEEN TWO CONSECUTIVELY ACQUIRED CINE LOOPS FOR WAVEFORM 1 DEVICE MOTION. 'X' IS ONE OF SEVERAL POINTS WHERE INSTEAD OF BLUE TDI PIXELS, INDICATING THE EXPECTED EXPANSION OF THE DEVICE 'WALLS', RED WAS INCORRECTLY ASSIGNED BY TDI AND THEREFORE INTERPRETED BY THE AWM SOFTWARE AS WALL CONTRACTION.	81
FIGURE 3.9: IMAGE FRAMES FROM THE RISE PHASE OF TWO WAVEFORM A PHYSIOLOGICAL MOTION CYCLES WITHIN THE SAME CINE LOOP, ONE UNAFFECTED (A) AND ONE AFFECTED (B) BY THE 'BUNCHING' ARTEFACT IN FIGURE 3.7.	83
FIGURE 3.10: PERCENTAGE DEVIATION IN TDI DERIVED MAXIMUM DILATION, MX_{TDI} VERSUS ACTUAL MAXIMUM DILATION, MX_0	85
FIGURE 3.11: SEGMENTED TDI FRAMES SHOWING (A) ALIASING IN A CINE LOOP OF WAVEFORM 5 (MARKED BY ARROW) (B) SPURIOUS COLOUR THOUGHT TO RESULT FROM VELOCITIES OUTSIDE THE PVA LAYER IN A WAVEFORM 3 CINE LOOP. BOTH FRAMES ARE TAKEN FROM THE EXPANSION PHASE OF THE AWM.	86
FIGURE 4.1: DELRIN®/ACRYLIC MOULD FOR PREPARATION OF VMM AND TMM SAMPLES FOR TENSILE TESTING.	105
FIGURE 4.2: THE INSTRON TABLETOP MATERIALS TESTING RIG (A) OVERALL SET UP (B) A CLOSE-UP VIEW DEMONSTRATING THE GRIPS FOR SAMPLE ATTACHMENT.	106
FIGURE 4.3: STRESS-STRAIN DATA AND BEST FIT LINES FOR (A) TMM (B) VMM. EACH SHOW FITS OVER (I) THE ENTIRE STRAIN RANGE MEASURED AND (II) OVER 0 - 10 % STRAIN.	108
FIGURE 4.4: VARIATION IN TMM TANGENT MODULUS, E_T WITH SAMPLE AGE FOR RECIPES A, B AND C. DATA POINTS REPRESENT THE AVERAGE OVER BATCHES OF TYPICALLY EIGHT SAMPLES. ERROR BARS REPRESENT ± 1 SD OF THE INTRA-BATCH MODULI.	111
FIGURE 4.5: VARIATION IN VMM TANGENT MODULUS, E_T , WITH SAMPLE AGE FOR VMM STORED IN WATER, ENCASED IN TMM (RECIPE B) AND ENCASED IN TMM (RECIPE C). DATA POINTS REPRESENT THE AVERAGE OVER BATCHES OF TYPICALLY EIGHT SAMPLES. ERROR BARS REPRESENT ± 1 SD OF THE INTRA-BATCH MODULI.	111
FIGURE 4.6: VARIATION IN VMM TANGENT MODULUS, E_T , WITH FREEZE-THAW CYCLE FOR 5 % STRAIN. DATA POINTS REPRESENT THE AVERAGE OVER BATCHES OF TYPICALLY EIGHT SAMPLES.	113
FIGURE 4.7: EXPERIMENTAL SET-UP FOR ACOUSTIC PROPERTY MEASUREMENTS USING A SCANNING ACOUSTIC MACROSCOPE (SAM).	115
FIGURE 5.1: AN ILLUSTRATION OF AWM CHARACTERISTICS.	123
FIGURE 5.2: A PVA CRYOGEL VMM MOULD IN CROSS SECTION.	126

FIGURE 5.3: AN ILLUSTRATION DEFINING THE ANGULAR CO-ORDINATE, θ IN RELATION TO VMM CROSS-SECTIONAL GEOMETRY. VARIATIONS IN WALL THICKNESS WERE MEASURED OVER 12 VALUES OF θ IN THE RANGE 0 - 360° ...	129
FIGURE 5.4: MANUALLY SEGMENTED MINIMUM (SOLID BLUE) AND MAXIMUM (RED DASHED) INNER WALL POSITIONS AND CROSS SECTIONAL B-MODE VIEWS FOR VMM SEGMENTS WITH (A) A SYMMETRICAL WALL AND (B) AN ASYMMETRICAL WALL.....	130
FIGURE 5.5: A SPECIMEN PHANTOM WITH A VESSEL OF UNIFORM ELASTICITY CONNECTED INTO A FLOW CIRCUIT.....	133
FIGURE 5.6: VOLUME FLOW WAVEFORM SHAPES GENERATED AT THE PUMP HEAD.	138
FIGURE 5.7: MEAN AWM WAVEFORMS RESULTING FROM SINUSOID, SAW-TOOTH, SQUARE WAVE AND CAROTID VOLUME FLOW.....	138
FIGURE 5.8: A SCHEMATIC DIAGRAM OF AN APPLIED FLOW CYCLE DEMONSTRATING RISE TIME, T_{QPEAK} , PEAK FLOW, Q_{PEAK} , AND FULL WIDTH HALF MAXIMUM, FWHM.	141
FIGURE 5.9: AWM (A) DILATIONS (B) VELOCITIES AND (C) ACCELERATIONS RESULTING FROM VARIATIONS IN RISE TIME.....	144
FIGURE 5.10: AWM DILATIONS, VELOCITIES AND ACCELERATIONS DERIVED FROM <i>IN VIVO</i> TDI SCANNING OF AN ASYMPTOMATIC COMMON CAROTID ARTERY IN CHAPTER 2.....	145
FIGURE 5.11: VARIATION IN (A) MAXIMUM DILATION (B) MAXIMUM VELOCITY AND (C) MAXIMUM ACCELERATION WITH FLOW RISE TIME. THE PHYSIOLOGIC RANGE DERIVED FROM CHAPTER 2 DATA IS REPRESENTED BY THE DASHED LINES.....	147
FIGURE 5.12: VARIATION IN AWM RISE TIME, $T_{AWMPEAK}$ WITH FLOW RISE TIME, T_{QPEAK} . THE PHYSIOLOGIC RANGE DERIVED FROM CHAPTER 2 DATA IS REPRESENTED BY THE DASHED PINK LINES. $T_{AWMPEAK} = T_{QPEAK}$ IS REPRESENTED BY THE BLUE DASHED LINE.....	148
FIGURE 5.13: AWM (A) DILATIONS (B) VELOCITIES AND (C) ACCELERATIONS RESULTING FROM VARYING PEAK FLOW.....	149
FIGURE 5.14: VARIATION IN (A) MAXIMUM DILATION (B) MAXIMUM VELOCITY AND (C) MAXIMUM ACCELERATION WITH PEAK FLOW. THE PHYSIOLOGIC RANGE DERIVED FROM CHAPTER 2 DATA IS REPRESENTED BY THE DASHED LINES.....	150
FIGURE 5.15: AWM (A) DILATIONS (B) VELOCITIES AND (C) ACCELERATIONS RESULTING FROM VARYING FWHM.....	152
FIGURE 5.16: VARIATION IN (A) MAXIMUM DILATION (B) MAXIMUM VELOCITY AND (C) MAXIMUM ACCELERATION WITH FWHM. THE PHYSIOLOGIC RANGE DERIVED FROM CHAPTER 2 DATA IS REPRESENTED BY THE DASHED LINES.....	153
FIGURE 5.17:AWM (A) DILATIONS (B) VELOCITIES AND (C) ACCELERATIONS RESULTING FROM VARYING OUTFLOW IMPEDANCE.....	155
FIGURE 5.18: VARIATION IN (A) MAXIMUM DILATION (B) MAXIMUM VELOCITY AND (C) MAXIMUM ACCELERATION WITH OUTFLOW IMPEDANCE. THE PHYSIOLOGIC RANGE DERIVED FROM CHAPTER 2 DATA IS REPRESENTED BY THE DASHED LINES.....	156
FIGURE 5.19: AWM RISE TIME VARIATION WITH PHANTOM OUTPUT IMPEDANCE.....	157
FIGURE 6.1: VOLUME FLOW, Q APPLIED AT THE PUMP FOR VARIABLE GEOMETRY PRECISION MEASUREMENTS.....	162
FIGURE 6.2: REFERENCE MEASUREMENT GEOMETRY.....	163
FIGURE 6.3: TRANSDUCER – VESSEL ANGLE VARIATION MEASUREMENT GEOMETRY.....	164
FIGURE 6.4: CALCULATION OF THE TRANSDUCER-VESSEL ANGLE.....	165
FIGURE 6.5: SCAN PLANE VARIATION MEASUREMENT GEOMETRIES.....	165
FIGURE 6.6: TDI DERIVED AWM ENVELOPES FOR VESSEL DEPTHS OF (A) 20 MM (RED DASHED) AND (B) 44 MM (BLUE SOLID).....	167
FIGURE 6.7: VARIATION IN NORMALISED STANDARD DEVIATION OF DILATION, $SD(N)$ WITH VESSEL DEPTH.....	167
FIGURE 6.8: VARIATION IN NORMALISED MAXIMUM DILATION, $MX(N)$ WITH VESSEL DEPTH.....	167

FIGURE 6.9: SEGMENTED TDI FRAMES DURING WALL CONTRACTION FOR VESSEL DEPTHS OF (A) 20 MM AND (B) 44 MM. NOTE THE PRESENCE OF ADJACENT BLUE AND RED PIXELS PARTICULARLY APPARENT IN (B) INDICATING THE PRESENCE OF NOISE.	168
FIGURE 6.10: TDI DERIVED AWM ENVELOPES FOR TRANSDUCER-VESSEL ANGLES OF (A) 1° (RED DASHED) AND (B) 24.1° (BLUE SOLID).....	169
FIGURE 6.11: VARIATION IN NORMALISED STANDARD DEVIATION OF DILATION, SD(N) WITH TRANSDUCER-VESSEL ANGLE.	169
FIGURE 6.12: VARIATION IN NORMALISED MAXIMUM DILATION, MX(N) WITH TRANSDUCER-VESSEL ANGLE.	170
FIGURE 6.13: B-MODE IMAGES OF SCAN PLANES FOR (A) SCAN PLANE COINCIDENCE WITH THE CENTRAL VESSEL AXIS (B) 0.5 MM FROM THE VESSEL CENTRAL AXIS (C) 2 MM FROM THE VESSEL CENTRAL AXIS.....	171
FIGURE 6.14: TDI DERIVED AWM ENVELOPES FOR (A) THE VESSEL CENTRAL AXIS (RED DASH) (B) 0.5 MM OFF THE VESSEL CENTRAL AXIS (BLUE SOLID) (C) 2 MM FROM THE VESSEL CENTRAL AXIS (GREEN SOLID).	172
FIGURE 6.15: NORMALISED MAXIMUM DILATION, MX(N) VARIATION WITH SCAN PLANE.	172
FIGURE 6.16: TDI DERIVED AWM ENVELOPES FOR VESSEL DIAMETERS OF (A) 5.2MM (CONTACT PRESSURE-RED DASH) AND (B) 4.1MM (HIGH PRESSURE-BLUE SOLID).	173
FIGURE 6.17: VARIATION IN NORMALISED STANDARD DEVIATION, SD(N) OF DILATION WITH EXERTED TRANSDUCER PRESSURE.....	173
FIGURE 6.18: VARIATION IN NORMALISED MAXIMUM DILATION, MX(N) WITH EXERTED TRANSDUCER PRESSURE.....	173
FIGURE D.1: SCHEMATIC PLOTS OF PRESSURE AT LOCATION 'A' AND 'B' (PA AND PB), AND PRESSURE GRADIENT VARIATIONS (DP/DX) BETWEEN THE TWO.....	183

List of Tables

TABLE 1.1: PULSE WAVE VELOCITIES (PWV) AT THREE SITES WITHIN THE CIRCULATORY SYSTEM.	18
TABLE 1.2: YOUNG'S MODULUS OF ELASTICITY OF PLAQUE CONSTITUENTS ^{74,75}	22
TABLE 1.3: THESIS AIMS.	37
TABLE 2.1: AWM INDICES INVESTIGATED.	40
TABLE 2.2: SETTINGS FOR TDI AWM <i>IN VIVO</i> ACQUISITION. '*' INDICATES A PHILIPS RECOMMENDED SETTING.	43
TABLE 2.3: SOURCES OF VARIABILITY IN AWM INDICES.	48
TABLE 2.4: INTER-CYCLE COEFFICIENT OF VARIATION (COV) VALUES.	58
TABLE 2.5: INTER-LOOP COEFFICIENT OF VARIATION (COV) VALUES.	59
TABLE 2.6: T-TEST P-VALUES FOR DIFFERENCES IN PAIRED AWM INDICES.	60
TABLE 2.7: A COMPARISON OF MEAN BIASES & LIMITS OF AGREEMENT (LOA) FOR RESULTS GATHERED HERE AND TWO OTHER CAROTID ULTRASOUND INVESTIGATIONS IN THE LITERATURE. MONTAUBAN VAN SWIJNDREGT ET AL QUOTE RESULTS FOR THE TWO OBSERVERS SEPARATELY. THE SEPARATE UPPER AND LOWER LOA QUOTED IN THE SAME PAPER HAVE BEEN AVERAGED TO GIVE ONE LOA VALUE HERE.	63
TABLE 2.8: OBSERVER AVERAGED INTRA-OBSERVER REPEATABILITY COEFFICIENTS (RC) OBTAINED HERE AND LONG ET AL. THESE ARE QUOTED WITH MEAN AWM INDEX VALUES TO PROVIDE AN INDICATOR OF THE SCALE OF THE VARIABILITY.	64
TABLE 2.9: SUMMARY OF AWM INDEX VARIABILITY, AVERAGED OVER OBSERVERS AND SESSIONS.	65
TABLE 3.1: KEY PROPERTIES OF SINUSOIDAL AWM (1 – 5) AND PHYSIOLOGIC (A – B) WAVEFORMS APPLIED TO THE VALIDATION DEVICE FOR ACCURACY ASSESSMENT.	73
TABLE 3.2: ($MX_{B_LEFT} - MX_{B_RIGHT}$) FOR ALL ACQUIRED CINE LOOPS.	78
TABLE 3.3: CYCLE AND LOOP AVERAGED SD VALUES NORMALISED TO MAXIMUM DILATION FOR EACH VALIDATION DEVICE WAVEFORM.	82
TABLE 3.4: COMPARISON OF TDI DERIVED MAXIMUM DILATION, MX_{TDI} WITH DEVICE MAXIMUM DILATION, MX_0 FOR 5 SINUSOIDAL WAVEFORMS.	84
TABLE 4.1: PHANTOM MATERIAL PROPERTIES FOR CONSIDERATION.	91
TABLE 4.2: PROPERTIES OF PHANTOM MATERIALS IN THE LITERATURE & <i>IN VIVO</i> VASCULAR TISSUE.	93
TABLE 4.3: SUMMARY OF CANDIDATE TMM AND VMM LIMITATIONS.	98
TABLE 4.4: PERCENTAGE BY MASS CONTRIBUTION OF CONSTITUENTS IN THREE GELATIN TMM RECIPES, WITH CA24 PRESERVATIVE AND SCATTERERS (A), WITH CA24 AND NO SCATTERERS (B) AND FORMALDEHYDE AND NO SCATTERERS (C).	100
TABLE 4.5: A SUMMARY OF THE PROPERTIES OF THE MATERIAL TANGENT ELASTIC MODULI, E_T INVESTIGATED.	104
TABLE 4.6: TANGENT MODULI OF ELASTICITY, E_T AT 5 % & 50 % STRAIN FOR VMM AND TMM.	108
TABLE 4.7: INTRA-BATCH & INTER-BATCH VARIABILITY IN TANGENT MODULUS OF ELASTICITY, E_T AT 5 % STRAIN DEMONSTRATED BY THE RESPECTIVE STANDARD DEVIATIONS, $SD_{INTRA-BATCH}$ AND $SD_{INTER-BATCH}$	109
TABLE 4.8: COMBINED INTER-BATCH AND INTRA-BATCH VARIABILITY, $SD_{OVERALL}$ IN TANGENT MODULUS OF ELASTICITY AT 5% STRAIN.	109
TABLE 4.9: VARIATION IN VMM TANGENT MODULUS, E_T , WITH FREEZE-THAW CYCLE FOR 5 % STRAIN. VALUES REPRESENT THE AVERAGE OVER BATCHES OF TYPICALLY EIGHT SAMPLES. QUOTED ERRORS REPRESENT ± 1 SD OF THE INTRA-BATCH MODULI.	112
TABLE 4.10: MEASURED SPEED OF SOUND IN MATERIAL SAMPLES. QUOTED ERRORS COMBINE ± 1 SD OF THE INTRA-SAMPLE AND INTER-SAMPLE MEANS.	116
TABLE 4.11: ATTENUATION COEFFICIENTS FOR VMM & TMM AT 5 MHZ & 12 MHZ.	117

TABLE 4.12: PHYSICAL PROPERTIES SUMMARY FOR VMM AND TMM.....	118
TABLE 5.1: OBSERVER AND DATA ACQUISITION SESSION AVERAGED AWM INDICES FOR 12 ASYMPTOMATIC CCA SEGMENTS SCANNED USING THE TDI/AWM SOFTWARE TECHNIQUE.....	125
TABLE 5.2: OBSERVER AND DATA ACQUISITION SESSION AVERAGED TEMPORAL AWM PARAMETERS FOR 12 ASYMPTOMATIC CCA SEGMENTS SCANNED USING THE TDI/AWM SOFTWARE TECHNIQUE.....	125
TABLE 5.3: BMF CONSTITUENTS BY PERCENTAGE MASS ¹⁴⁷	132
TABLE 5.4: TDI ACQUISITION SETTINGS.....	137
TABLE 5.5: MAXIMUM AND MINIMUM CYCLE-AVERAGED DILATIONS FOR THE FOUR FLOW WAVEFORM SHAPES.....	139
TABLE 5.6: RANGES AND DEFAULT VALUES OF THE FLOW CHARACTERISTICS & OUTPUT IMPEDANCE USED.....	142
TABLE 5.7: A COMPARISON OF AWM SECONDARY MINIMUM VELOCITIES IN THE LAST 0.1 S OF THE AWM CYCLE GENERATED BY 0.50 S FWHM AND 0.90 S FWHM FLOW.	151
TABLE 5.8: A COMPARISON OF AWM PRIMARY MINIMUM VELOCITIES GENERATED BY FLOW OF 0.25, 0.50 AND 0.90 S FLOW CYCLES.....	154
TABLE 5.9: SUMMARY OF MAXIMUM DILATIONS, MAXIMUM VELOCITIES, MAXIMUM ACCELERATIONS AND RISE TIMES OBTAINED USING THE PHANTOM COMPARED TO THE <i>IN VIVO</i> VALUES.	158
TABLE 6.1: VARIATIONS IN SCANNING GEOMETRY & TRANSDUCER PRESSURE AND THEIR MAIN EFFECTS.	161
TABLE 6.2: REFERENCE SCANNING GEOMETRY AND RANGE OF GEOMETRY TESTED.	163
TABLE C.1: COMPARISON OF E_T VALUES OBTAINED AT TWO CANDIDATE STRAIN RATES FOR MECHANICAL TESTING.....	182
TABLE D.1: VARIATION OF FLOW, Q_A AND PRESSURE, P_A AT LOCATION 'A' IN THE PHANTOM ON THE APPROACH AND RETREAT OF A SINGLE FLOW CYCLE TRANSMITTED FROM THE PUMP.	184

Chapter 1 Cardiovascular disease and assessment of disease severity

1.1 Cardiovascular Disease (CVD), Atherosclerosis and Stroke

1.1.1 Introduction

Cardiovascular Disease (CVD) is the largest cause of death accounting for one third of all deaths worldwide¹. Diseases of the blood vessels and heart fall under the umbrella of CVD, including coronary heart disease, cerebrovascular disease, peripheral vascular disease and heart failure. These are predominantly manifest in the form of atherosclerosis, a chronic condition thought to be largely a result of overexposure to universally recognised risk factors such as high blood pressure, tobacco smoke and high dietary saturated fat levels^{2,3}. Atherosclerosis is a form of arteriosclerosis, where in addition to diffuse thickening and hardening of the arteries, there are focal areas of degeneration of the wall. The disease is a phenomenon of the medium and large arteries such as the Carotid artery and the Aorta (Figure 1.1). The lesions, also known as plaques, typically form in areas of the circulatory system where there is branching (such as the carotid bifurcation), tortuosity (such as the internal carotid artery) and confluence⁴.

Growth of the lesions may ultimately lead to thrombosis, embolism or to a lesser extent, direct occlusion of the vessel by the lesion. These events can result in inadequate blood supply to tissue distal to the lesion and consequent loss of tissue function and in extreme cases, death. An event in the coronary territory is known as a Myocardial Infarction (MI) or heart attack, and such an event in the cerebral territory is known as an Ischaemic Stroke.

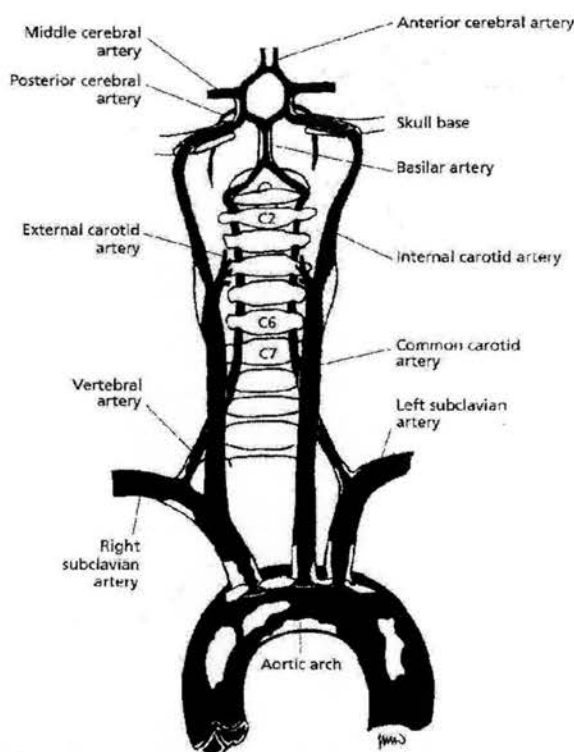


Figure 1.1: Sites of atheroma formation in arteries supplying the head and neck⁵. Reprinted from 'Stroke, A practical guide to management', 2nd edition, Warlow, C.B. et al, Copyright (2001), with permission from the Blackwell Science.

Stroke overall accounts for approximately 30 % of CVD deaths and of these 80 % are estimated to be ischaemic strokes⁶. It is also the 'most important single cause of severe disability in people living in their own homes'⁷. As such it is a heavy burden on health service resources. Of ischaemic strokes (and transient ischaemic attacks) there are four main categories of cause (Figure 1.2)⁶. Embolic and thrombotic events, complications of atheroma plaque rupture, are most common accounting for 50 % of all ischaemic strokes.

Given the typical locations of atheroma formation there is a high probability that a given atherothromboembolic ischaemic stroke may have resulted from carotid artery disease. As such, the following sub-sections while covering aspects that are common to atheroma in any location in the circulatory system, focus upon carotid disease in particular.

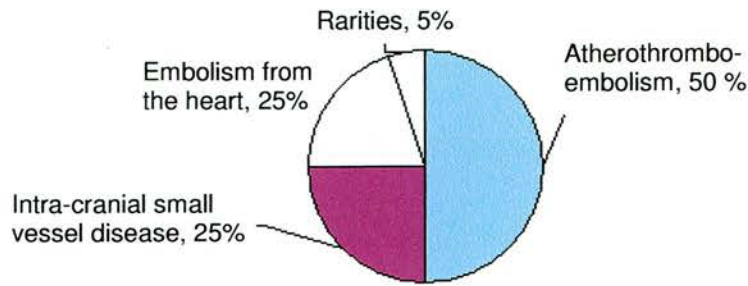


Figure 1.2: Approximate distribution of cause of cerebral ischaemic events (both permanent & transient) in white populations⁶.

1.1.2 Atherogenesis and changes in the artery wall

Atherogenesis, the formation of atherosclerotic lesions is a complex process, characterised by changes in the artery wall. It is informative to consider first the structure of the healthy artery wall. For a more detailed account the reader is referred to 'MacDonald's Blood flow in arteries'⁸.

The wall comprises of three discrete concentric sections, the intima, the media and the adventitia (Figure 1.3). The intima lines the lumen, and is characterised by a layer of endothelial cells which act as a permeable layer for cell and molecule transport in and out of the artery wall. It also contains an extracellular matrix of connective tissue. The intima is surrounded by the media, the thickest layer. It is approximately ten times thicker than the intima and is judged to dominate the arteries biomechanical properties. It consists of concentric layers or lamellae of smooth muscle cells (SMC) and elastin. Isolated elastin and collagen fibres lie between the lamellae. The outermost layer of the wall, the adventitia, contains collagen fibres, vasa vasorum (small blood vessels supplying the vessel) and nerves amongst other constituents. The intima, media and adventitia are separated by two complex elastic laminae.

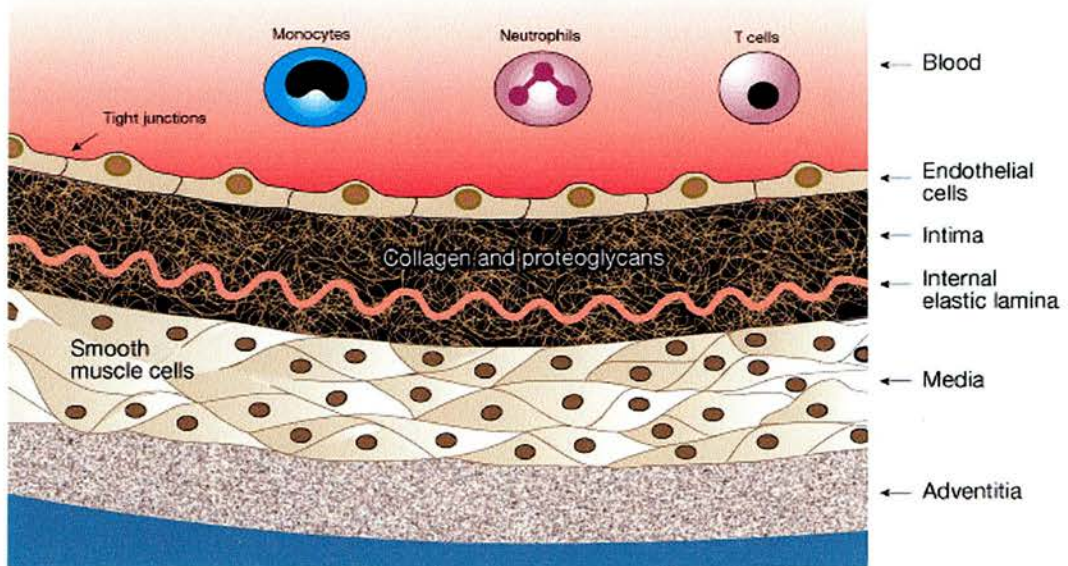


Figure 1.3: Cross sectional view of the artery wall⁹. Reprinted from Nature, 407, Lusis, A.J. et al, 'Atherosclerosis', 233 - 241, Copyright (2000), with permission from Nature Publishing Group.

The earlier stages of lesion formation affect only the intima¹⁰ and are characterised by accumulation of Low density Lipoprotein (LDL) from the blood, followed by macrophages (or scavenger cells). The macrophages are derived from monocytes and lymphocytes in the blood which are attracted as a result of an inflammatory response of the artery wall to LDL accumulation.

Still confined to the intima, the early lesions develop further when the macrophages take up LDL to form fat globule laden cells known as foam cells. The foam cells eventually undergo apoptosis, spilling their lipid content and other cell debris into the extracellular space. This acts to increase wall thickness. Over time these can act to form and develop a lipid rich core, characteristic of the more advanced atherosclerotic lesion. Initially lesion growth associated with the formation of the lipid core is directed outwards towards the media, minimising obstruction of the lumen however as the lesion size increases it begins to encroach on the lumen.

Involvement of the media and adventitia occurs in advanced lesions. The presence of agents such as homocysteine initiates SMC migration from the media to the intima. Proliferation of SMC in the intima is also initiated which in turn produces an extracellular connective tissue matrix forming a thin fibrous cap over the lipid core. Calcium deposits are generated by SMC activity. White cell, LDL and foam cell accumulation may also occur in the media and the adventitia. Vasa vasorum also extend from the adventitia to the lesion providing the lesion with a blood supply. In tandem with the physiological changes associated with atherogenesis, the physical properties of blood flow, vessel geometry and wall mechanics change with age and degree of atheroma. These are discussed in section 1.4.

Atherogenesis is a complex process, and many of the finer details are yet to be understood. Main aspects of lesion development are outlined above, and there is scope for significant variation in plaque structure and composition. The reader is referred to a number of sources for more detailed descriptions of atherogenesis^{3,9-11}.

1.1.3 The high risk plaque

The advanced atherosclerotic lesion as described in the previous section on the whole is thought not to be a direct cause of ischaemic events. However acute complications may result from the lesion, which in turn could cause a transient or permanent ischaemic event. Firstly, intact plaques encourage thrombosis by the release of chemical agents which may increase the plaque size ultimately occluding the vessel, or result in emboli with the potential for distal vessel occlusion. Secondly, certain plaques are more likely to become unstable and be prone to rupture. This in turn may initiate thrombosis and/or embolism, leading to an ischaemic event.

Numerous factors have been found to be associated with plaques with a propensity to rupture though the exact importance and association of each are not fully understood^{3,11,12}. These include the presence of inflammatory agents, which may degrade the connective tissue in the lesion, mechanical stresses which act directly to tear the plaque and structural weaknesses resulting from plaque composition. The

primary clinically applied risk factor is the degree of narrowing or stenosis and this is discussed in Section 1.2.

1.1.4 Clinical management of carotid atherosclerosis

Surgery is the primary method of treatment for those with severe disease (70-99 % stenosis). The procedure is known as Carotid Endarterectomy (CEA) and involves removing the affected segment. During surgery the open segment is bypassed with tubing to maintain cerebral flow and stitched closed following plaque removal, sometimes using a patch of prosthetic material or vein from a remote site. There are several complications associated with CEA, including cardiac failure, myocardial infarction, hypertension and hypotension, cranial nerve injury, wound infection and peri- and post-operative stroke.

Large scale randomised controlled trials for risk/benefit assessment of surgery were carried out in both Europe and North America establish the patient group that would benefit most from CEA^{13,14}. They both found that risk of stroke was only sufficiently great to merit the risk of preventative surgery in symptomatic individuals with a stenosis of 70-99 %. The European Carotid Surgery Trial (ECST) evaluated the difference in risk of fatal or disabling stroke or surgical death between those who underwent CEA and a control group at 3 years following surgery¹³. Risks of 6 % and 11 % were obtained respectively, with $p < 0.05$ for the 5 % difference.

However, not all carotid stenoses ≥ 70 % result in strokes. For example the North American Symptomatic Carotid Endarterectomy Trial (NASCET) found that 75 % of symptomatic patients with a severe stenosis did not stroke. Furthermore, individuals with a carotid stenosis less than < 70 % have a finite, if smaller risk of stroke.

1.1.5 Summary

Cardiovascular disease and atherosclerosis have been introduced. The clinical burden due to CVD and stroke in particular is large. Processes by which acute disability and life-threatening events may arise as a result of atheroma have also been identified, with a particular focus on carotid artery disease, an important cause of

stroke. Surgery is the primary method of management for patients with severe disease. The decision to operate is dependent on the degree of stenosis in the artery, as evaluated by diagnostic imaging. Techniques in clinical use are discussed in Section 1.2.

1.2 Clinical Imaging of carotid artery disease

Currently, degree of stenosis is measured by characterising geometry of the stenosis or blood flow through a stenosis. X-ray and Magnetic Resonance (MR) angiography both deduce degree of stenosis by demonstrating the change in geometry of the arteries in anatomical imaging. Ultrasound imaging provides functional data, assessing the degree of stenosis by measuring change in blood flow velocities induced by the stenosis.

1.2.1 X-ray angiography

This procedure is the gold standard in carotid stenosis investigation. The procedure involves selective catheterisation of the common carotid artery through insertion into the femoral artery, followed by injection of a bolus of X-ray contrast agent. Digital fluoroscopic imaging is typically carried out to visualise the contrast. Image subtraction methods are available, providing an image predominantly of the contrast material, thereby providing better contrast resolution. Spatial resolution typically varies between 0.1 and 0.4 mm¹⁵.

The degree of stenosis is defined by the ratio of the lumen diameter at the tightest region of the stenosis to the lumen diameter of an unaffected region of the carotid arteries. The exact choice of region used as the denominator varies from centre to centre. X-ray angiography's status as the gold standard in carotid artery stenosis assessment originates from the use of the technique in ECST and NASCET trials cited earlier. At this time it was the only accurate imaging method available for stenosis assessment. 'Reference standard' might be more appropriate a term, since there are considerable limitations in using angiography. Error in stenosis measurement is inherent, given the 2D projection of the 3D data on to the film or intensifier screen. This is overcome to an extent by bi-planar techniques, but some

centres do not have access to these. There is also a considerable risk associated with the procedure; the catheter may disrupt plaques producing emboli, potentially causing stroke. Thrombus can form on the catheter tip. The catheter may also dissect the artery wall during the procedure. Such complications contribute towards a risk of TIA or Stroke of approximately 4 %, which differ according to expertise and experience of the personnel performing the procedure¹⁶.

1.2.2 Magnetic Resonance Angiography (MRA)

Magnetic Resonance Angiography generates 2D and 3D images of the extra-cranial circulation, including the carotid arteries. Time of flight and phase contrast techniques are most common. The intensity of the blood in the image is proportional to the velocity of the blood. The degree of stenosis can be calculated in the same way as in X-ray angiography.

Advantages of the technique are the non-invasive nature and high resolution (typically 0.5 - 1.0 mm^{17,18}) in optimum conditions of laminar flow in mildly stenotic vessels. However, image quality is significantly impeded by the inherent nature of heavily diseased arteries. Reduced flow through a stenosis, turbulence in blood flow at the high velocities produced by a tight stenosis, and the associated retrograde flow can diminish, and in extreme cases, completely remove signal from the region of interest.

The diminishing signal associated with increase in degree of stenosis results in a systematic overestimation of the degree of stenosis¹⁹ which has serious implications clinically as the use of MRA alone would result in over-selection of patients for carotid endarterectomy. Current research into the use of contrast agents seeks to improve the technique by increasing the MR signal intensity²⁰.

There are several contraindications of the technique. These include claustrophobia or anxiety of the patient on being scanned, inability of the patient to lie still for the several minutes required to perform the scan due to their poor health and the presence of metal in the patient due to pacemakers or aneurysmal clips or similar

devices. Levy, Baum and Carpenter excluded 3 % of their sample from studies due to contraindications²¹. Magnetic resonance angiography is also relatively expensive.

1.2.3 Ultrasonography

Ultrasonography provides both anatomical and functional information on the cerebral circulation. While in principle the same geometrical technique of stenosis assessment could be employed with B-mode ultrasound as with X-ray and MR angiography, Doppler colour flow and spectral Doppler are predominantly used. Historically, inadequate B-mode resolution excluded its use for geometrical evaluation. Shadowing due to calcification, the presence of echolucent thrombus and observation of an incorrect 2D scan plane, where the maximum extent of stenosis is not displayed can lead to the incorrect derivation of stenosis degree from the B-mode images²².

Virtually all forms of ultrasound employ the same basic pulse-echo principle, of transmitting an ultrasonic pulse from a transducer and receiving reflected echoes. According to the nature of the target upon which the ultrasound is incident, changes in intensity and phase of the reflected sound pulse are recorded. These are used with appropriate signal processing to generate different forms of ultrasound image. The changes in phase in particular exploits the Doppler effect and may be used to deduce velocities of structures and fluids moving relative to the beam.

Colour Flow Imaging (CFI) is routinely used in carotid disease assessment. The colour flow information is superimposed on the B-mode image (Figure 1.4). The colours represent the varying magnitude in the component of the blood velocity in the direction of the ultrasound beam, as determined by the varying phase in the reflected ultrasound. The modality can demonstrate a number of interesting features including post-stenotic turbulence and recirculation, however along with B-mode it is primarily used to examine the anatomy of the stenosis and identify the location of the greatest lumen reduction in order that quantitative interrogation may be carried out with spectral Doppler.

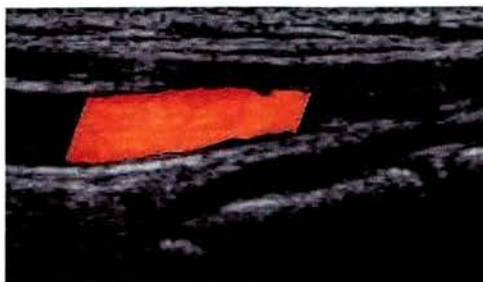


Figure 1.4: A Colour flow image of a healthy common carotid artery. Colour pixels representing flow velocity are superimposed on a B-mode image which demonstrates tissue anatomy in the scan plane.

Spectral Doppler ultrasound allows the interrogation of small volumes within the image and provides a time varying waveform of the frequency shift which is representative of the velocity of the blood with a temporal resolution of the order of 10 ms^{23} . The velocity component measured in the direction of the beam by the scanner is corrected by a user-defined vessel-beam angle in order to obtain the velocity of the blood. The brightness of the trace at a particular point is related to the volume of blood moving at the velocity corresponding to that Doppler shift.

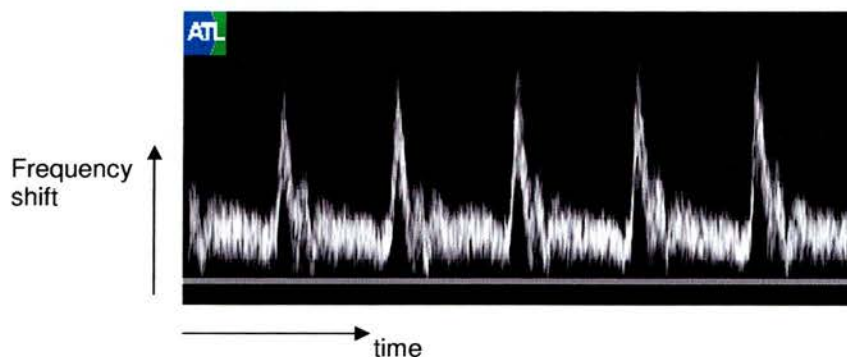


Figure 1.5: Spectral Doppler trace of an asymptomatic common carotid artery.

A representative index is required from the velocity waveform with which correlations with degree of stenosis may be drawn. However there is no single universally recognised index; a number are employed by centres worldwide. These include single parameters such as the internal carotid peak systolic velocity (ICPSV) and common carotid end diastolic velocity (CCEDV), and ratios such as

ICPSV/CCEDV. Several studies have compared angiography-measured stenoses with spectral Doppler indices to find an index which provides strong correlation with degree of stenosis. The strength of correlation between the two is especially important in the range of 70-99 % stenosis since it was this group that was identified to be at a great enough risk of stroke to warrant the risk of carotid endarterectomy. Moneta et al calculated the ratio of peak systolic velocities of internal carotid arteries to common carotid arteries, ICA/CCA PSV, for 100 angiograms of stenosed carotid arteries²⁴. ICA/CCA PSV values were compared to the angiogram-calculated degree of stenosis and it was found that arteries with a ratio greater than 4.0 were 'excellent' indicators of the high risk 70 - 99 % stenosis group.

As with other imaging modalities, ultrasound has limitations in assessing degree of stenosis. Calcification of the vessel wall is a relatively common phenomenon in heavily diseased arteries. The resultant heavy attenuation creates acoustic shadows in areas of interest and no information may be obtained on flow or anatomy in the areas of the shadow unless an alternative scan plane with less calcification can be found. Internal carotid arteries, especially those which are heavily diseased, are often tortuous and dive deep into the skull. The associated attenuation, reduced penetration and weaker reflections due to the deviation from a normal beam-vessel angle make it more difficult to obtain meaningful images of areas of interest.

In order to convert Doppler frequency shift to velocity an angle correction is applied by the sonographer. This is applied by positioning a marker on the screen in the direction of flow. The application of the angle correction is not without error. Typically flow parallel to the vessel wall is assumed. This is not always the case, especially in stenosed regions where flow is complex and discrepancies between the true direction of flow and the assumed direction may be as large as 25 degrees²⁵. A further source of uncertainty is geometrical spectral broadening of the received ultrasound. This is an effect of the finite size of the Doppler aperture can typically lead to overestimation in maximum velocity of 20-30 %²⁵.

Operator dependence of the results is also another shortcoming of quantitative measures obtained using the modality. In the Trømso study intra-observer variability was measured using two observers who scanned 51 volunteers with varying degree of stenosis²⁶. Variation in stenosis assessment by three different methods was assessed, velocity measurement, diameter reduction and area reduction. Reproducibility in velocity measurement was found to be worst, with a median difference in the degree of stenosis between observations of 10.8 % and limits of agreement of ± 26.5 %. Velocity measurements are also subject to variation across different scanners which have varying performance²⁷. Despite these shortcomings, ultrasound is considered to be ‘...the best way to diagnose stenosis that is severe enough for carotid endarterectomy to be worthwhile’⁵.

1.2.4 Summary

The clinical techniques described in Section 1.2 are based upon assessment of lumen reduction. It is clear that lumen reduction is insufficient to predict which patients are at risk of plaque rupture. Sections 1.3 and 1.5 discuss other methods of atherosclerosis assessment.

1.3 Geometric and morphological methods of carotid disease assessment

1.3.1 Measurement of wall thickness

It is well established that wall thickness increases with age and onset of atherosclerosis²⁸. Measurement of artery wall thickness is of value in a number of research areas. Studies such as the ARIC study have investigated the relationship between the risk of cardiovascular events and carotid wall thickness²⁹. This particular study demonstrated increased risk of a first stroke by a factor between 3.6 and 8 for a mean carotid Intima-Media thickness (IMT) of ≥ 1 mm when compared to < 0.6 mm. Measurement of wall thickness is also of interest from a mechanical perspective in the derivation of the elastic modulus of wall in order to characterise different levels of disease³⁰. The reader is referred to Simon et al for a more detailed account of the application of IMT measurements³¹.

Ultrasound offers the only non-invasive *in vivo* method for wall thickness evaluation. Both B-mode and M-mode modalities have been employed. Wall thickness in this context is defined as the Intima-Media thickness (IMT), since the adventitia may not easily be differentiated from surrounding tissue in the grey scale image³². Using B-mode, approaches include manual placement of distance cursors on the lumen-intima boundary and the media-adventitia boundary at a small number of points³³, manual delineation of the boundaries over a segment of artery³⁴ (both for single B-mode frames) and manual approximate boundary location followed by computerised edge detection over multiple sites and multiple time frames³⁵. Typically the posterior wall only is used in IMT measurement since the identification of the boundaries at the anterior wall is impeded by superimposed multiple reflections³⁶.

Accuracy of IMT measurement by B-mode has improved with advances in B-mode resolution (typically 0.5 - 1.0 mm at the time of writing). However, despite the number of clinical studies carried out measuring IMT there is still controversy over whether accuracy is adequate given the small physiologic range of IMT and the small magnitude of IMT itself. One particular study compared intravascular ultrasound,

extravascular ultrasound and histologic measurements of excised arteries. A mean difference between extravascular and histologic far wall measurements of -0.12 mm (SD = 0.13 mm) was obtained³⁷. Using computerised edge detection another study investigated reproducibility, and a coefficient of variation of 3.46% was obtained for IMT measured at diastole³⁵.

1.3.2 Plaque characterisation for identification of high risk plaques

Many publications have attempted to characterise plaques by their appearance using various modalities including Magnetic Resonance Imaging (MRI), X-ray Computed Tomography (CT) and extra- and intra-vascular B-mode ultrasound³⁸.

The varying T1 and T2 relaxation times along with proton density have been exploited with MRI in order to determine plaque constituents³⁸. Fibrous tissues exhibit shortened T1 times, lipids exhibit shortened T2 times and calcified regions have a relatively low proton density. These characteristics produce different appearances in MRI images according to how the image is weighted, for example, in a T1 weighted image, the low T1 of fibrous regions will be visible with high signal intensity. Furthermore, plaque components volumes may be quantified: Trivedi et al found good agreement between *in vivo* MRI and histologically evaluated fibrous cap and lipid core contents in 25 carotid plaques³⁹. While having relatively good resolution (the study above used voxel sizes of $0.4 \times 0.4 \times 3.0$ mm³) MR still suffers from being relatively expensive, requiring specialist equipment and can typically sometimes have acquisition times of the order of minutes in which the patient must remain still.

In addition to using ionising radiation, CT is more limited than MRI in its ability to distinguish different plaque constituents given the relatively small differences in X-ray attenuation between different soft tissue types at diagnostic energies⁴⁰. However, it can distinguish calcium deposits from surrounding soft tissue, and the extent of the deposits may be quantified⁴¹.

Both intra- and extra-vascular ultrasound provides a greater dynamic contrast range in terms of plaque constituents than CT, in addition to being non-ionising and relatively inexpensive. The appearance of the plaque in the image is determined by the changes in acoustic impedance as the beam passes across boundaries between the different constituents. In broad terms, plaque appearance on B-mode images can be seen to vary depending on its composition. Lipids and haemorrhage are typically echolucent, whereas calcification and fibrous tissue typically appear as echogenic.

Many extravascular studies have been carried out in this area, with varying degrees of success⁴²⁻⁴⁶. One study assessed carotid plaques by duplex ultrasound prior to carotid endarterectomy, and categorised them as predominantly echolucent, heterogeneous or predominantly echogenic, as defined by the European Plaque Study Group. Post-endarterectomy video frames of the excised plaques were subjected to automated analysis which calculated volumes of the plaque constituents including lipid deposits, calcification and fibrous intimal thickening. No association was found between volumes of the constituents and their echogenicity, intra-observer agreement was moderate and inter-observer agreement was found to be poor. A further duplex study by Tegos et al also demonstrated lack of association between carotid plaque echogenicity and histopathologic composition, though a positive association was found with retinal and cerebrovascular symptoms⁴⁷.

1.3.3 Summary

Diagnostic techniques for wall thickness measurement and plaque characterisation have been explored. Whether existing techniques for wall thickness measurement are sufficiently accurate and precise is questionable. Qualitative plaque characterisation shows poor reproducibility, while quantitative characterisation appears to show more promise. These techniques exploit the change in composition and structure of the artery wall. In parallel with these changes the artery wall undergoes mechanical changes, which are described in the next section and offer scope for characterisation of the artery wall and possible identification of the high risk plaque.

1.4 The mechanical properties of arteries

The stress – strain response of the artery vary widely, according to the distending forces applied by blood pressure and the composition of the wall, which in turn varies with site in the circulatory system. Of more potential clinical value however, is the fact that the wall mechanical properties are known to vary with age and level of disease. This provides motivation for investigation of the exact nature of these properties and in turn, relation to clinical events such as ischaemic stroke. A review of measured mechanical properties of healthy and diseased arteries is provided, followed by a discussion of available techniques to quantify these properties *in vivo* in the next section.

The properties of the healthy and diseased arteries are discussed in turn. Discussion is provided of both diffuse changes associated with aging and early stage atherosclerosis and focal changes associated with developed atherosclerosis. There are a large number of parameters that may be used to express the different aspects of the stress – strain response of the artery (Appendix A). The parameters often have confusingly similar names, such as stiffness parameter (β), Distensibility (DC), and compliance (CC), and care is needed to avoid ambiguity when discussing arterial biomechanics. In the following sections, ‘elasticity’ is used as a generic term to describe the extension of the wall for a given distending force where a ‘elastic’ wall is relatively extensible when subject to a given distending force.

The parameters available are useful in the empirical sense to compare properties of vessels perhaps from different sites or between individuals. However, given the complex nature of the artery wall these are limited in their ability to provide a complete picture of the behaviour of the artery with which one could hope to evaluate and understand the mechanical influences in situations such as plaque rupture and graft failure. Towards this end there has been the development of a number of ‘constitutive’ equations in the literature, which describe the stress-strain relationship of the artery wall. These are based on experimental observations and

make varying assumptions about such characteristics as incompressibility and anisotropy of the wall. They are also highly specific to particular arterial sites and levels of stress and strain. While of importance this area is not a focus of this thesis and the reader is referred to reviews of the subject by Zhao and Humphrey^{48,49}.

1.4.1 The healthy artery

An effective demonstration of the inherent mechanical behaviour of the artery wall is the stress-strain curve. These or related forms have been measured *in vivo* and *in vitro* by several studies^{50,51,51,52}. An example is that obtained by Topoleski et al from compressive tests on excised human aortoiliac segments from healthy 20 - 30 year old individuals (Figure 1.6).

The circles in Figure 1.6 represent an initial phase of compression 15 cycles long, and the solid line represents a second phase of compressions of the same length carried out 10 - 15 minutes later. One can see the gradient of the curve and therefore the effective moduli of the wall at a given moment depend on the stress applied, whether the vessel is being loaded or unloaded and the loading history of the segment in question. The observed hysteresis and relaxation (the latter is the phenomena of increased strain under constant stress) are illustrations of the viscoelastic non-linear behaviour of the asymptomatic artery wall.

Due to its viscoelastic properties, the distension of the artery wall is also dependent on the rate of application of the distending force. This is illustrated by an increase in 'stiffness' with frequency of distension which has been measured in both healthy and diseased tissues⁵³⁻⁵⁵. For example, Bergel reported an increase in E_{dyn} of 63 % from 0 Hz to 2 Hz for a dog's excised carotid artery, measured by distension on inflation.

The elasticity of the artery vary from site to site within the circulatory system. Some examples measured *in vivo* in humans, expressed using the pulse wave velocity are given in Table 1.1. One can see the marked differences, the abdominal aorta being markedly more distensible than the peripheral brachial artery.

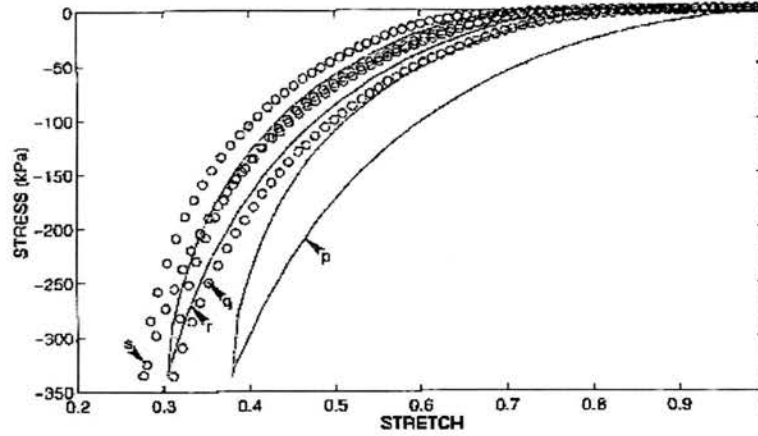


Figure 1.6: Stress-strain behaviour of an excised human aortoiliac artery. Reprinted from the Journal of Biomedical Materials Research, 35, Topoleski, L.D.T. et al, 'Composition- and history-dependent radial compressive behaviour of human atherosclerotic plaque', 117 - 127, Copyright (1997), with permission from John Wiley and Sons Inc.

Site	PWV/ms ⁻¹
Abdominal Aorta	5.7 ⁵⁶
Brachial	15.1 ⁵⁷
Common Femoral	8.9 ⁵⁸

Table 1.1: Pulse Wave Velocities (PWV) at three sites within the circulatory system.

The variation between sites is due to differences in composition and geometry. These differences and *in vitro* and *in vivo* measured distensions have lead to deductions about the arrangement of components within the artery wall. It has been shown that three constituents of the wall; collagen, elastin and smooth muscle cells (SMC), their varying elasticity, arrangement, proportion and in the case of SMC, activity, together with the distending force dictate the overall dynamic behaviour of the vessel wall^{57,59,60}. Collagen and elastin are passive components of the artery wall, responding to stresses applied by the blood. In contrast SMC dictate the elasticity actively, varying tension in the wall by relaxing or contracting. A number of studies have deduced the elastic moduli of the passive components. Armentano obtained values of $0.05 \pm 0.02 \times 10^6$ Pa for elastin, and $11 \pm 5 \times 10^6$ Pa for collagen^{50,51}, making collagen over 100 times stiffer than elastin.

In the simplified case of inactive SMC, obtained in excised canine arteries, the elastic moduli of the wall has been measured to be over 20 times greater at 180 mm Hg pressure compared to that at 20 mm Hg⁶¹. These reflect a greater influence on the vessel properties of elastin at low pressures and collagen at high pressures, illustrated by an increase in gradient of the stress-strain curve with compressive strain in Figure 1.6. This is consistent with a parallel arrangement of elastin and collagen, where as stress applied increases, the stiffer collagen fibres become increasingly recruited to the stretch, and have an increasing influence on the effective moduli of the artery for a given stress^{51,61-63}. Smooth muscle cell activity can have a significant effect on the elastic modulus. The area is complex and the reader is referred to detailed studies by Bank et al^{52,57,63,64}. However, an example of the scale of the effect of SMC activity is the 42 % decrease in elastic modulus in the brachial arteries on SMC relaxation using the vasodilator nitroglycerin.

The central arteries have relatively high elastin content and are described as elastic, while the peripheral arteries, such as the brachial artery have a relatively high collagen and SMC content and are described as muscular, reflected by PWV values in Table 1.1. The carotid arteries lie between the two extremes.

1.4.2 Effects of aging & atherosclerosis

The preceding account describes the 'healthy' case. Aging and early stage atherosclerosis causes diffuse changes to occur in the artery structure and composition and therefore, wall elasticity.

1.4.2.1 Diffuse changes in wall thickness

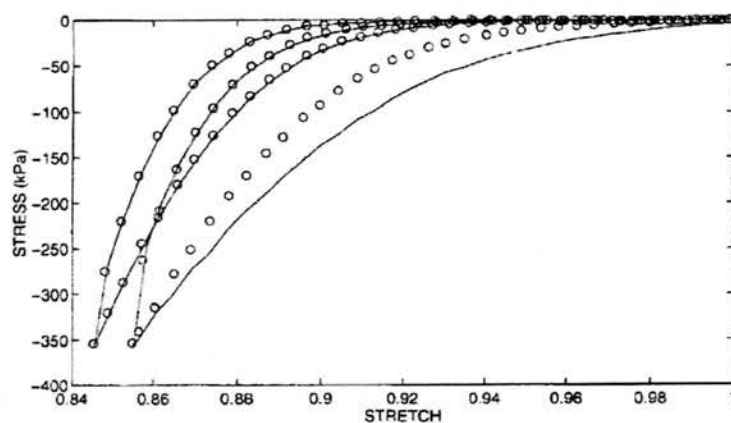
The increase of wall thickness with age and onset of atherosclerosis is important in a description of the change in wall elasticity. Howard et al reported the variation in intima-media thickness (IMT) with age; measured using B-mode ultrasound an increase of 0.01 mm / year was deduced²⁸. The same study reported IMT values in the range 0.3-0.25 mm for a sample of men and women aged between 45 - 64 (n = 13, 870).

Intuitively, one might expect an increase in stiffness with wall thickness; however the increase in structural stiffness induced by wall thickening is offset by a fall in material stiffness resulting in unchanged or even decreased functional or overall stiffness. This was demonstrated by Riley et al, using B-mode ultrasound, in arteries with an IMT of 0.8 mm or less, the 90th percentile value of the sample⁶⁵. Stiffness was expressed by the change in vessel diameter between diastole and systole, corrected for variations in blood pressure and height. For data averaged over the sample subgroup of white females (n = 4538), corrected diameter change was 0.385 mm for a 0.45 mm thick wall compared to 0.43 mm for a wall 0.8 mm thick.

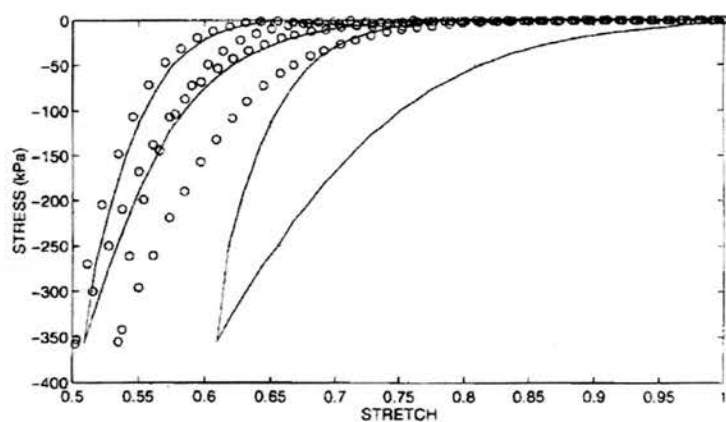
An increase in stiffness with wall thickness was reported in the same study, though only for arteries with IMTs greater than 0.8 mm, the top 10 % of the measured population. This is thought to be due to the increase in collagen content and reduction in elastin content associated with age. Disorder in the layered structure of the wall also increases with age and the elastic lamellae begin to fray from fatigue transferring more load to the stiffer collagen fibres⁶⁶. An increase in stiffness in the human carotid artery with age was found by Hansen et al using an ultrasonic phase-locked echo tracking system⁶⁷. The mean stiffness parameter, β measured in the 15 year old group was 4.1 ± 0.7 (n = 16), compared to 13.2 ± 3.6 (n = 11) for the 70 year old group. Other studies report comparable results⁶⁸⁻⁷⁰.

1.4.2.2 Focal changes in wall properties

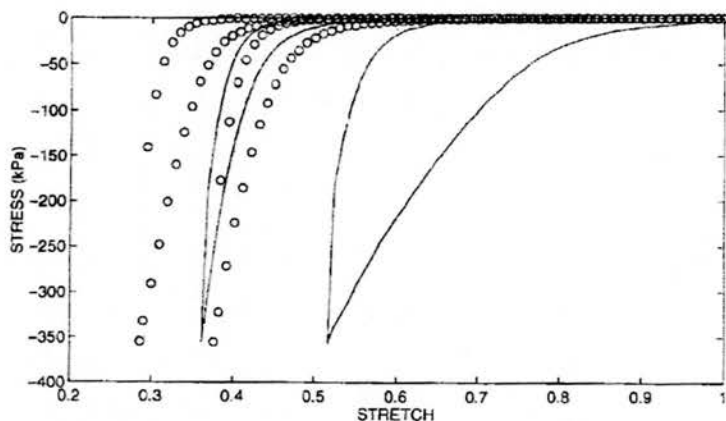
On top of the 'normal' diffuse changes associated with aging, artery wall elasticity alters with focal onset of atherosclerosis and the subsequent formation of lesions. As with healthy arteries, the elasticity of the lesion depends not only on its composition but also the arrangement of its constituents. There are few studies directly quantitating elasticity of the diseased artery. Richardson commented '*...the paucity of experimental data for artery walls in general and plaques in particular is outstanding*'⁷¹. Atherosclerotic tissue is known to exhibit non-linear behaviour, as demonstrated by compression testing data obtained by Topoleski et al from excised diseased aortoiliac human arteries (Figure 1.7)⁷². One can see that atherosclerotic tissue is also much stiffer compared to the healthy vessel data shown in Figure 1.6.



(a) Plaque type 1



(b) Plaque type 2



(c) Plaque type 3

Figure 1.7: Variations in stress-strain curves observed on compression testing of atherosclerotic plaque. Reprinted from the Journal of Biomedical Materials Research, 35, Topoleski, L.D.T. et al, 'Composition- and history-dependent radial compressive behavior of human atherosclerotic plaque', 117 - 127, Copyright (1997), with permission from John Wiley and Sons Inc.

As with healthy arteries, plaques have viscoelastic characteristics. This was demonstrated by Lee et al⁵⁴ who measured a variation in the dynamic modulus of fibrous plaque caps of excised human abdominal aortas subject to cyclic compression testing. A mean increase of 14 % was obtained between loading frequencies of 0.5 Hz and 2 Hz.

Plaque composition can vary widely and consequently, elasticity can also vary widely. One study reported a range in stresses of the order of 300 kPa required to achieve a 25 % strain across 23 samples of fibrous, calcified and atheromatous plaques⁷³. Variation in geometry and morphology and therefore, mechanical properties in an individual plaque may also vary widely. This is illustrated by the Young's Moduli, E of different plaque constituents (Table 1.2).

Constituent	Youngs moduli, E /kPa
Normal artery	100
Fibrous plaque tissue	1000
Calcified plaque tissue	10000
Lipid	0.5

Table 1.2: Young's modulus of elasticity of plaque constituents^{74,75}.

Of the sparse literature that does exist, there have been attempts to classify plaques or plaque caps according to mechanical characteristics and find differences in mechanical behaviour between these classes by measurement. Only two of these studies have tested entire plaques, as described below.

Topoleski et al measured change in stress-strain characteristics for 2 phases of radial compression testing, which each consisted of 15 cycles and were separated by 10-15 minutes⁷². Three characteristic mechanical behaviours (Type 1, Type 2 and Type 3) were identified (Figure 1.7). These were distinctive from one another in the nature of the viscoelastic properties, measured by the degree of reproducibility measured between consecutive loading cycles and consecutive loading phases. Type 1 plaques were characterised by relatively little change in stress-strain behaviour between cycles and phases. In histological terms type 1 plaques were found to be heavily

calcified, a feature absent from type 2 plaques and type 3 plaques. While no other statistically significant difference in mechanical behaviour was found to correlate with histological findings, this result supported a composition dependence of plaque elasticity.

Salunke et al subjected plaques (classified as fibrous, calcified or atheromatous) and healthy tissue to the same compression methods but instead measured the relaxation properties after application of a 25 % strain⁷³. Fibrous and calcified plaques were found to exhibit greater relaxation, with mean normalised stresses 60 seconds after loading of 0.068 and 0.074 respectively compared to 0.189 and 0.285 for atheromatous plaques and healthy tissue respectively.

Lendon and co-workers have carried out two studies investigating variation in tensile properties of plaque caps with composition^{76,77}. In the first study intact sections were taken from caps which already had some ulceration or tearing present. They had a greater strain and a relatively low applied stress at fracture (approximately 200 kPa for ulcerated plaques (n = 18) compared to 600 kPa for non-ulcerated plaques (n = 22)). There was also a significantly higher macrophage density in ulcerated plaques (approximately 450 per mm² for ulcerated plaques (n = 18) compared to 150 per mm² for non-ulcerated plaques (n = 22)) suggesting possibly that an increase in macrophage density may increase risk of plaque rupture.

The second study measured fracture stress along with amount and type of collagen in ulcerated and non-ulcerated plaque caps and adjacent sections of intima. Similar differences in fracture stresses were obtained as in the previous study between the two groups. Furthermore, the caps were found to have higher collagen content compared to the adjacent intima. The authors suggested collagen production in the plaque caps was not 'as efficiently organised to resist fracture as a similar amount of collagen in the adjacent intima'.

These mechanical tests are carried out in an environment quite different to that *in vivo*, and so caution must be applied in making inferences about *in vivo* behaviour

from *in vitro* measurements and in comparing study results. Factors such as the uni-axial loading applied *in vitro* compared to the multi-axial loading *in vivo*, morphological change in the plaque specimens between mechanical testing and histological examination and differences in behaviour on compression testing and tensile testing need to be taken account of⁷².

In determining which individuals are at risk of acute atherosclerotic complications, one must not only consider the material properties of the lesion but also the stress distributions to which they are subject as a result of blood flow through the vessel. This is typically investigated by computer modelling and in particular finite element analysis (FEA)^{55,74,78-82}. The studies in the literature are almost exclusively 2D, with inputted material properties gathered from mechanical testing of excised specimens. Much of the work focuses on coronary plaques though the findings in these studies are still of value in investigating high risk plaques in other locations, such as the carotid bifurcation. Assumptions concerning the material properties used from study to study vary, as do the values of the material properties, the geometries and morphologies employed. Both non-linear and linear material properties have been used^{78,83}. Some studies use idealised models of plaques^{81,83} while others use geometric and histologic data obtained on analysis of sections of individual excised plaques^{82,84,85}. The stress distributions produced by FEA have been analysed to determine such parameters as the location and magnitude of peak stresses and the effect of changes in geometry and changes in composition.

In general the investigations reveal stress distributions which vary widely across individual plaques and between plaques. A number of studies have revealed stresses to peak around the fibrous cap of the plaque, and in particular at the junction between the plaque and the normal artery^{78,83,84}. Interestingly, one of these studies found that on increasing the degree of stenosis from 70 % to 99 %, the peak stresses on the cap decreased⁸³.

Kilpatrick et al examined the effect of changes in composition rather than geometry, replacing the necrotic cores of two carotid plaques with calcified tissue and a

calcified region with a necrotic core in a third carotid specimen⁸². In the case of each specimen, peak fibrous cap stresses were greater for the plaques with a necrotic core by up to 16.5 % suggesting the presence of a necrotic core may increase risk of rupture, though other factors such as the fracture stress of the plaque in question and biological changes also play a part.

1.4.3 Summary

The elastic properties of healthy vessels and the changes that occur with aging and disease progression vessels have been described. Much of the current understanding has been derived from a combination of mechanical testing of excised specimens and computational modelling. As described above, both the results of mechanical testing and modelling have a number of caveats attached however, despite this, the findings of the studies discussed are of value in determining differences in characteristics between healthy tissue and diseased tissue, and between different stages of lesion development and lesion pathology.

While it is recognised more work is required, the investigations could help guide patient management in the future, in addition to existing anatomy and flow-based techniques. For example, one may be able to recognise which plaques will respond best to balloon angioplasty, if treatment outcome is lesion dependent⁷². In particular, the identification of high risk plaques would be of value; in order to refine patient selection for procedures such as carotid endarterectomy. However, in order to make use of observations of elastic properties in the literature in patient management one must first have the diagnostic tools in place with which to investigate these properties *in vivo*. These are discussed in the next section.

1.5 *In vivo* measurement of the elastic properties of the arteries

1.5.1 Assessment by quantitative mechanical parameters

As described by Pannier et al there are three levels of expression of arterial biomechanics; systemic (an overall measure of stiffness of the circulatory system in a given individual), regional (corresponding to a site of 'major physiologic importance') and local (a measure of stiffness at a specific site)⁸⁶. The approach for measurement of elasticity varies according to the level of expression as classified above.

1.5.1.1 Systemic stiffness

Systemic stiffness is typically evaluated from a blood pressure waveform and is commonly expressed using the Augmentation index (Aix) which is derived from a central artery pressure waveform. Typically, the central artery waveform in turn is derived from a peripheral waveform with the aid of a transfer function. The Aix demonstrates the degree of coincidence between the outgoing pressure pulse generated by the left ventricle, and the reflected pulse from the peripheral arteries. For stiffer arteries, the reflected pulse travels faster, and therefore becomes more and more closely coincident with the outgoing pulse. These interfere constructively to produce higher blood pressures and higher index values. Mathematically, Aix is defined as the difference in P_2 and P_1 expressed as a percentage of the pulse pressure PP (Figure 1.8)⁸⁷.

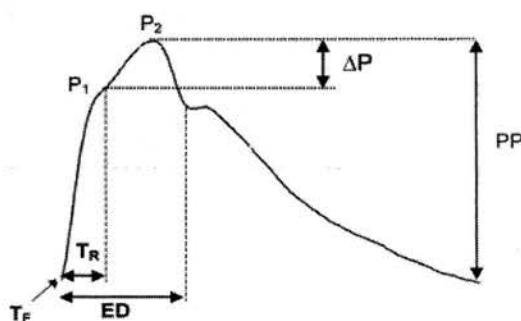


Figure 1.8: Ascending aortic pressure waveform measured on a middle-aged subject. Reprinted from American Journal of Hypertension, 15, Wilkinson, I.B. et al, Heart rate dependency of pulse pressure amplification and arterial stiffness, 24 - 30, Copyright (2002), with permission from the American Journal of Hypertension, Ltd.

Non-invasively, the pressure waveform may be measured by applanation tonometry, where a piezoelectric transducer is placed against the artery of interest⁸⁷, or by plethysmography, where an inflatable cuff or phototransistor (together with a light source) detects local change in blood volume over the cardiac cycle⁸⁸.

Systemic stiffness is of value in evaluating overall responses to drugs⁸⁸. In epidemiological studies, a single measure is useful to compare many individuals. However, it is of questionable direct use in individual patient management where focal changes in stiffness (such as carotid plaques) occur which may pose a particular threat to health (such as stroke). Local properties are of more use in such situations.

1.5.1.2 Regional stiffness

Regional stiffness can be expressed using pulse wave velocity (PWV), giving an indication of the characteristics of an individual artery or group of arteries. It is mathematically defined in terms of geometry and material properties (Appendix A). In essence its evaluation involves the simultaneous measurement of pressure, flow or distension waveforms at two different sites, between which the arterial segment of interest lies. Sites used include the ascending aorta coupled with the right common femoral artery⁷⁰ and the common femoral artery coupled with the carotid artery⁸⁹. By dividing the separation of the two sites by the measured time delay between pulses being detected at the two sites the PWV can be obtained.

A complicating factor in PWV measurement using this method is the selection of the region of the propagating waveform with which to calculate time delay. The shape of the waveform distorts with location in the circulatory system as a result of interference by reflected waves from the peripheral arteries and the variation in transmission of different frequency components. To overcome this, the 'foot' of the waveform is typically used, that is, the point corresponding to just prior to systolic increase in pressure. Investigations have revealed the region of the waveform surrounding this point to be unaffected by distortion⁸.

Pressure measurement may involve the use of invasive pressure transducers or an air filled cuff coupled with an ECG waveform as a surrogate for a second pressure waveform⁸⁶. Flow or distension have an advantage over pressure in that they may be measured non-invasively using ultrasound⁹⁰, including the case of sites which are inaccessible by non-invasive pressure measurement⁷⁰.

1.5.1.3 Local stiffness: Pulse wave velocity (PWV) measurement

Arterial stiffness and therefore, PWV may vary significantly along a single artery, let alone a group of arteries especially where atherosclerosis is present and so the measurement approach described in the previous section lacks specificity, reporting only an overall value. It is therefore of limited value in reporting the effect of focal changes in stiffness that may be induced by atherosclerosis locally. However, a couple of strategies are available for local PWV assessment. The first is by means of technological advances and the second by a different theoretical expression of PWV which allow identification of PWV over smaller segments of artery, and even single locations.

The first approach exploits the relatively high frame rate afforded by a modified Tissue Doppler Imaging (TDI) system⁹¹. The scanner was set to perform B-mode scans over a small number of scan lines (32) and other parameters, such as the number of TDI scan lines were optimised (to a low value of 16). The PWV was estimated by calculating the time delay in arrival of peak velocity shift between scan lines by cross correlation. The delay introduced by the finite TDI scanning time was compensated to obtain the delay due to the wall dilation pulse wave travel alone. The technique resulted in a single value for PWV of $8.29 \pm 0.64 \text{ m s}^{-1}$ over an 18 mm segment of *in vivo* scanned carotid artery.

The second alternative strategy approaches PWV evaluation using Wave-Intensity analysis. Too complex to discuss here, the analysis involves breaking the pressure waveform down into a large number of discrete wave fronts and applying 1D equations of continuity for an elastic tube. This results in an expression relating the

change in pressure at a single location, dP , change in fluid velocity, dU , density of the fluid, ρ , and the PWV, c ⁹⁰ (Equation 1.1).

$$-dP = \pm \rho c dU \quad (\text{Equation 1.1})$$

Therefore, by measuring a pressure waveform and a flow waveform at a single location one can deduce the PWV for that location. There appear to be few studies which have evaluated *in vivo* PWV using this approach, despite no limiting factors in its applications being reported. One practical limitation in its application is the requirement for a pressure waveform, which for non-peripheral arteries is likely to require an invasive approach or an inferred waveform derived from a peripheral measurement, which has associated inaccuracies.

1.5.1.4 Local stiffness: Arterial wall motion (AWM) measurement

Rather than PWV assessment, local stiffness of the artery walls is more commonly assessed by measurement of arterial wall motion (AWM) from which changes in vessel diameter may be extracted. These measurements are coupled with blood pressure measurements to express stiffness. The stiffness is typically expressed using the pressure strain elastic modulus, E_p or similar, as described in the Appendix A. It is valuable at this point to remember that due to the non-linear viscoelastic properties of the artery wall, values obtained are specific to the magnitude of the pressure and the rate of pulsation. The bulk of the reported work in the literature uses extra-vascular ultrasound to evaluate wall motion and/or diameter changes. Reviews of the subject are available³².

M-mode is perhaps the simplest method for measurement of arterial wall motion and therefore, changes in diameter. It has been used in cardiology departments for around two decades, displaying the movement of structures at a single location. With only one scan line along which to interrogate, high temporal resolutions of less than a millisecond are possible⁹². The movement along the line of interrogation is displayed on the scanner monitor. Evaluation of wall motion is real time when performed in

this way; the following techniques are typically performed off line post-acquisition by dedicated software.

With manipulation of the raw radiofrequency (RF) signal one can also evaluate artery diameter and wall motion; phase-locked tracking^{67,68} and displacement tracking⁹³ (which uses cross-correlation methods) of the signal from the walls have both been employed. B-mode images may also be analysed to deduce wall separation and displacements over time. Using a frame grabber to obtain video frames of the images, automated analysis packages can measure the displacements between frames^{35,94}. Also using B-mode data, speckle tracing has been employed to measure wall displacement⁹⁵.

Tissue Doppler Imaging (TDI) is the other main method by which tissue motion, and artery motion in particular may be measured. By integrating the raw TDI velocity values one can calculate displacement of the wall between time frames over a number of scan lines. The integral principle of this approach is more robust compared to differential evaluation of wall movement. Superior signal-noise ratios are obtained compared to flow Doppler given the some 30 dB greater amplitude of tissue reflections. Smaller pulse ensembles may be used per scan line to evaluate velocity at a given instant, and higher temporal resolutions are possible. Furthermore, temporal resolution may be enhanced to frame rates as high as 100 Hz by reducing the number of B-mode and TDI scan lines⁹¹. This allows superior resolution of velocities at systole and therefore maximum dilation, a quantity required to derive many of the wall stiffness parameters.

Many of the techniques already discussed measure AWM at a single location in the artery. This provides no information on AWM of the artery as a whole. A small number of techniques in the literature allow for measurement at several points within a segment of artery. Meinders et al developed an echo tracking technique which evaluated AWM at sixteen scan lines in an 18 mm segment of artery⁹³. The potential for greater spatial resolution is offered by a TDI-based technique⁹⁶. Prototype software derives AWM for 6.7 scan lines per mm within a user selected colour box

which can collect TDI data over segments of artery up to 35 mm long. Frame rates for TDI data acquisition range from 25 to 75 Hz depending on scanner settings.

An example of a TDI derived AWM image frame of an asymptomatic artery is provided, together with a spatial plot of maximum dilation derived from raw AWM data (Figure 1.9). Arterial wall motion across the scanned segment is uniform, as illustrated by the approximately horizontal nature of the plot. In this instance access to AWM data for an entire segment of artery is of limited value given the uniform nature of the dilations. However, heavily diseased arteries may exhibit marked variation in AWM across a scanned segment. An example of an AWM image frame and associated spatial plot of maximum dilation of a severely stenosed carotid bifurcation is provided (Figure 1.10). This demonstrates a marked change in dilation (and therefore strain) with location in the TDI colour box which coincides with the plaque location.

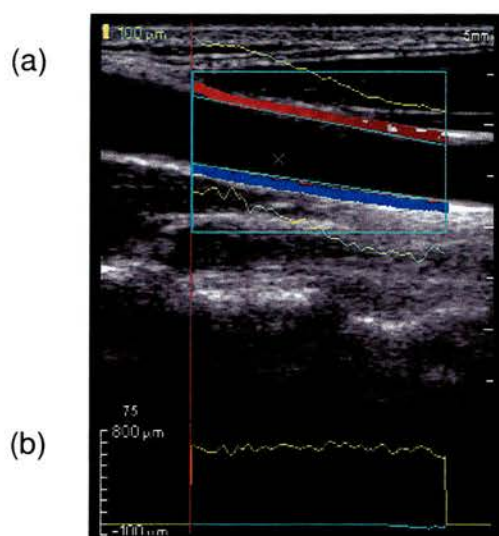


Figure 1.9: (a) TDI derived AWM superimposed upon a grey scale image of an asymptomatic common carotid artery at systole. (b) Associated spatial plot of maximum dilation.

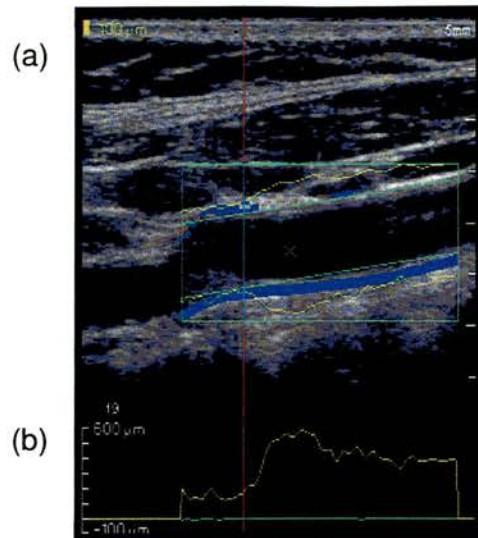


Figure 1.10: (a) TDI derived AWM superimposed upon a grey scale image of a severely stenosed carotid bifurcation at systole. (b) Associated spatial plot of maximum dilation.

Given AWM data obtained using one of the above techniques, in order to quantify wall elasticity, the distending force of blood pressure must also be quantified. Therein lies a problem; less accessible arteries such as the aorta require an invasive approach for pressure measurement which is undesirable. However, non-invasive measurement of blood pressure is possible at more peripheral sites, such as the brachial artery using the conventional sphygmometric approach, or using plethysmography. Therefore, as in PWV derivations, transfer functions can be applied to these readings which infer the shape and size of the blood pressure pulse at the less accessible site of interest⁹⁷. Systems which perform this operation are now commercially available. However, the transfer functions are devised over populations, although such functions are individual specific.

Without the use of a transfer function one has one other option. The peripheral pressure reading can be applied directly, giving a nominal index of elasticity which while not purely applicable to the site of interest, may still be compared with other results measured in the same way.

1.5.2 Assessment by Elasticity Imaging

An extension of the calculation of representative indices of stiffness is that of elasticity imaging or 'elastography'. By accurately measuring displacement which results from an applied force across multiple locations demonstrated in an anatomical image, the elastic properties may be evaluated and mapped. Whereas in oncological applications the force is often applied externally, in arterial examinations the force exerted by the blood pressure on the walls is typically used. Where ultrasound is employed to measure the reaction of the tissue the technique is referred to as 'sonoelastography'. In terms of the mapped tissue reaction parameter there are several types of elasticity imaging which fall under the umbrella of elastography. These are reviewed in the literature⁹⁸ and include vibration amplitude elastography, where the amplitude of tissue motion is mapped, and strain elastography where as the name suggests, strain is mapped.

Strain elastography has been investigated by de Korte et al using intravascular ultrasound and a technique devised by Ophir and Cespedes^{99,100}. *In vitro* strain sonoelastograms of plaques resulted in the successful differentiation of fatty, fibrofatty and fibrous material. With strain data and information on plaque composition, inferred by elastography there is potential for vulnerable plaques to be identified¹⁰¹.

From the perspective of risk to the patient, a non-invasive approach to elastography is more desirable. Magnetic Resonance Imaging (MRI) offers this possibility⁹⁸ as does extravascular ultrasound¹⁰². However in the case of the latter, one is limited to lower ultrasound frequencies and greater attenuation of the signal from the region of interest. In the case of intravascular ultrasound, the proximity of the artery wall to the transducer and low attenuation by the blood in the lumen allows superior resolution.

1.5.3 Indirect assessment of wall elasticity

The field of image based Computational Fluid Dynamics (CFD) to date has been more focussed on evaluation of haemodynamic parameters such as wall shear stress, however it may also be used to estimate moduli and tensile wall stresses induced by

blood pressure¹⁰³. The basis for the technique is the acquisition of 3D image data sets providing detailed geometry of a particular vessel. X-ray, MR and ultrasound data sets have all been used as a geometrical basis for the modelling. The Navier-Stokes equation is applied together with assumptions concerning the velocity distribution. The technique produces detailed 3D parametric maps of the imaged region revealing locations of maxima and minima of the parameters concerned, specific to that site and that individual. The technique involves large data sets and requires a large amount of computing power to calculate solutions.

1.5.4 Summary

Three main ways in which *in vivo* elastic properties may be determined have been described. The latter, image-based CFD, provides the most detailed information, specific to a site in a specific individual. However this requires the processing of large amounts of data and therefore does not have potential as a real time technique. Evaluations of AWM directly from 2D images provide less detailed information on a particular site and at present, are typically performed offline post-acquisition. However, given the relative simplicity involved in their calculation, there is far greater scope for integration of the relevant signal processing into commercially available equipment in clinical use. An added advantage of ultrasound imaging in particular, is the potential for real time viewing of the elastic properties. Several techniques have been described for AWM evaluation. Typically these only allow evaluation at single points in the artery. However, one TDI based technique in particular, allows for detailed spatial interrogation of arterial segments up to 35 mm long⁹⁶. This provides scope for two types of AWM investigation, namely, (i) Assessment of overall segment AWM and (ii) Assessment of intra-segment spatial variation in AWM.

1.6 Outline of thesis

The burden presented to health services by CVD, and stroke in particular, has been highlighted. It is thought that a significant number of strokes are a result of carotid atherosclerotic complications. The current criteria for carotid endarterectomy, the degree of stenosis, is anatomically based. While identifying many individuals that are at risk of stroke, some patients may unnecessarily be subjected to surgery, and some which are not considered high risk may still stroke. This points to the need for an additional or alternative diagnostic indicator. Given that the elastic properties of the artery wall change with disease progression, this is a prime area for investigation for such an indicator. Work to date for *in vivo* assessment of elastic properties fits into three main categories. Image based CFD is a relatively cumbersome technique, while direct evaluation of simpler, 2D parameters offers a more convenient, quicker method for assessment, albeit providing less information. Ultrasound in particular has scope for non-invasive real time assessment. In particular Bonnefous's TDI/AWM software technique^{96,104} (Section 1.5.1.4) allows the evaluation of wall motion and therefore strain and elastic properties over approximately 200 scan lines on a 3 cm segment of artery.

The greater clinical potential of the technique to provide indicators of AWM, strain and elasticity, compared with others described in the literature, has been highlighted. In particular, the ability to examine spatial variations in AWM, is of interest because the clinical application may be used to identify high-risk carotid plaques as discussed earlier. However there is limited data in the literature detailing technique efficacy. Only two studies examining technique accuracy, both using test objects, have been published^{104,105}. The first used a simplified moving plate device to simulate the movement of the artery wall by known displacements. By comparing the TDI derived motion with the known motion of the plate, technique accuracy was evaluated. However, this investigation was limited in scope; performance of the technique was only assessed for one AWM waveform and variation in accuracy with scanner settings was limited to velocity scale range and sensitivity setting variation

only. This study is discussed in more detail in Chapter 3. The second study used a wall-less flow phantom to compare TDI derived AWM with M-mode derived AWM and as with the first study, investigated the effects of variations in scanner velocity scale setting. No investigation was made of the effects of variations in beam-vessel geometry, such as vessel depth, on technique efficacy.

Available *in vivo* data on the TDI/AWM technique is also limited. At the time the work in this thesis was performed, no *in vivo* studies existed in the literature quantifying technique variability. A reproducibility study has since been published. However, this involved the scanning of abdominal aortas and used a different version of the AWM software, which was specially modified for use on such vessels rather than on the carotid arteries¹⁰⁶. This study is described in further detail in Chapter 2.

It is concluded, therefore, that there are three main ways in which AWM data in the literature is limited:

(i) AWM accuracy

In vivo AWM covers a range of dilations and wall velocities corresponding to a range in elasticity, while only one AWM waveform has been used in previous studies investigating technique accuracy. Furthermore, there are several scanning parameters that may vary TDI/ AWM software performance, and these have not been investigated in the literature.

(ii) Variations in AWM precision with beam-vessel geometry

Parameters such as beam-vessel angle and vessel depth are thought to have a marked effect on AWM precision and accuracy. Their effects have not been investigated in the literature at all.

(iii) *In vivo* technique performance

A quantitative study of TDI/AWM technique variability in the carotid arteries has yet to be performed, including a detailed description of sources of variability associated with the technique.

Given the lack of data on the above aspects, clinical application of the TDI/AWM technique would benefit from a more detailed investigation of accuracy and

precision, both *in vivo* and in the laboratory where individual sources of uncertainty may be investigated in isolation. Such investigations are the main aims of this thesis. These aims are summarised chapter by chapter in Table 1.3. Each chapter is outlined in further detail in the succeeding paragraphs.

Chapter	Aim
2	In vivo assessment of TDI/AWM technique reproducibility in asymptomatic arteries.
3	Laboratory assessment of TDI/AWM technique accuracy.
4	Development and characterisation of materials for a compliant wall flow phantom design.
5	Development and characterisation of a compliant wall phantom design for generation of realistic AWM.
6	Laboratory assessment of TDI/AWM technique precision upon scanning geometry variation, using the phantom developed in Chapters 4 and 5.

Table 1.3: Thesis aims.

Chapter 2 describes an *in vivo* reproducibility study of the carotid arteries. Intra- and inter-observer reproducibility was examined for two observers and two data acquisition sessions. The study also served as an opportunity to observe limitations in the TDI/AWM technique that could give rise to spurious AWM data. Furthermore, the study was of value in that the initial *in vivo* experience of the technique provided a basis for laboratory based studies that were to follow; sources of variability observed *in vivo* could be investigated later using phantoms and AWM data acquired provided reference physiologic data with which to compare phantom generated AWM.

Chapter 3 describes an investigation of TDI/AWM accuracy. A validation device, with simplified planar wall geometry, similar to that used by Bonnefous et al was designed in-house for this purpose¹⁰⁴. AWM accuracy variation for a range of dilations and wall velocities was investigated.

In order to investigate the geometrical factors affecting TDI/AWM technique efficacy, a compliant wall phantom capable of generating physiological AWM was required. Chapters 4 and 5 detail the design and characterisation of such a phantom. As close a possible mechanical and acoustic resemblance to the *in vivo* case was sought. To address this, Chapter 4 details the choice of materials and their mechanical and acoustic characterisation. Chapter 5 describes the design and the performance of the phantom and its 'working range' of AWM parameters such as dilation and wall velocity observed upon varying flow and output impedance conditions. The aim of this work was to produce as realistic AWM as possible. With a phantom design in place, an investigation of the relationship between AWM precision and variation in beam-vessel geometry could be performed. This is described in Chapter 6. Variations in derived AWM with vessel depth, beam-vessel angle, degree of vessel axis-scan plane coincidence and exerted transducer pressure were investigated.

As mentioned earlier, TDI imaging in conjunction with the prototype AWM software presents the opportunity for two types of AWM assessment: (1) properties of the scanned segment as a whole, and (2) detection of local occurrence of differential motion within a scanned segment, as might be exhibited at a plaque boundary. The first relies upon evaluation of dilation alone and therefore overall accuracy of velocity estimation by the scanner. The second requires sufficient spatial resolution of TDI velocities to detect change in velocity over the scanned segment and adequate velocity resolution by TDI in order to demonstrate differing wall velocities between adjacent locations in a given segment of artery. Clinical investigation of (1) and (2) require the analysis of two different AWM properties: dilation and dilation gradients respectively. Technique efficacy with respect to these two different AWM properties requires separate analysis and to analyse both is beyond the scope of this thesis. For this reason all investigations of technique efficacy detailed in this thesis are limited to the special case of investigating spatially uniform AWM. A sound understanding of technique performance without the added level of complexity introduced by spatial gradients was deemed a priority. Future investigations may extend to investigate spatial variations in AWM.

Chapter 2 *In vivo* intra- and inter-observer variability of TDI derived Arterial Wall Motion (AWM)

2.1 Introduction

While laboratory based studies such as those discussed in later chapters are valuable, ultimately the goal of arterial wall motion (AWM) derivation is its application in the clinical environment. With this in mind, it is of value to examine the performance of the technique *in vivo* and in particular quantify the derived AWM variability when data acquisition is performed by different observers and upon different occasions. This is the first study to do so for this technique. Variability in measured AWM will place limits on the detectable differences in AWM and therefore elasticity, in comparing individuals, different sites within the same individual or mapping changes over time at a single site. Such an investigation has the additional benefit of establishing practical and technical difficulties in acquiring and analysing AWM data, and provides a basis for laboratory investigations described later in this thesis.

A study protocol was devised by the author and discussed with accredited National Health Service Medical Technologists, Miss Sarah Jane Johnson and Mrs Karen Gallagher, Principal Physicist Dr. Peter Hoskins and Consultant Radiologist Dr. Paul Allan. Data was acquired in the Vascular Laboratory of The Royal Infirmary of Edinburgh between March and May 2002. The technologists performed all scanning and the author provided on site advice on implementation of the scanning protocol and managed data acquisition. Professor Robin Prescott and Ms Mandy Lee of The Medical Statistics unit at The University of Edinburgh were consulted during data analysis for advice on statistical techniques.

2.1.1 Definition of AWM indices

The measurement of AWM curves provides a large number of data points, typically in the region of 18, 000. In order to measure quantitative variation in AWM four representative indices of any given data set were chosen (Table 2.1).

AWM index	Units
Maximum dilation, Mx	μm
Mean dilation, Mn	μm
Standard deviation of dilation, Sd	μm
Maximum spatial gradient of dilation, Mg	$\mu\text{m}/\text{mm}$

Table 2.1: AWM indices investigated.

The indices chosen have potential for clinical application, providing information on different aspects of the artery wall dynamics. This is the first known use of the latter three indices. Each index was calculated for each cardiac cycle, averaged over four cycles per acquisition, then averaged over three cine loop acquisitions. The indices are defined below with the aid of temporal and spatial AWM plots (Figure 2.1).

2.1.1.1 Mean maximum dilation, Mx

Maximum dilation can be used to calculate various elasticity parameters quoted in the literature such as the stiffness parameter, β and the elastic modulus, E (defined in Appendix A). In a given cardiac cycle, Mx is obtained from each scan line (as denoted by 'x' in Figure 2.1), and averaged over all scan lines, giving a measure of maximum dilation over the entire segment.

2.1.1.2 Mean dilation, Mn

In a given cardiac cycle, the mean dilation is calculated for each scan line, then averaged over all scan lines.

2.1.1.3 Temporal standard deviation of dilation, Sd

Standard deviation of dilation, Sd gives an indication of heterogeneity in dilation along an examined segment of artery. In a given cardiac cycle, Sd is calculated in each time frame, then the mean Sd calculated.

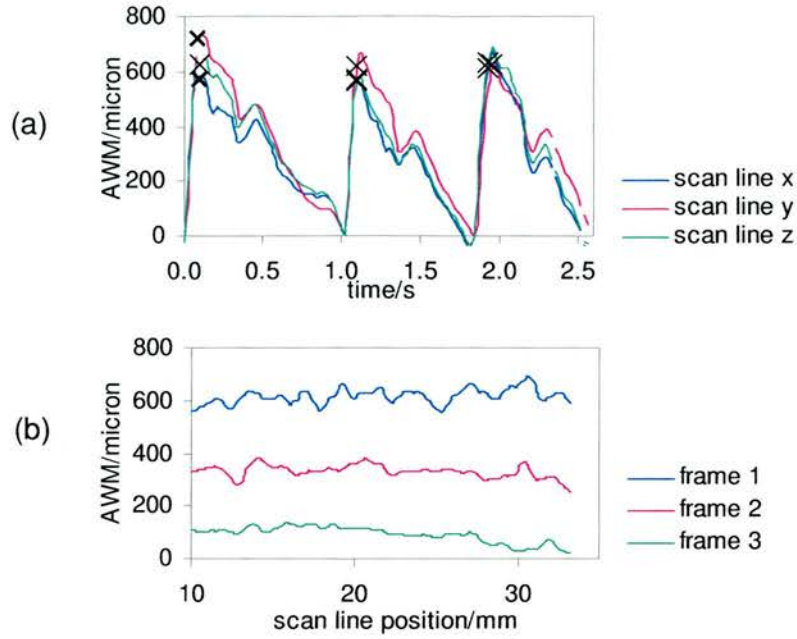


Figure 2.1: *In vivo* AWM derived from TDI data from a common carotid artery plotted (a) temporally and (b) spatially. Dilations from only 3 scan lines and 3 frames are shown for clarity.

2.1.1.4 Maximum spatial gradient of dilation, M_g

Maximum spatial gradient of dilation, M_g , in principle allows identification of regions where AWM varies rapidly with location along the longitudinal axis of the artery, which correspond to regions of high radial strain. It is defined as the absolute value of the maximum rate of change of dilation with change in longitudinal position in the vessel segment. M_g was calculated for each time frame in a given cycle, and the maximum over all time frames in a given cycle identified. Figure 2.2 demonstrates the spatial gradients associated with the dilation curves in Figure 2.1.

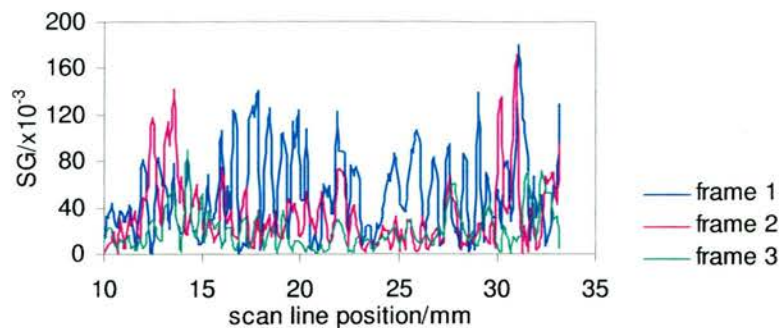


Figure 2.2: Variation in spatial gradient of dilation for the AWM in Figure 2.1.

2.2 Methodology

2.2.1 Logistics

Six volunteers were chosen from the Department of Medical Physics at the University of Edinburgh, aged 21 - 51. All individuals were asymptomatic of carotid artery disease. Tissue Doppler data was acquired using an HDI 5000 ultrasound scanner. Cine loops of left and right internal and common carotid arteries were acquired on two visits to the Vascular Laboratory by both observers. On each occasion, three loops were acquired of each segment. Patterns of data acquisition are summarised in Figure 2.3. Overall, 288 cine loops were acquired. Sections of artery were scanned using the same protocol in order to standardise data acquisition.

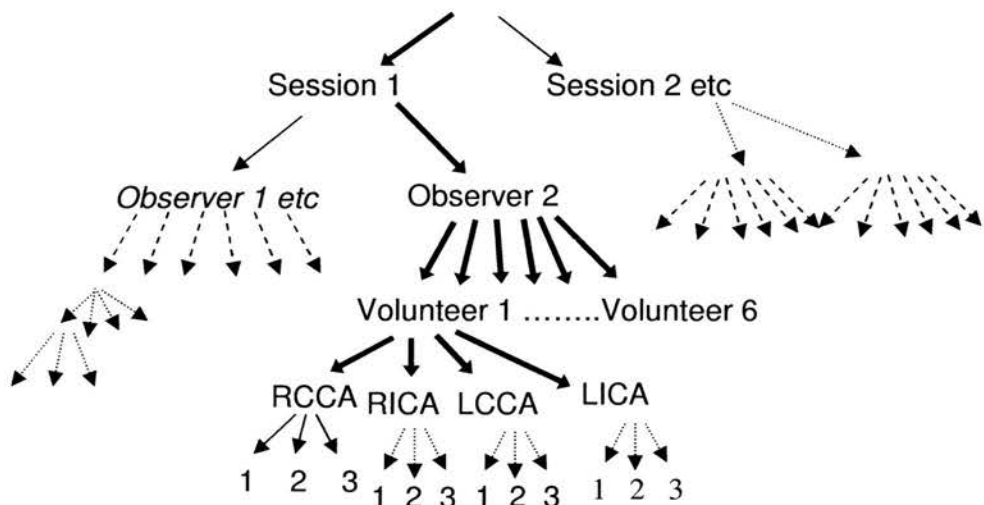


Figure 2.3: Pattern of TDI data acquisition.

2.2.2 Scan protocol

Scanner settings recommended by Philips for AWM extraction were employed (Table 2.2). Each volunteer was positioned supine on the couch. For each site, TDI data was acquired over the same length (25 mm), denoted by the colour box length. The colour box depth was also fixed (15 mm). The colour box was located at a standard axial distance from the carotid bifurcation and aligned with the central axis of the artery, ensuring the walls were enclosed by the box at systole. Common carotid data was acquired 8 – 33 mm from the bifurcation, and internal carotid data was acquired from the point of the bifurcation (Figure 2.4). Four cardiac cycles were acquired in each loop. Note that due to time restrictions, the loops were acquired ‘blind’, that is to say the AWM was not examined at the time for artefacts, precluding the chance to re-scan and obtain artefact free loops.

Parameter	Setting
*Probe	L12-5 linear array
*Sensitivity	Medium
*Line density	A
*Dynamic motion differentiator (DMD)	Off
*Colour gain	Saturated ($> 85\%$)
Velocity scale	2.2 cm s^{-1}
2D gain	Minimum for clear wall definition
Frame Rate Optimisation (FRO)	Maximum
Time Gain Control (TGC)	Mid range

Table 2.2: Settings for TDI AWM *in vivo* acquisition. ‘*’ indicates a Philips recommended setting.

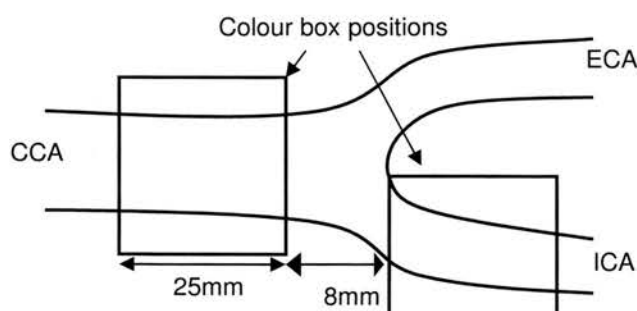


Figure 2.4: TDI data acquisition locations.

2.2.3 Data extraction & analysis

The cine loops containing the raw TDI data were transferred to a pc for analysis offline. The AWM software was applied, producing Excel spreadsheets containing the AWM. The AWM cine loops were also examined by eye by the author and Dr. Odile Bonnefous of Philips Research France, the AWM software developer, to identify the presence of any artefacts that would affect resulting AWM curves. An audit was carried out on a subset of the data acquired, quantifying the incidence of different sources of variability. Custom-written Matlab code (MathWorks Inc., Natick, MA) was employed to calculate the AWM indices from the spreadsheets.

The statistical analysis of the AWM indices consisted of two main aspects:

- (i) Intra-segment variability for fixed observers and fixed acquisition sessions (Section 2.3.2).
- (ii) Intra-segments agreement and variability between observers and acquisition sessions (Section 2.3.3).

In particular, (i) assessed variability between cardiac cycles in a given cine loop and between the three cine loops acquired at a given scanning appointment (see Figure 2.3). This reflects the inherent variability of the technique before the effects of different observers and data acquisition sessions are taken into account in (ii). Inter-loop and inter-cycle variability was expressed using the Coefficient of Variation (CoV) (Equation 2.1), defined as the ratio of the standard deviation in a given AWM index for n cardiac cycles or cine loops over the mean value of the AWM index for the sample, expressed as a percentage).

$$CoV = \frac{SD_n}{mean_AWM_index_n} \times 100\% \quad (\text{Equation 2.1})$$

Part (ii) of the statistical analysis involved three stages. Firstly, agreement of AWM indices from cine loops acquired by different observers and at different data acquisition sessions was tested using the parametric students t-test. In particular, the differences between AWM indices derived from a given segment of artery were examined. The differences were obtained by calculating a mean AWM index for

each batch of three cine loops acquired by a given observer in a given acquisition session. These AWM index mean values were then paired and the differences between to the two calculated. For example, Mx for observer 1, session 1 was paired with Mx for observer 2, session 1 in order to evaluate agreement between observers in session 1. The strategy of analysis of differences between AWM index values rather than the AWM index values themselves is recommended by Bland & Altman¹⁰⁷.

Agreement between observers and acquisition sessions were analysed in four groups:

- (i) Observer 1 versus Observer 2 (Session 1 data)
- (ii) Observer 1 versus Observer 2 (Session 2 data)
- (iii) Session 1 versus Session 2 (Observer 1 data)
- (iv) Session 1 versus Session 2 (Observer 2 data)

Prior to t testing Bland & Altman plots were made of the differences versus their mean values to exclude any systematic relationship between the AWM index values and their variability. Histograms were also plotted to assess the distribution of the differences. Conditional on obtaining no more than moderate deviations from normality (assessed with the assistance of Professor Robin Prescott and Miss Mandy Lee from the Medical Statistics Unit at The University of Edinburgh), the parametric students t-test could be applied to the paired data. Testing was performed at the 95 % confidence level using commercially available software, Minitab (Minitab Inc, State College, Pennsylvania). The following null hypothesis was tested: *'There is no statistical difference in AWM indices derived from data acquisitions made by observer A and observer B and data acquisition session 1 and data acquisition session 2 when compared over all segments of artery scanned'*. Conditional on this observation, agreement among the paired values was quantified using the mean difference (an estimate of the bias) and limits of agreement (LOA), which are defined in Equation 2.2. Note that the use of CoV was inappropriate as an indicator of variability given this analysis examines differences rather than the AWM index values themselves; the denominator in Equation 2.1 will likely be close to zero and very small relative the standard deviation, creating large CoV values which lack meaning.

$$LOA = Bias \pm 2SD \quad (\text{Equation 2.2})$$

SD is calculated from the differences. The LOA provides a range, based on the sample, within which one could expect an AWM index value to differ from another when derived from data acquired by a different observer or in a different acquisition session. Note that the LOA obtained here included all cine loops acquired, regardless of artefact presence, as a 'first look' at AWM variability. While a less intuitive measure of variability, the repeatability coefficient (RC) recommended by Bland & Altman was also quantified (Equation 2.3). This allowed comparison of results obtained here with those obtained by Long et al, who used a modified form of the AWM software to assess reproducibility in abdominal aortas¹⁰⁶. Only RC values were provided in this study and so their calculation was necessary to compare with results obtained here.

$$RC = \sqrt{\frac{\text{Sum_of_observation_differences}}{n}} \quad (\text{Equation 2.3})$$

2.3 Results & Discussion

2.3.1 Sources of variability

Prior to quantifying the reproducibility of the sample, individual cine loops were examined for sources of variability. The sources of variability encountered are listed in Table 2.3 (1 - 8). The effects of each source of variability are illustrated in turn with semi-quantitative comparisons either between AWM from affected and unaffected parts of the TDI colour box or by comparing AWM from affected and unaffected cine loops. There are additional sources of variability in AWM (9-10) whose effects may not be clearly visible or quantifiable in the acquired cine loops due to the presence of other sources of variability and the lack of control over scanning geometries, as is the case in *in vivo* scanning. For example, no information was gathered at the time of the study concerning the pressure applied to the scanned site by the observer using the transducer. Quantitative comparisons between cine loops affected and unaffected by sources 1-10 are not made, since unaffected cine loops were not always available. Furthermore, many of the imaged segments are affected by more than one source of variability; therefore, to compare segments for the effect of a single artefact alone is difficult.

ID	Source of variability	Type of source	Effect on AWM
1	Segmentation error: Reverberation artefact in lumen	Imaging/AWM software limitations	Alters local dilations, depending on relative motion of the artefact incorrectly identified as wall.
2	Sub-optimal artery wall definition	Imaging limitations	Genuine AWM is masked by noise.
3	Segmentation error: Presence of strongly reflecting planes other than the artery wall	AWM software limitations	Alters dilations of affected region according to how segmented structure is moving.
4	Spurious high velocities from blood	TDI/AWM software limitations	Decreases dilation in affected region.
5	Lack of scan line synchronisation	TDI/AWM software limitations	Discontinuities in AWM with location.
6	Patient motion eg. swallowing or movement of transducer by observer	Observer error/subject motion	Variable effects.
7	Reverberation of artery due to presence of jugular vein between artery & transducer	Physiologic/ Anatomical variations	Sometime atypically high dilations and increased number of nodes in AWM curve.
8	Lack of coincidence between scan plane and central artery axis	Intra- and inter-observer error	Decreased dilations off axis. Investigated in Chapter 6.
9	Non-normal beam-vessel angle	Imaging/AWM software limitations/Intra and inter-observer variability/ Anatomical variability	Underestimate of dilation. Investigated in Chapter 6.
10	Transducer pressure	Intra- and inter-Observer variability	Effect unknown. Investigated in Chapter 6.

Table 2.3: Sources of variability in AWM indices.

2.3.1.1 Variability source 1: segmentation error due to B-mode reverberation artefact

Where reverberation artefacts are present in 2D images, the segmentation process in the AWM software can mistake them for the genuine artery wall and reduce dilations in the affected area. Figure 2.5a shows the B-mode artefact, marked with an arrow and Figure 2.5b demonstrates the effect on the cycle-averaged maximum dilation curve, comparing an affected loop with an unaffected loop. The AWM indices are compared with those acquired from the same segment by the other observer where there is no reverberation artefact. The marked difference in maximum dilation can be seen. This artefact would also affect Mn, Sd and Mg and undetected could result in the incorrect identification of rapidly varying elastic properties along the length of the scanned segment.

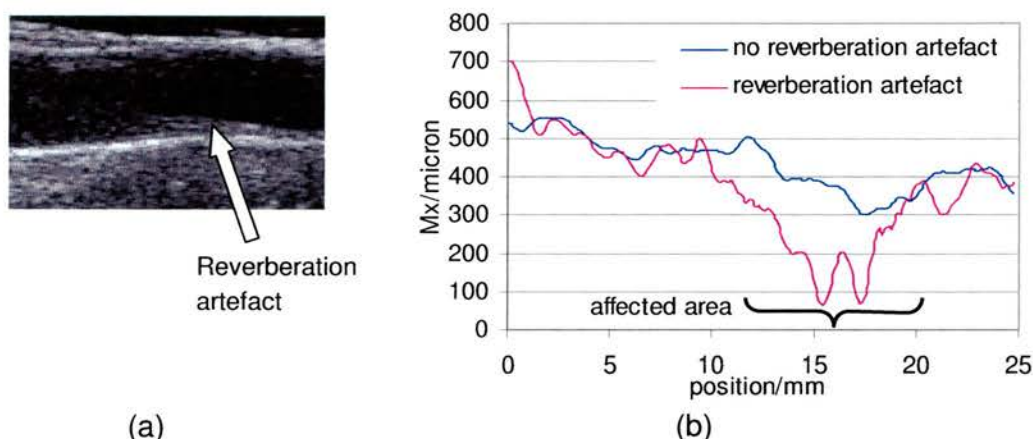


Figure 2.5: (a) A B-mode frame demonstrating a reverberation artefact, marked with an arrow (b) a comparison of spatial variation in maximum dilation for one loop unaffected by the artefact and another affected by the artefact. A trough is evident at the artefact site (Volunteer 5, session 1, observer 1, loop 1).

2.3.1.2 Variability source 2: Sub-optimal definition of the artery walls

It was often difficult to acquire 2D images where the walls were well defined over the entire length of the segment. The quality of the 2D image dictates the accuracy of the segmentation process, and is an indicator of the strength of the received Doppler signal. Therefore, both factors dictate the quality of the AWM data. This was particularly an issue with ICAs where the segment of interest may be relatively deep-seated and tortuous. In such cases the resulting AWM data is dominated by noise effects, producing smaller dilations and relatively large Sd (Figure 2.6).

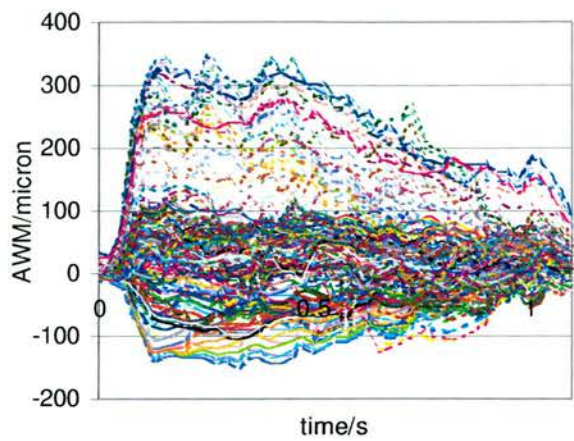


Figure 2.6: AWM masked by noise due to poor definition of the artery walls (Volunteer 3, LICA session 2 Observer 1 loop 1). Each line represents the mean dilation of each scan line averaged over several cardiac cycles.

2.3.1.3 Variability source 3: Segmentation error due to the presence of strongly reflecting structures other than the artery walls

Other strongly reflecting planes other than the artery wall may result in the misinterpretation as part of the artery wall by the AWM software. The example shows how part of the wall of the jugular vein is interpreted to be part of the CCA wall (Figure 2.7) resulting in wall velocities in the opposite direction to the true AWM and therefore, low anomalous dilations (Figure 2.7). This artefact has implications for all four AWM indices.

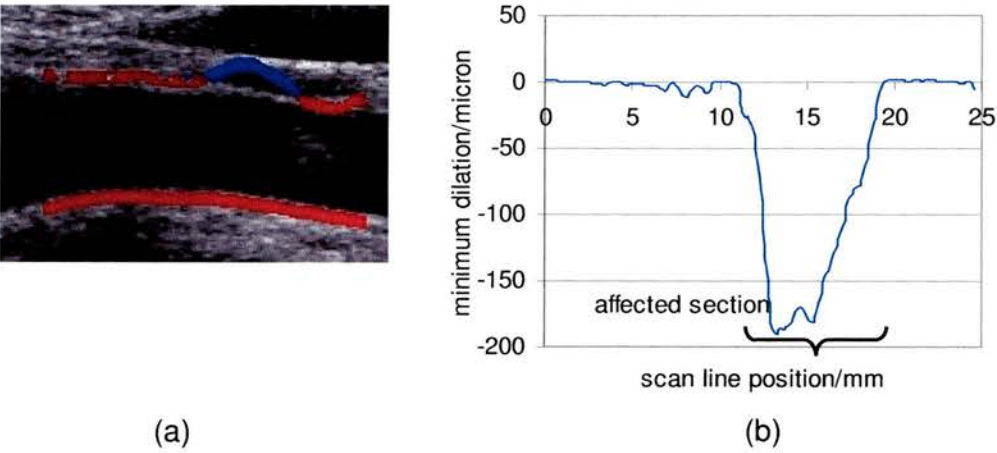


Figure 2.7: (a) A segmentation error in a CCA due to a strongly reflecting jugular vein wall (b) the effect on AWM is seen in cycle-averaged minimum dilation curves (Volunteer 3, session 1, observer 1, loop 1).

2.3.1.4 Variability source 4: Spurious high velocities originating from blood misinterpreted as wall velocities

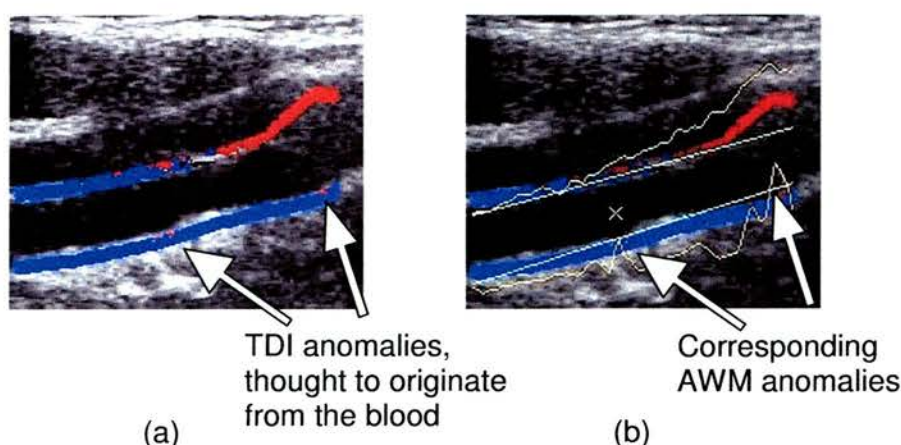


Figure 2.8: (a) TDI and (b) AWM data demonstrating the effect of inclusion of blood velocities with tissue velocities (Volunteer 3, LICA, session 2, observer 2, loop 1). Brightness in (a) is enhanced in order to visualise the TDI colours.

On occasion isolated bright pixels have been observed, opposite in colour to the predominant colour displayed in the wall at that instant. These correspond to velocities at the other extreme of the velocity scale when compared to the surrounding pixels. These pixels appear to occur only on the edge of the TDI colour strips adjacent to the vessel lumen. They are thought to be due to the incorrect interpretation of blood velocity as tissue velocity. This may be a result of inadequate TDI spatial resolution of the and/or inadequate tracking of the vessel wall by the AWM software; the segmented TDI colour strip may lag behind the true wall position as it accelerates rapidly in the expansion phase of the AWM cycle. This may explain why the artefact is most marked in this phase of the AWM cycle. An example is given, demonstrating the effect in terms of the TDI image, and the AWM which results (Figure 2.8). At and just after systole the artefact shows itself in the AWM as a relatively low dilation due to the cancelling affect of the artefact on the surrounding areas. Given the relatively small area the artefact occupies, it has little effect on Mn, Mx and Sd. However, it can elevate the value of Mg since, as with sources 1 and 2, changes in dilation are highly localised but marked enough to be observable by eye.



2.3.1.5 Variability source 5: Lack of scan line synchronisation

In acquiring the TDI data, the scanner scans left to right across the length of the colour box. This process takes a finite amount of time, and so non-simultaneous dilations are interpreted as occurring simultaneously (Figure 2.9). This has implications for all four AWM indices. Its effect is present in all acquisitions, though in some it is particularly noticeable (Figure 2.10).

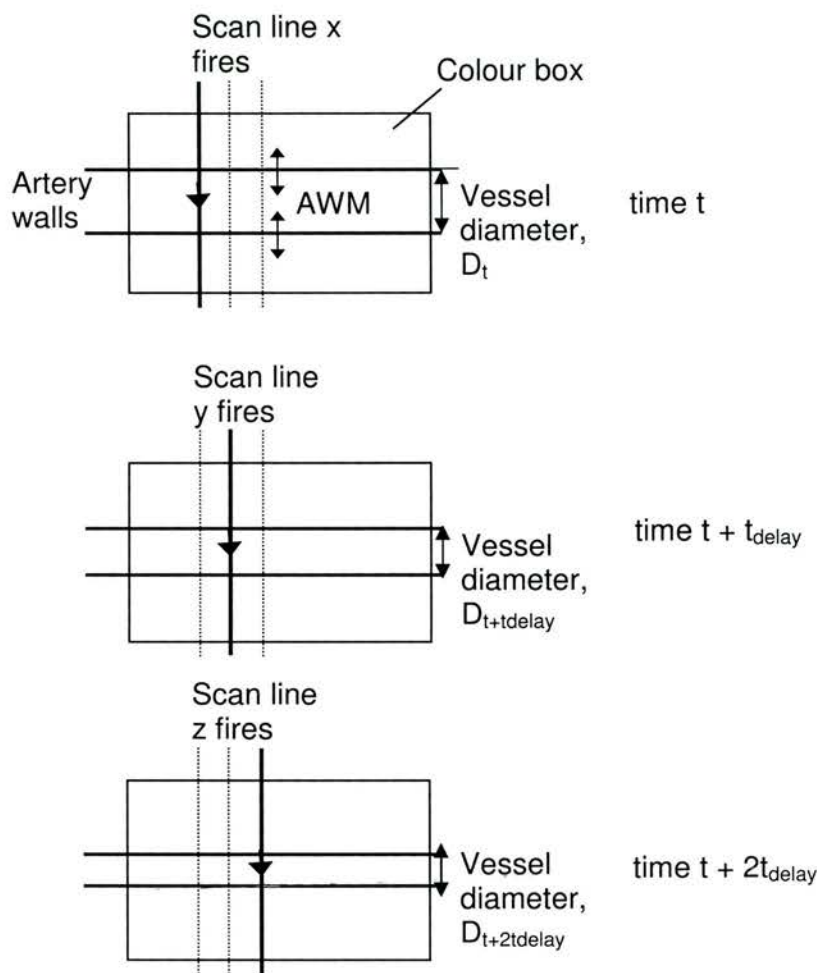


Figure 2.9: A schematic diagram demonstrating the mechanism resulting in misinterpretation of non-simultaneous dilations as simultaneous, due to a finite scanning time across the colour box length.

The plot shows maximum dilation decreases as scan line increases. The delay between successive pulse ensembles emitted by the transducer moving from left to right across the colour box produces the gradual decrease in maximum dilation, as velocity is measured later and later after the emission of the first pulse ensemble. A

TDI software release that became available subsequent to this study incorporates a correction to reduce this effect as demonstrated by Bonnefous et al¹⁰⁴.

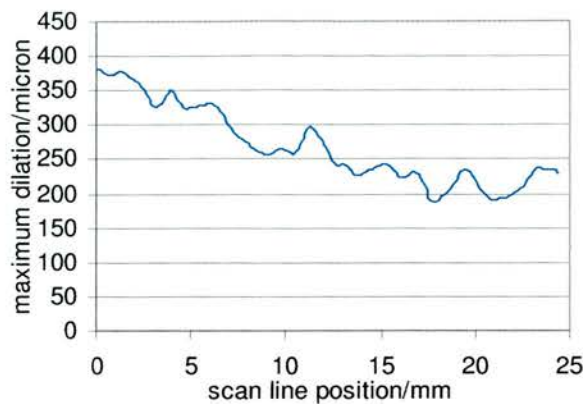


Figure 2.10: Maximum cycle-averaged dilation showing a lack of synchronisation between scan lines (Volunteer 1, LCCA, Session 2, Observer 2, loop 1).

2.3.1.6 Variability source 6: Patient/transducer motion

Either the patient may move or the observer’s hand may slip during acquisition of the cine loop. This produces a motion artefact whose effect on AWM can vary in nature. In this example, the artery moves out of the beam plane, and therefore records a lower dilation (Figure 2.11). This could affect any of the four AWM indices, but should be easily detected and therefore avoided.

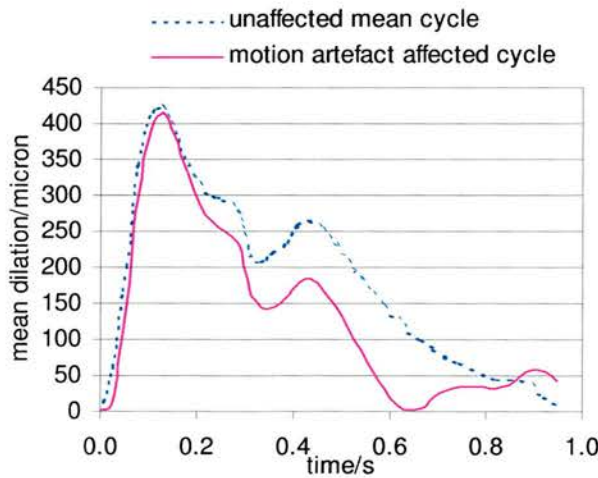


Figure 2.11: Reduction in mean dilation due to the presence of a motion artefact (Volunteer 5, LCCA, session 1, observer 2, loop 1).

2.3.1.7 Variability source 7: Motion artefact due to presence of the jugular vein between the transducer and segment of interest

Atypical AWM curves have been observed where a jugular vein is present in the field of view; the presence of the jugular vein appears to induce oscillations or ‘bouncing’ in the wall additional to the typical expansion and contraction of the artery wall. This effect is illustrated in Figure 2.12 where the upper wall seems most affected. It has a quite different shape to the AWM for the lower wall at the same longitudinal position. As the example shows, this artefact can increase the range of the AWM observed and so can affect S_d and M_n . There may also be implications for M_g if a segment is partially affected.

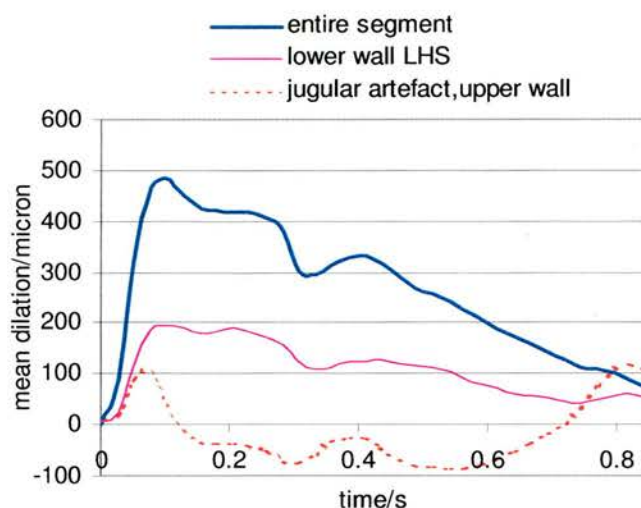


Figure 2.12: Comparison of cycle and scan line averaged AWM of the entire scanned segment, the lower wall only and the upper wall only demonstrating the effect on AWM shape of the jugular induced motion (Volunteer 4, LCCA, session 1, observer 2, loop 3).

2.3.1.8 Variability source 8: Lack of coincidence between the beam and the central axis of the artery

Should the transducer be offset from the central axis of the artery it will detect smaller velocities (if one assumes largely radial AWM) and therefore smaller dilations. An example is given below, showing incorrect positioning of the transducer on the left hand side of the segment (Figure 2.13a). The AWM data is also shown (Figure 2.13b). This source of variability would have particularly marked effects on M_n and S_d since it introduces more low dilation values to a given AWM

data set. Where a segment is partially affected, one may see an effect on Mg , as there will be a change in dilation across the interface of the affected section to the unaffected section. Where an entire segment is affected, Mx will be reduced. Such an artefact is relatively easy to detect, from the lack of bright reflection obtained when the beam is normally incident on the artery wall. This source of variability may not always be avoidable; where arteries are tortuous, it may only be possible to gain in-plane images of shorter segments of artery than those scanned here. This was the case in a number of acquisitions in this study. The effect of off-axis positioning was quantified in Chapter 6 using a compliant wall flow phantom.

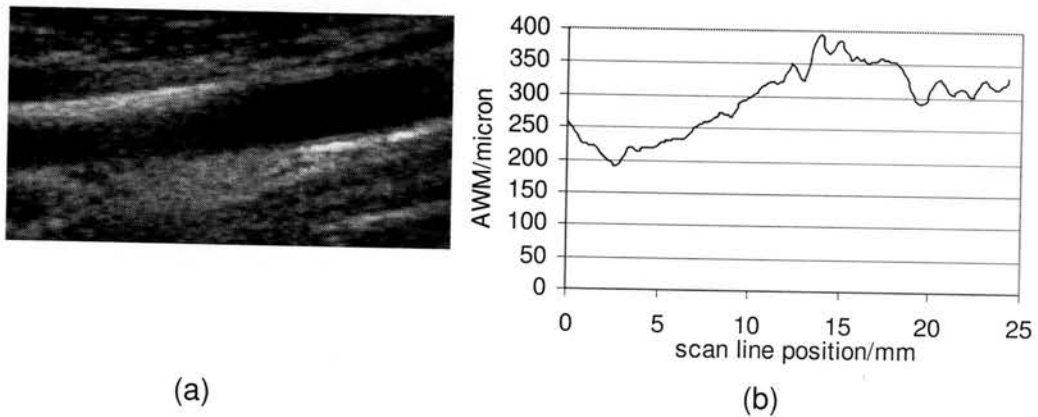


Figure 2.13: Demonstration of the effect of off-axis positioning of the transducer (a) B-mode frame (b) Maximum cycle averaged dilation variation with position (Volunteer 2, LCCA, session 2, observer 1, loop 1).

2.3.1.9 Variability source 9: Sub-optimal beam-vessel angle

Tissue Doppler Imaging is limited to detecting velocity in the direction of the beam alone, as with other Doppler ultrasound modalities. Therefore, variations in beam-vessel angle vary the component of AWM velocities measured by the scanner. The effect of non-normal beam incidence alone was difficult to assess here given the number of variables involved and so a compliant wall flow phantom was used to investigate the effect as described in Chapter 6. Such a source of variability could be minimised on comparing repeat scans of the same segment of artery if the same beam-vessel angle is employed at each scan. However, comparisons of AWM from different segments of artery would need to take into account any differences in beam-vessel angle between acquisitions.

2.3.1.10 Variability source 10: Transducer pressure

The pressure applied to the artery on placement of the transducer may vary. The observer may apply further pressure to that required normally if this assists in obtaining an image that is more satisfactory. One specific scenario where this occurs is when the jugular vein lies close the segment of interest. By applying pressure in a particular direction, one may remove the jugular from the scan plane. However, doing so may alter AWM. There was no methodology in place to quantify such variations in this study so testing was performed using a compliant wall flow phantom in Chapter 6.

2.3.1.11 Variability source 11: Other variations

One particular source of variation was noticed on reviewing cine loop data, in some cases it seemed that the actual nature of AWM was different between observations, rather than the AWM software's interpretation of AWM. While in one observation typical dilative AWM movement can be observed, (that of expansion of the walls outward from the vessel axis at systole followed by contraction at diastole) the observations recorded on another occasion may demonstrate a movement that involved more translatory motion than dilative motion. An example is provided (Figure 2.14). In this example, the translatory motion resulted in M_x of 143 μm compared to 365 μm , illustrating the large differences which may occur. An exploration of this phenomenon is beyond the scope of this work but has implications for the quantitative use of AWM data. If considering reproducibility in AWM measurements one must also consider natural fluctuations in AWM. Blood pressure may be a controlling factor here. However, at present it is difficult to quantify such effects.

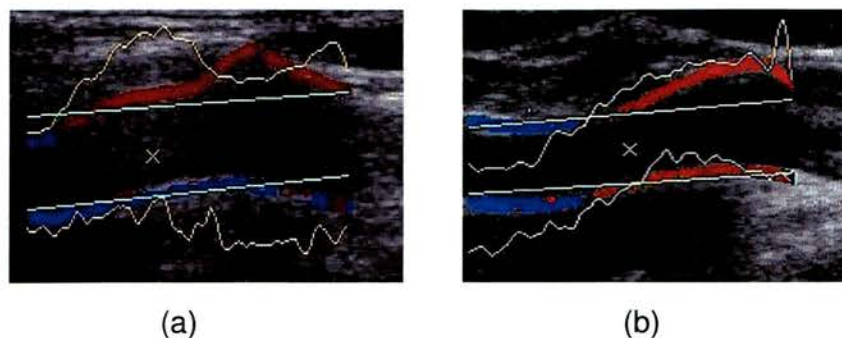


Figure 2.14: A comparison of two AWM frames at systole of the same artery segment imaged in the same session by different observers exhibiting (a) dilative AWM and (b) translatory AWM (Volunteer 5, RICA, session 1).

2.3.1.12 Frequency of occurrence of AWM variability sources

The following analysis treated CCA and ICA data separately. Overall incidence of the different sources of variability, some of which may be labelled ‘artefacts’, was quantified in terms of artefact occurrence per scanning episode (Figure 2.15). A scanning episode was defined as the three loops acquired successively on a segment of artery by a given observer in a given measurement session. This eliminated repeat counts of certain artefacts or sources of variability, which if they occurred in one loop in an episode would often occur in all three. An artefact was registered for a source of variability regardless of its extent. Note that sources of variability 5 (lack of scan line synchronisation) and 10 (transducer pressure) were excluded from analysis since the former is present in all data and the latter is not quantifiable.

Given these criteria, of the 48 scanning episodes ($4 \text{ artery sites} \times 6 \text{ volunteers} \times 2 \text{ observers}$), only 8 had cine loops acquired which were completely free of artefacts or obvious sources of variability. All 8 unaffected segments were CCAs, reflecting the relative ease with which artefact free images of the artery wall may be obtained in CCAs compared to ICAs. The most common source of variability for the CCAs was the reverberation artefact in the 2D image. This is to be expected given the presence of the relatively strongly reflecting artery and veins present on scanning CCAs. For the ICAs, the most common source of variability was by far, poor definition of the artery. This is to be expected given the ICAs more tortuous nature and greater depth relative to the CCAs.

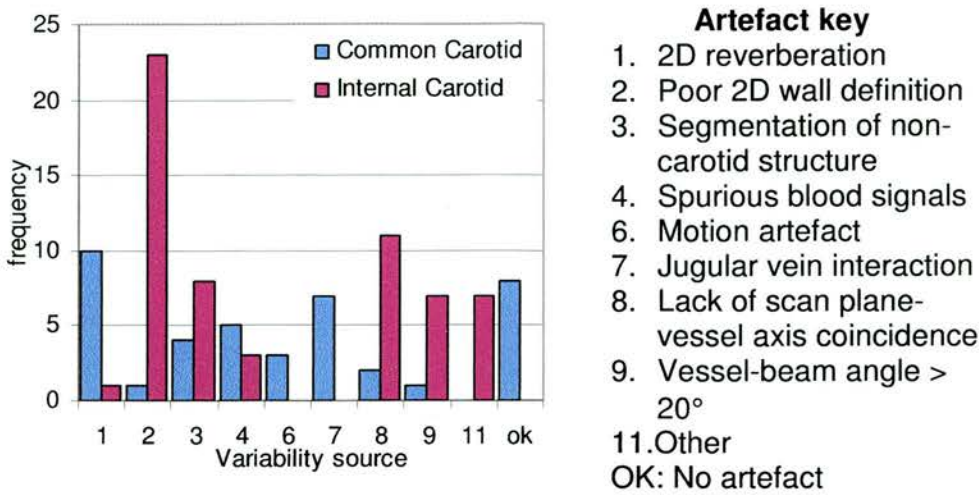


Figure 2.15: AWM artefact frequency for a sample of 24 scanning episodes for each artery type. Note contributions from different sources of uncertainty sum to more than the sample size since more than one artefact may occur in a given scanning episode. Also note the absence of sources 5 and 10; the former is present in all scanning episodes and the effect of the latter is unknown.

2.3.2 Intra-segment variability for fixed observers and fixed acquisition sessions

2.3.2.1 Inter-cycle variation

The Coefficients of Variation (CoV) calculated on comparison of AWM indices obtained for different cardiac cycles were found to be of similar magnitude with the exception of Mg, which is over double the magnitude of the other three (Table 2.4)

AWM index	CoV/%
Mn	7
Mx	11
Sd	8
Mg	21

Table 2.4: Inter-cycle Coefficient of Variation (CoV) values.

2.3.2.2 Inter-loop variation

Similar variation across the 4 AWM indices was obtained at this level. Mn proved the least variable, being under half of the value of the most variable index, Mg (Table 2.5).

AWM index	CoV/%
Mn	8
Mx	12
Sd	16
Mg	17

Table 2.5: Inter-loop coefficient of variation (CoV) values.

2.3.3 Intra-segment agreement and variability between observers and acquisition sessions

2.3.3.1 Assessment of agreement

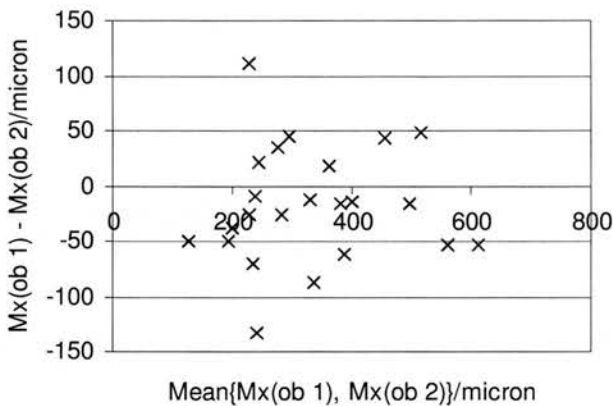


Figure 2.16: A Bland & Altman plot of the difference in Mx obtained by the two observers versus the mean values of the two observations averaged over both data acquisition sessions. The random nature of the data excludes the systematic variation of the differences with index magnitude.

An example of a Bland & Altman plot is provided for observer comparison of Mx (Figure 2.16). No systematic relationship between the differences in AWM indices is apparent and so calculation of LOA was carried out. The histograms of differences between paired AWM indices produced reasonably symmetrical distributions, which could be approximated as normal for the purposes of carrying out a paired t-test. An example is provided (Figure 2.17). P-values obtained from paired t-testing of the

differences in observations are demonstrated (Table 2.6). Of the 16 values obtained, 2 are significant at the 95 % confidence level (Mx and Sd, both for a comparison of observers, Session 1). However, the occurrence of these may be a phenomenon of multiple testing. If the null hypothesis was true for all 16 tests (that is, there is agreement between data from observers and sessions) using the properties of the binomial distribution, one can calculate a probability of 0.19 that 2 or more significant results may be observed due to chance over the 16 tests performed (see Appendix B for probability calculation). The two p-values less than 0.05 in Table 2.6 are therefore not deemed to be statistically significant.

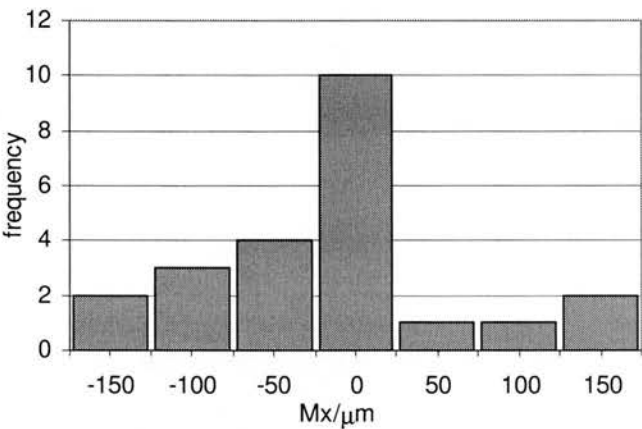


Figure 2.17: A histogram demonstrating a normal distribution of differences between paired Mx values for inter-observer variability in session 2.

Comparison set	Mn	Mx	Sd	Mg
Sessions, Observer 1	0.09	0.25	0.36	0.79
Sessions, Observer 2	0.89	0.14	0.15	0.99
Observers, Session 1	0.73	0.02	0.04	0.43
Observers, Session 2	0.23	0.61	0.80	0.11

Table 2.6: t-test p-values for differences in paired AWM indices.

2.3.3.2 AWM variability: Limits of Agreement (LOA)

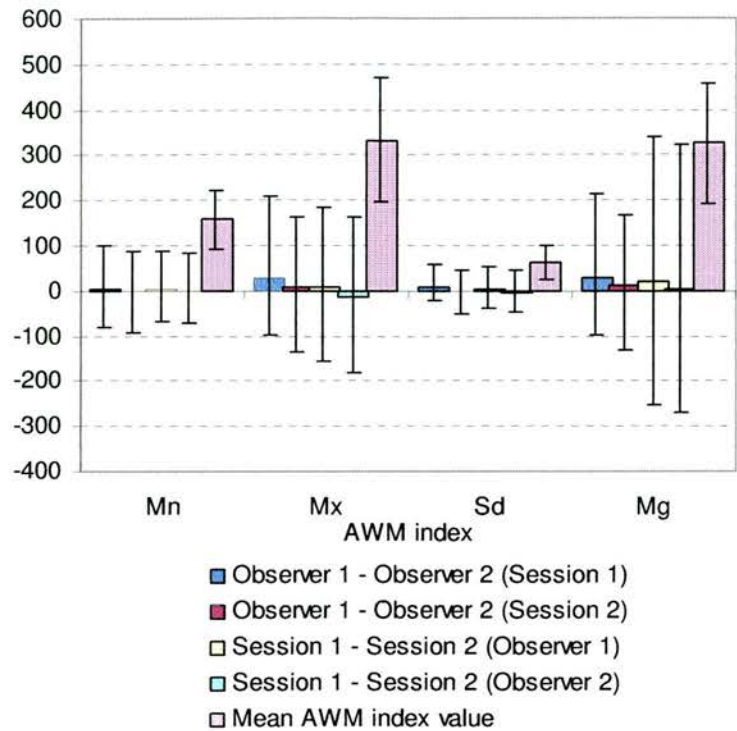


Figure 2.18: Bar chart of mean biases of differences in paired AWM indices for given segments of artery. LOA are represented by the error bars attached to the difference bars. Mean AWM values are plotted alongside LOA values and their error bars represent ± 1 SD. Y-axis units are microns, with the exception of Mg whose units is $\times 10^{-3}$.

Mean biases between paired AWM indices are demonstrated for each of the four AWM indices (Figure 2.18). The error bars in Figure 2.18 represent the calculated LOA. The mean value of each index, averaged over all artery segments scanned is plotted alongside the biases. Note the LOA apply to the biases only and not the values of the indices themselves. The mean AWM index values are therefore only plotted alongside to give an idea of the scale of the differences relative to the indices themselves. The LOA are of a similar order to the index values, suggesting large inter-acquisition variability between observers and sessions.

It is of value to put these results in to the context of other similar ultrasound variability studies. While Long has provided RC values for abdominal aortic AWM derived with the same technique used here, no other variability studies for carotid

AWM exist in the literature¹⁰⁶. Consequently, comparisons of variability are made with investigations of other carotid disease quantitative parameters derived using ultrasound and in particular clinically used parameters. Mathiesen, Joakimsen and Bønaa investigated inter-observer variability in the stenotic peak systolic velocity, PSV_s and the degree of stenosis as derived using measured velocities amongst other parameters²⁶. Montauban van Swijndregt et al investigated intra- and inter-observer variability between intima-media thickness measurements¹⁰⁸. The derived mean biases and LOA from these studies along with mean values of the parameter under investigation are shown alongside results obtained here (Table 2.1:). The table shows that other carotid artery disease indicators can also have high associated variability, as quantified by LOA, relative to the scale of the parameter being investigated. Results obtained by Mathieson et al are of particular interest since these results are in use clinically and therefore provide a gold standard with which to compare AWM index variability. For example, LOA of $\pm 0.71 \text{ m s}^{-1}$ were obtained for PSV_s , compared to the average measured PSV_s value of 1.39 m s^{-1} . This was obtained over a sample size nearly three times as big as the one used here.

Data source	Parameter investigated	Number of observers	Number of sessions	n	Mean value	Mean bias	LOA
Dineley, 2005	AWM, Mn/ μm	2	2	24	157	-1	± 92
Dineley, 2005	AWM, Mx/ μm	2	2	24	353	-17	± 153
Dineley, 2005	AWM, Sd/ μm	2	2	24	61	-4	± 43
Dineley, 2005	AWM, Mg/ $\times 10^{-3}$	2	2	24	325	-13	± 237
Mathieson et al, 2000 ²⁶	PSV _S / m s^{-1}	2	1	60	1.39	0.22	± 0.71
Mathieson et al, 2000 ²⁶	Stenosis degree/ %	2	1	60	46.3	11.4	± 26.5
Van Swijndregt et al, 1999 ¹⁰⁸	IMT/ mm	2	2	31 (1) 34 (2)	1.46 (1) 1.31 (2)	0.02 (1) -0.01 (2)	± 0.96 (1) ± 1.54 (2)

Table 2.7: A comparison of mean biases & limits of agreement (LOA) for results gathered here and two other carotid ultrasound investigations in the literature. Montauban Van Swijndregt et al quote results for the two observers separately. The separate upper and lower LOA quoted in the same paper have been averaged to give one LOA value here.

2.3.3.3 AWM variability: Repeatability coefficients (RC)

Intra-observer repeatability coefficients are provided for the mean intra-observer differences in Mx over all scanned segments and are compared to values obtained Long et al (Table 2.8).

Parameter	Study	Mean value/ μm	RC/ μm
Carotid Mx	Dineley, 2005	333 ± 136	51
Abdominal Aorta systolic diameter	Long et al, 2004 ¹⁰⁶	12472 ± 1542	2106

Table 2.8: Observer averaged intra-observer repeatability coefficients (RC) obtained here and Long et al. These are quoted with mean AWM index values to provide an indicator of the scale of the variability.

The RC values obtained here are of a similar magnitude relative to mean index values on comparison with the Long study. The Long study is thought to have been carried out with a more up to date version of the TDI software, and so would not be subject to the same extent of scan line asynchronisation artefacts that were observed here. Furthermore, the velocities and dilations exhibited by the abdominal aorta are much greater than those observed in the carotid arteries. This may result in a lower limit on relative uncertainties in AWM. Therefore, there may be scope to provide superior reproducibility in carotid arteries than that obtained in abdominal aortas.

2.4 Summary and conclusions

On inspection of the TDI and AWM data a number of sources of variability were identified. These included imaging, AWM software, operator and subject dependant factors. Quantifying the effect of the different sources over all the cine loops acquired is not a straightforward task, given that several artefacts may be present in the same segment. For this reason quantitative effects were demonstrated for individual examples only.

Variation in actual AWM (with location in an artery in the segment and with time) in asymptomatic arteries is particularly important to understand, before one can be confident in determining which aspects of the AWM data is attributable to the

segment measured, and which is attributable to the technique. For example, it may be possible that AWM varies with location around the carotid bulb due to changes in geometry and/or elasticity. *In vitro* measurements of excised arteries would be one potential strategy for evaluating such factors.

At the lowest level, intra-loop variability in AWM indices between cardiac cycles in given cine loops was found to be significant, with Mg having the highest variability (CoV = 21 %). The implication for AWM *in vivo* measurements is that it is of value to acquire as many cardiac cycles as practically possible, since averaging the indices over the cycles will provide better reproducibility than on comparing single cardiac cycles. Variation in reproducibility with number of cycles acquired has not been quantified here. This requires a separate study.

At the next level of analysis, inter-loop variability for a given scanning episode of three loops was also found to be significant, with Mg again demonstrating the highest variability (CoV = 17 %). Variability at this level contributes towards the overall variability obtained on comparing measurements derived from different observers and measurement sessions. This could imply there is an advantage to taking mean AWM values over a number of acquisitions rather than using a single acquisition. However, inspection of the cine loop data often revealed that where a single loop was affected by particular sources of variability, the other two were similarly affected, and so averaging over several cine loops provides little advantage. Instead, a single cine loop that is relatively free of sources of variability is of more value.

AWM index	Mean Bias	Mean LOA
Mn/ μm	-1	± 92
Mx/ μm	-17	± 153
Sd/ μm	-4	± 43
Mg/ $\times 10^{-3}$	-21	± 237

Table 2.9: Summary of AWM index variability, averaged over observers and sessions.

Intra-observer and intra-session variability is summarised (Table 2.9). Overall, paired AWM indices were found to agree with mean biases close to zero. However, overall LOA were found to be high. These high values are attributed to the sources of variability identified earlier. It is thought that the availability of an upgraded version of TDI software (not available at the time of this study), which applies a scan line synchronisation correction, will significantly improve reproducibility. In addition, in removing one source of variability, it will be easier to identify others. Many of the identified sources of variability have the potential to be significantly reduced, with more scanner operator training and if AWM data are examined for artefacts at the time of acquisition allowing rescanning, rather than the 'blind' acquisition methods used here where access to clinical resources was restricted. A comparison with two other studies in the literature revealed that other carotid disease indicators (including those used clinically) also suffer from high variability. Therefore, the use of quantitative AWM clinically should not be dismissed based on these results.

Mn, Mx and Sd were defined with a view to assessing overall properties of the segment in question whereas Mg was defined to identify extremes in AWM within a segment. The problem with such an index as Mg however, is that it may also reflect extremes introduced by spurious AWM data due to artefacts rather than genuine AWM. Non-genuine effects may have a relatively large effect in this study since asymptomatic arteries are likely to have lower values for Mg in comparison to diseased arteries, which are more likely to demonstrate more rapidly spatially varying AWM. Nevertheless, modifications to the method for Mg calculation may be of benefit: given the apparent sensitivity of the technique to scanning conditions, further averaging of raw maximum gradient data may improve Mg variability.

Chapter 3 Arterial Wall Motion (AWM) technique accuracy assessment using a controlled validation device

3.1 Introduction

Technique accuracy of Tissue Doppler Imaging (TDI) coupled with the Arterial Wall Motion (AWM) software must be known in order for *in vivo* AWM data to be interpreted meaningfully, including its use in the derivation of elasticity parameters such as the elastic modulus. The *in vivo* reproducibility study in Chapter 2 revealed a large number of artefact types, which introduce uncertainty in the derived AWM. While the findings of this study were valuable, there are three main limitations of *in vivo* scanning in assessing TDI/AWM technique efficacy. Firstly, there is no gold standard *in vivo* for measuring wall displacement therefore while these results give an indicator of precision, they give no indication of accuracy of the derived AWM. Secondly, given the relatively wide variability in AWM indices for a given segment of artery obtained in Chapter 2, it would be difficult to assess variation in technique performance for changes in scanner acquisition parameters. Thirdly, the cine loops in Chapter 2 often exhibited one or more artefacts. Therefore, in order to assess inherent precision and accuracy without the complicating factors of artefacts, it is necessary to investigate the AWM technique in the laboratory, with a device of simplified geometry whose motion, unlike *in vivo*, is accurately known and directly controllable.

Indeed Philips have performed some accuracy measurements, which are now described¹⁰⁴. A device was used that consisted of two layers of agar, the first of which was fixed above the transducer of a Philips HDI 5000 scanner, and the second attached to a moving piston, above the first layer. This arrangement was used to simulate the near and far artery walls observed clinically in an ultrasound image. The rig was immersed in a water bath for acoustic coupling, and the motion of the piston was induced by a pc driven controller and d.c motor. The motion waveforms applied to the piston were compared to the ultrasound TDI/AWM software derived 'dilations' or displacements. This was carried out for the available range of

sensitivity settings on the scanner and a number of velocity scale settings in the physiological range (0.5 cm/s to 3.3 cm/s). In the case of the HDI 5000 scanner, Philips use the term 'sensitivity' as an indicator of the ensemble length delivered by the transducer. The higher the sensitivity setting out of 'Low', 'Medium', 'High' and 'Maximum', the greater the ensemble length.

Though the study was valuable as a first indication of accuracy of the AWM technique, it has some limitations. No indicator of the piston motion accuracy is provided in the publication. Relatively little information is provided on the methodology, including scanner settings, and the analysis of the AWM data such as cycle or cine loop averaging of AWM or the presence of any AWM artefacts. Furthermore, there are no experimental uncertainties attached to the data points. The authors provide plots of the bias of the TDI derived 'maximum dilation' relative to the actual maximum dilation and the 'standard deviation of dilation'. It is important to note that the parameters maximum dilation and standard deviation of dilation have not been defined in the text by the authors. As such, they may have been calculated slightly differently from the Mx and Sd parameters used in this thesis. An aspect of the TDI/AWM technique that has not been investigated is variation in performance with velocity and dilation ranges of the AWM under interrogation. Furthermore, there are a number of scanning parameters not included in the Philips study which may in part dictate the performance of the TDI/AWM software technique, such as Time Gain Control (TGC) and colour box size.

All the factors stated above justify a further, more detailed investigation of AWM accuracy. Therefore the aim of this chapter is to assess accuracy of the TDI and AWM software technique.

This necessitates the design and construction of a suitable test object. Vessel flow phantoms do not offer the possibility of directly controllable, accurately known AWM since the coupled fluid and solid mechanics involved are complex, even for simple geometries such as the one used later in this thesis. The uses of vessel mimicking flow phantoms also introduce further uncertainties of a geometric nature

such as scan plane-vessel axis coincidence, which are discussed in Chapter 6. For this reason a simpler device, similar to that used by Philips, with two planar sections of tissue mimicking material (TMM) simulating the artery walls, was devised for accuracy assessment. The device was designed, constructed and accompanying software programmed by Mr. Steven Hammer, a research associate in the Department of Medical Physics and Engineering at the University of Edinburgh. An optical validation of the device for sinusoidal and physiological AWM waveforms was performed in order to quantify the device movement accurately. Optical data was collected by Steven Hammer, while the author performed analysis of the data. This work, along with the methodology or TDI/AWM accuracy assessment is described in the following section.

Analysis of acquired AWM data has been divided into three main sections. Firstly, a TDI independent assessment of the validation device motion using B-mode data from the raw cine loops is described (Section 3.3.1). This served as a further check of maximum dilation and allowed detection of any differential motion along the length of the scanned TMM. Secondly, an examination of the raw AWM data is presented (Section 3.3.2). Thirdly, a subset of the raw AWM data is used to quantify technique accuracy (Section 3.3.3).

3.2 Materials and methodology

3.2.1 The AWM validation device

Photographs of the AWM validation device demonstrate the two vessel mimicking layers of polyvinyl alcohol (PVA) cryogel (Figure 3.1). The method for manufacture of PVA cryogel with added acoustic scatterers is described in Chapter 4. Polyvinyl alcohol cryogel was chosen over other materials with acoustic tissue equivalence such as gelatin and agar based materials since it is robust and can tolerate the high stresses required to attach it to the validation device securely without breaking. The upper PVA layer, which represents the near artery wall in the ultrasound image (Figure 3.2) was secured to the transducer (Figure 3.1c). A further layer of PVA cryogel was placed between it and the transducer to provide a 5 mm separation between the wall simulating layer and the transducer face. The appearance of the two PVA layers when imaged using TDI is demonstrated (Figure 3.2). The 2D gain in Figure 3.2 has been enhanced in order that the upper PVA layer may be visualised.

The PVA layer was coated in water-based acoustic coupling gel prior to attachment to the transducer, to remove air from between it and the transducer. The transducer was secured with a clamp attached to the main structure of the validation device. The lower layer of PVA that represents the far artery wall in the resulting ultrasound images was secured to an aluminium frame on top of a piece of acoustic absorber, which minimised reflections from the frame and the base of the water bath it was seated in. The aluminium frame was driven in the vertical plane, moving the lower PVA layer relative to the upper, stationary layer attached to the transducer, thereby simulating AWM. The frame was driven by a lead screw table coupled with a stepper motor. The table has a 50 mm range, and was therefore easily capable of producing displacements over the entire physiologic range of AWM. The water bath used as an acoustic couplant was earthed to minimise electrical interference in the acquired ultrasound signal while the stepper motor was running. The device has rubber feet attached to its base to absorb vibrations produced by the device. A stepper motor drive provided an interface for control of the lower PVA layer motion. This was set to induce displacements by the motor of 1.25 μm per step. A custom-written

LabView program generated the desired AWM waveforms for testing, and converted them into a program written using EASI code for application to the drive.

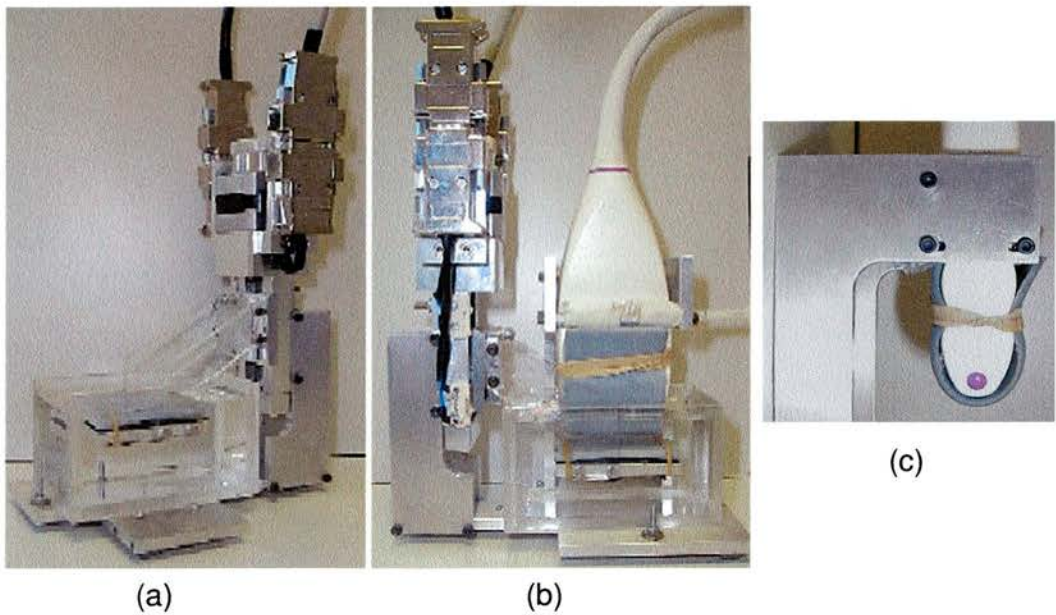


Figure 3.1: The AWM validation device (a) with only the lower, moving TMM layer in place (b) with the transducer in place and a layer of TMM secured to it, acting as the near artery wall (c) a close up of the transducer holder.

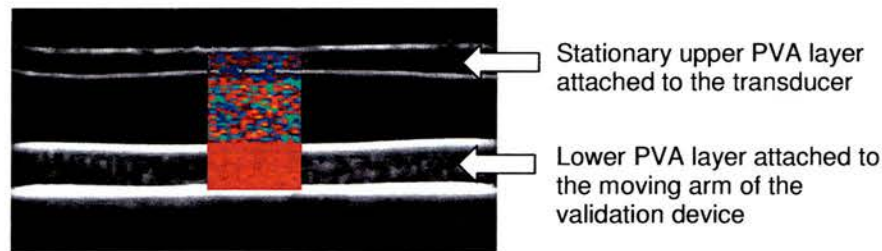


Figure 3.2: A raw TDI image of the AWM validation device with the two cryogel layers in place. 2D gain has been enhanced in order to visual the near PVA layer.

An optical evaluation of the device movement using laser Doppler vibrometry was carried out for comparison with the ultrasound derived AWM. This involved measurement of the position of the lower moving part of the device by a reflected laser beam. This was performed without the PVA cryogel layers in place since it did not provide a sufficiently reflective surface for the laser beam. Optical data was acquired for each of the AWM waveforms tested with ultrasound in this chapter. The device provided an output in Volts that could be converted to microns, using the

calibration of the vibrometer. For each AWM waveform to be used for TDI/AWM accuracy assessment, for ultrasound interrogation five motion sequences of approximately five cycles were acquired. Analysis revealed the device produced highly consistent AWM cycles. Variability in device maximum dilation was quantified using inter- and intra-sequence (equivalent to inter-cycle) standard deviations. Inter-sequence standard deviations were under 0.8 % of the device maximum dilations for all motion waveforms tested. Intra-sequence standard deviations were under 1.2 % of the maximum dilations for all waveforms tested.

3.2.2 AWM waveforms investigated

TDI/AWM software technique efficacy was investigated using two different AWM waveform shapes; sinusoid and physiologic. Tissue Doppler data was acquired for five sinusoidal and two physiologic device motion waveforms. Key properties of all waveforms are summarised (Table 3.1) and temporal plots are shown (Figure 3.3). The waveforms were chosen to cover the physiological ranges for dilation, velocity and acceleration as well as possible within the validation device specification. The two physiological waveforms are shown alongside two typical *in vivo* AWM curves acquired in Chapter 2. The device simulated displacements and velocities are similar to those found *in vivo*.

By definition, physiological AWM waveforms are the more realistic of the two waveform shapes and therefore provide the most representative AWM *in vivo* accuracy estimate. However, use of sinusoid waveforms has two advantages. Firstly, there is value in the use of the simplified shape of the sinusoid since any distortion by the TDI/AWM software technique is easier to identify. Secondly, there is a lack of flexibility and control over physiologic AWM waveform properties imposed by the validation device software. For example, the choice of physiological AWM maximum dilation dictates the cycle period produced by the software. For waveforms with maximum dilations at the upper extreme of the *in vivo* carotid range, this can result in AWM waveforms longer than typically found *in vivo*, which limits the number of cycles of TDI data which may be acquired per cine loop using the fixed buffer length of the HDI 5000 scanner. For example, when using waveform B, typically only 2 – 3 AWM cycles may be captured.

Waveform	Maximum displacement, Mx_0 / μm	Maximum velocity/ cm s^{-1}	Rise time/s	Cycle period/s
1	248 ± 1	0.32 ± 0.02	0.19	0.47
2	494 ± 1	0.59 ± 0.02	0.19	0.47
3	740 ± 2	0.85 ± 0.03	0.19	0.47
4	991 ± 3	1.03 ± 0.01	0.19	0.47
5	1190 ± 1	1.20 ± 0.02	0.19	0.47
A	295 ± 3	0.68 ± 0.03	0.11	1.07
B	594 ± 2	0.65 ± 0.02	0.15	1.49

Table 3.1: Key properties of sinusoidal AWM (1 – 5) and physiologic (A – B) waveforms applied to the validation device for accuracy assessment.

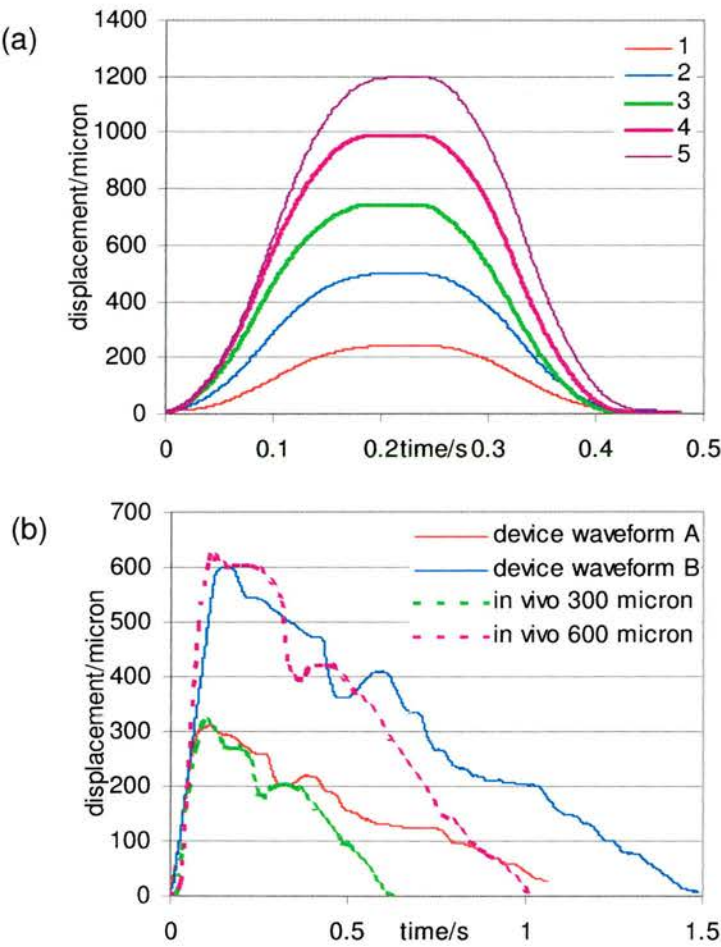


Figure 3.3: (a) Sinusoidal (b) Physiological displacement waveforms performed by the validation device for accuracy assessment of TDI/AWM software technique.

3.2.3 TDI data acquisition

As in Chapter 2, TDI data was acquired using a Philips HDI 5000 scanner. The first half of this chapter's investigation comprised tests of AWM accuracy upon varying maximum dilation and velocity, using the waveforms described. These were performed using the same settings recommended by Philips and used *in vivo* in Chapter 2. The colour box width was set to its minimum value of 0.7 cm to maximise frame rate and therefore temporal resolution of the raw TDI data. In the case of 2D gain and Time Gain Control (TGC) settings, no absolute quantitative settings are provided by the scanner. Standardisation of TGC settings was achieved by moving the scanner sliders to the middle of their range. The 2D gain was standardised by reducing the gain until the near wall PVA layer was not visible. The 2D gain dial was then wound up slowly, one click at a time, increasing the 2D gain until the near layer just became visible. The far PVA layer produced a far stronger reflection than the near wall and so this was easily identifiable in the resulting 2D image while minimising spurious echoes. For each waveform tested three TDI cine loops were acquired, each containing as much data as the scanner buffer would allow (typically 5 - 7 for the sinusoidal AWM and 2 - 4 for the longer physiological AWM cycles).

3.2.4 TDI independent verification of device motion

A further TDI independent check of device motion, in addition to the optical measurements was carried out. In particular, actual maximum dilation by the device was evaluated in compared to maximum dilation as evaluated optically. B-mode data in the TDI cine loops from which TDI AWM accuracy was derived in section 3.3.3 was used to evaluate AWM. This investigation was used in particular to exclude any gross differential motion of the PVA cryogel layer across the TDI scanned length since, as stated in section 3.2.1, optical vibrometry measurements which evaluated actual device motion were performed with the cryogel layer absent. The B-mode analysis was also useful as a check to exclude any gross deviations in maximum dilation of the device from motion cycle to motion cycle or cine loop to cine loop.

Analysis was carried out using the ultrasound image analysis software, HDILab (Philips Medical Systems, Bothell, WA). One of the software's tools produces plots of lumen diameter versus time for user defined regions of interest (ROI) of the vessel

walls, which can be exported as delimited files for analysis. Maximum dilation was evaluated for 2×2 mm wide ROI positioned at the left and right extremes of the TDI colour box length (M_{XB_LEFT} and M_{XB_RIGHT}). Overall maximum dilation M_{XB} averaged over the two ROI was then calculated. Differences between M_{XB_LEFT} and M_{XB_RIGHT} were also calculated for each cycle in each cine loop. The B-mode measurement technique resolution is limited by the image pixel size of $148 \mu\text{m}$. The pixel size is provided by HDILab and is dependent on the image depth. Therefore, any given dimension of maximum dilation may lie, in theory, as much as $\pm 75 \mu\text{m}$ from the value obtained. However, this resolution of dilation was deemed sufficient for the detection of gross differences in maximum dilation between cycles and cine loops and differential movement along the PVA cryogel layer.

3.2.5 TDI Data analysis

Similar methods were used for AWM index extraction from raw TDI data as in Chapter 2. This included the application of custom written Matlab code (MathWorks Inc., Natick, MA) to calculate the characteristic indices of the TDI derived AWM cycles. Maximum dilation, M_{XTDI} was derived from TDI to compare to the actual motion of the validation device as evaluated by laser vibrometry, M_{x0} , to determine technique accuracy. This was deemed to be the most important AWM parameter given that it may be applied to derive values for several elasticity and compliance parameters quoted in the literature. M_{XTDI} is equivalent to the M_x defined in Chapter 2 (see Section 2.1.1). It is renamed M_{XTDI} for clarity upon comparison with device maximum dilation, M_{x0} .

Standard deviation of dilation, S_d , also defined in Chapter 2, is of interest. Unlike the scanned arteries in Chapter 2, where uniform elasticity along the scanned segment could only be supposed, the validation device used here should demonstrate no spatial gradients in dilation since the PVA layers are attached to rigid structures. All points along the ‘walls’ should be moving at the same velocity and by the same displacements at any given time, unlike an artery *in vivo* which may or may not demonstrate spatial variations in elasticity and therefore AWM. Therefore, S_d obtained here reflects distortion of the true motion of the device by the TDI/AWM software technique. S_d is not a direct indicator of accuracy but it is a quantitative

measure of the broadening introduced by the TDI/AWM technique. This is of interest since such an effect will mask any genuine variations in dilation across the length of a scanned segment of artery or phantom.

A statistical power test was performed to determine the value of one-way analysis of variance (ANOVA). ANOVA at the 95 % confidence level identified significant differences between technique accuracy estimations for the different AWM waveforms.

3.3 Results and discussion

3.3.1 TDI independent verification of device motion

An example of the pseudo-M-mode data produced from the B-mode image frames by HDILab is provided (Figure 3.4). An example of the temporal plots generated is also demonstrated (Figure 3.5). The percentage difference between B-mode and laser vibrometry estimated maximum dilations (cycle and loop averaged) are plotted for each waveform (Figure 3.6). The error bars are the combined inter-cycle and inter-loop standard deviations for both B-mode and laser data. There are two main features of note in this graph.

Firstly, no percentage difference exceeds 20 % and most are under 5 %. This suggests good agreement between the two techniques within the limited resolution of the B-mode data. The limited resolution of the B-mode technique ($148\text{ }\mu\text{m}/\text{pixel}$) is thought to be the cause of the largest differences of 20 % obtained for waveforms 1 and 2 in Figure 3.6. Maximum dilations of $297\text{ }\mu\text{m}$ and $594\text{ }\mu\text{m}$ were registered using B-mode data for waveforms 1 and 2 respectively. In the case of waveform 1, $297\text{ }\mu\text{m}$ is the most accurate value that could be produced given the B-mode resolution and the actual maximum dilation of the device, as measured optically ($248\text{ }\mu\text{m}$). For waveform 2 this was not the case. The closest possible B-mode value, $444\text{ }\mu\text{m}$ ($= 148\text{ }\mu\text{m} \times 3$), was not obtained. However, the actual maximum dilation of the device, as measured optically ($494\text{ }\mu\text{m}$) falls within $24\text{ }\mu\text{m}$ of the mid-point between the two closest possible B-mode values, $444\text{ }\mu\text{m}$ and $594\text{ }\mu\text{m}$ ($= 148\text{ }\mu\text{m} \times 4$). This

may explain why the next closet value, 594 μm , was obtained using the B-mode measurements.

Secondly, the error bars are small, with all but two data points having errors less than $\pm 0.5\%$. This reflects the consistency in maximum dilation of the validation device between motion cycles and loops.

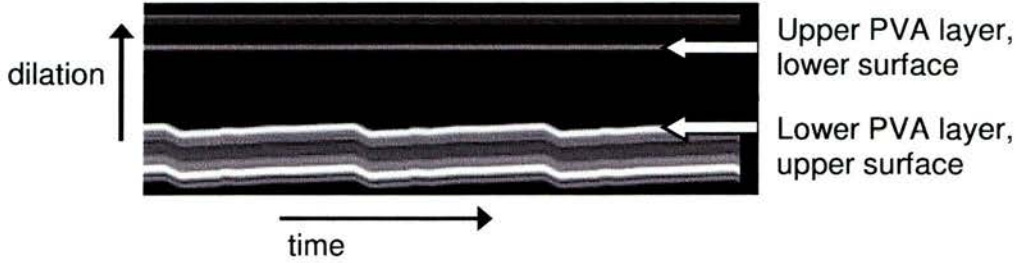


Figure 3.4: An example of pseudo-m-mode image generated from a 2 mm wide ROI in the TDI scanned segment of B-mode data for waveform B.

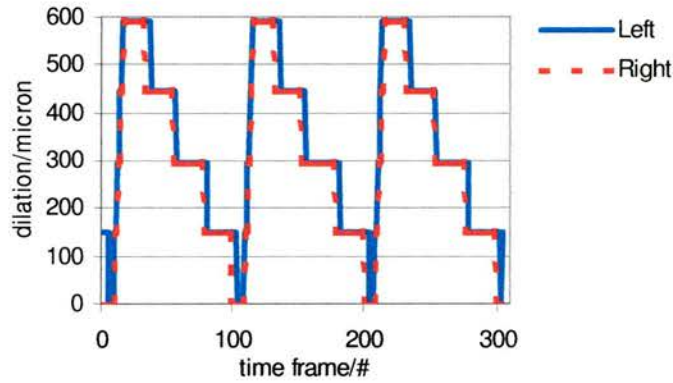


Figure 3.5: An example of the dilation plots for waveform B motion generated from B-mode data for 2×2 mm wide ROI of the TDI scanned segment.

Evidence of differential motion across the PVA cryogel layer is quantified by $(M_{XB_LEFT} - M_{XB_RIGHT})$ (Table 3.2). The uncertainty attached to each $(M_{XB_LEFT} - M_{XB_RIGHT})$ value is $\pm 106 \mu\text{m}$, and is calculated by combining the individual uncertainties of $\pm 75 \mu\text{m}$ in M_{XB_LEFT} and M_{XB_RIGHT} in quadrature. All but 3 of the 21 cine loops (7 waveforms \times 3 loops each) demonstrated no difference between M_{XB_LEFT} and M_{XB_RIGHT} , within experimental error bounds. Gross differential motion across the PVA layer can therefore be excluded.

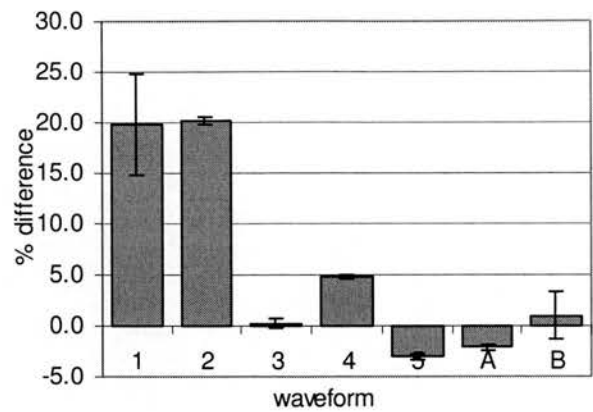


Figure 3.6: Percentage difference between laser vibrometry and B-mode estimates of maximum dilation.

Waveform	Cine loop	Cycles per loop	Cycles where $M_{x_{B_LEFT}} - M_{x_{B_RIGHT}} \neq 0$	$M_{x_{B_LEFT}} - M_{x_{B_RIGHT}} / \mu m$
5 (Sinusoid)	2	6	5	148 ± 106 (all affected cycles)
5 (Sinusoid)	3	6	5	148 ± 106 (all affected cycles)
A (Physiologic)	2	3	1	148 ± 106
All other data	-	-	-	0 ± 106

Table 3.2: $(M_{x_{B_LEFT}} - M_{x_{B_RIGHT}})$ for all acquired cine loops.

3.3.2 Qualitative assessment of TDI derived AWM accuracy

Typical examples of TDI derived AWM cycles are demonstrated for three of the validation device motions investigated: waveform 3 (deemed representative of most of the sinusoidal data acquired), waveform A and waveform B (Figure 3.7). The actual motion of the validation device as measured optically is superimposed upon the TDI derived AWM, demonstrating TDI/AWM software accuracy.

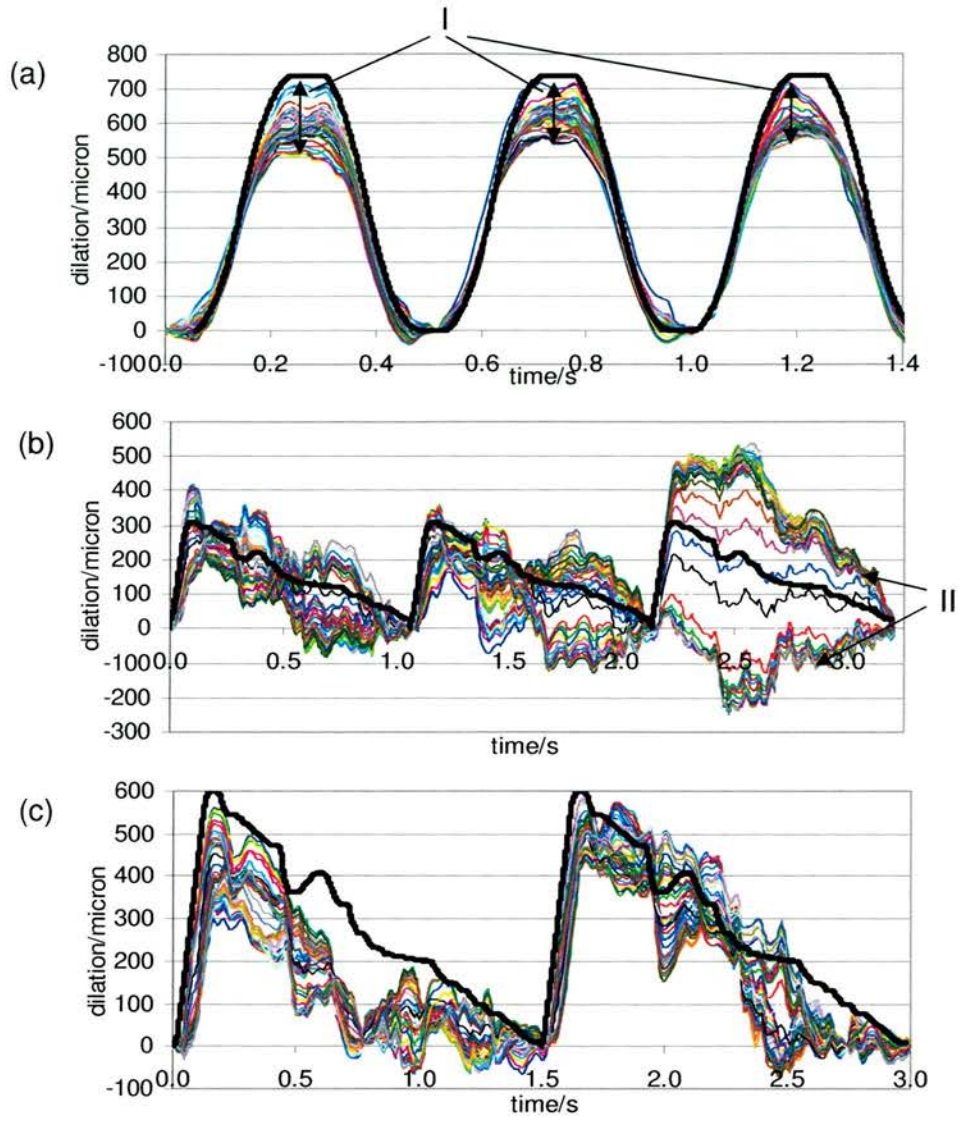


Figure 3.7: TDI derived AWM for typical (a) sinusoidal motion (waveform 3) (b) physiological motion (waveform A) (c) physiological motion (waveform B). The solid black line represents the actual device motion as measured by laser vibrometry. 'I' demonstrates broadening of dilations (see 3.3.2.1). 'II' demonstrates spatial bunching of dilations (see 3.3.2.2).

3.3.2.1 Sinusoidal AWM

On the whole, the sinusoidal AWM in Figure 3.7 resembles the motion of the validation device. However, it appears that the TDI/AWM software has systematically under-estimated AWM amplitude. The degree of under-estimation is quantified in the following section. Another key feature ('I' in Figure 3.3a) of the sinusoidal data is the 'broadening' of the TDI derived AWM curves. Dilations from each scan line at a given time do not coincide precisely with one another as one might expect, given the validation device exhibits uniform motion over the length of the cryogel layers. For example, in the plot shown, at the peaks of the AWM cycles, there is a range in maximum dilation of 150 - 200 μm over all scan lines. This exceeds any differential movement estimated by the B-mode analysis in section 3.3.1.

While the plot in Figure 3.7a is typical of the derived sinusoidal AWM, some of the TDI derived AWM for waveform 1 was somewhat different to that expected. Plots of AWM averaged over all TDI scan lines for two cine loops, one acquired directly after the other, demonstrate a marked difference between the two (Figure 3.8). Loop 1 exhibits a series of cycles much smaller than the 248 μm expected amplitude, with exception of the last cycle. In comparison, in loop 2 all cycles are registered and reproduced with reasonable accuracy by the TDI/AWM software technique. Inspection of the segmented TDI cine loops reveals red TDI pixels during the supposed expansion phase of the AWM cycle (e.g. at point X in Figure 3.8) in the affected cycles. This implies motion towards the transducer rather than the expected motion away from the transducer represented by blue pixels, therefore a decrease in dilation is registered before the PVA layer has reached its maximum dilation. Such TDI behaviour is not observed in unaffected cycles in Figure 3.8.

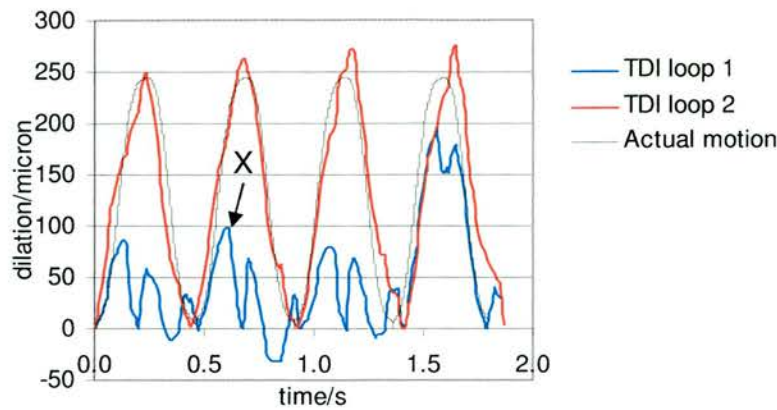


Figure 3.8: Mean AWM versus time demonstrates the variability in derived AWM between two consecutively acquired cine loops for waveform 1 device motion. ‘X’ is one of several points where instead of blue TDI pixels, indicating the expected expansion of the device ‘walls’, red was incorrectly assigned by TDI and therefore interpreted by the AWM software as wall contraction.

Validation device motion consistency from cycle to cycle has been proven by the laser vibrometry measurements (see Section 3.2.1) and B-mode estimates of maximum dilation and so variations in actual motion of the device are excluded as the cause of the variability. The artefact therefore appears to be a result of some limitation in TDI. The transient nature of this artefact is puzzling, given that it affects some cine loops and not others, and some cycles and not others within a given cine loop. Furthermore, this artefact has only occurred for sinusoidal waveform 1. Misinterpretation of AWM data due to this artefact may be avoided by acquiring more than one cine loop of the site under investigation and excluding affected cycles from further analysis. Affected cycles are easily identified when adjacent to the markedly larger unaffected cycles.

3.3.2.2 Physiological AWM

The TDI derived physiological AWM resembles the validation device motion to an extent; the rapid rise to a peak dilation followed by a slower decay to zero dilation is mimicked. However, there are two types of distortion introduced by the TDI/AWM software technique. Firstly, the broadening described for the sinusoidal AWM also occurs for the physiological curves. However, broadening appears to occur to a greater degree here. This is illustrated by Sd values (derived as in Chapter 2)

normalised to maximum dilation for both types of device motion and averaged over all cycles and cine loops obtained (Table 3.3). It can be seen that the normalised physiologic Sd values are up to eight times greater than those of the sinusoidal waveforms.

Waveform	Sd /Mx / %
1 (Sine)	10.0 ± 0.8
2 (Sine)	4.7 ± 0.2
3 (Sine)	4.2 ± 0.2
4 (Sine)	3.2 ± 0.1
5 (Sine)	3.3 ± 0.2
A (Physiological)	26.5 ± 2.0
B (Physiological)	12.4 ± 2.4

Table 3.3: Cycle and loop averaged Sd values normalised to maximum dilation for each validation device waveform.

The second type of distortion ('II' in Figure 3.7b) shows variation in dilation depending on the scan line location in the colour box. One can see discrete 'bunches' of dilations. Further examination of the raw dilation data reveals these bunches to correspond to scan lines in the left (with dilations peaking at approximately 450 - 500 μm) and right (with dilations peaking at approximately 50 - 100 μm) halves of the colour box. Examination of the segmented cine loops corresponding to this AWM data reveals the TDI data responsible for the artefact (Figure 3.9). Tissue Doppler data is shown for two image frames. The frames are taken from the rise phases of the second and third motion cycles in Figure 3.7. The unaffected cycle (a) demonstrates largely homogenous colour along the lower moving PVA cryogel layer. The affected cycle (b) demonstrates a region in the lower moving wall in the right hand quarter of the colour box which is a markedly darker blue than the rest of the wall, representing lower estimated velocities.

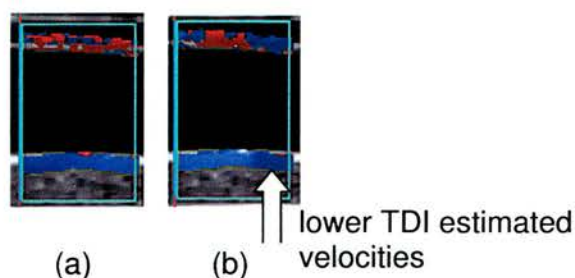


Figure 3.9: Image frames from the rise phase of two waveform A physiological motion cycles within the same cine loop, one unaffected (a) and one affected (b) by the ‘bunching’ artefact in Figure 3.7.

Such gross differential movement of the cryogel layer across the TDI box length has been excluded by the B-mode investigation in section 3.3.1. Furthermore, one would expect such large differential motions to be observable by eye. However, this is not so. These observations and the TDI data in Figure 3.9 suggest a limitation in the TDI estimation by the scanner rather than a validation device error. However, this type of distortion has only been observed for the physiological waveforms (most markedly for waveform A motion but also for waveform B motion) and was not observed in flow phantom AWM data acquired in Chapters 5 and 6. A potential source of distortion concerns the electromagnetic noise and the stepper motor operation by which physiological AWM is generated by the device, which is different to that used for sinusoidal AWM generation. Sinusoidal AWM generation by the validation device involves the following operation of the stepper motor:

- Stepper motor switches on
- Drives at constant acceleration until maximum dilation is reached
- Stepper motor switches off
- Stepper motor switches on
- Drives at constant acceleration until original zero displacement is reached.

Physiological AWM waveforms exhibit a range of accelerations and the stepper motor is switched on and off continuously throughout the cycle to generate these. It is postulated that the switching on and off of the stepper motor provides a source of

radio-frequency (RF) radiation which interferes with the genuine RF signal generated by the device motion.

Identification of the mechanism by which the bunching artefact arises in the physiological waveforms requires further experimental investigation which is beyond the scope of this chapter. It is deemed therefore, given their lack of reproducibility and lack of understanding as to why the artefact arises, that physiological waveforms should not be used in the following quantitative assessments of TDI/AWM technique accuracy. Instead, sinusoidal AWM alone is used for accuracy assessment.

3.3.3 Quantitative assessment of TDI derived AWM accuracy

Accuracy of the TDI/AWM software is assessed in two ways, firstly by comparison of TDI derived maximum dilation, $M_{x_{TDI}}$ with the optically measured maximum dilation of the device, and secondly, by considering the variability associated with $M_{x_{TDI}}$.

3.3.3.1 Maximum dilation, $M_{x_{TDI}}$ accuracy

Maximum dilations, $M_{x_{TDI}}$, averaged over all cycles and cine loops acquired for each sinusoidal waveform are shown, together with the percentage deviation from the actual maximum dilation, M_{x_0} for each AWM waveform investigated (Table 3.4). The errors quoted for each are the combined intra-loop (or inter-cycle) and inter-loop standard errors. The TDI derived maximum dilation, $M_{x_{TDI}}$ are also plotted against actual maximum dilation (Figure 3.10).

Waveform	$M_{x_0} / \mu\text{m}$	$M_{x_{TDI}} / \mu\text{m}$	$M_{x_{TDI}} - M_{x_0} / \%$
1	248 ± 3	241 ± 20	-3 ± 8
2	494 ± 2	432 ± 7	-12 ± 1
3	740 ± 1	603 ± 6	-19 ± 1
4	991 ± 3	775 ± 6	-22 ± 1
5	1140 ± 1	917 ± 6	-23 ± 1

Table 3.4: Comparison of TDI derived maximum dilation, $M_{x_{TDI}}$ with device maximum dilation, M_{x_0} for 5 sinusoidal waveforms.

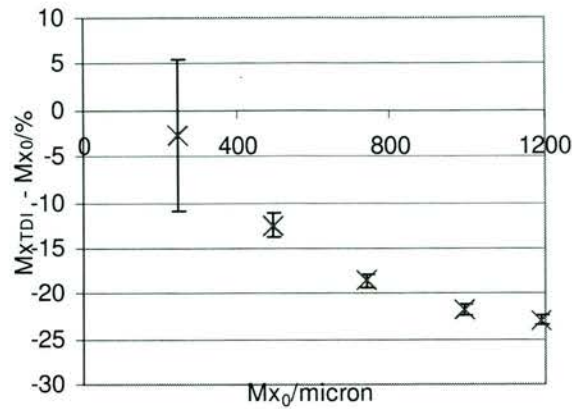


Figure 3.10: Percentage deviation in TDI derived maximum dilation, Mx_{TDI} versus actual maximum dilation, Mx_0 .

Maximum dilation is underestimated for every AWM waveform tested. The degree of underestimation appears to increase with Mx_0 . If one excludes the first data point, which has a relatively high associated variability (waveform 1, $Mx_0 = 248 \mu\text{m}$) ANOVA demonstrates that the trend is significant (p-value < 0.005, power = 1.00). Percentage differences are of a similar order to those measured by Bonnefous, who obtained an accuracy of 10 - 15 % for a physiological AWM waveform with a rise time of approximately 0.1 s and amplitude of approximately $400 \mu\text{m}^{104}$. The same study also derived similar Sd values (5 - 10 %) to those quoted in section 3.3.2.2.

Two possible causes of the underestimation of dilation are observable in the segmented TDI images. Firstly, despite the use of a scanner velocity range of 1.5 cm s^{-1} which is somewhat bigger than the maximum velocities of the AWM waveforms tested (see Table 3.1), a small amount of aliasing is observable in the segmented TDI strips for the three largest sinusoids. An example is shown for waveform 5 (Figure 3.11a). The aliasing does not occur in every image frame or in every location in the TDI strip in the colour box, and it is difficult to quantify its overall effect on the AWM accuracy. However, it will reduce the amplitude of the derived dilations as the measured velocity is lower. The effect of any aliasing will become more marked as the peak velocity of the AWM increases, which could explain why the degree of underestimation by Mx increases across the sinusoidal waveforms.

Secondly, throughout all AWM waveforms, colour pixels of opposite colour to that corresponding to the direction of motion can be seen. For example, during the expansion phase of the AWM cycle the moving PVA layer appears predominantly blue as it moves away from the transducer, but regions of red can be seen in the TDI strip, appearing consistently along the upper edge of the TDI strip (Figure 3.11b). These appear differently to the aliased pixels; one does not see the full range of colours one would expect to see in an aliased colour image. It is thought that these regions are registering velocities from outside of the PVA layer, as observed *in vivo* in Section 2.3.1.4. This phenomenon is possibly due to limitations in spatial resolution of the TDI image and inadequate tracking of the wall as it accelerates sharply. This artefact, like aliasing, will reduce the mean estimated velocity and any derived dilations.

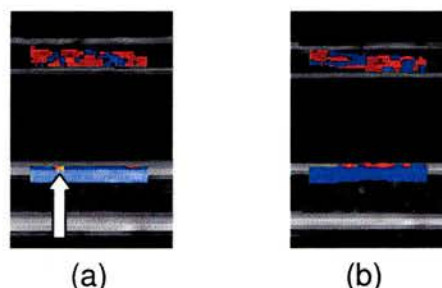


Figure 3.11: Segmented TDI frames showing (a) aliasing in a cine loop of waveform 5 (marked by arrow) (b) spurious colour thought to result from velocities outside the PVA layer in a waveform 3 cine loop. Both frames are taken from the expansion phase of the AWM.

The efficacy of mean velocity estimation by the scanner is fundamental in accurate determination of maximum dilation. Tissue Doppler Imaging, as with colour flow imaging provides a mean velocity estimate for a given pixel and time interval. The results of the estimation may vary with the exact nature of filtering of the ultrasound signal prior to estimation. Unfortunately, the exact nature of these factors is unknown due to the proprietary nature of the ultrasound scanner. Scan line asynchronicity already mentioned in Chapter 2 and limitations of the correction applied by the AWM software to account for the phenomenon may also be responsible for

maximum dilation underestimation. Beyond these hypotheses, it is difficult to ascertain the exact mechanisms by which the inaccuracies are introduced, given the 'black box' proprietary nature of both the scanner and AWM software signal processing.

Clinically, the underestimation of maximum dilation means elasticity parameters such as the pressure-strain elastic modulus will be underestimated. This underestimate will be especially marked for larger, relatively elastic arteries which exhibit large dilations. For example, Long et al measured abdominal aortic dilations using an adapted version of the TDI/AWM technique *in vivo*¹⁰⁶. They obtained a 'mean maximal segmental dilation' (MMSD) (thought to be similar to the Mx parameter defined in this thesis) of $1160 \pm 301 \mu\text{m}$ ($n = 24$). There is an associated under-estimation of maximum dilation of 23 % at this magnitude compared to an under-estimate of $-3 \pm 8 \%$ for maximum dilations of $250 \mu\text{m}$. Therefore, actual maximum dilation over all scanned subjects may be as high as $1427 \mu\text{m}$. The variable degree of underestimation of maximum dilation introduces a source of variability to *in vivo* estimation of AWM additional to those discussed in Chapter 2.

3.3.3.2 TDI derived AWM variability

Variability in Mx_{TDI} illustrated by the error bars in Figure 3.10 are small except for those associated with the waveform 1 motion, which are 3 times larger than for the other sinusoids. This difference is thought to be in part due to the small number of cycles available for analysis. A number of cycles affected by the artefact demonstrated in Figure 3.8, which is thought to be a TDI error, were excluded from quantitative analysis. This left one loop of four cycles and a second loop with only one cycle in the sample. Standard deviation in dilation, Sd are a further measure of variability but reflect the variability or broadening over a whole AWM cycle rather than just the estimation of maximum dilation that is discussed above. Normalised values have been quoted for each sinusoid in Table 3.3. An increase is observed as dilation decreases, therefore TDI derived AWM of smaller motion cycles are visibly more broadened than AWM of larger motion cycles.

3.3.4 Validation device limitations

The AWM validation device has succeeded to a degree in providing a measure of *in vivo* TDI/AWM software technique accuracy. The device produced precise AWM for measurement with ultrasound, with maximum inter-sequence and intra-sequence (equivalent to inter-cycle) standard deviations in device maximum dilation of 0.8 % and 1.2 %. It also allowed the generation of AWM waveforms covering the entire physiological range of velocities and displacements. However there were two main limitations.

Firstly, on the basis of preliminary results presented here, physiological AWM derived from the device motion using TDI was deemed too variable for use in quantitative analysis of TDI/AWM software performance. Specifically, the reasons for the marked bunching of dilations from different locations in the TDI scanned segment were not fully understood and required further investigation, which was beyond the scope of this chapter. The artefact appears to be unique to physiological AWM generated by the validation device. Sinusoidal AWM produced by the device and various AWM produced by the compliant wall flow phantom in Chapters 5 and 6 did not demonstrate such behaviour. Also related to physiological AWM generation, the software accompanying the validation device was not flexible enough to generate physiological waveforms of shorter duration than the 1.1 s and 1.5 s cycles used here without markedly reducing maximum dilation. A shorter cycle would allow more cycles to be captured per cine loop, and would allow for the representation of a greater range of heart rates.

The second main limitation of the device is the scanning geometry. The current design places the PVA layer closest to transducer approximately 5 mm from the transducer face. A value of 10 – 15 mm would be more appropriate, increasing attenuation of the ultrasound beam by 200 – 300 % and providing more realistic received signal strengths.

3.4 Conclusions

Quantitative assessment of technique accuracy has been performed on a range of AWM dilations, velocities and accelerations for the first time. This was performed using a custom built validation device which has been shown to produce highly reproducible motion cycles. The TDI derived AWM index of maximum dilation, M_x , differed from the true maximum dilation of the device by between $-3 \pm 8 \%$ and $-23 \pm 1 \%$ for sinusoidal device motion. A statistically significant increase in underestimation was found on increasing device motion amplitude. Further work is required concerning the optimisation of scanner settings for TDI data acquisition.

Further work on the validation device is needed before physiologic motions may be used for TDI derived AWM accuracy assessment, though this is not within the scope of this project. One important conclusion of this study is that for the current state of development of the TDI/AWM software technique, AWM indices cannot be blindly calculated then used to investigate AWM phenomena or aid in patient management. Close scrutiny is required of the segmented TDI loops to detect the presence of any artefacts such as those described earlier that will affect the quality of the derived AWM.

Chapter 4 Phantom material characterisation

4.1 Introduction

The primary motivation for the development of a compliant wall vascular phantom has been outlined in Chapter 1, that realistic AWM may be generated in the laboratory for assessment of TDI derived AWM precision. This chapter concerns the identification of appropriate materials for phantom construction (section 4.2), their preparation (section 4.3) and the subsequent mechanical (section 4.4) and acoustic characterisation (section 4.5). Desired characteristics of a material for phantom manufacture are identified in the following section followed by a comparison with a list of materials short-listed from the literature. Based upon this comparison the most appropriate materials are chosen for use in a compliant wall vascular phantom.

4.2 Choice of materials

A number of options present themselves as potential tissue and vessel mimicking materials (VMM). From the literature, a shortlist of gelatin based materials, agar based materials, polyvinyl alcohol (PVA) cryogel, latex, silicon rubber and C-flex was identified¹⁰⁹⁻¹¹⁷. PVA cryogel is perhaps lesser known than other VMM. It is an alcohol-based polymer, which is moulded by heating the gel, then freezing and thawing. The freeze-thaw cycle induces intermolecular cross-linking between hydroxyl groups and the number and nature of the freeze-thaw cycles varies the mechanical properties.

In order to choose the most appropriate materials from the list, a number of important characteristics must be assessed for each material and compared (Table 4.1). These are summarised for the materials shortlist in the previous paragraph and for vascular tissue (Table 4.2). *In vivo* values for the human carotid artery and aorta are stated where available. Each of the material characteristics is then discussed.

Property
Geometry
Mechanical
Acoustic
Optical appearance
Stability
Durability
Ease of preparation
Availability
Safety considerations

Table 4.1: Phantom material properties for consideration.

4.2.1 Geometry

A basic requirement of the potential phantom materials is that they may be moulded into realistic *in vivo* geometries. It was also judged that walled phantoms with separate VMM and TMM would provide greater scope for investigating AWM phenomena compared to wall-less models. Wall-less model construction is often more straightforward than for walled models and avoids distortion of the ultrasound beam which is known to occur if the VMM material used is highly attenuating in comparison to the TMM used¹¹⁸ (this is discussed in more detail in Section 4.2.3). However, a walled phantom allows the investigation of the effects of varying wall thickness together with lumen geometry. The use of a separate VMM also allows control over longitudinal ‘tethering’, the longitudinal strain the *in vivo* artery is subject to which results in retraction on removal from the body and is known to have an effect on the pulse wave velocity⁸.

There are a number of ‘off the shelf’ tubing types available, including latex, silicon rubber and C-flex, which can be used as VMM. While convenient, these provide less opportunity for geometry variation. This is in part because the increments between tube diameters and wall thickness commercially available are often larger than would be of interest for this work. However, in-house manufacture of latex tubing is possible with the appropriate facilities. The manufacture of tubing of varying wall thickness (and therefore compliance) was described by Walker et al¹¹⁹. Polyvinyl

alcohol (PVA) cryogel and gelatin-based gels are available commercially in powder and gel form, and powder form respectively. These may be moulded in-house, also presenting the potential for a range of geometries^{113,115,116}.

4.2.2 Mechanical properties

Ideally, the constituent phantom materials should be capable of exhibiting a range of Young's elastic moduli allowing the simulation of AWM in both healthy tissue and for varying stages of disease as described in Chapter 1. A mimic is desired in mechanical terms in order that the AWM characteristics, including displacement, velocity and acceleration correspond as closely as possible to *in vivo* values (Table 4.2). Note that this is a key aim for phantom development, rather than an exact match in Young's modulus of human vascular tissue. While not within the scope of this thesis, the potential to produce variable mechanical properties within a single piece of VMM is also desired. Together with variable geometries, this capability would allow the mechanical and geometric mimicking of stenoses and grafts.

Latex and silicon rubber tubing have relatively high Young's moduli when compared to the other potential mimicking materials, and coincide with moduli for human arteries at physiologic stresses. An elastic modulus is not known for C-flex, however preliminary testing by the author using the flow rig described in the next chapter demonstrated undetectable AWM with off the shelf tubing sizes. A serious limitation of all three of these tubing types is that they provide no opportunity for variation in mechanical properties, other than varying structural stiffness by altering vessel diameter and wall thickness. Furthermore, unless very thin walled tubes are used they are too stiff to produce realistic AWM dilations for the pump system used in this work. However, PVA cryogel and agar based gels and gelatin based gels can exhibit a wide range of Young's modulus including the lower end of the physiologic range, depending on their concentration and in the case of PVA cryogel, the nature of the freeze-thaw cycles it has been subjected to.

Material	TMM &/or VMM	Young's Modulus E/kPa	Acoustic velocity c/m s ⁻¹	Attenuation coefficient α /dB cm ⁻¹ MHz ⁻¹ ,*
Average soft tissue	N/A	–	1540 ¹²⁰	0.3 - 0.6 ¹²⁰
Aorta (no pathology present)	N/A	40 – 2000 [†] , ¹²¹	1501 ¹²² @ 10 MHz	0.6 ¹²² @ 10 MHz
Carotid artery (healthy)	N/A	678 [‡] , ¹²³	–	–
Aorta (porcine)	N/A	175 [§] , ¹¹⁵	–	–
Fibrous plaque tissue	N/A	1000 ⁷⁴	1514 ¹²²	7.1 ¹²²
Calcified plaque tissue	N/A	1466 ¹²⁴	–	–
Fat	N/A	18 - 24 ¹²⁵	1476, 1430 ^{126,127}	0.35 ¹²⁸
Gelatin based TMM	TMM &/or VMM	1 - 2200 ¹²⁹	1559 - 1600 ¹³⁰	0.2-1.3 ¹²⁸ @ 6 MHz
Agar based TMM	TMM &/or VMM	8 - 195 ¹³⁰	1551 ¹¹¹	0.52 ¹¹¹
Polyvinyl alcohol (PVA) cryogel	TMM &/or VMM	43 - 89 ¹¹⁶ 190 - 1840 ^{†15}	1530 - 1545 ¹³¹	0.12, 0.22 (2 and 4 freeze-thaw cycles) ¹³¹
Latex	VMM	858, 1502 ¹¹⁷	1566 ¹³²	5.2 ¹³²
Silicon rubber	VMM	1678, 2917 ¹¹⁷	1005 ¹³²	4.6 ¹³²
C-flex (Thermoplastic elastomer)	VMM	–	1556 ¹³²	5.6 ¹³²

Table 4.2: Properties of phantom materials in the literature & *in vivo* vascular tissue.

* @ 5 MHz unless otherwise stated.
† 0 – 12 kPa.
‡ At physiologic pressures.
§ 20 – 50 kPa

4.2.3 Acoustic properties

The relative acoustic properties of the components of a walled phantom dictate the nature of ultrasound beam propagation through the phantom. In particular, changes in acoustic velocity across interfaces between TMM and VMM, and VMM and TMM will determine the extent of reflection and refraction of the beam and any consequent distortion of the ultrasound beam. Furthermore, differential attenuation of the ultrasound beam can occur because of the different path lengths traversed in the VMM, a further source of Doppler signal distortion. A typical effect is the loss of low frequency components of the Doppler signal, which can result in the underestimate of the mean frequency and therefore mean velocity¹³³. The effects of these phenomena in terms of flow measurement have been well documented in the literature¹³⁴⁻¹³⁶ but not for Tissue Doppler Imaging (TDI) or AWM derivation in particular, which rely on mean velocity estimates. In the absence of any data on the subject, a similar attitude is taken as with flow measurement phantoms, that any VMM, TMM and BMF used should preferably be matched acoustically to minimise such distortions. Spectral variation in attenuation is another potential source of distortion. A linear variation in attenuation with frequency is observed in tissue¹³⁴ and as such is sought in phantom materials.

Of the potential VMM, latex, silicone rubber and C-flex exhibit large attenuation at diagnostic ultrasound frequencies, approximately an order of magnitude higher than soft tissue and vascular tissue. In addition, silicon rubber exhibits a large disparity between its acoustic velocity and that found *in vivo* (35 % lower than for typical soft tissue). Due to their high attenuation, should a large wall thickness be desired in a phantom to simulate a stiff artery, low signal to noise ratios will result. Higher attenuation will increase distortion of derived AWM, as illustrated by data in section 6.1.5 and encountered *in vivo* in the study in Chapter 2, increase the possibility of segmentation artefacts through inadequate wall definition. These effects are in addition to the distortion effects described in the previous paragraph. PVA cryogel and the agar and gelatin gels exhibit acoustic velocities close to those for typical soft tissue and vascular tissue. Attenuation by these mimics is also much more similar to tissue than that exhibited by latex, Silicon rubber and C-flex tubing (see Table 4.2).

The gelatin and agar based mimicking materials can potentially be moulded for use as TMM or VMM. Acoustic velocity and attenuation of both these materials are controlled independently by varying the proportions of the constituents. In particular, acoustic velocity is controlled by the proportion of alcohol. Originally, n-propanol was employed¹¹⁰ but glycerol has since been adopted since it is non-flammable and less volatile¹¹¹. Attenuation is varied according to the proportion of microscopic particles such as graphite¹¹⁰, carborundum (SiC powder) and aluminium oxide¹¹¹. Within this, absorption and backscatter may be controlled independently; carborundum in particular is known to primarily affect backscatter while Aluminium oxide primarily affects absorption¹³⁷. Using these constituents, the mimicking materials have been found to simulate tissue with varying degrees of success. Typical values are provided (Table 4.2).

The ability to control speed of sound and attenuation independently in a TMM is of particular relevance to this work. As described in Chapter 1, there are three types of measurements to be made on a compliant wall vascular phantom. The first two are the assessment of AWM measurement technique efficacy and the investigation of AWM and haemodynamic phenomena. However, prior to performing such investigations measurements are required to characterise the response of the phantom to varying flow conditions. While the former requires a phantom which mimics the *in vivo* scanning environment (as used in Chapter 6), the latter two have no such requirement. In fact, optimisation of TDI signal strength from the vessel wall is desirable in order to gain the most information about the wall movement. A TMM surrounding the VMM that matched it in velocity terms but exhibited markedly lower attenuation would be of value. This should be achievable with a gelatin or agar based mixture by adjusting the various components as described.

4.2.4 Optical transmission

While not within the scope of this thesis, the optical appearance of the phantom is of interest since optical interrogation methods together with a transparent phantom provide a strategy for ultrasound independent measurement of AWM. This is especially helpful for investigating AWM measurement accuracy for complex

configurations of geometry and elasticity. Uniform elasticity only can be simulated by the fixed simple geometry of the validation device used in Chapter 3. A further advantage of an optically transparent phantom is that the phantom behaviour may be 'eye-balled', assisting in the set-up of experiments and detection of faults such as VMM rupture and collapse.

Each of the mimicking materials in Table 4.2 is optically opaque when prepared with acoustic absorbers and scatterers. However, particle free gelatin TMM is transparent and practical experience of the author with PVA cryogel has revealed that for thin walled VMM segments (1.73 mm), the inner and outer walls are visible when an opaque liquid such as blood mimicking fluid (BMF)¹³⁸ is pumped through it.

4.2.5 Remaining properties

Reasonable stability over time in terms of mechanical, acoustic and chemical properties is sought with a view to minimising inter-measurement variability and the need for frequent manufacture of phantoms. In a similar vein, durability is of importance; the phantom should be able to withstand flows and pressures required to produce physiologic AWM. A phantom composed of constituents that are readily available, relatively easy to prepare and non-hazardous are also preferred.

Latex is well known to be prone to perishing over time with exposure to heat and light and so its properties in a phantom would be expected to change over its lifetime. C-flex is stable in comparison, being able to tolerate a wide temperature range and exposure to a range of chemical agents. To the authors knowledge there are no quantitative studies concerning acoustic and mechanical stability of PVA cryogel, though the information sheets provided with the product state cross-linking (and therefore an increase in elastic modulus) occurs over time in PVA samples. Gradual cross-linking over time is also known to occur in formaldehyde/gelatin gels, as used by Madsen, increasing its elastic modulus¹¹⁰. Hall et al reported a 2.5 fold increase in elastic modulus over a 246-day period for a gelatin-based material containing 0.3 % formaldehyde by mass¹³⁰. Without the presence of formaldehyde, in acoustic terms, de Korte et al reported increases in speed of sound and attenuation at 25 MHz but only measured over the first four hours after gelling¹¹². There appears

to be little information in the literature regarding longer-term acoustic stability for such materials.

Agar based gels are often chosen as an alternative to gelatin gels given the reported temperature instability of the latter¹³⁹. Gelatin has a low melting point (28°C) compared to agar (85°C). The addition of a cross-linking agent such as formaldehyde and glutaraldehyde has been found to increase temperature stability¹¹⁰. However, both agents are toxic and the associated mechanical instability has been highlighted. In addition, experience in the author's laboratory has shown glutaraldehyde to cross-link so rapidly on addition to a gelatin mixture that thorough mixing is difficult to achieve.

In terms of durability, it is known from practical experience that the tensile strengths of agar and gelatin based gels are much lower than that of PVA cryogel, which has been found to be a very robust material¹¹⁵. The relatively low breaking stress of agar-based gels in particular is documented by Ramnarine et al¹³⁷, who demonstrated the rupture of wall-less stenosis phantoms for mean flows of around 1 m s⁻¹.

From a safety point of view, of the materials stated in Table 4.2, the constituents are on the whole non-hazardous. Polyvinyl alcohol in particular has no recognised hazardous effects. Exceptions are formaldehyde, whose toxicity is mentioned earlier, and benzalkonium chloride which is classed 'harmful'. Each agent has a number of associated adverse effects on exposure.

4.2.6 Conclusion

Key disadvantages of each candidate material for use as TMM and VMM, as discussed in the previous section, are summarised (Table 4.3). These inform the selection of TMM and VMM materials for use in compliant wall phantom design.

Material	Limitation
Agar gels	<ul style="list-style-type: none"> × Low breaking strain × Optical opacity
Gelatin gels	<ul style="list-style-type: none"> × Mechanical instability due to cross linking agents
PVA cryogel	<ul style="list-style-type: none"> × Time consuming preparation
Latex	<ul style="list-style-type: none"> × Acoustic mis-match × Limited geometries available × No variation in elastic modulus possible
Silicon rubber	<ul style="list-style-type: none"> × Acoustic mis-match × Limited geometries available × No variation in elastic modulus possible
C-flex	<ul style="list-style-type: none"> × Acoustic mis-match × Limited geometries available × No variation in elastic modulus possible

Table 4.3: Summary of candidate TMM and VMM limitations.

4.2.6.1 Choice of VMM

Primary drawbacks of the PVA cryogel are the difficulty of manufacture (the process taking a number of days) and the relatively high expense and limited availability compared to materials such as gelatin and agar. However, the optical transparency at physiologic vessel wall thickness, high breaking strains, appropriate acoustic properties, the ability to produce variable geometries and a range of elastic moduli make it the optimum choice for a VMM for compliant wall phantom design.

4.2.6.2 Choice of TMM

A gelatin based TMM was chosen as a medium to surround the VMM. The stated similarities of this TMM to tissue in acoustic and mechanical terms are advantageous, as is the potential for optical interrogation of a transparent gelatin based TMM. Three variations on a gelatin-based recipe, A, B and C, were devised and investigated in the following sections with three main motives in mind:

- (i) To devise a TMM with physically realistic properties in both acoustic and mechanical terms for TDI/AWM technique precision assessment
- (ii) To devise a further TMM similar in mechanical properties to the first but with low acoustic attenuation and optical transmission, to allow phantom characterisation and investigations of AWM and haemodynamic phenomena by both acoustic and optical means.
- (iii) To devise a TMM with greater temporal mechanical stability than the formaldehyde gels, with the use of an alternative preservative.

Recipe A described in the following section was devised to satisfy point (i) above. Microscopic particles as used by Teirlinck et al were used to provide attenuation and glycerol was used to control the acoustic velocity¹¹¹. Recipe B was devised to satisfy (ii). The omission of the microscopic particles in Recipe A provided an optically transparent medium with reduced acoustic attenuation. Recipes B (with the preservative CA24) and C (with the preservative formaldehyde) described in the following section are used to investigate (iii).

The preparation of each of the materials is discussed in the next section. Some data exists in the literature characterising mechanical and acoustic properties of PVA cryogel and TMM of similar composition to those used in this thesis. However, it was necessary to quantify the mechanical and acoustic properties to account for in-house manufacture methods and in the case of TMM, variations in the basic gelatin based recipe. Mechanical and acoustic measurements were therefore performed. The measurements are described in the following sections (4.4 and 4.5 respectively). Emphasis is placed upon mechanical characterisation over acoustic characterisation given that AWM, the focus of this thesis, is directly dependent on the mechanical properties of the materials being interrogated.

4.3 Phantom material preparation

4.3.1 Tissue mimicking material (TMM)

The compositions of the three recipes prepared are shown (Table 4.1). All three were based upon the Madsen recipe¹¹⁰. The glycerol: water ratio in all three recipes was left unchanged from the Madsen recipe in order to preserve the quoted speed of sound. The gelatin: water and preservative: water concentrations were also fixed across all three recipes in order to minimise variations in elastic modulus. Silicon carbide and aluminium oxide particles were used to provide realistic attenuation and backscatter in A. The same proportions of particles were used as in the Teirlinck recipe, which with agar have been shown to produce realistic attenuation properties¹¹¹. The preservative CA24 (ISP Biochema Schwaben, Memmingen, Germany) used in Recipe A and Recipe B is a non-toxic white powder formed on mixing chloroacetamide and sodium benzoate. Recipe 'C' contains formaldehyde as a preservative and cross-linking agent. The graphite particles have been removed from the Madsen recipe. Recipe C was intended for a comparison of mechanical stability with recipe B.

Constituent/Recipe version	A	B	C
Water	82.3	82.3	83.0
Gelatin	13.1	13.4	12.7
Glycerol	3.4	3.5	3.5
Preservative	0.87 (CA24)	0.89 (CA24)	0.84 (Formaldehyde)
Scatterers (SiC 0.52 %, 0.3 μm Al ₂ O ₃ 0.92 %, 3 μm Al ₂ O ₃ 0.86 %)	2.3	-	-

Table 4.4: Percentage by mass contribution of constituents in three gelatin TMM recipes, with CA24 preservative and scatterers (A), with CA24 and no scatterers (B) and formaldehyde and no scatterers (C).

Recipe A was prepared by first dissolving and mixing the scatterers and CA24 in a slurry of hot water and beating vigorously with a balloon whisk to ensure no clumping of the particles. The slurry was added to a steel beaker containing the

required volume of water in a temperature controlled water bath at 65 - 75°C. The gelatin powder was then added gradually to the water whilst constantly stirring the mixture vigorously using an automated stirrer. Rapid addition of the powder was avoided to minimise clumping and premature setting of the clumps. The temperature used while adding gelatin was employed to reduce water losses through evaporation. The mixture was then covered and heated to greater than 90°C for thirty minutes to encourage the gelatin to dissolve and clarify the mixture. Glycerol was added to the mixture after the gelatin was completely dissolved and the mixture stirred for a further 10 minutes.

The mixture was subsequently cooled to approximately 50°C, when it was placed in a degassing vacuum chamber for five minutes to remove the large amounts of air introduced on stirring. Previous experience in TMM preparation had shown that setting the TMM without degassing left a number of visible air bubbles. This caused attenuation artefacts when scanning the resulting phantom. Cooling was employed prior to degassing to reduce losses by evaporation. After degassing, the mixture was returned to the magnetic stirrer. This was in order to maintain the suspension of the scattering particles which otherwise would settle out, though a reduced stirring speed was used to avoid introduction of excessive amounts of air to the mixture. The mixture was then cooled to 28°C, when it was poured into an appropriate mould (described in the following sections). At this temperature the mixture is very close to setting, and so on stopping stirring the constituents remain suspended throughout the volume rather than sinking to the base of the container, an effect observable by eye during the development of the TMMs. Preparing recipe 'B' involved simply omitting the scatterers. The preparation of recipe 'C' involved adding formaldehyde with the glycerol after the mixture had been somewhat cooled, in order to avoid evaporation of the volatile formaldehyde.

4.3.2 Vessel-mimicking material (VMM)

A 15 % concentration of PVA cryogel in water was used to prepare VMM samples. Preliminary ultrasound scanning revealed PVA cryogel provided no visible backscatter except at interfaces and so had a similar appearance to water. This lack of image contrast between wall and blood mimicking fluid (BMF) resulted in

difficulties in segmentation of the artery wall by the AWM software. The addition of 0.75 % 400-grain Silicon Carbide (SiC) particles was found to remedy this. Scatterers were added while heating the cryogel to 100°C and stirring the mixture until the particles were evenly distributed throughout the volume of gel.

The moulding procedure involved heating the cryogel to 100°C for 30 - 60 minutes in a water bath until it liquefied, allowing it to be loaded into a syringe. It was then injected into an appropriate mould described later (Sections 4.4.1 & 5.4.1.1). Moulds were lubricated sparingly with silicone grease. The moulds were left to stand upright for up to 24 hours to allow air bubbles to settle. The moulds were then placed in a thermostat-controlled freezer at -29.3°C^* for 7 hours, after which they were removed and thawed for at least 7 hours at room temperature[†]. The freeze-thaw cycle was then repeated as required to achieve the desired mechanical properties. Once these were achieved the VMM was removed from the moulds and stored in water, as recommended by the suppliers, to prevent dehydration.

Note that freeze and thaw rates of the cryogel are known to affect the mechanical properties of the PVA cryogel and some published work has used programmable thermostat controlled freezers which could control freeze and thaw rates^{115,116}. Such facilities were not available here, however it was deemed acceptable to assume a constant freezer temperature and a constant ambient room temperature that provide constant freeze and thaw rates.

* Freezer temperature averaged $-29.3 \pm 0.5^{\circ}\text{C}$ over 7 measurements made at time of VMM manufacture.

† Room temperature averaged $22.3 \pm 0.5^{\circ}\text{C}$ over 7 measurements made at time of VMM manufacture.

4.4 Mechanical characterisation

4.4.1 Methodology

Different aspects of the mechanical properties of the materials, represented by the tangent elastic modulus, E_t , were assessed by tensile testing. This was carried out in The School of Engineering and Electronics at The University of Edinburgh using an Instron® material testing rig (Instron Corporation, Norwood, Massachusetts). A definition of E_t is provided in Appendix A. The groups of measurements are described (Table 4.3). Mechanical testing procedures were devised with the assistance of materials science colleagues and Dr. Tamie Poepping of the Department of Medical Physics. The findings of each investigation have implications for phantom preparation and experimental methodologies, in addition to providing a measure of how well the materials mimic vascular tissue and the carotid artery in particular. The elastic moduli of the three TMM were also compared.

Stress-strain data was collected up to either the breaking strain or 100 % strain (whichever was reached first for a given sample) for potential further analysis. However, only the E_t at 5 % strain was used in this instance as a physiologically representative measure of material elasticity with which to compare results. This was evaluated as the mean gradient of a 'best fit' line fitted to data from 0 to 10 % strain.

Extension rates used in all experiments were as small as logistically allowable to obtain the best approximation of a static modulus for ease of comparison with other static moduli in the literature. Preliminary measurements revealed no measurable difference in behaviour in gelatin based TMM at extension rates of 5 mm/min and 15 mm/min (corresponding to strain rates of $0.5 \% s^{-1}$ and $1.4 \% s^{-1}$) and so the latter faster rate was used for convenience (Appendix B). These findings were supported by the work of te Nijenhuis et al who demonstrated near frequency independence, and therefore strain rate independence in modulus for cyclically tested gelatin¹⁴⁰. The extent of strain rate dependence of the VMM was not known. Preliminary measurements did not prove or disprove a difference between the two candidate strain rates so a slower extension rate of 5 mm/min was used.

E_t property	TMM and/or VMM	Methodology	Rational
Linearity within the strain range 0-100%	Both	For recently prepared samples (< 4 days old) Assessed with 'best fit' stress-strain plots	To ascertain if phantom generated AWM is strain level dependant in order to: Adapt & standardise phantom construction accordingly Assist in the interpretation of AWM results Assess similarity to vascular tissue
Inter & intra-batch variability	Both	Comparison of E_t at 5 % strain amongst 3 batches each of TMM (Recipe C) & VMM (3 freeze thaw cycles)	Assess associated uncertainty level on comparing AWM derived from different phantoms Highlight potential areas for improvement in VMM/TMM preparation methodology
Temporal stability	Both	Test VMM and TMM batches over a one-month period. TMM recipe A, TMM recipe B, TMM recipe C VMM encased in (i) Water, (ii) Recipe B TMM (iii) Recipe C TMM Compared using E_t at 5 % strain	Assess variability of TMM & VMM over time to aid interpretation of results from different phantoms To assess mechanical effects of any osmotic transfer between TMM & VMM Primarily investigating the effect of the preservative used. Therefore tested for only Recipe B & C TMMs.
Effect of freeze-thaw cycle number	VMM only	Prepare & test samples subjected to 1, 2, 3, 4, 5, 7 & 10 freeze thaw cycles Compared using E_t at 5 % strain	To assess the range of modulus available using PVA cryogel as a VMM

Table 4.5: A summary of the properties of the material tangent elastic moduli, E_t investigated.

Batches of samples of PVA cryogel and Recipes 'A', 'B' and 'C' of TMM were prepared for mechanical testing. The mimicking materials were typically prepared in batches of eight samples each. The samples prepared were of nominal cross sectional area 15.55×3.80 mm. The custom built mould consisted of a Delrin[®] base with rectangular strips of the dimensions stated above machined into it, and an acrylic lid which was screwed on top (Figure 4.1). VMM and TMM materials were injected into the mould via the ports using a syringe, filling from the bottom upward to minimise introduction of air bubbles. Once the material had set, the strips were removed from the mould and divided into samples approximately 50 mm long for testing. Both VMM and TMM samples were prone to retraction on removal from the mould. This produced samples somewhat smaller than the mould dimensions. It was therefore necessary to measure the sample dimensions after manufacture in order for stresses to be accurately calculated. Sample measurements were performed using a micrometer. TMM samples were sealed in plastic film and placed in sealed air-tight bags. VMM samples were stored in water, as recommended by the PVA cryogel suppliers.

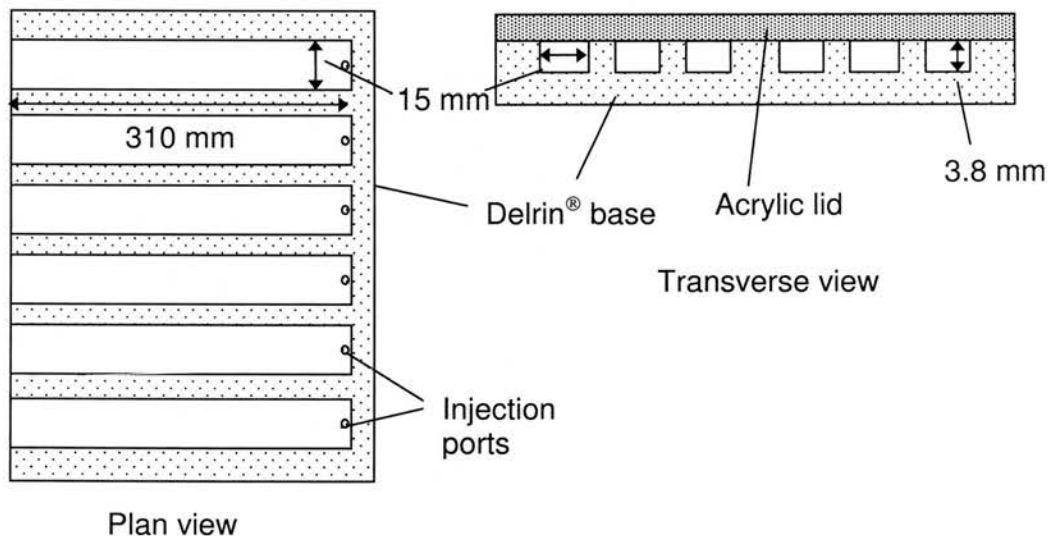


Figure 4.1: Delrin[®]/acrylic mould for preparation of VMM and TMM samples for tensile testing.

The Instron® rig used to collect the data is a tabletop frame consisting of two columns that support two precision ball screws (Figure 4.2). Their rotation produces linear motion of a frame cross head in the vertical plane. A pair of grips is attached to the crosshead and to the base of the frame. On attaching the sample to the grips and setting the separation of the two at the zero strain sample length, the extension of the sample was initiated at a rate chosen by the user. Once in place, the sample length was measured and entered into the machine software in order that strain can be calculated. Sample lengths typically measured 15 - 20 mm. The extension was applied through a PC interface, which also records extension and force data. From this data, stresses and strains were derived using the sample dimensions, which were entered by the user into the machine software.

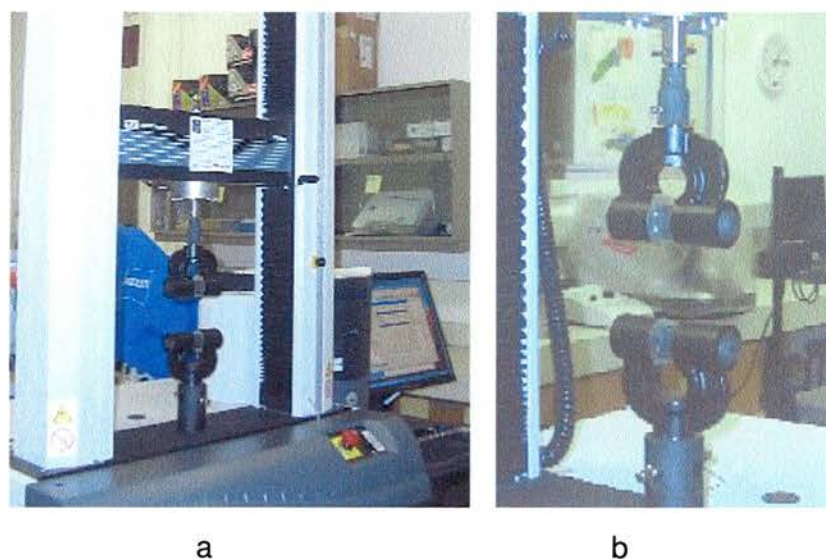


Figure 4.2: The Instron tabletop materials testing rig (a) overall set up (b) a close-up view demonstrating the grips for sample attachment.

Raw data files containing sample dimensions, force and extension data were obtained from the INSTRON software. These were then processed using custom-written MATLAB code (MathWorks Inc., Natick, MA) to obtain the E_t averaged over each batch.

4.4.2 Results & discussion

4.4.2.1 Linearity

Stress-strain data is shown for VMM and each TMM recipe over the whole strain range gathered of 0 – 100 %, with the region for moduli evaluation (0 – 10 % strain) magnified in the windows below (Figure 4.3). Each of the four graphs has a linear best-fit curve superimposed. The ease of fit has not been quantified using the p-value or R^2 parameter since preliminary linear regression testing (using MINITAB software) revealed these parameters to be relatively insensitive indicators of the linearity of this data. Note that the gradient of the fit is equivalent to E_t .

Visual inspection of the entire strain range for VMM suggests a non-linear stress-strain relation, however if one examines the physiologic vascular range (< 10 % strain) a linear trend fits the data well. A linear trend fits the TMM data well compared to the VMM over the entire strain range for all recipes. However, comparison of moduli at 5 % and 50 % demonstrates decreases in moduli of 29 %, 21 % and 4.6 % for recipes A, B and C respectively (Table 4.6). The decrease is most likely due to the transformation of the material from elastic to plastic prior to breaking.

The degree of linearity exhibited by a material has implications for the choice of elastic modulus to use. For linearly elastic materials, the secant and the tangent modulus are equivalent. However, if one cannot assume material linearity the tangent modulus of elasticity provides a more representative measure of the behaviour of a material at a given strain level. Presence or absence of linearity may also have implications for phantom measurement reproducibility. While an increasing stress-strain gradient with increasing strain more closely resembles *in vivo* tissue behaviour, the phantom-generated wall distension will depend on baseline strain levels of the VMM and TMM at phantom construction. Given the small *in vivo* strain range required to be mimicked (0 – 10 % at most) and the results of the investigation above, the effects of VMM or TMM non-linearity are deemed small. Nevertheless, to minimise any variations in modulus due to variations in baseline VMM strain in particular, phantom construction was standardised as much as practicably possible to

allow measurement reproducibility between phantoms. VMM longitudinal and radial strain was standardised and this is described in the next chapter.

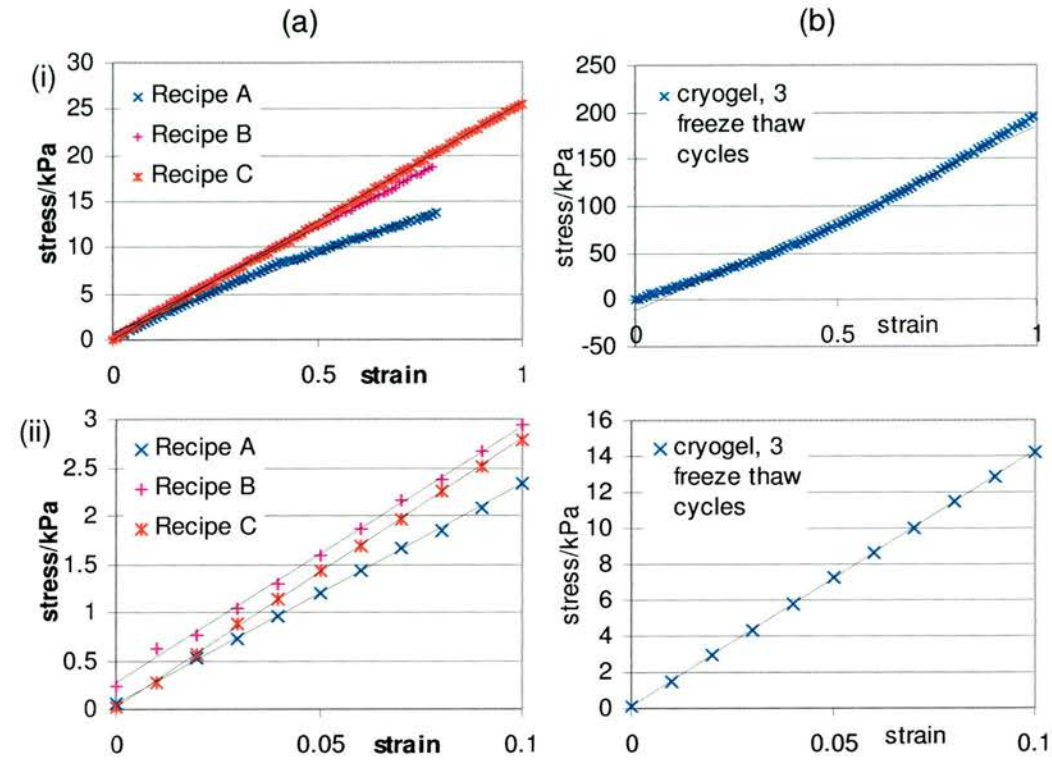


Figure 4.3: Stress-strain data and best fit lines for (a) TMM (b) VMM. Each show fits over (i) the entire strain range measured and (ii) over 0 - 10 % strain.

Material	E _t /kPa	
	5 %	50 %
VMM	137.3 ± 9.7	157.2 ± 26.7
TMM (A)	22.7 ± 0.8	16.1 ± 2.0
TMM (B)	27.7 ± 1.4	21.8 ± 2.1
TMM (C)	28.1 ± 1.2	26.8 ± 2.0

Table 4.6: Tangent moduli of elasticity, E_t at 5 % & 50 % strain for VMM and TMM.

4.4.2.2 Inter-batch and intra-batch variability

Intra-batch variability and inter-batch variability is demonstrated for each material batch and is measured in terms of standard deviation, $SD_{\text{intra-batch}}$ and $SD_{\text{inter-batch}}$ of E_t (Table 4.7). The corrected overall standard deviation, SD_{overall} was calculated from intra-batch and inter-batch standard deviations (Table 4.8). The SD_{overall} are used to calculate coefficients of variation (CoV), which are equal to the SD_{overall} of the results expressed as a percentage of the mean value of the modulus.

VMM			TMM		
Batch	E_t /kPa	$SD_{\text{intra-batch}}$	Batch	E_t /kPa	$SD_{\text{intra-batch}}$
1	141.7	14.5	1	27.8	1.8
2	143.1	18.1	2	28.6	2.4
3	127.1	16.8	3	27.8	1.3
$SD_{\text{inter-batch}}$		2.1	$SD_{\text{inter-batch}}$		0.5

Table 4.7: Intra-batch & Inter-batch variability in tangent modulus of elasticity, E_t at 5 % strain demonstrated by the respective standard deviations, $SD_{\text{intra-batch}}$ and $SD_{\text{inter-batch}}$.

VMM			TMM		
E_t mean/kPa	SD_{overall} /kPa	CoV/%	E_t mean /kPa	SD_{overall} /kPa	CoV/%
137.3	9.7	7.1	28.1	1.2	4.3

Table 4.8: Combined inter-batch and intra-batch variability, SD_{overall} in tangent modulus of elasticity at 5% strain.

It can be seen that overall the VMM tangent modulus is more variable, with a CoV 0.6 times bigger than that of the TMM. The dominant component of VMM modulus variability is the intra-batch variability. Possible reasons for the greater variability than TMM are insufficient mixing of the molten gel prior to mould injection, and non-standardised pre-stress conditions. Prior to testing, the sample was clamped in the Instron grips and then the grip separation adjusted until the sample appeared by eye, to be at zero strain. Given the VMM modulus is non-linear, slight deviations from zero strain prior to sample extension could result in differing modulus values at a given strain level. Such an effect would be marked for VMM compared to TMM given the relatively linear response of the gelatin based TMM.

The inherent variability in VMM and TMM properties has implications for the comparison of AWM data derived from different batches or samples within a batch of VMM or TMM. One must take account of the uncertainty introduced by elastic moduli variability when comparing AWM derived from different phantoms. Dilation amplitude is inversely proportional to the wall elastic modulus (see Equation 5.3 in Chapter 5) and so the quantified variability will in part determine the smallest resolvable difference in AWM between phantoms.

4.4.2.3 Temporal Stability

A marked difference can be seen between recipes A and B TMM and Recipe C TMM. While recipe A and recipe B moduli increase by factors of 0.49 and 0.31 over an approximate period of 30 days, recipe C experiences an increase by a factor of 3.56 over the same interval. The increase in modulus over time in formaldehyde gels is in agreement with work published in the literature¹³⁰. The difference in stability may be attributed to the different preservatives used in the two recipes. The implication of these results is that recipes A and B (containing CA24 preservative rather than formaldehyde) will allow greater consistency on comparing AWM derived from phantoms of different ages.

The variation in E_t at 5 % strain with sample age is demonstrated for the mimicking materials listed in Table 4.4 (Figure 4.4, Figure 4.5). The error bars represent the inter-batch standard deviation. It can be seen in Figure 4.5 that the VMM sees an increase in E_t for each of the three surrounding media (by factors of 0.38, 0.32 and 0.40 over a one month period for VMM in water, in recipe B TMM and in recipe C TMM respectively). This increase in modulus is due to the gradual cross-linking of the VMM at room temperature, as described in material data sheets provided by the supplier. This must be taken account of when comparing AWM derived from different phantoms and comparing results from the same phantom taken at different times. When intra-batch variability is taken into account, there is no measurable difference between VMM aging when placed in different materials. Therefore, it can be concluded that if any osmotic processes take place between VMM and TMM when placed in a phantom, they have no measurable effect on VMM properties.

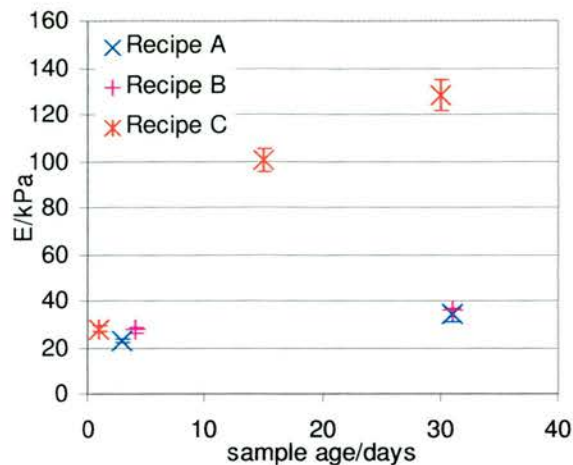


Figure 4.4: Variation in TMM tangent modulus, E_t with sample age for recipes A, B and C. Data points represent the average over batches of typically eight samples. Error bars represent ± 1 SD of the intra-batch moduli.

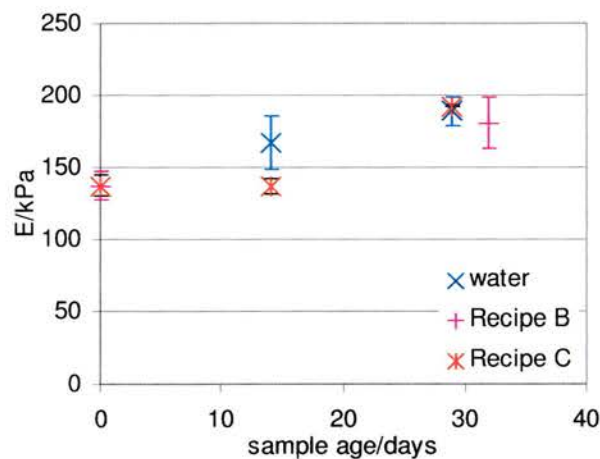


Figure 4.5: Variation in VMM tangent modulus, E_t , with sample age for VMM stored in water, encased in TMM (recipe B) and encased in TMM (recipe C). Data points represent the average over batches of typically eight samples. Error bars represent ± 1 SD of the intra-batch moduli.

4.4.2.4 Variation in VMM with number of freeze-thaw cycles

Variation in VMM tangent modulus with freeze-thaw cycle is demonstrated for 5 % strain (Table 4.9, Figure 4.6). An increase in modulus with freeze-thaw cycle number is observable. Moduli values obtained ranged from 57.0 ± 6.2 kPa to 330.0 ± 21.1 kPa, increasing with the number of freeze thaw cycles. Modulus values for two and three freeze thaw cycles overlap when the associated uncertainty is taken

into account. There is also coincidence in the moduli of seven freeze-thaw cycle cryogel and ten freeze-thaw cycle cryogel batches. The overlap in modulus values has implications for future work, which may involve comparisons of separate segments of VMM with different elastic moduli, and single segments with variations in elastic moduli. Sections of VMM of different freeze-thaw cycles may have the same E_t and therefore produce the same amplitude AWM. This limits the differences in AWM that can be produced by varying the freeze-thaw cycle number. The plateau effect in Figure 4.6 for freeze-thaw cycles greater than seven is possibly a result of intermolecular cross-linking saturation of the cryogel. This effect has been observed elsewhere¹¹⁵ and places an upper limit on elastic moduli available for a given concentration of cryogel.

Freeze-thaw cycles	E_t /kPa
1	57.0 ± 6.2
2	122.4 ± 8.4
3	137.4 ± 9.7
4	176.8 ± 16.8
5	233.2 ± 14.8
7	333.4 ± 31.7
10	330.0 ± 21.1

Table 4.9: Variation in VMM tangent modulus, E_t , with freeze-thaw cycle for 5 % strain. Values represent the average over batches of typically eight samples. Quoted errors represent ± 1 SD of the intra-batch moduli.

In-house methods have been used to generate a range of elastic moduli that are at the lower end of the physiologic range for healthy arteries. Moduli observed in fibrous and calcified tissue are not achieved.

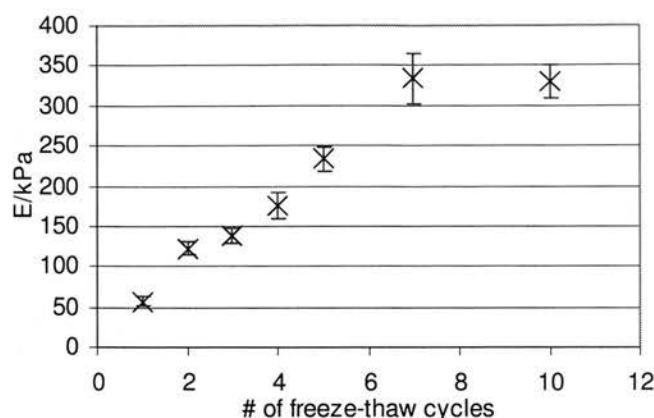


Figure 4.6: Variation in VMM tangent modulus, E_t , with freeze-thaw cycle for 5 % strain. Data points represent the average over batches of typically eight samples.

4.4.2.5 Comparison of TMM recipes

The elastic moduli in Table 4.6 for recently prepared samples of the three TMM recipes are similar, falling within 20 % of each other. However, recipe C was tested 2 - 3 days sooner after preparation than the other recipes. The difference in modulus between the three tested at precisely the same age is therefore likely to be larger, taking into account the marked increase in modulus with age that has been known to occur in formaldehyde gels. As such, it can be concluded CA24 does not induce intermolecular cross-linking as formaldehyde does and therefore results in less elastic gels.

A 2-sample t-test was carried out on recipe A and recipe B data to test the effect of ultrasonic scatterers and absorbers on the elastic modulus. The null hypothesis of no difference between recipe A and recipe B, i.e. that the added particles have no effect on the TMM modulus, was tested. This resulted in a p-value of less than 0.001 at a confidence level of 95 % (test power = 0.99). One can conclude therefore, that the scatterers decrease the TMM modulus, by some 18 %. Other work in the field has found the addition of particles to have some effect on the mechanical properties^{112,130}. Hall et al in particular measured an effect opposite to that obtained here, though different particles and a different preservative was used in this case. On addition of graphite particles to a gelatin based TMM containing formaldehyde he found the elastic modulus to increase by approximately 12 %.

The elastic modulus of breast fat is stated in Table 4.1. It is used as an approximation of the elasticity of tissue surrounding the carotid artery and is compared to the measured TMM to assess how realistic the mimicking materials are. Recipe A falls within the range, while recipes B and C fall 15.4 % and 17.1 % above the upper limit measured by Krouskop et al¹³⁰.

4.5 Acoustic characterisation

4.5.1 Background

Both the speed of sound and attenuation characteristics were investigated for polyvinyl alcohol VMM and recipes A, B and C TMM. A number of techniques are available for assessment of these properties as described by Dunn and Goss¹⁴¹ however, in this case the insertion method using a Scanning Acoustic Macroscope (SAM) was employed. The basic principle of measurement involves the comparison of two reflected ultrasound signals. A transducer emits an ultrasound pulse that is reflected at a target and received by the transducer. The first 'reference' signal passes through a homogenous coupling material alone (of which the speed of sound is known at the measurement temperature) and the second passes along the same path but a sample of the material for testing is placed within the beam path. The second sample signal experiences a change in amplitude and a shift in time of flight compared to the reference signal and these differences are used to determine the relative attenuation and speed of sound of the sample material.

4.5.2 Methodology

The experimental set-up using the SAM system (Ultrasonic Sciences Limited, Fleet, UK) used is shown (Figure 4.1) and has previously been used by Browne, who provides a detailed description of data acquisition and analysis¹⁴². However, in brief, a focussed broadband transducer provides ultrasound pulses centred on a 7MHz frequency. The water bath provides a coupling medium between the transducer and the reflecting target positioned at the focal length. The transducer is secured to a 2D micro-manipulating scanner, driven by a stepper motor and controlled by an analogue and digital input/output board coupled with a PC. This allows raster scans of the reflector and/or the sample over an area selected by the user. In-house

MATLAB code (MathWorks Inc., Natick, MA) has been written by colleagues to process the reference and sample radio-frequency (r.f) data sets. This requires the input of acquisition and sample parameters such as transducer central frequency, area scanned and sample thickness. The code allows the selection of a region of interest (ROI) from the total sample area scanned, generating 2D plots of speed of sound and attenuation in addition to overall values for the ROI.

Degassed water was placed in the tank at least three hours prior to measurement to allow the set up to reach thermal equilibrium with its surroundings. Immediately prior to measurement, the submerged transducer face was inspected for artefact inducing air bubbles, any of which were removed by syringing water across it. The temperature of the water was noted and monitored throughout data acquisition. Temperatures during acquisition averaged 20.3 °C and all fell within 0.6 °C of the mean. In addition, prior to data acquisition, fine adjustments were made to ensure the target and transducer were coaxial, so that the ultrasound path lengths would be uniform across the area to be scanned.

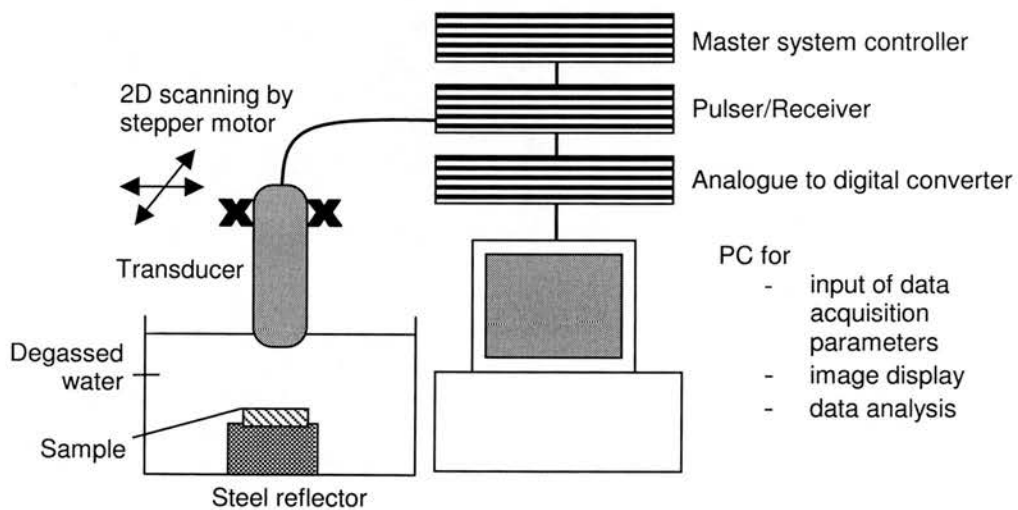


Figure 4.7: Experimental set-up for acoustic property measurements using a Scanning Acoustic Microscope (SAM).

4.5.3 Results & discussion

4.5.3.1 Acoustic velocity

The following speeds were calculated for the scanned materials (Table 4.10). All have similar values to one another. PVA cryogel is the lowest at 1546 m s^{-1} and when measurement uncertainty is taken into account, agrees with the range $1530\text{-}1545 \text{ m s}^{-1}$ given by Surry (Table 4.2). On comparison to tissue, VMM compares favourably to general soft tissue (1540 m s^{-1} , 0.4 % difference) and the calibrated speed of sound in ultrasound scanners, which takes the same value. The VMM velocity is some 3 % larger than values quoted for aorta (mean value 1501 m s^{-1} , range of $1492\text{-}1534 \text{ m s}^{-1}$ ¹²²). The three TMM results agree well with existing TMM data. Tissue mimicking material results are all higher than the *in vivo* tissue values previously quoted; 1 % higher than the typical soft tissue value of 1540 m s^{-1} and 6 % higher than the speed of sound for fat of 1476 m s^{-1} quoted by Bullen *et al*¹²⁶.

Material	$c/ \text{ m s}^{-1}$
VMM	1546 ± 9
TMM (A)	1550 ± 3
TMM (B)	1562 ± 9
TMM (C)	1555 ± 2

Table 4.10: Measured speed of sound in material samples. Quoted errors combine ± 1 SD of the intra-sample and inter-sample means.

4.5.3.2 Attenuation

Attenuation coefficients at 5 MHz and 12 MHz are shown for the scanned materials (Table 4.11). Results for VMM are at the lower extreme of attenuation values obtained from soft tissues and are 1.5 times bigger than the values quoted earlier for 2 freeze-thaw cycle 10 % concentration PVA cryogel in Table 4.2. Some differences are to be expected since manufacturing methods and PVA cryogel concentration used here differ from those used to produce the published values. Furthermore, the greater attenuation measured here is to be expected, given that the referenced values are for

PVA cryogel alone, whilst here silicon carbide particles were added to increase backscatter.

Material	α/f @ 5 MHz /dB cm ⁻¹ MHz ⁻¹	α/f @ 12 MHz /dB cm ⁻¹ MHz ⁻¹
VMM	0.33 ± 0.04	0.27 ± 0.05
TMM (A)	0.50 ± 0.00	0.47 ± 0.00
TMM (B)	0.16 ± 0.01	0.18 ± 0.01
TMM (C) ^{††}	0.07	0.19

Table 4.11: Attenuation coefficients for VMM & TMM at 5 MHz & 12 MHz.

Values measured for recipe A TMM are found to fall within the physiological range, and are similar to values obtained in different recipes by Teirlinck et al and Madsen et al^{109,111}. As discussed in section 4.2.4 recipes B and C TMM were designed with the intention of maximising the ultrasound signal received at the transducer, to allow for the most accurate characterisation of arterial wall motion (AWM) rather than faithfully recreate the physiologic scanning environment. The values obtained here satisfy this aim, with attenuation values ranging from 0.07 - 0.18 dB cm⁻¹ MHz⁻¹ at the frequencies investigated, up to 86 % lower than the attenuation measured in recipe A where attenuating particles are present.

^{††} Measurements were conducted on a single sample therefore no standard deviation was calculable as an indicator of uncertainty.

4.6 Summary & conclusion

Materials and manufacturing methods have been selected for use as TMM and VMM. Key properties of the materials are summarised (Table 4.12). Each material is discussed in turn.

Material	E_t / kPa	E_t change in 30 days/ %	c / m s ⁻¹	α/f @ 5 MHz /dB cm ⁻¹ MHz ⁻¹
VMM	$57 \pm 6.2 - 330 \pm 21.0$	+ 32	1546 ± 9	0.33 ± 0.04
TMM (A)	22.7 ± 0.8	+ 49	1550 ± 3	0.50 ± 0.00
TMM (B)	27.7 ± 1.4	+ 31	1562 ± 9	0.16 ± 0.01
TMM (C)	28.1 ± 1.2	+ 356	1555 ± 2	0.07

Table 4.12: Physical properties summary for VMM and TMM.

Polyvinyl alcohol (PVA) cryogel has been selected as an appropriate VMM for a vascular compliant wall flow phantom. In-house manufacturing methods have been established, producing VMM with elastic moduli that can be varied according to the nature of the freeze-thaw cycles and fall at the lower extreme of the healthy human physiological range. The ability to vary VMM elasticity presents the opportunity for construction of phantoms with non-uniform elasticity. The upper limit of this range could be increased by using a more concentrated solution of PVA cryogel and possibly (with adequate temperature control) with the use of different freeze and thaw rates. The upper physiologic range of Young's moduli values stated in Table 4.2 is not covered by the VMM values generated here. This is not considered a limiting factor since as stated earlier, the ultimate aim of compliant wall phantom development is that physiologic AWM may be generated, which does not necessarily require the higher *in vivo* values of Young's modulus stated. For the flow generation rig used in this thesis, realistic AWM amplitudes were still found to be possible using the VMM manufactured by the methods described in this chapter.

In practice the VMM was confirmed to be very robust in comparison to gelatine and agar based mimicking materials in the literature, withstanding strains greater than 200 % before breaking. Acoustic attenuation at Tissue Doppler Imaging (TDI)

frequencies used by the AWM technique was found to fall within the physiologic range of soft tissue and the speed of sound through the VMM was also found to be close to that of soft tissue in general. This is far superior to the acoustic properties of other vessel mimicking materials in the literature such as latex and C-flex. Work in the subsequent chapter also revealed that for thin-walled VMM tubes, both the inner and outer wall was visible by eye when embedded in non-scattering TMM and opaque BMF was pumped through it. This presents the opportunity for optical interrogation of the phantom AWM.

Three different recipes of a tissue mimicking material (TMM), all of which were gelatin based, were investigated. The use of CA24 preservative was found to provide greater mechanical stability over time, exhibiting a mean increase in tangent elastic modulus by a factor of 0.37 compared to 3.56 for formaldehyde over the first 30 days after preparation. Methodologies for two versions of the TMM containing CA24 preservative were established. CA24 proved an adequate preservative, with phantoms showing no sign of degradation over several months. It does not initiate cross-linking as with other preservatives mentioned but the moduli obtained are similar to subcutaneous fat and are therefore deemed appropriate for use in vascular flow phantoms.

The first TMM recipe (recipe A) behaved similarly to soft tissue in mechanical, acoustic velocity and attenuation terms. The second (recipe B) was found to have similar characteristics to A in all but attenuation terms, which was intentionally lower due to the absence of attenuating particles. A difference in tangent elastic modulus between the two at 5 % strain of 22 % was found. Potential future work could decrease this difference by adjusting gelatin concentrations in the recipes. The two versions provide both an ultrasonically realistic scanning environment and an environment suitable for optical interrogation (which when scanned also provides the strongest possible signal from the vessel wall embedded in it). With further modifications to the recipes, the elastic modulus of A and B could be matched. This would allow direct comparison of ultrasound measurements made on a phantom having realistic attenuation properties (using recipe A), with gold standard optical

measurements made on a phantom of the same mechanical properties (using recipe B). This would be a useful capability for TDI/AWM technique validation. In practice, the reported temperature instability of gelatin gels was not a problem. It dictated the temperature to which the TMM had to be cooled before it could be poured (ensuring attenuating particles did not settle out). Otherwise, there was no problem in conducting experimental work with the resultant phantoms, experimental measurements being conducted in a laboratory some 8 degrees lower than the melting point. No deterioration was observed in the TMM in this respect.

Chapter 5 Compliant wall flow phantom design & characterisation

5.1 Introduction

As discussed in Chapter 1, a compliant wall flow phantom is of use in order to simulate physiologic carotid AWM. This allows the evaluation of AWM interrogation techniques and the investigation of variations in AWM with flow, wall geometry and wall elasticity. Such investigations are of value in the identification of potential diagnostic AWM indicators.

The specific aims of the work contained in this chapter were as follows:

- To identify a compliant wall flow phantom design which is capable of physiologically realistic AWM waveforms (in terms of dilation, velocity and acceleration) and to characterise the flow conditions required to do so.
- To find practicable methods for phantom preparation and construction which allow standardisation of phantom characteristics (this includes the preparation of the individual components of vessel, tissue and blood-mimicking materials)

Compliant wall phantom designs in the literature are considered and from this discussion a basic phantom design is decided upon (Section 5.2). A number of key phantom design requirements, governed by the nature of *in vivo* geometry and AWM are then described (Section 5.3). Construction of the phantom and methodology for flow generation is described (Section 5.4). This section includes consideration of a quality control (Q.C) issue; specifically variations in wall thickness of manufactured VMM and its effect on AWM. Characterisation of the phantom's behaviour on variation in applied flow and outflow impedance is then investigated, primarily in order to ascertain how physiologic AWM could be generated (Sections 5.5 and 5.6). The results of section 5.6 are compared with physiologic data gathered in the *in vivo* reproducibility study described in Chapter 2.

5.2 Choice of AWM phantom design

The nature of the AWM software imposes a restraint on any AWM phantom design for investigations of technique precision. Phantoms testing the efficacy of TDI alone do not require a specific geometry and several mechanisms have been used to generate known velocities for validation studies, including rotating tissue mimicking material discs¹⁴³ and radially distending foam cylinders viewed axially to imitate the left ventricle¹⁴⁴. However, operation of the AWM software requires two reflecting planes, which represent the near and far artery walls and exhibit relative motion to one another. The two planes are segmented by the software, and it uses the associated velocity data provided by TDI to derive their AWM. In the study in Chapter 3, the reflecting planes were generated by the two PVA layers attached to the transducer and the validation device. This simplified geometry was appropriate for TDI/AWM technique accuracy measurement. However, technique precision is thought to vary with beam-vessel geometry parameters such as vessel depth and scan plane-vessel axis coincidence. Variations in such parameters were not possible with the simplified geometry of the device used in Chapter 3. To investigate these parameters fully, a geometry similar to that encountered *in vivo* must be simulated, i.e. a cylinder capable of expansion and contraction at realistic dilations, velocities and accelerations.

Of the few examples in the literature, vessel mimick AWM has been achieved in two main ways; with the application of pulsatile flow through a vessel open at both ends^{91,105,145,146} and with the injection of fluid into a vessel closed at one end^{93,116,146}. The latter strategy has the advantages of being a simpler experiment to set up. A column of fluid separated by a valve from the vessel, or a syringe connected to it may be used to apply pressure to the vessel. The pressure applied may be quantified using a manometer. However, flow phantoms offer the possibility of intra-lumen pressure variation and therefore AWM by varying the size and shape of applied flows waveforms. Furthermore, flow phantoms offer the potential of varying downstream resistance, thereby simulating different locations in the circulatory system. The flow phantom is therefore deemed more versatile with the potential for

generating more realistic AWM than phantoms with a tube sealed at one end. Flow phantoms also allow the investigation of flow phenomena in addition to AWM studies. These features justified the design a compliant wall flow phantom in this chapter. Phantom design requirements are discussed in the next section.

5.3 Phantom design requirements

Material requirements of the phantom components of TMM and VMM have already been discussed in the previous chapter. However, it is also necessary to consider geometric and AWM specifications of the phantom design to mimic the *in vivo* case, which include the following:

- VMM wall thickness, h and diameter, D
- AWM dilation, velocity and acceleration magnitude
- AWM rise time and cycle duration

Arterial wall motion characteristics are illustrated in the diagram (Figure 5.1).

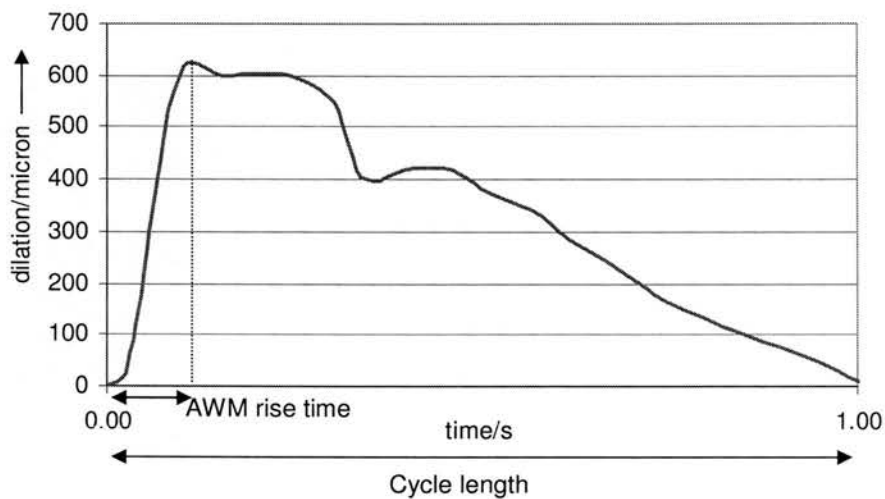


Figure 5.1: An illustration of AWM characteristics.

It is desirable that phantom design should be adaptable to generate both common carotid artery (CCA) and internal carotid artery (ICA) AWM. However, in the first instance, the generation of CCA AWM was focussed upon for simplicity. It is anticipated that the generation and measurement of ICA AWM will be more difficult for two reasons:

- (i) A smaller VMM geometry is required for manufacture
- (ii) Smaller AWM, as shown in Chapter 3, are associated with greater inter-measurement variability using the TDI/AWM technique.

The following design requirements are therefore discussed only in terms of the CCA properties.

5.3.1 VMM wall thickness, h , and diameter, D

As stated in Chapter 1, the elastic properties of the artery are dominated by the properties of the media. Therefore, data in the literature of carotid intima-media thickness (IMT) provides a range of wall thickness to aspire to in the compliant wall phantom. Howard et al measured IMT over a 13, 870 sample of four race-gender groups of the general population in the U.S.²⁸. They obtained median values for the four groups in the range 0.5 – 1 mm. Fifth percentile IMT values were as low as 0.31 mm and ninety-five percentile values were as high as 2.51 mm. The wall thickness used in the compliant wall phantom should fall within this range. Ideally, one should be able to produce a range of values to simulate aging and different levels of arteriosclerosis and atherosclerosis in particular.

Data acquired *in vivo* in Chapter 2 is used to provide typical values of CCA lumen diameters upon which to base VMM geometry. Lumen diameters were derived from the B-mode images and averaged over all the arteries scanned giving a mean diameter ± 1 SD of 5.8 ± 0.5 mm.

5.3.2 AWM dilation, velocity and acceleration magnitude

The data acquired in Chapter 2 was used to provide typical *in vivo* values for maximum dilation, maximum velocity and maximum acceleration (Table 5.1). Matlab code (MathWorks Inc., Natick, MA) adapted from that used in Chapter 2 was used to extract these indices. Indices for each of the artery segments were averaged over data acquisition sessions and observers.

	Max dilation / μm	Max velocity / cm s^{-1}	Max acceleration / cm s^{-2}
Mean	426	0.686	18.8
Mean – 2SD	216	0.373	10.4
Mean + 2SD	636	0.998	27.2

Table 5.1: Observer and data acquisition session averaged AWM indices for 12 asymptomatic CCA segments scanned using the TDI/AWM software technique.

5.3.3 AWM rise time and cycle duration

The rapid rise of dilation to a maximum is characteristic of physiologic AWM, as was seen in Chapter 2. Phantom rise times similar to those found *in vivo* were sought. Data acquired in Chapter 2 were used to provide an indicator of *in vivo* values (Table 5.2). Typical AWM cycle lengths in the same data are also provided. From these values, a flow cycle length of 1 s was chosen for use in all subsequent experiments.

	AWM rise time/s	AWM cycle length/s
Mean	0.14	0.95
Mean – 2SD	0.08	0.89
Mean + 2SD	0.20	1.11

Table 5.2: Observer and data acquisition session averaged temporal AWM parameters for 12 asymptomatic CCA segments scanned using the TDI/AWM software technique.

5.4 Phantom design & flow generation

The basic construction of the compliant wall phantom comprises of a length of vessel mimicking material (VMM) attached to inlet and outlet tubes within a Perspex tank ($320 \times 110 \times 100$ mm) embedded in tissue mimicking material recipe B (TMM) as described and justified in Chapter 4. Preparation of segments of VMM is described in the next section.

5.4.1 Vessel mimicking material (VMM)

5.4.1.1 VMM segment manufacture

Moulds were designed and prepared with the assistance of Mr. Robert Hogg of the School of Engineering and Electronics workshop at The University of Edinburgh. To prepare segments of VMM, the polyvinyl alcohol (PVA) cryogel was injected into an annular mould via an injection port (Figure 5.2) after heating a vial of the cryogel for up to one hour in a water bath, as described in the previous chapter. The basic mould design consisted of a rod centred within a tube. The rods were greased sparingly prior to cryogel injection to aid removal of the VMM. Several variations upon this basic design were tested before producing VMM for phantom construction. Design features investigated were the mould material, geometry and sealing mechanism.

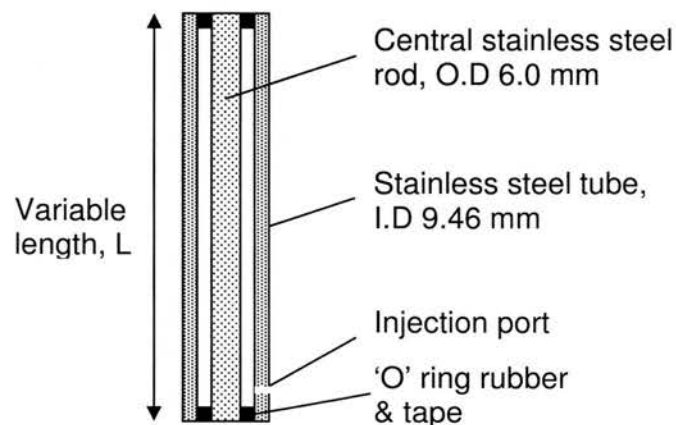


Figure 5.2: A PVA cryogel VMM mould in cross section.

Two mould geometries were tested. Both used a tube of inner diameter 9.46 mm but with two different rod diameters (6.0 mm and 8.0 mm) with the aim of producing VMM of two different wall thickness (1.73 mm and 0.73 mm). In practice, the viscous PVA gel demonstrated considerable resistance to injection into the narrow air cavity of the mould, partly as it cooled and thickened rapidly after leaving the syringe. This was especially so in the case of the 0.73 mm wide air cavity and the resulting VMM were relatively fragile and difficult to remove from the mould without tearing them. Consequently, in the experiments that follow, only 1.73 mm thick VMM was used.

Three different mould materials were tested; acrylic, polycarbonate plastic and stainless steel. The plastics had the advantage of being transparent. This allowed viewing of the progress of the cryogel along the tube as it was injected. The mould could also be checked for air bubbles prior to freezing. Stainless steel moulds had the advantages of superior mechanical strength, lower susceptibility to chemical attack by the PVA cryogel and greater machined precision than the plastic pieces. The latter two properties of the mould material proved to be the most critical; the plastic moulds were found to craze after only a couple of uses, and so for the experiments described later, VMM was prepared using stainless steel moulds.

Two different methods for centring the rod within the tubes and sealing the mould at either end were also tested, the first using flanges of the mould material and the second using a combination 'o' ring rubber and tape wrapped around the rod to ensure a snug fit. The use of flanges was found to precipitate warping and even rupture of the stainless steel tubing as they restricted contraction and expansion of the PVA cryogel and tube over the wide temperature ranges necessary to form the VMM (-29.3°C to 100°C). Given the small separation of the rod and tube, even small deviations in the position of the rod relative to the tube induced by warping in either component, was found to create non-uniform wall thickness in the manufactured VMM. Such effects were found to be less marked where 'o' ring rubber was used and so this design feature was used when preparing the VMM for experiments in this chapter.

Three different mould lengths were tested (20 cm, 30 cm and 50 cm). The 50 cm length was found to produce more variable wall thickness VMM along its length compared to the shorter lengths since any warping in the components would produce greater deviations in wall thickness over the longer mould. Therefore this length was abandoned in favour of the shorter lengths. The issue of variations in wall thickness is investigated in the next section.

5.4.1.2 Wall thickness variability & AWM

Arterial wall motion is dependant on the geometrical parameters of vessel radius and wall thickness, amongst other factors and this has important implications for phantom Q.C. For a material of a given Young's elastic modulus, E , AWM is proportional to the square of the radius of the vessel, R , and the inverse of the wall thickness, h . Such effects are due to associated changes in structural stiffness. They are illustrated quantitatively if one substitutes the Moens-Korteweg equation defining pulse wave velocity, c_0 , (Equation 5.1) into an equation defining wall excursion, 2ξ , derived by Womersley for an elastic tube with very stiff longitudinal tethering (Equation 5.2) to obtain Equation 5.3⁸.

$$c_0 = \left(\frac{E_c h}{2\rho R} \right)^{1/2} \quad (\text{Equation 5.1})$$

$$2\xi = R(1 - \sigma^2) \left(\frac{P e^{i\omega t}}{\rho c_0^2} \right) \quad (\text{Equation 5.2})$$

$$\xi = R^2 (1 - \sigma^2) \left(\frac{P e^{i\omega t}}{E_c h} \right) \quad (\text{Equation 5.3})$$

E_c is the circumferential elastic modulus of the wall, ρ is the density of the fluid, σ is Poisson's ratio and $P e^{i\omega t}$ is the variation of pressure with time at a single location which has an angular cycle frequency of ω . Thus, smaller radii, thick walled, tubes distend less than thin walled tubes subjected to the same pressure and flow conditions.

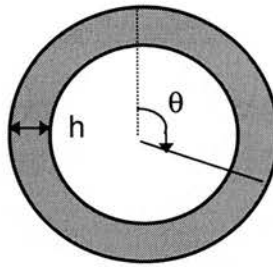


Figure 5.3: An illustration defining the angular co-ordinate, θ in relation to VMM cross-sectional geometry. Variations in wall thickness were measured over 12 values of θ in the range $0 - 360^\circ$.

Such a source of variation in AWM is of interest in terms of inter-measurement variability. It was desired that VMM wall thickness be consistent between phantoms and within the same phantom. This includes consistency with variation in θ for a given VMM cross-section in a given phantom (Figure 5.3). Such an aspect is particularly important since the TDI/AWM software technique does not obtain data for motion over all θ , rather it only interrogates AWM in one direction, that of $\theta = 0^\circ$. Therefore, if there is a range in h in a given cross section, the technique will generate AWM which reflects only h in the beam plane.

An additional motivation for Q.C of h concerns the development of more complex wall phantoms with deliberate variations in h , in addition to other geometrical properties and elasticity. Before one can interpret results acquired from such a phantom, any uncertainty in h must be quantified and controlled. Only then can one be confident that the observed AWM characteristics are due to deliberate variations in the vessel properties rather than uncertainties due to variations introduced by the manufacturing process.

The effect of non-uniform h on AWM within a given cross section was investigated briefly for symmetric and asymmetric VMM samples. The samples were connected into a flow circuit and immersed in a water/glycerol mixed to achieve tissue equivalence in terms of speed of sound. A sinusoidal flow of BMF was applied to

the VMM segments. B-mode cine loops of the VMM cross-section in the middle of the segment were acquired. Two images showing inner wall maximum and minimum dilations were selected from each cine loop. These were manually segmented using custom-written Matlab code (MathWorks Inc., Natick, MA). The code superimposes the maximum dilation wall position onto the minimum dilation wall position enabling the symmetry of the AWM to be visualised (Figure 5.4). The variation in AWM at different positions on the VMM circumference is quantified using the standard deviation in displacement measured over twelve different θ values in the range $0 - 360^\circ$.

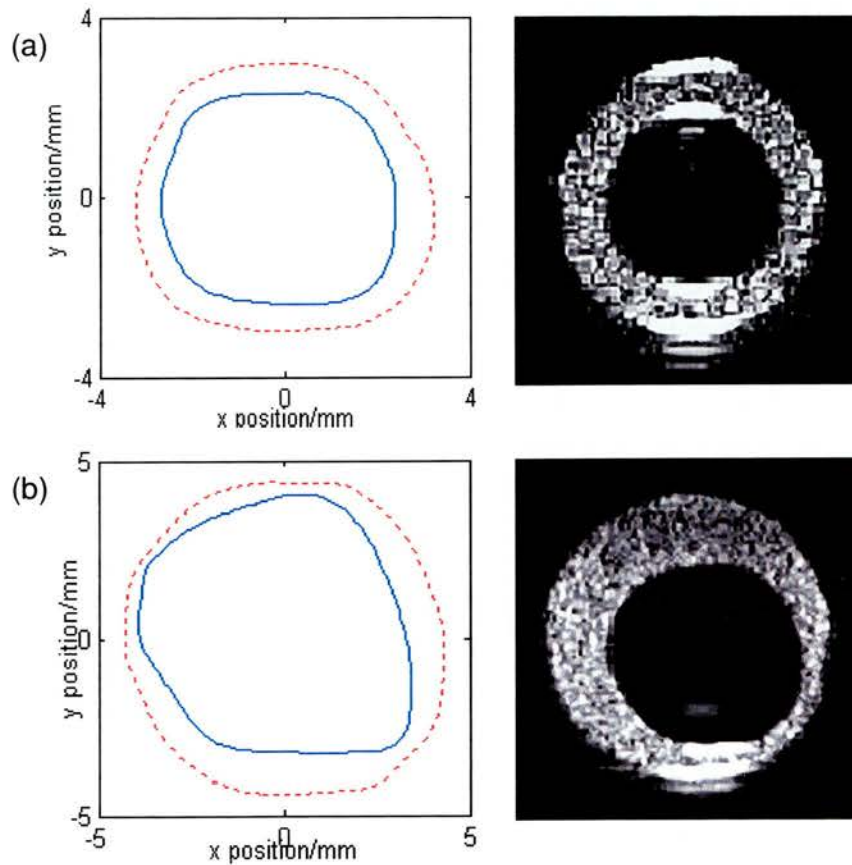


Figure 5.4: Manually segmented minimum (solid blue) and maximum (red dashed) inner wall positions and cross sectional B-mode views for VMM segments with (a) a symmetrical wall and (b) an asymmetrical wall.

Note, in the case of the asymmetric wall, the AWM is also asymmetric and the largest dilations occurring in the regions of lowest structural stiffness; those areas which have the smallest wall thickness. As one might expect, for the VMM with

radially symmetrical walls, the associated AWM is largely symmetric. The mean dilations for the symmetric and asymmetric segments were calculated as 0.63 ± 0.09 mm and 0.68 ± 0.25 mm respectively. The standard deviation in each is quoted as the uncertainty. Thus, the variability in dilation over the range of θ illustrates the variability induced by non-uniform wall thickness.

A particular problem in manufacturing VMM already alluded to is the production of a uniform wall thickness segments. Should the central rod of the mould not be centred correctly on freezing the cryogel, due to incorrect positioning or imperfections in the rod or tube, VMM of asymmetric wall thickness could be produced, as in the example in Figure 5.4b. Variations in wall thickness are thought to be the main source of variability in AWM symmetry, given that phantom housing is fixed and that sufficient mixing of the TMM and VMM mixtures prior to setting excludes local variations in elasticity. For this reason a Q.C procedure was introduced to minimise variability in AWM due to wall thickness.

The Q.C procedure involved cutting two 2 mm cross-section slices (one from each end) from a VMM segment. The slices were placed on the sample platform of an Intel® Play™ QX3™ Computer Microscope. JPEG images of the slices were acquired and saved for analysis by Image Pro Plus image analysis software (Media Cybernetics, USA). The package allowed the manual segmentation of the inner and outer wall and the calculation of the wall thickness using a calibration image of a distance scale. It derived the mean, minimum and maximum wall thickness over the VMM slice circumference. The range in wall thickness over the circumference in a given slice could then be calculated as a percentage of the mean wall thickness. This was averaged over the two slices measured per VMM segment. For a batch of twelve VMM segments the stainless steel mould with flanges produced a mean range in wall thickness per segment of 26 ± 8 % about the mean wall thickness. For a batch of ten VMM segments made using a mould with 'o' rings to centre the rods, a mean range in wall thickness per segment of 18 ± 6 % about the mean wall thickness was obtained. These values demonstrate the superior precision in VMM manufacture with the use of 'o' rings compared to the flanges. Using the 'o' ring mould design, a

ceiling of 16 % variation in wall thickness about the mean was set, such that VMM cross sections exceeding this variability would not be used for phantom construction. Similarly, wall thickness variability was compared for sections cut from opposite ends of a VMM segment. If the wall thickness variability differed by more than 3 %, a given segment was rejected on grounds that the wall thickness was not consistent across the length to be used in the phantom. The acceptance levels chosen were a compromise between the consistency that was practically achievable and the maintenance of reasonable consistency in wall thickness between samples and within samples.

5.4.2 Blood-mimicking fluid (BMF)

Blood-mimicking fluid was manufactured according to a standard technique described by Ramnarine et al¹⁴⁷. The constituent proportions are shown (Table 5.3). As in the case of TMM, the relative amounts of water and glycerol control the acoustic velocity. Orgasol particles (2001UDNAT1 Orgasol, ELF Atochem, Paris, France) act as scatterers, Sigma D4876 dextran 185000D provides the appropriate viscosity and ICI synperonic-N acts to prevent aggregation of the orgasol particles. In between uses, the BMF was kept in a sealed container to avoid evaporation of water from the mixture and any associated changes in properties. If the BMF was left to stand for prolonged periods it was magnetically stirred prior to use to redistribute settled orgasol particles, and filtered to remove clumps using a precision 32 μm sieve (100BBW.032, Endecotts Ltd., London, UK).

Constituent	% by mass
Water	83.86
Glycerol	10.06
Dextran	3.36
5 μm Orgasol	1.82
Synperonic-N surfactant	0.90

Table 5.3: BMF constituents by percentage mass¹⁴⁷.

5.4.3 Phantom & flow rig construction

As for the *in vivo* case, the VMM is subjected to longitudinal tension by extending it over the length of the phantom case. The human large and medium sized arteries exhibit retractions of 10 – 40 % while the carotid arteries in particular exhibit retractions of around 18 – 25 % on excision from the body¹⁴⁸. For each phantom, an approximate extension of 25 % was applied to the VMM. Typically, VMM segment lengths in the range 100 – 150 mm were used. The VMM was secured onto inlet and outlet tubes of the tank using plastic couplings and cable ties then filled with water. This prevented dehydration of the PVA cryogel and provided a baseline distending pressure at which to set the VMM wall on addition of the TMM. Care was taken to ensure no torsional or shear forces were applied to the VMM upon attachment to the couplings and attachment of the couplings to the phantom housing, so that the VMM was extended solely in the longitudinal direction. The VMM is covered by 20 mm of TMM, a depth at which the common carotid artery is typically found. A specimen model with scatter-less TMM, forming part of the flow circuit is shown (Figure 5.5).

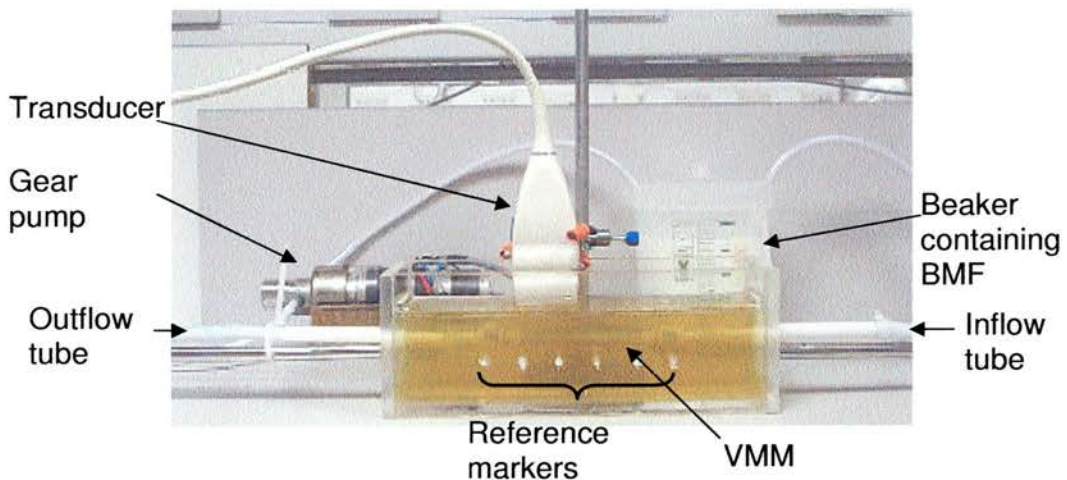


Figure 5.5: A specimen phantom with a vessel of uniform elasticity connected into a flow circuit.

Prior to pouring the TMM, a number of hollow plastic rods (2.46 mm outer diameter) were inserted across the width of the tank, at right angles to the VMM and in the

horizontal plane. These produced bright focal areas of reflected ultrasound upon scanning when placed in TMM. They were placed at predetermined locations along the length of the tank in order to guide measurement locations.

On construction and setting of the phantom, it was connected at the inflow with 750 mm of 9.5 mm inside diameter PVC tubing (Nalge Europe, Hereford, UK) and at the outflow with tubing of the same dimensions. Both inflow and outflow tubes were bound to 500 mm long stainless steel rods, which were secured at the height of the tank inlet and outlet. These held the non-rigid tubing straight, thereby minimising non-axial flow. This was desired in order to standardise incoming flow profiles and outflow resistance. The inflow tube was connected to a magnetically driven gear pump head (Micropump Ltd., Cambridgeshire, UK), which is coupled with a D.C servo motor (McLennan Servo Supplies Ltd., Surrey, UK), capable of generating volume flows of 0.0095 - 0.32 lpm. For all measurements, the pump and motor assembly were positioned at the same height relative to the flow rig in order to further standardise flow conditions. The motor is controlled using a servo amplifier (Aerotech Ltd., Berkshire, UK), interfaced with a PC and controlled by a LabView program (National Instruments Corporation, Austin, Texas) written in-house by Dr. Jacinta Browne. The software allows selection of a volume flow waveform using either customised text files as input, or one of a number of simple waveform types such as sinusoids and saw tooth waveforms. These text files dictate the variation in voltage input applied to the pump motor. The outflow from the phantom carries BMF back to the beaker which acts as a BMF reservoir. The flow rig layout is shown (Figure 5.5).

5.5 Variations in AWM with applied flow waveform shape: A pilot study

5.5.1 Background

This and the next section establish how physiological AWM may be generated by the compliant wall phantom. In broad terms, AWM generated by the phantom is dependent on its mechanical impedance and the flow and pressure field characteristics.

The underlying theory relating AWM to flow is less than straightforward, flow dictates the nature of AWM indirectly; flow is driven by the spatial pressure gradient across the length of the vessel. This in turn is related to the temporal pressure gradient, which in turn dictates the AWM generated. Flow, pressure, pressure gradients and therefore AWM will also vary from the waveforms applied by the pump depending on the mechanical impedance of the VMM and the rest of the flow circuit. In simple terms, the mechanical impedance can be described as the frequency dependent resistance of a vessel to flow; and is dependent on geometry and mechanical properties of a flow circuit. The presence of pulsatile physiologic flow rather than the simple cases of constant or sinusoidal flow considerably complicates the mathematics involved. A further complication is the nature of wave reflections superimposed on the forward travelling pressure wave, dictated by changes in mechanical impedance in the flow circuit. A full explanation with the accompanying mathematics is beyond the scope of this work. The reader is referred to 'MacDonald's Blood flow in arteries' for detailed discussions of both the pressure-flow relationship and mechanical impedance^{149,150}.

Given the complexity of the relationship between flow and AWM, a heuristic approach is taken to the generation of physiological AWM characteristics. Flow rig geometry is fixed for all but one set of experiments carried out in this chapter. Instead, investigations focus upon the effect of variations in applied flow. Furthermore, given the complexity of the flow-AWM-phantom interaction, explanations of the phenomena observed in the following sections are restricted to

qualitative descriptions and are greatly simplified. Of the few compliant wall flow phantoms in the literature none have undergone such characterisation as performed here.

5.5.2 Methodology

An AWM phantom was constructed and connected to form a flow circuit as described in Section 5.4. Four different volume flow waveforms of varying shape were applied; sinusoidal, saw tooth, square wave and *in vivo* measured carotid volume flow (Figure 5.6). The carotid flow waveform was obtained from a study by Holdsworth et al which evaluated the mean common carotid volume flow over 17 individuals using pulsed Doppler ultrasound and Womersley's analytical solution for velocity profiles in pulsatile flow conditions¹⁵¹. Note that except in the case of the carotid flow, peak flow and minimum flow are the same for each of the flow curves. Tissue Doppler acquisition settings used in this and the following section are provided (Table 5.4). While there has not been scope to perform a quantitative examination of TDI/AWM precision across the range of settings available, experience gained from the studies in chapters 2 and 3 revealed settings providing optimum AWM reproducibility. Cine loops of 3 - 5 flow cycles for each volume flow waveform were captured and transferred to a PC for extraction of AWM data and analysis. AWM rise time, AWM FWHM, maximum dilation, maximum velocity and maximum acceleration are extracted from the AWM data and compared for the different flow shapes.

It was thought advantageous to make pressure measurements in the phantom. Pressure variation at a given point in the phantom is directly related to AWM, and so access to pressure data was thought to be helpful in interpreting AWM obtained for different flows. Attempts were made to make pressure measurements at points within the vessel mimick upon the application of pulsatile flow. This involved inserting a 40 mm long catheter into the VMM through the open surface of the phantom TMM with the aid of a needle. Pressure from inside the VMM was transmitted by the catheter to a transducer, which in turn was connected to a S & W Medico Teknik Tri-scope meter (Albertslund, Denmark). The signal from the transducer was recorded by a pc which was connected to the meter. The meter had two channels allowing

which was connected to the meter. The meter had two channels allowing measurement at two sites within the phantom. This allowed simultaneous measurement of pressure and potentially, the evaluation of pulse wave velocity. However, the set up was difficult and time consuming to perform. A primary limitation was the slipping of the catheter, either further into the VMM such that the open end rested on the bottom of the VMM, or out of the VMM altogether, leaking BMF into the TMM. Either way, transmission of pressure along the catheter to the transducer was impeded, invalidating any resulting pressure measurements. The insertion of the needle and the catheter into the VMM could also sometimes result in separation of the VMM from the TMM, resulting in spurious AWM. For these reasons the pressure measurements were abandoned.

Parameter	Setting
* Probe	L12-5 linear array
* Sensitivity	Medium
* Line density	A
* Dynamic motion differentiator (DMD)	Off
* Colour gain	Saturated (> 85 %)
Velocity Scale	1.5 cm s ⁻¹
2D Gain	Minimum required for clear wall definition
Frame Rate Optimisation (FRO)	Maximum
Time Gain Control (TGC)	Mid range
Colour Box Dimensions	0.7 cm long × 1.0 cm deep

Table 5.4: TDI acquisition settings.

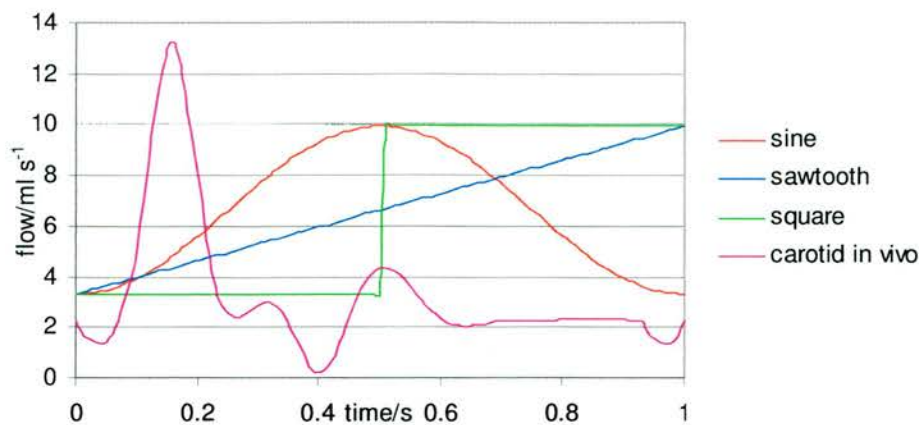


Figure 5.6: Volume flow waveform shapes generated at the pump head.

5.5.3 Results and discussion

Mean AWM waveforms resulting from the different flow shapes are demonstrated (Figure 5.7). Three features of the waveforms of particular interest are their magnitude, their shape and the extent of inward collapse of the walls beyond their resting position, demonstrated by negative AWM in Figure 5.7 and negative values for the AWM index, minimum dilation. Maximum and minimum cycle averaged dilations are provided (Table 5.5); it can be seen that sinusoidal flow provided the largest dilations followed by square wave, saw tooth and carotid flow. Sinusoidal and square wave flow generated AWM exhibited minimum dilations close to zero. Carotid flow demonstrated a markedly lower minimum dilation, which can also be seen in the temporal AWM plots (Figure 5.7).

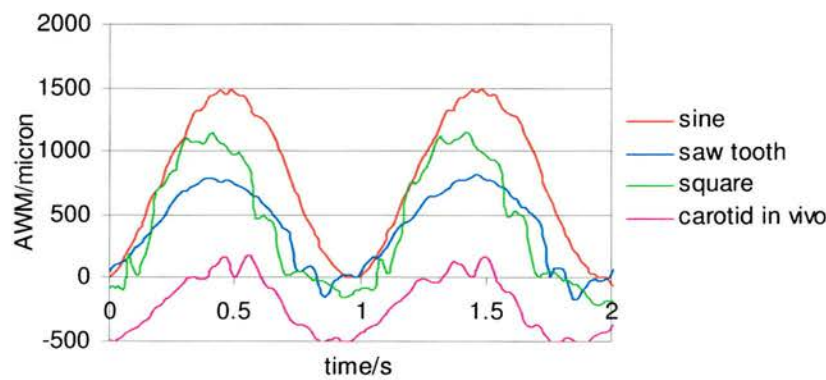


Figure 5.7: Mean AWM waveforms resulting from sinusoid, saw-tooth, square wave and carotid volume flow.

Flow waveform	Mx/ μm	Min/ μm
Sinusoidal	1495 ± 3	-7 ± 12
Square wave	1139 ± 46	4 ± 3
Saw tooth	1017 ± 105	-93 ± 86
<i>In vivo</i> carotid	191 ± 15	-515 ± 5

Table 5.5: Maximum and minimum cycle-averaged dilations for the four flow waveform shapes.

Sinusoidal flow was found to produce waveforms that most closely match the flow profile shape. The remaining AWM profiles bear little resemblance to the corresponding flow profiles. Also of note, every AWM waveform demonstrates some degree of high frequency oscillation in wall position superimposed on the basic cyclic motion. However, on visual inspection, these are far more marked in saw-tooth, square wave and carotid volume flow generated AWM in comparison to the sinusoid generated AWM. There are a number of reasons why these differences are observed. To understand these requires a consideration of the variations in pressure and flow as flow-pressure cycles propagate through the phantom, towards and away from the point of data acquisition. A qualitative explanation of flow and pressure propagation is provided in Appendix C and is applied to the results obtained here.

A comparison of sinusoidal and carotid flow generated AWM provides an illustration of the phenomena which determine the nature of the generated AWM. While the carotid flow primary peak is 1.8 times larger than the sinusoid, it is significantly narrower with a width of approximately 0.16 s compared to 1 s for the sinusoidal flow waveform. The rise times of carotid and sinusoidal flow are also markedly different, that of carotid flow being 0.24 of the sinusoidal rise time. Therefore, when subjected to carotid flow, the VMM is subject to higher temporal flow and pressure gradients. As the rise phase of the flow and pressure cycles approach the point of AWM measurement, this may explain why applied carotid flow produces greater negative dilations. It is thought the larger pressure gradients applied after the flow peak has passed the point of AWM measurement accelerate the contracting VMM walls such that they overshoot their resting position and exhibit negative dilations. It is thought the short duration of the rise phase flow and pressure peaks compared to the other cycles, in addition to the overshoot of the VMM walls

are responsible for the smaller maximum dilation observed for carotid flow AWM. It is postulated that despite the larger temporal pressure gradients associated with the rise phase of the carotid flow cycle, due to BMF inertia, the short duration of the rise time outweighs this and so the carotid flow generates smaller dilations than sinusoidal flow.

A number of conclusions were drawn from the preliminary observations described here that assisted in the further investigation of phantom behaviour that follows in Section 5.6:

- Smaller flow pulse heights should be used to generate AWM of a realistic size given the large magnitude of AWM produced here.
- Wider flow peaks should be used to avoid inward collapse of the vessel wall, which is not typically observed in the carotid arteries. The phenomenon was investigated further with flow curves of varying width but fixed rise times and minimum and maximum flow.
- To prevent retrograde flow in the vessel (which does not typically occur *in vivo* in a carotid artery) minimum flow was doubled for all subsequent flow waveforms.
- Flow waveform shapes with discontinuities in flow were avoided. This had the aim of minimising the short-lived small amplitude oscillations observed largely in saw-tooth, square wave and carotid flow generated AWM, a further phantom AWM characteristic which is not exhibited *in vivo*.
- Output impedance has not been considered in this study. However, *in vivo* this dictates pressure and AWM, both directly and indirectly (through wave reflection). Flow rig impedance is grossly simplified compared to that *in vivo*, therefore an heuristic approach is taken to its investigation in the following section.

5.6 Variations in AWM with characteristics of a generic flow waveform & outflow impedance

5.6.1 Methodology

Based upon the results of the pilot study described in the previous section, a generic flow waveform was employed to investigate the effect of variation in three flow characteristics; rise time, $t_{Q_{\text{peak}}}$, peak flow, Q_{peak} , and full width half maximum (FWHM) (Figure 5.8). The flow waveform text files used to apply flow were constructed using a custom written MATLAB program (MathWorks Inc., Natick, MA), which combined the rise and fall of two sine waves of varying frequency and magnitude with a region of uniform flow between the two. The program allowed peak flow, minimum flow, rise time and full width half maximum to be selected by the user. This simple method of waveform generation was preferred to the use of more complex equations, such as that of damped simple harmonic motion where it is often difficult to vary one flow characteristic without at the same time changing another. All flow waveforms used have a non-zero offset to maintain forward flow at all points in the flow cycle, as in the carotid arteries. The cycle frequency was set to 1 Hz to mimic a typical cardiac cycle length.

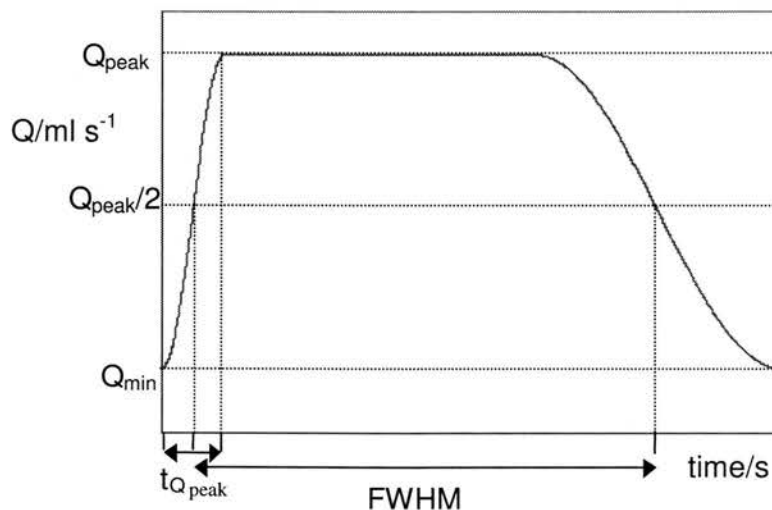


Figure 5.8: A schematic diagram of an applied flow cycle demonstrating rise time, $t_{Q_{\text{peak}}}$, peak flow, Q_{peak} , and full width half maximum, FWHM.

Parameter	Range investigated	Default selection
Minimum applied flow, $Q_{\min}/\text{ml s}^{-1}$	–	6.7
Peak applied flow, $Q_{\text{peak}}/\text{ml s}^{-1}$	8.0 - 11.4	10.0
Mean applied flow, $Q_{\text{mean}}/\text{ml s}^{-1}$	7.7 - 10.2	9.2
Flow rise time, $t_{Q_{\text{peak}}}/\text{s}$	0.025 – 0.25	0.025
FWHM/ s	0.25 - 0.90	0.75
Outflow impedance	Tube A: 9.6mm ID Tube B: 6.4mm ID	Tube A

Table 5.6: Ranges and default values of the flow characteristics & output impedance used.

Ranges in flow parameters for investigation are detailed in Table 5.6. The values were chosen according to the criteria described below. Values of $t_{Q_{\text{peak}}}$ were varied with the aim of generating AWM skewed towards the start of the dilation cycle. A lower limit was placed on $t_{Q_{\text{peak}}}$ such that the initial rise of the flow curve could easily be resolved by the pump controller software. Preliminary rough measurements revealed an appropriate working range for Q_{peak} , which produced realistic wall displacements and velocities without damaging the phantom. The application of too large a volume flow curve results in separation of the VMM from the TMM and irreversible collapse of the VMM. The minimum value for Q_{peak} was chosen, partly through trial and error, such that the AWM dilations generated could be derived with a reasonable degree of reproducibility, since as shown in Chapter 3, TDI/AWM software technique reproducibility deteriorates as wall velocity and dilation decrease. Upon varying each of the above parameters over the ranges described, the remaining flow parameters were kept constant to allow meaningful comparison of results. A default set of flow parameter values was chosen which was known to produce reproducible AWM waveforms within the physiological range (Table 5.6).

In order to investigate the effects on changing outflow impedance two different outflow tubes, tube A and tube B, were in turn attached to the phantom. For each set up the same flow was applied to the phantom and TDI data acquired. Tube A is the default choice described in Section 5.4.3. It has an inner diameter of 9.6 mm. Tube B, made of the same material, has a smaller inner diameter of 6.4 mm. Both have a

wall thickness of 1.6 mm. The same TDI acquisitions parameters as used in the pilot study in Section 5.5 were used here.

5.6.2 Results and discussion

5.6.2.1 Variation in flow rise time

AWM dilation, velocity and acceleration waveform shape

The AWM waveforms resulting from variations in flow rise time are demonstrated (Figure 5.9a), along with *in vivo* AWM, velocity and acceleration waveforms acquired for a common carotid artery in Chapter 2 for comparison (Figure 5.10). The AWM dilation waveforms all adopt the same basic shape of a rapid rise phase followed by a second smaller peak in dilation before dropping off to zero. While the corresponding velocity and acceleration waveforms demonstrate basic oscillatory patterns similar to that observed *in vivo*, of a large peak followed by a number of smaller oscillations (Figure 5.9b,c) the second peak in dilation of the amplitude exhibited here is not typically observed *in vivo*.

An additional feature of the AWM curves, superimposed on the basic oscillation pattern is the presence of higher frequency oscillations of the order of 20Hz. These are not present in AWM waveforms derived *in vivo*. One possible cause of this is the presence of multiple pressure reflections between the two ends of the VMM segment, resulting from the mismatch in mechanical impedance between the VMM segment and the rigid acrylic tubing it is attached to. The plausibility of this explanation can be explored by considering the propagation of the incident flow/pressure waveform.

By Fourier theory, one can interpret the incident 1 s flow (and therefore pressure) waveform in Figure 5.8 to be composed of a number of higher frequency sinusoids. Therefore, one can consider the transmission of these components of the overall incident waveform separately, acting as multiple sources of reflected waves. The time scale of these reflections can be approximated using the pulse wave velocity, c_0 of the VMM material, which is defined by the Moens-Korteweg equation (Equation 5.1).

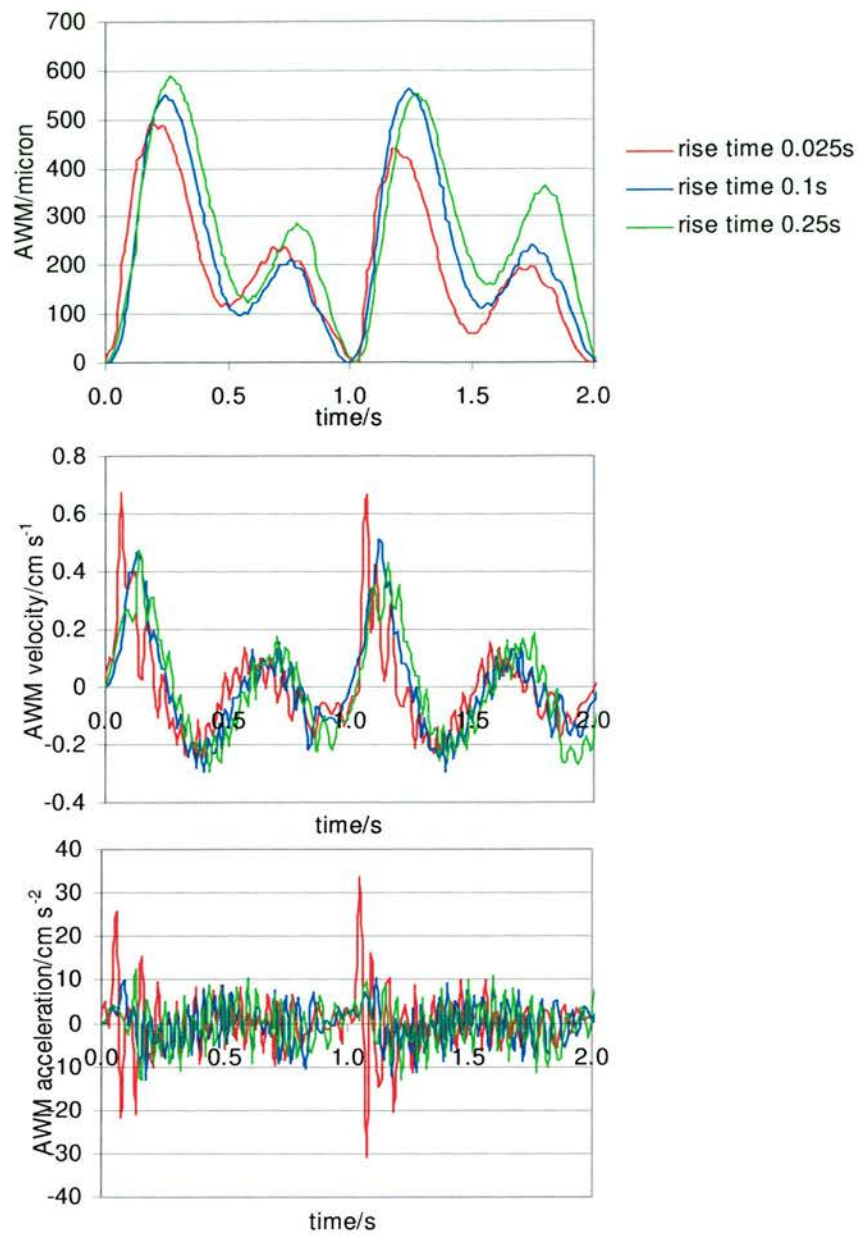


Figure 5.9: AWM (a) dilations (b) velocities and (c) accelerations resulting from variations in rise time.

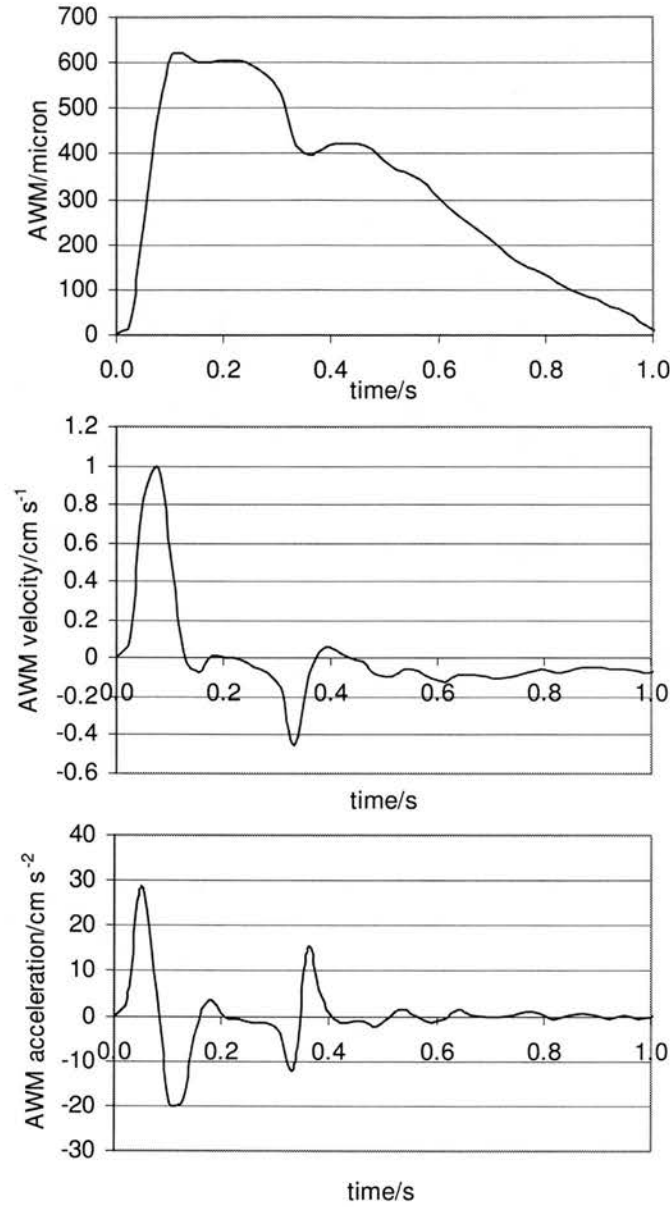


Figure 5.10: AWM dilations, velocities and accelerations derived from *in vivo* TDI scanning of an asymptomatic common carotid artery in Chapter 2.

Using the modulus obtained in the previous chapter for PVA cryogel subjected to 2 freeze-thaw cycles (122 ± 8 kPa), along with the VMM geometry stated earlier, a value for c_0 of 5.8 ± 0.2 m s⁻¹ was obtained. It will therefore take 0.034 s for an incoming pressure wave to traverse a typical VMM length of 10 cm from the point of TDI data acquisition to the end of the VMM segment, be reflected and travel back to

the point of data acquisition (a total path length of 20 cm). Reflections will also occur at the interface between the VMM and the inflow tubing of the phantom. Depending on damping by the VMM, there may be several reflection events before the initial component of the incident pressure wave is completely attenuated.

It is apparent that the traverse times of the reflected pressure waves are much smaller than the 1 s flow cycle length. Therefore reflected pressure pulses will arrive at the point of measurement while the incident overall pressure pulse that generated it is still passing. This is consistent with the observed high frequency oscillations that are superimposed on the fundamental low frequency AWM waveform shape.

5.6.2.1.1 *Maximum dilation, velocity and acceleration*

Variations in maximum dilation, velocity and acceleration are demonstrated (Figure 5.11). Maximum dilations fall within the upper half of the physiologic range and appear to increase with flow rise time. Arterial wall motion for all flow waveforms except that with a rise time of 0.25 s exhibit maximum velocities in the lower half of the physiologic range. Maximum accelerations span the physiologic range.

5.6.2.1.2 *AWM rise time, $t_{AWMpeak}$*

As a characteristic of physiologic AWM with which a match is desired (see 5.3.3), it is of interest to observe the variation in $t_{AWMpeak}$ with t_{Qpeak} (Figure 5.12). The *in vivo* $t_{AWMpeak}$ range is superimposed on the phantom results. For larger t_{Qpeak} values (0.25 s and 0.50 s) $t_{AWMpeak}$ are equal to the t_{Qpeak} . However, as t_{Qpeak} decreases the correspondence between the two rise times decreases. This is illustrated in Figure 5.12 as the deviation from the line representing equality between the two parameters.

A possible reason for the decrease in equality between AWM rise time and flow rise time is the distortion of the flow waveform in travelling from the pump to the point of measurement. The 750 mm of PVC tubing and the 25 mm of VMM the waveform must traverse to the point of data acquisition may remove the high frequency components of the flow and pressure cycles, which are responsible for the rapid rise time in the composite flow and pressure waveforms.

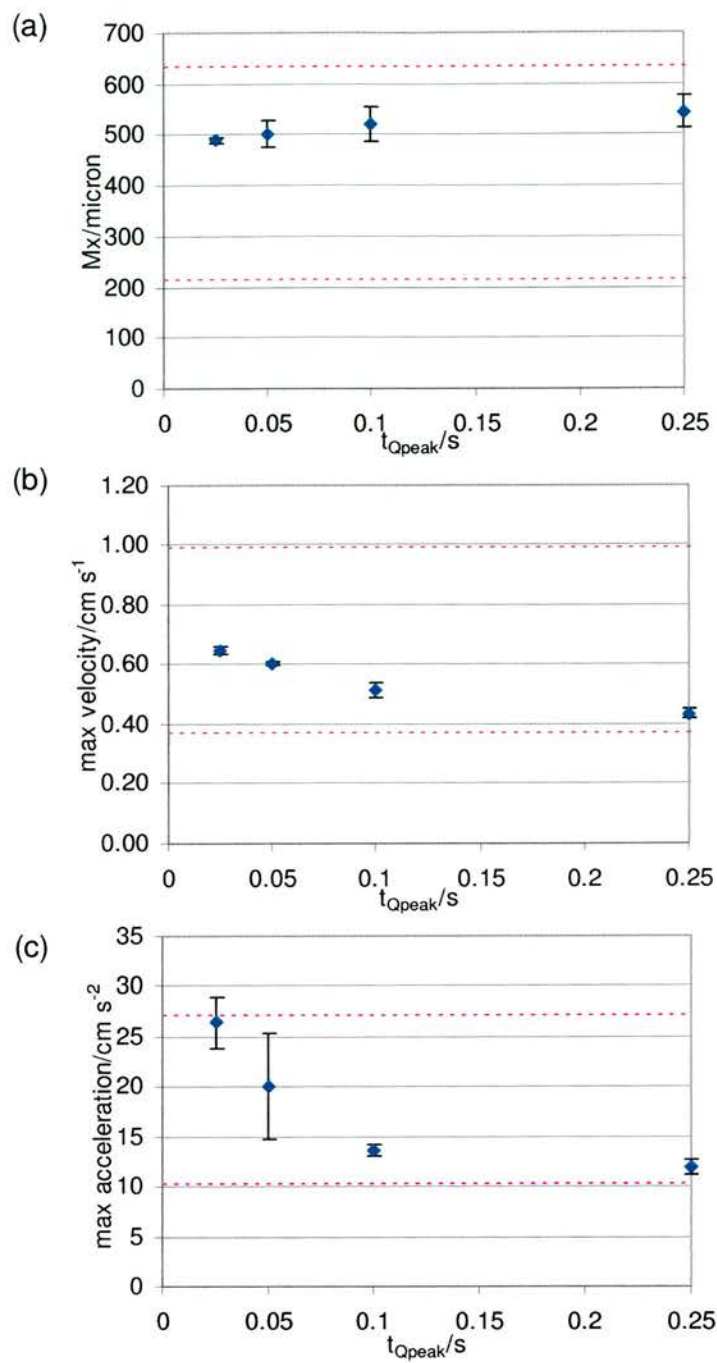


Figure 5.11: Variation in (a) Maximum dilation (b) Maximum velocity and (c) Maximum acceleration with flow rise time. The physiologic range derived from Chapter 2 data is represented by the dashed lines.

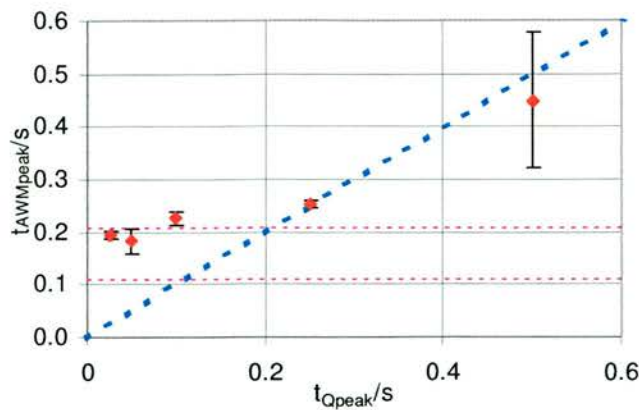


Figure 5.12: Variation in AWM rise time, t_{AWMpeak} with flow rise time, t_{Qpeak} . The physiologic range derived from Chapter 2 data is represented by the dashed pink lines. $t_{\text{AWMpeak}} = t_{\text{Qpeak}}$ is represented by the blue dashed line.

5.6.2.2 Variation in peak flow

The AWM dilations, velocity and acceleration resulting from flow waveforms with three different peak flows (Figure 5.13), and variations in maximum dilation, velocity and acceleration for all peak flow data (Figure 5.14), are demonstrated. It can be seen that maximum dilation increases as peak flow increases. Maximum dilation, velocity and acceleration all span the physiologic range.

The behaviour described above may be explained by the progressively larger peak pressures that result from increasing peak flow. As peak flow increases, the corresponding temporal pressure gradients at a given location increase. Since each flow has the same rise time, when this is combined with the increasing temporal pressure gradient, peak pressure also increases, distending the walls to a greater extent.

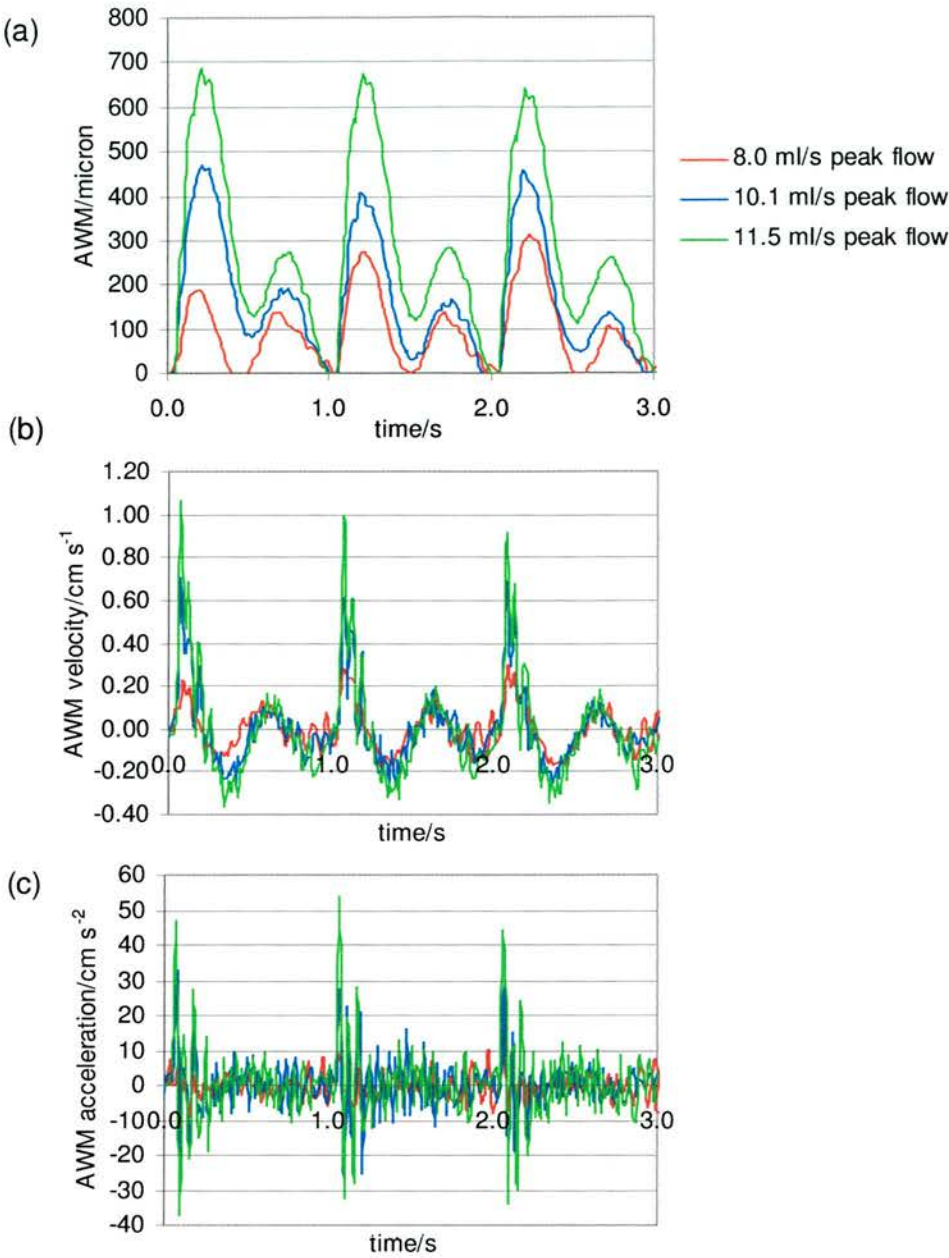


Figure 5.13: AWM (a) dilations (b) velocities and (c) accelerations resulting from varying peak flow.

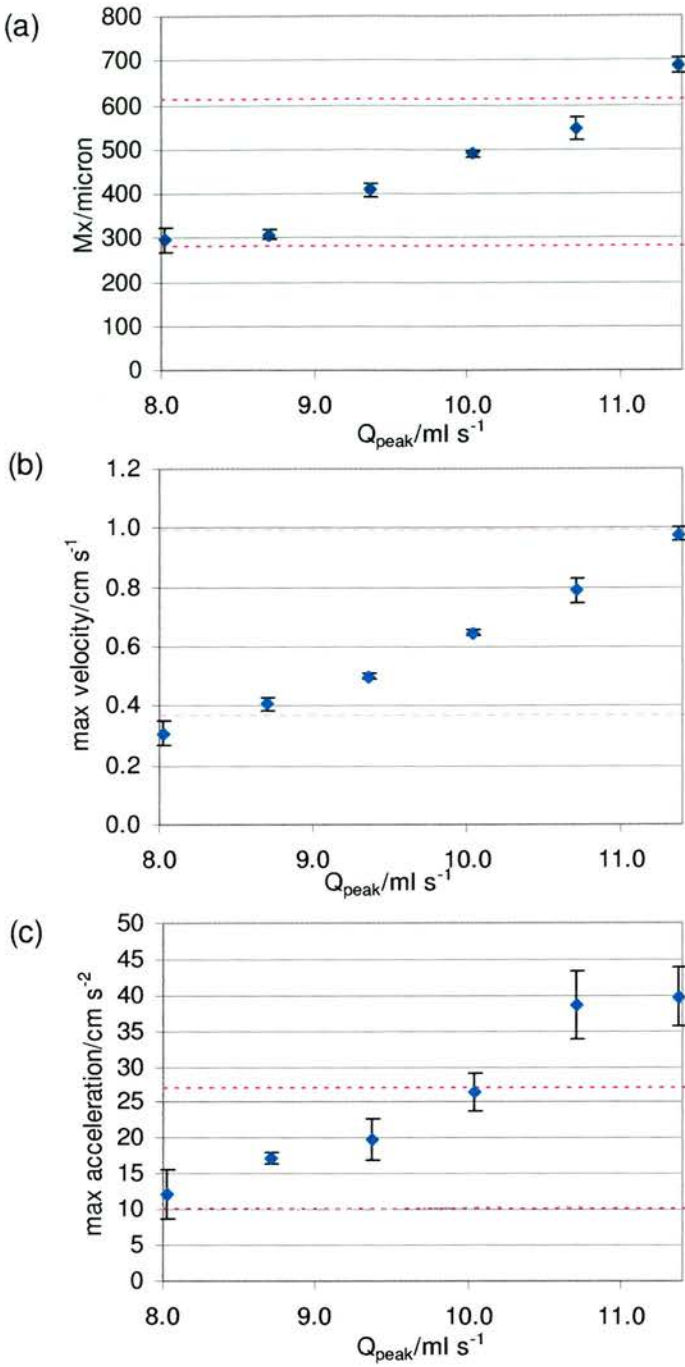


Figure 5.14: Variation in (a) Maximum dilation (b) Maximum velocity and (c) Maximum acceleration with peak flow. The physiologic range derived from Chapter 2 data is represented by the dashed lines.

5.6.2.3 Variation in flow full width half maximum (FWHM)

The AWM dilations, velocity and acceleration resulting from flow waveforms with three different FWHM (Figure 5.15) are demonstrated, as are variations in maximum dilation, velocity and acceleration are plotted for all flow waveforms tested (Figure 5.16). In qualitative terms, variations in AWM shape are apparent in Figure 5.15, with the second maxima or node in dilation being much higher for a high FWHM. Trends in maximum dilation, velocity and acceleration are less clear for this data compared to previous sections however, all the derived maximum dilations fall within the physiologic range, as do all maximum velocities, though they are limited to the lower half of the physiologic range. Conversely, maximum accelerations for every data point except for 0.5 s FWHM lie above the physiologic range by up to 15.0 % of the physiologic maximum.

The decrease in maximum dilation for a flow waveform of FWHM 0.90 s seen in Figure 5.16a may be a result of the increasingly steep fall off in flow as FWHM increases. As postulated in Section 0, the steep negative flow gradient (and therefore pressure) causes the vessel walls to reach higher negative velocities in the last 0.1 s of the flow cycles (see region 'B' in Figure 5.15). This phenomena can be seen in the first cycle in Figure 5.15b, which is typical of the data. A comparison of minimum velocities in this region of the AWM cycle between data generated by a 0.5 s FWHM and a 0.90 s FWHM is illustrative (Table 5.7). The lower velocities exhibited by the 0.90 s FWHM mean that subsequent incoming flow cycles expend more energy in slowing the collapsing walls to their resting position before the vessel walls can enter the expansion phase of the AWM cycle. This results in the lower maximum dilation in the following cycle for the 0.90 s FWHM flow.

Flow FWHM/ s	Secondary minimum velocity/ cm s ⁻¹
0.5	-0.12 ± 0.03
0.90	-0.32 ± 0.02

Table 5.7: A comparison of AWM secondary minimum velocities in the last 0.1 s of the AWM cycle generated by 0.50 s FWHM and 0.90 s FWHM flow.

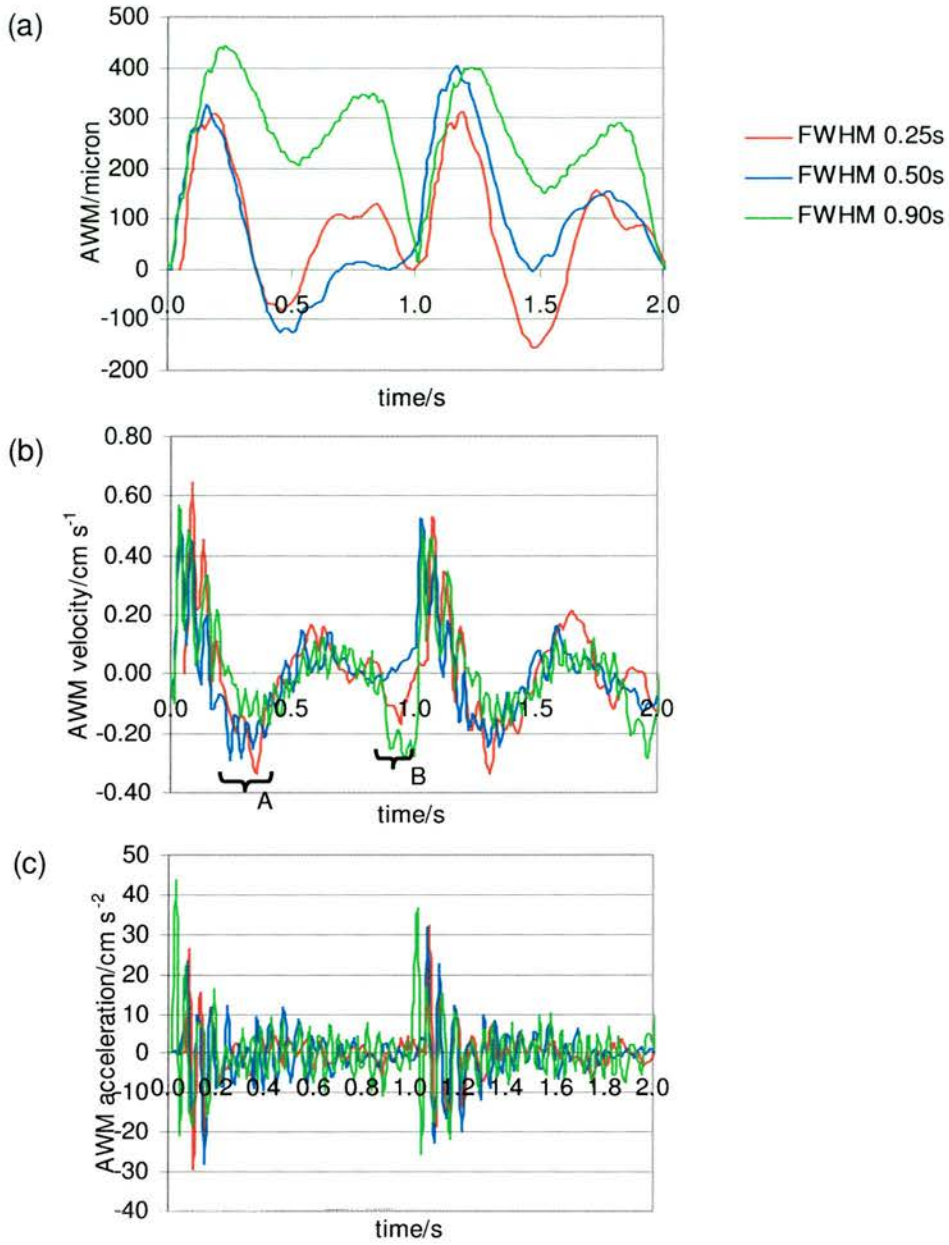


Figure 5.15: AWM (a) dilations (b) velocities and (c) accelerations resulting from varying FWHM.

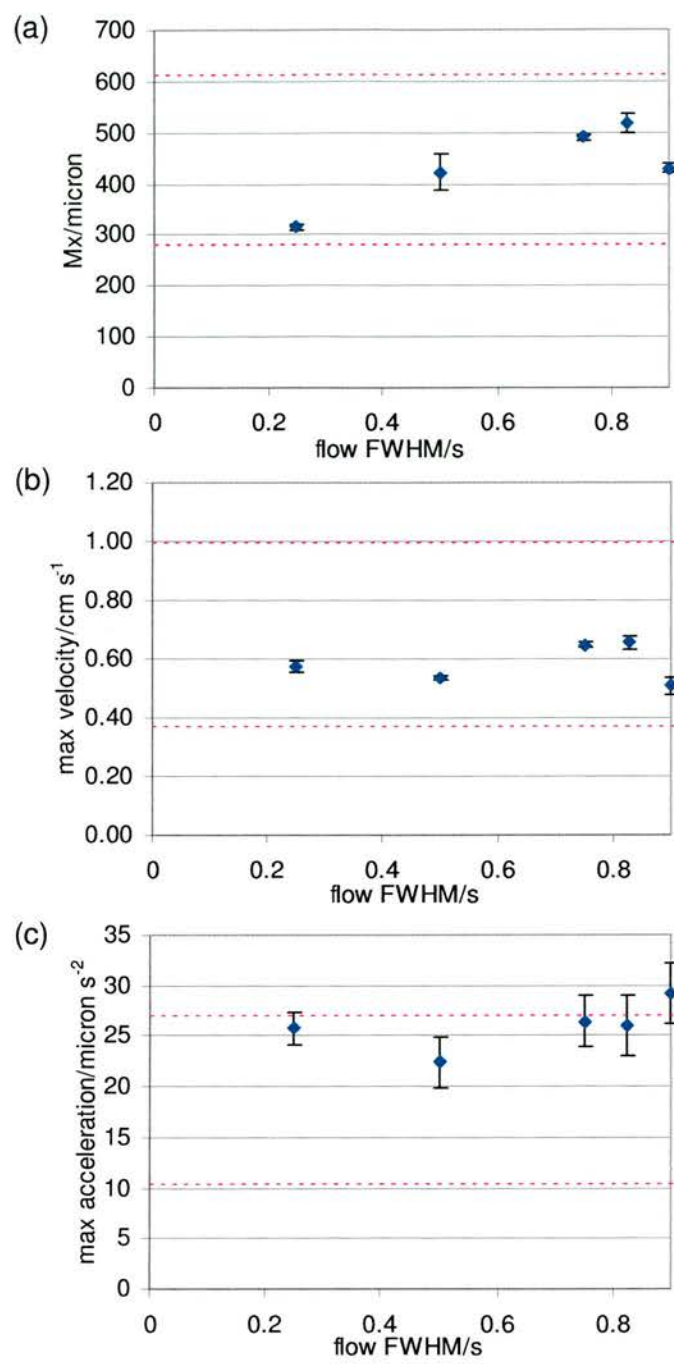


Figure 5.16: Variation in (a) Maximum dilation (b) Maximum velocity and (c) Maximum acceleration with FWHM. The physiologic range derived from Chapter 2 data is represented by the dashed lines.

Another interesting feature of these AWM curves is that as the width of the flow peak decreases, the extent of negative AWM dilations increases, as postulated in Section 5.5. After the initial primary peak of maximum dilation, the negative velocities experienced by the walls in the contraction phase of the AWM cycle at approximately 0.2 - 0.5 s in the AWM cycle (labelled 'A' in Figure 5.15) for 0.25 s FWHM and 0.50 s FWHM flows are greater in magnitude than those experienced by those subjected to 0.90 s FWHM flow (Table 5.8). This effect is observable in Figure 5.15. Thus, for these examples, the vessel walls have not reached zero velocity when they reach zero displacement after the initial dilation peak and so they produce negative dilations.

FWHM/ s	Primary minimum velocity/ cm s^{-1}
0.25	-0.33 ± 0.01
0.50	-0.28 ± 0.01
0.90	-0.18 ± 0.01

Table 5.8: A comparison of AWM primary minimum velocities generated by flow of 0.25, 0.50 and 0.90 s flow cycles.

5.6.2.4 Variation in phantom output impedance

The AWM dilations, velocities and accelerations are demonstrated for the two different output impedances created by tube A and tube B (Figure 5.17). Variations in maximum dilation, velocity and acceleration are plotted for the same data (Figure 5.18). Of interest is the significant change in shape of the AWM dilation curves on increasing output impedance (that is, swapping tube A for tube B). The high frequency oscillations superimposed on the basic AWM dilation shape observed in previous figures remain. However, the labelled secondary maximum or node seen in previous AWM curves disappears. Instead, an AWM curve that rises rapidly to a peak then falls off more gradually to zero dilation is observed. This AWM shape more closely resembles physiologic AWM. Preliminary *in vivo* observations of AWM (including those described in Chapter 2) suggest the secondary maximum in the AWM obtained with output impedance A is much more exaggerated than any secondary dilation maxima that would be observed *in vivo*.

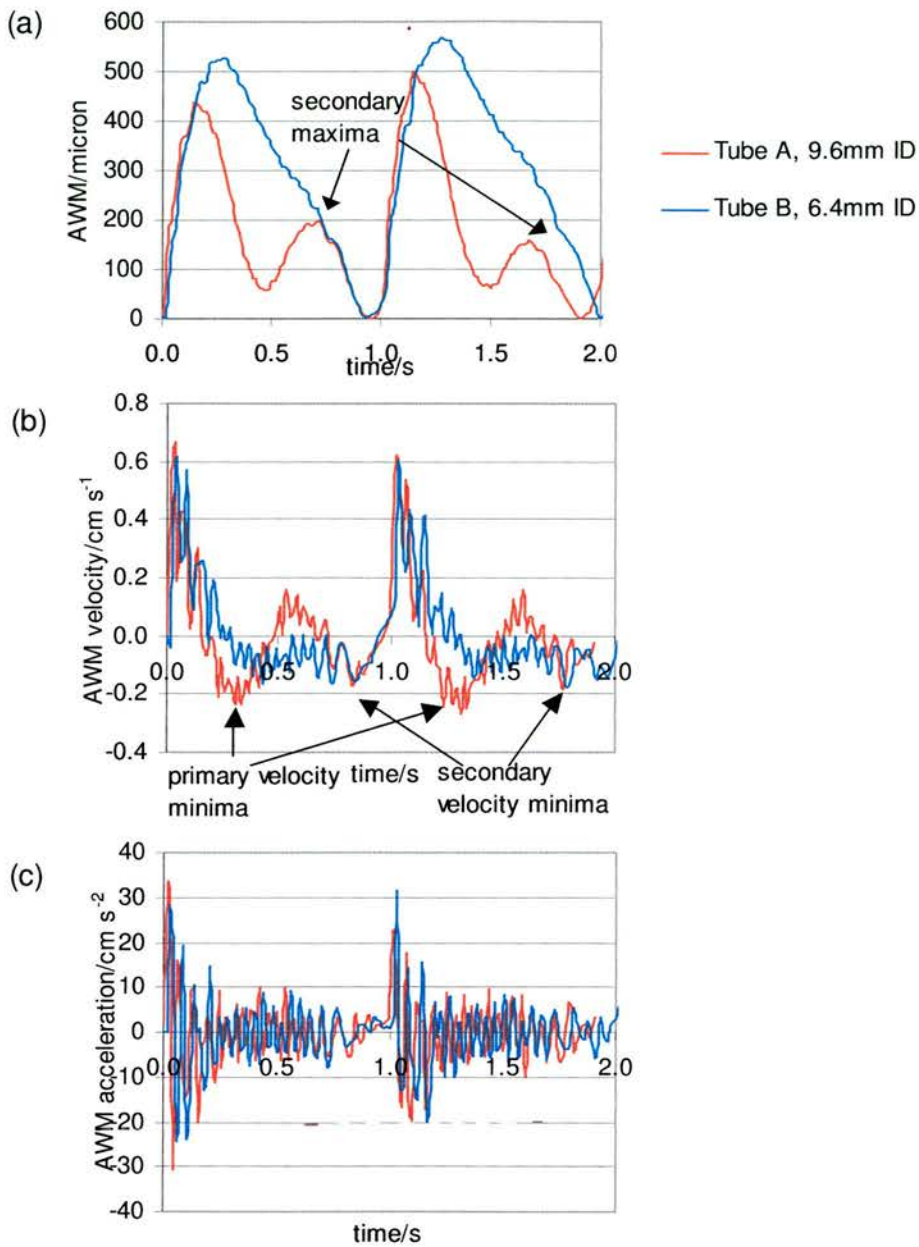


Figure 5.17:AWM (a) dilations (b) velocities and (c) accelerations resulting from varying outflow impedance.

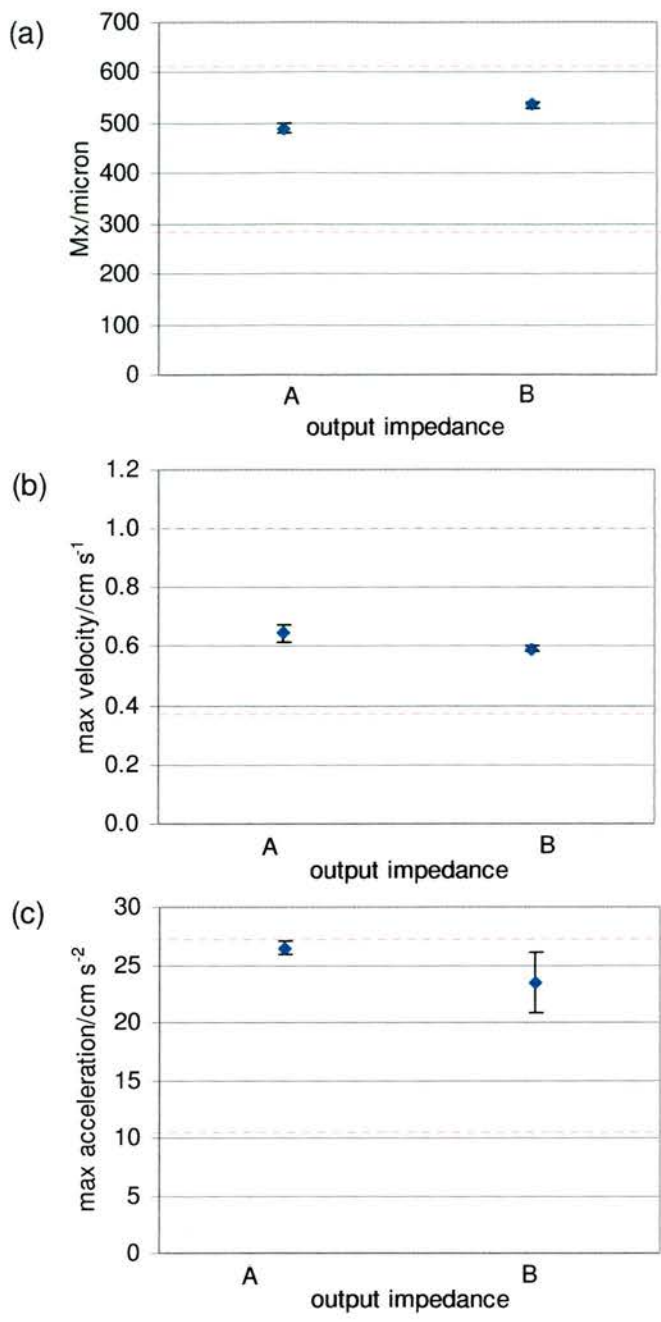


Figure 5.18: Variation in (a) Maximum dilation (b) Maximum velocity and (c) Maximum acceleration with outflow impedance. The physiologic range derived from Chapter 2 data is represented by the dashed lines.

Increasing output impedance is also found to increase maximum dilation. This increase can be explained in qualitative terms by the higher pressures generated in the phantom in order to maintain the same flow rate generated by the pump through

the higher impedance outflow tubing. Maximum dilations for both output impedances lie within the physiologic range. Maximum velocity and acceleration both decrease with increasing output impedance. The maximum velocities fall within the physiologic range as do the maximum accelerations. The decreases in maximum velocity and acceleration with increasing output impedance are coupled with an increase in AWM rise time (Figure 5.19).

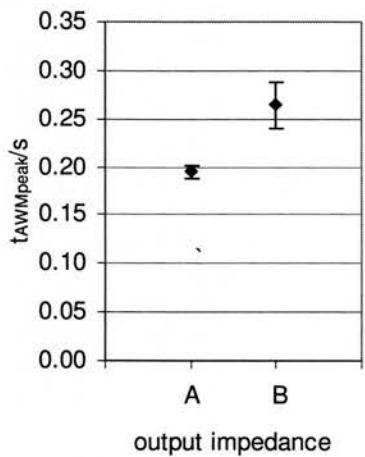


Figure 5.19: AWM rise time variation with phantom output impedance.

5.7 Summary and conclusion

A compliant wall vascular phantom has been designed which can generate AWM waveforms sharing a number of features with *in vivo* common carotid artery AWM waveforms. Derived maximum dilations, velocities and accelerations fell within the physiologic range. These parameters were varied upon altering the inputted flow. A summary of the ranges obtained in the data described is provided (Table 5.9). The basic AWM waveform shape was altered on varying outflow impedance and the applied flow FWHM. Both these parameters acted to vary the relative height of the second node in dilation, a feature common to all the AWM waveforms gathered. One limitation in the phantom was the range of rise times observed on application of the described flow waveforms. AWM rise times were limited to the upper half of the physiologic range derived from Chapter 2. The use of a shorter inlet tube may minimise the distortions of the flow and pressure waveforms described in section 5.6.2.1 and allow the shorter physiological AWM rise times to be mimicked.

AWM characteristic	Phantom Range	<i>In vivo</i> range
Maximum dilation/ μm	295 - 686	216 - 636
Maximum velocity/ $\text{cm s}^{-1} \times 10^3$	0.31 - 0.98	0.373 - 0.998
Maximum acceleration/ $\text{cm s}^{-2} \times 10^5$	11.9 - 39.7	10.4 - 27.2
Rise time/ s	0.15 - 0.25	0.08 - 0.20

Table 5.9: Summary of maximum dilations, maximum velocities, maximum accelerations and rise times obtained using the phantom compared to the *in vivo* values.

A further limitation of the derived AWM waveforms was the presence of high frequency small amplitude oscillations superimposed on the basic waveform shape, observable in Figure 5.7, Figure 5.9, Figure 5.13, Figure 5.15 and Figure 5.17. These are not observed *in vivo*. It is thought these are due to reflected pressure-flow cycles within the VMM length. The timescale for pulse propagation derived from the VMM pulse wave velocity, compared with the incident overall flow cycle length are consistent with this. Two approaches could be employed to minimise the reflections. Firstly, the change in mechanical impedance across the VMM-phantom housing interface could be minimised. This could be achieved by using less rigid tubing on

the phantom housing, or by allowing the VMM segment to taper before attaching it to the phantom housing. The latter option gradually increases mechanical impedance along the VMM length such that it is more closely matched to the outflow tubing impedance at their interface. Secondly, the reflections could be damped out by insertion of a damping material at the interface between the VMM and phantom housing. This idea was devised by a research student in the Department of Medical Physics at the University of Edinburgh and initial results were promising.

A further area of interest is the required flow waveforms to produce the AWM characteristics described in Table 5.6. Mean applied flows fell in the range $7.7 - 10.2 \text{ ml s}^{-1}$. Comparison with an *in vivo* value, 6.2 ml s^{-1} reveals the values employed here are somewhat higher than that found *in vivo*¹⁵¹. From this comparison it is deduced that in fact the outflow impedances employed here are lower than found *in vivo* downstream of the carotid arteries, since while greater mean flows are applied to the phantom than found physiologically, only similar magnitude dilations to those physiologically occurring are produced.

In practical terms, the phantom is relatively easy to manufacture. Tissue mimicking material manufacture requires readily available materials and while PVA cryogel is a relatively specialist material, it is required in small volumes only. Care was required in VMM manufacture to ensure only segments with adequately symmetric wall thickness were used to prepare phantoms. The phantom design was subjected to rapid rise times as low as 0.025 s and flow pulse heights ($Q_{\text{peak}} - Q_{\text{min}}$) of up to 4.7 ml s^{-1} without separation of the VMM from the TMM or rupture of the VMM. This corresponded to maximum wall dilations greater than maximum dilations observed *in vivo* in Chapter 2. A cautious approach was employed, and so it is likely that higher peak flows could be applied, resulting in larger dilations and wall velocities.

Given the scope for moulding the VMM and TMM, it is possible that geometries of vessels could be varied to mimic lumen diameters of all arteries in the circulatory system and not just the carotid arteries. However, work here encountered difficulties in preparing VMM with thinner walls at the lower end of the physiologic scale. Furthermore, current mould design is limited to the dimensions of steel rod and tubing that are mass-produced since cost of custom geometries is high. The work detailed here used only uniform elasticity and geometry VMM, however, there is scope to introduce non-uniformities. Indeed, the former has been demonstrated in the literature^{115,116}. Therefore, together with the data relating freeze-thaw cycles with elastic modulus in Chapter 4, a range of disease levels could be simulated using the phantom designed here.

Chapter 6 Evaluation of Arterial Wall Motion (AWM) precision with varying acquisition geometries

6.1 Introduction

Previous chapters have described TDI/AWM data acquisition under what was thought to be optimal scanning geometries: the vessel depth was fixed and aligned normal to the ultrasound beam in the depth plane of the image and the transducer was aligned exactly with the vessel central axis. A further variable in scanning set-up is the pressure exerted by the transducer upon the vessel. This is not a geometrical parameter but is thought to affect AWM precision. In the previous chapters, no pressure was exerted on the VMM by the transducer. In clinical practise, the scanning environment described above is often not the case, and deviations from these conditions will affect TDI/AWM technique performance. Main implications for TDI and B-mode data quality upon varying each set-up parameter are outlined below (Table 6.1).

Parameter	Effect of variation
Vessel depth	Varies image clarity & signal strength at transducer
Beam-vessel angle	Varies image clarity and signal strength as extent of beam reflected in the direction of the transducer varies.
Beam-vessel axis alignment	Varies image clarity, signal strength and the component of the AWM velocity detected at the transducer.
Transducer pressure	Query direct effect on AWM and indirect effect of potential variations in flow impedance by compression of the vessel.

Table 6.1: Variations in scanning geometry & transducer pressure and their main effects.

This chapter explores the consequences for AWM of these effects upon variation in the parameters, using the compliant wall vascular flow phantom designed in the previous chapters with recipe A TMM (see sections 4.3.3.1 and 5.4) to simulate the attenuation of the ultrasound beam provided by soft tissue. No direct measure of AWM accuracy was possible with such a phantom since AWM is indirectly controlled using the applied volume flow, however assessments of precision could still be made. Specifically, the AWM obtained for varying geometries could be

compared to AWM measured using the reference optimal scanning geometry as described above.

6.2 Method

The same generic set up, flow generation and scanning methods were used as described in previous chapters. The same scanner settings described in Chapter 5 were employed, based upon experience of TDI/AWM technique performance in previous work. Pulsatile volume flow was applied to the compliant wall phantom (Figure 6.1). As in the previous chapter, a short flow rise time was employed followed by a region of uniform flow. This and a baseline flow of 6.7 ml s^{-1} compared to the peak flow of 10 ml s^{-1} prevented wall collapse and retrograde flow. Each of the four geometrical factors was varied in turn while the others were fixed.

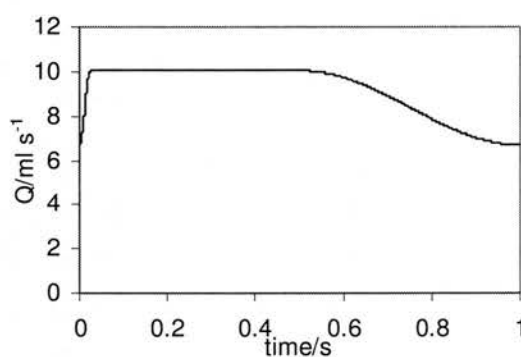


Figure 6.1: Volume flow, Q applied at the pump for variable geometry precision measurements.

In each study three TDI loops were acquired for each geometry setting. For example, in investigating the effects of vessel depth, three loops were acquired for each vessel depth. Maximum dilation over all cardiac cycles per loop was calculated, excluding those AWM cycles that had clearly not been registered correctly by the TDI/AWM technique (see Section 3.3). Maximum dilation, M_x for each cine loop was averaged over the three loops acquired. Intra- and inter-loop standard errors were calculated and plotted with all data. Maximum dilations obtained for each scan plane, beam-vessel angle, vessel depth and transducer pressure were normalised to the value obtained at the reference geometry. The reference scanning geometry and range of

values for each scanning parameter are provided (Table 6.2). The experimental set up for the reference scanning geometry is also illustrated (Figure 6.2). All data were acquired within the same session to minimise inter-measurement variability. This can be introduced by variations in VMM and TMM elastic properties, BMF viscosity, human error in configuring the scanner and incorrect set up of flow and measurement geometry.

Parameter	Reference Geometry	Range tested
Depth/ mm	20	20, 26, 32, 44
Transducer – vessel angle/ °	1	1, 5.4, 11.9, 17.5, 24.1
Scan plane – vessel axis coincidence (mm from the vessel axis)	0	0, 0.5, 1.0, 2.0
Transducer pressure	contact	Contact, moderate, high

Table 6.2: Reference scanning geometry and range of geometry tested.

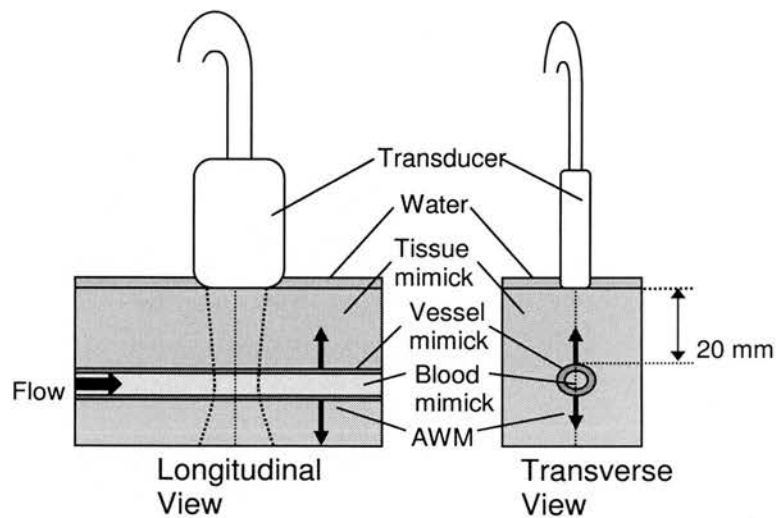


Figure 6.2: Reference measurement geometry.

6.2.1 Depth variation

Uniform thickness TMM slabs were placed on top of the phantom to vary vessel depth.

6.2.2 Transducer-vessel angle variation

A variation in transducer-vessel angle was introduced using wedges of TMM made from the same batch employed to prepare the phantom TMM. The angled wedges were placed on top of the section of phantom to be scanned. The transducer was placed on top of the wedges and aligned with the angled surface in the vertical plane (Figure 6.3). Wedges of nominal angles 5° , 10° , 20° and 30° were manufactured by pouring TMM into angled moulds. This was not a precise technique and subsequently acquired greyscale images of the vessels were used to calculate the transducer-vessel angles more accurately using the tangent trigonometric rule in custom written Matlab code (MathWorks, Natick, MA) (Figure 6.4). For one particular wedge angle (nominal angle 20°), the TMM wedge was removed, leaving water between the transducer and the top of the phantom. Therefore, the same transducer-vessel angle was still imposed but the attenuating affect of the TMM was removed.

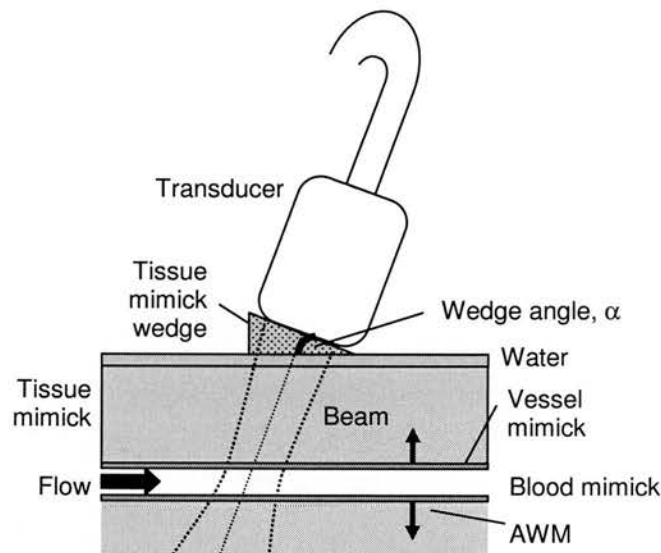


Figure 6.3: Transducer – vessel angle variation measurement geometry.

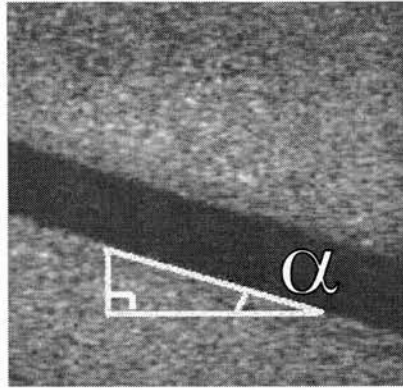


Figure 6.4: Calculation of the transducer-vessel angle.

6.2.3 Scan plane variation

In order to assess variation in AWM precision with scan plane coincidence, the transducer was first aligned with the central plane of the vessel. It was then moved through increments of 0.5 mm, 1 mm and 2 mm from the vessel central axis in both transverse directions using a micromanipulator (Figure 6.5). The central axis was located by aligning the transducer by eye, then fine adjusting its position to obtain a B-mode image with the strongest possible reflections of the vessel walls along the length of the imaged segment.

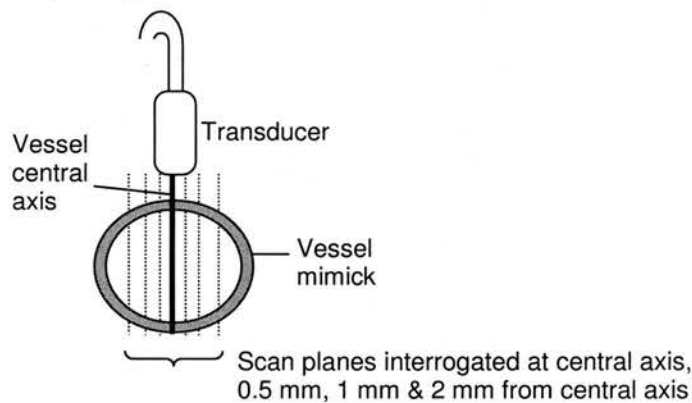


Figure 6.5: Scan plane variation measurement geometries.

6.2.4 Transducer pressure variation

Facilities for measuring pressure applied by the transducer to the vessel were not readily available. In addition, without values for typical clinically applied pressures results in SI units of Pascals have limited meaning. For these reasons, and as a first investigation into the effects of varying transducer pressure, a semi-quantitative yet

clinically relevant method was used to denote the force applied. Tissue Doppler data was collected for three pressure levels. These were classed as 'contact pressure' (as for all other phantom experiments, where the transducer merely makes contact with the TMM), 'moderate' and 'high'. The latter was limited to avoid damage to the phantom whilst exceeding any pressure that might be applied clinically by a sonographer. Pressure was increased by moving the clamp holding the transducer progressively lower down the clamp stand towards the vessel, further into the TMM surface. The clamp and transducer was moved 3 mm then 4.5 mm into the TMM surface to exert 'moderate' and high' pressures on the vessel. For each pressure level the minimum diameter of the vessel was measured, providing a further semi-quantitative indication of the pressure applied.

6.3 Results & Discussion

6.3.1 Variation in AWM precision with vessel depth

Dilation envelopes, that is, the minimum and maximum dilations for each time frame, are shown for two depths (Figure 6.6). Visual inspection reveals an increase in dilation envelope, which is reflected by increases in normalised standard deviation of dilation, $Sd(N)$ (Figure 6.7). A decrease in normalised maximum dilation, $Mx(N)$ with vessel depth is also demonstrated (Figure 6.8). However, two of the data points (depths 26 mm and 44 mm) have a large inter-loop variation as demonstrated by the error bars. For the first of these depths in particular, the wide variation is largely attributable to a single loop where 462 μm was obtained compared to 410 μm and 426 μm . There is no obvious reason why this has occurred since at the time of data collection, the three loops were acquired consecutively and there are no marked differences on visual inspection of the images. The results obtained were double checked by generating the excel AWM data a second time and re-running the Matlab AWM analysis code, only to produce the same values.

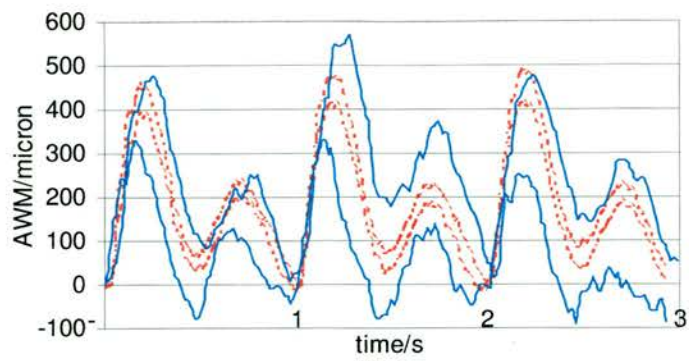


Figure 6.6: TDI derived AWM envelopes for vessel depths of (a) 20 mm (red dashed) and (b) 44 mm (blue solid).

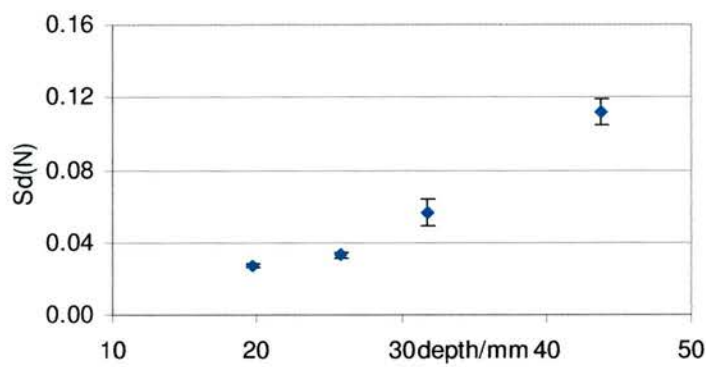


Figure 6.7: Variation in normalised standard deviation of dilation, Sd(N) with vessel depth.

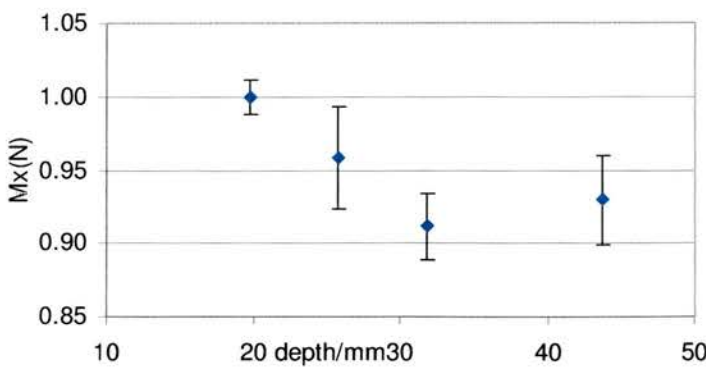


Figure 6.8: Variation in normalised maximum dilation, Mx(N) with vessel depth.

Aside from the points of wider variability, the increase in S_d and decrease in M_x with depth are of interest. These are thought to be manifestations of a reduced signal to noise ratio. Progressively less ultrasound reaches the vessel walls, and less is reflected back to the transducer as depth increases due to greater attenuation by the TMM. Noise is visible on the segmented TDI images as pixels opposite in colour to those surrounding it and becomes more noticeable as depth increases (Figure 6.9). The scanner misinterprets these pixels as phantom motion at lower velocities than the true phantom motion, resulting in lower derived AWM dilations and an increased spread in AWM due to the random nature of the noise. The influence of noise in this way is exacerbated by the application of saturated colour gain, a setting for TDI/AWM acquisition recommended by the software developers.

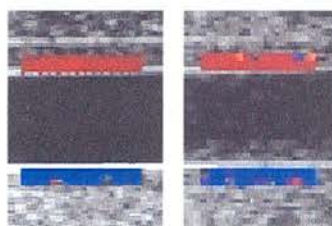


Figure 6.9: Segmented TDI frames during wall contraction for vessel depths of (a) 20 mm and (b) 44 mm. Note the presence of adjacent blue and red pixels particularly apparent in (b) indicating the presence of noise.

In addition to the influence of TDI noise, the greater heterogeneity observed in dilations from a vessel depth of 44 mm may also be attributed to the decrease in frame rate of 16.1 % from 62 Hz to 52 Hz. The decreased frame rate may increase any scan line asynchronisation effects. M_x is also affected as the decreased frame rate lessens the ability of the scanner to resolve the continuously changing velocities exhibited by the VMM.

To conclude, maximum dilation is systematically underestimated at depths greater than typical for a common carotid artery. This has important implications for the application of TDI/AWM to investigate internal carotid artery AWM in addition to other arterial sites deeper than 20 mm such as the abdominal aorta. Furthermore, the discrepancies between actual dilation and AWM/TDI derived dilation revealed here would likely be greater for internal carotid arteries given that they move with lower

velocity and dilation ranges than common carotid arteries, especially those which are diseased.

6.3.2 Variation in AWM precision with transducer-vessel angle

From inspection of the AWM curves for 1° and 24.1° wedges, one can see the increase in heterogeneity of dilation, similar to that obtained on varying vessel depth (Figure 6.10). This effect is illustrated by a plot of $Sd(N)$ against transducer-vessel angle where the standard deviation increases from 0.03 ± 0.01 to 0.15 ± 0.01 across the range of angles for which data was acquired (Figure 6.11). Also, in common with depth variation, one finds a decrease in $Mx(N)$ with transducer - vessel angle by a factor of 0.22 (Figure 6.12).

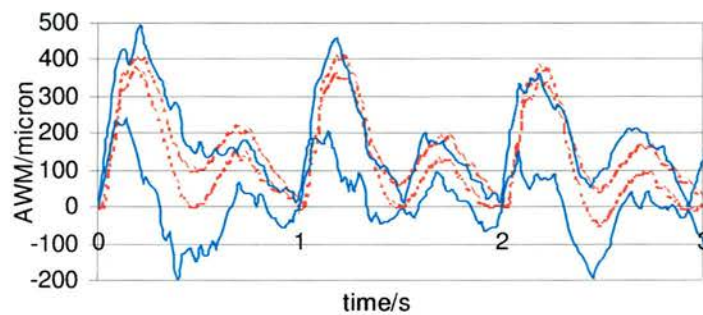


Figure 6.10: TDI derived AWM envelopes for transducer-vessel angles of (a) 1° (red dashed) and (b) 24.1° (blue solid).

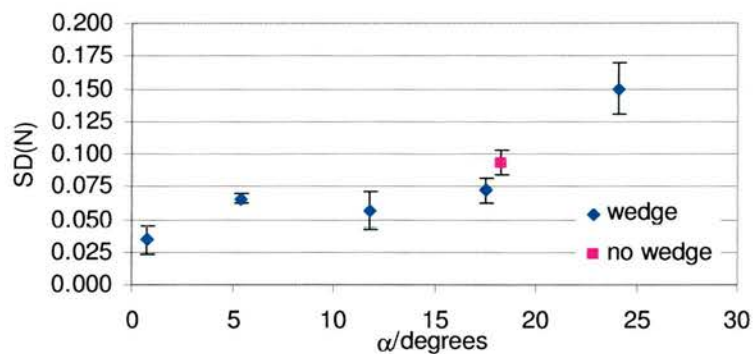


Figure 6.11: Variation in normalised standard deviation of dilation, $Sd(N)$ with transducer-vessel angle.

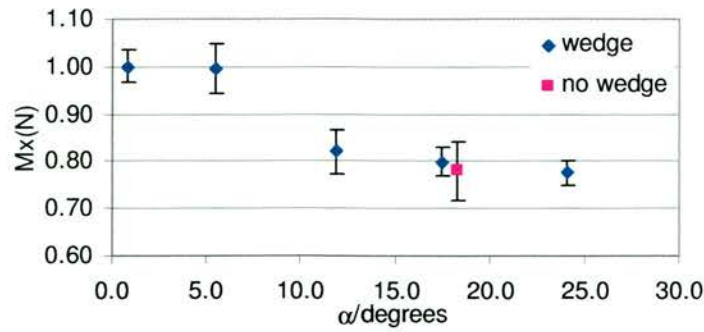


Figure 6.12: Variation in normalised maximum dilation, $M_x(N)$ with transducer-vessel angle.

The observed changes can be attributed in part to the progressively lower component of the wall velocity detected by the ultrasound beam. This varies as the cosine of the wall speed and so one would expect a drop by a factor of 0.09 for a transducer-vessel angle increase from 0° to 24.1° (compared to the observed drop in M_x of 0.22). The observed drop-off in M_x may be due to a reduced signal to noise ratio, as an increasing amount of the ultrasound beam is reflected away from the transducer compared to normal beam incidence. A comparison of results for the transducer-vessel angle of 17.5° with and without a TMM wedge was of value. Only a 2 % difference was found between the M_x values at this angle, suggesting that the transducer-vessel angle was the controlling factor rather than the additional attenuation introduced by the presence of the TMM wedge.

As with the other geometrical parameters considered there are clinical implications of this source of variability. Internal carotids are often tortuous, especially immediately prior to entering the skull, and especially so if diseased. The transducer-artery angle may also vary across the field of view resulting in spatial gradients, which may be misinterpreted as a change in strain and therefore elasticity.

6.3.3 Variation in AWM precision with scan plane variation

B-mode images of the varying scan planes and the derived AWM curves are shown for three different scan planes (Figure 6.13, Figure 6.14). The resultant variation in M_x is demonstrated (Figure 6.15). M_x decreases with distance from the vessel central axis, on average by 0.34 ± 0.02 of M_x at the central axis on moving 2 mm

from the central axis. The main reason for the decrease in M_x relates to the motion of the vessel wall off its central axis. Arterial wall motion is predominantly radial (as demonstrated in Chapter 5). Therefore, the further the transducer from the vessel central axis, the smaller the component of wall velocity will be detected. Furthermore, as the transducer moves off the vessel central axis the reflections back to the transducer decrease as the reflecting planes of the vessel walls are no longer normal to the beam. The decrease in backscatter intensity results in a smaller signal to noise ratio, compounding the decreased component of velocity detected. The non-normal beam incidence also creates less well-defined B-mode images of the vessel wall, which can hinder wall segmentation.

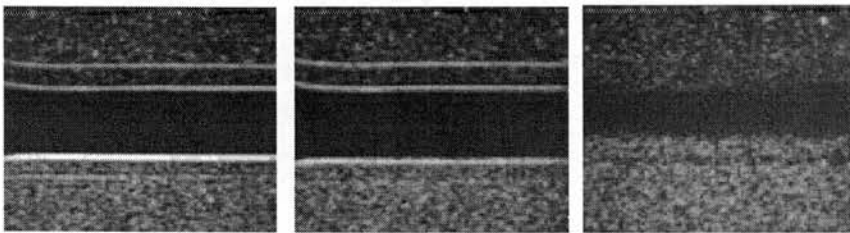


Figure 6.13: B-mode images of scan planes for (a) scan plane coincidence with the central vessel axis (b) 0.5 mm from the vessel central axis (c) 2 mm from the vessel central axis.

Given the observed effects, clinical scanning should optimise scan plane-vessel axis coincidence in order to measure the maximum component of radial motion and gain the strongest possible ultrasound reflections from the vessel walls. The differences in scan plane location for data gathered here is perceptible by eye (Figure 6.13). The central axis image is noticeably brighter and has the most well defined images of the vessel, therefore imprecision due to this geometrical factor should be relatively easy to minimise. Furthermore, spurious AWM spatial gradients resulting from partial alignment of the transducer with the central axis can be avoided. Chapter 2 provides an *in vivo* example, where the derived AWM could potentially be misinterpreted as implying variable elasticity.

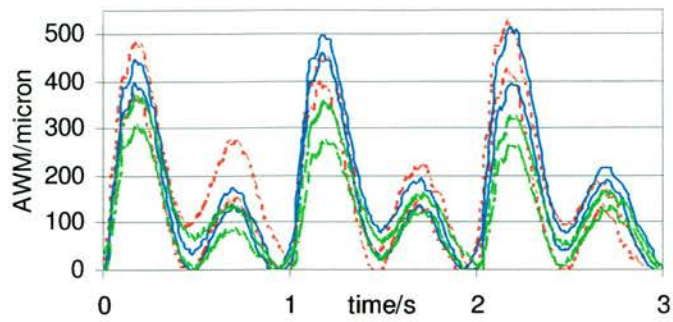


Figure 6.14: TDI derived AWM envelopes for (a) the vessel central axis (red dash) (b) 0.5 mm off the vessel central axis (blue solid) (c) 2 mm from the vessel central axis (green solid).

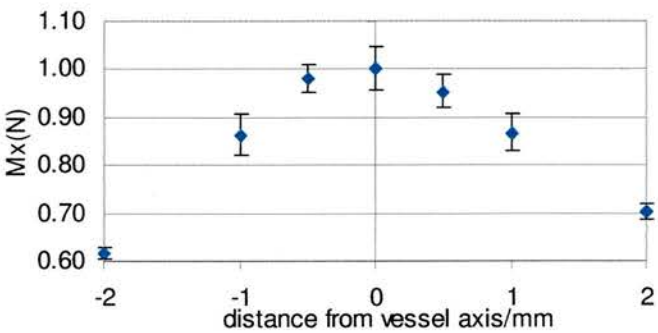


Figure 6.15: Normalised maximum dilation, $Mx(N)$ variation with scan plane.

6.3.4 Variation in AWM precision with exerted transducer pressure

Vessel diameters (measured with no applied flow) for the different exerted pressures were 5.2 mm (contact pressure), 4.6 mm (medium pressure) and 4.1 mm (high pressure), decreasing as the pressure exerted increased. Dilations obtained for vessel diameters 5.2 mm and 4.1 mm are shown (Figure 6.16). Heterogeneity of the AWM curves illustrated by $Sd(N)$ decreases as pressure increases, while at the same time $Mx(N)$ increases (Figure 6.17, Figure 6.18).

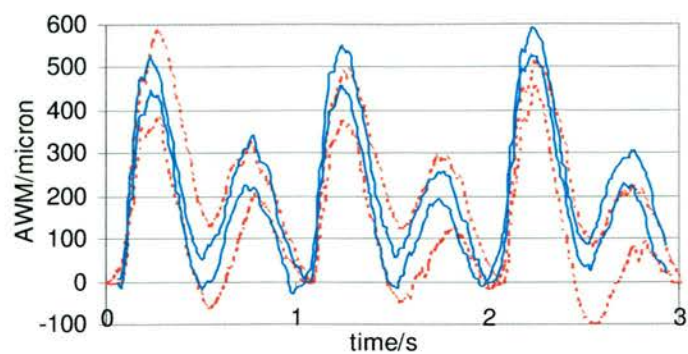


Figure 6.16: TDI derived AWM envelopes for vessel diameters of (a) 5.2mm (contact pressure-red dash) and (b) 4.1mm (high pressure-blue solid).

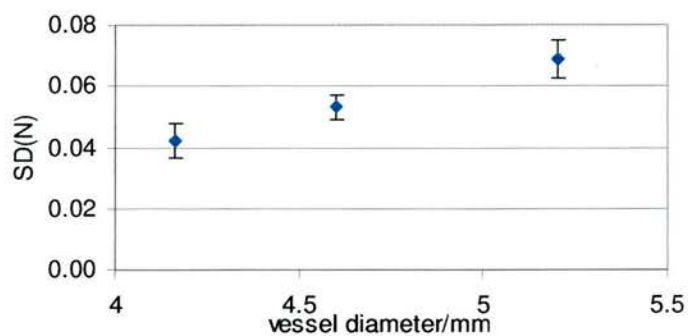


Figure 6.17: Variation in normalised standard deviation, Sd(N) of dilation with exerted transducer pressure.

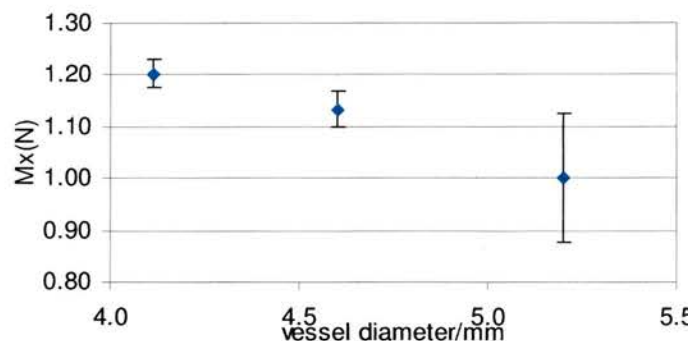


Figure 6.18: Variation in normalised maximum dilation, Mx(N) with exerted transducer pressure.

It is difficult to ascertain the mechanisms varying Mx without further investigation. One possibility however, is that the changes observed with increasing pressure applied by the transducer result from a change in mechanical impedance of the

vessel. More specifically, an increase in input impedance may be responsible for the observed increase in M_x . Input impedance provides a measure of resistance to flow at a given point and is defined as the ratio of pressure, P generating volume flow, Q at a particular point in a vessel. Input impedance increases as diameter decreases and results in an increase in pressure pulse height, the distending pressure responsible for AWM, resulting in an increase in maximum dilation¹⁵⁰. To achieve these dilations, the wall velocity range over the course of one flow cycle must also increase.

To summarise, measured AWM appears to vary with the pressure exerted by the transducer on the vessel walls. Ideally, therefore, this quantity should be standardised, to minimise variability between TDI/AWM acquisitions. This may be achieved by minimising pressure exerted by the transducer on the skin such that the transducer merely makes contact with the skin. In practise, this may not be straightforward. A problem arising in the Chapter 2 *in vivo* study was the presence of the jugular vein overlying the artery. This introduced motion artefacts as it and carotid artery moved over each other during scanning. To eliminate this movement greater pressure was exerted using the transducer. In light of the results obtained here, caution must be exercised in comparing AWM from these affected artery segments with others.

6.4 Summary & conclusions

To summarise, variations in AWM were found for each of the four transducer-vessel geometry factors investigated. Maximum dilation deviated from values obtained for reference scanning geometries by factors of -0.07 ± 0.03 (for a vessel depth of 44 mm), -0.34 ± 0.02 (for AWM data acquired with a scan plane 2 mm from the vessel central axis), -0.22 ± 0.03 (for a transducer-vessel angle of 24.1°) and $+0.20 \pm 0.03$ (for a high transducer exerted pressure).

The implications for clinical and *in vitro* application of the TDI/AWM technique are two-fold. Firstly, where possible, deviations from the reference scan geometry should be minimised. The scope for this *in vivo* may be limited given the nature of the carotid circulation, in which healthy and diseased states can be tortuous, exhibit a range of variable skin-vessel angles and vessel depths. There is also likely to be variability in the pressure exerted by the transducer on the region scanned. To the authors knowledge there are no published investigations of this parameter.

Secondly, where deviations from reference scan conditions have been minimised, interpretations of AWM data must account for these factors before making inferences about the overall elastic properties of a scanned segment of artery wall or the spatial distribution of the elastic properties across a scanned segment. Furthermore, there must be an awareness of these factors in comparing AWM from different arterial sites and different individuals.

Chapter 7 Conclusion and future work

The evaluation of arterial wall motion (AWM) has potential value in the assessment of elasticity of the vessel wall and staging of disease. A relatively new technique has been identified which derives AWM from Tissue Doppler Imaging (TDI) velocity estimates using a prototype software developed by Philips Research France. Data concerning technique accuracy and precision in the literature is limited. Therefore, the overall aim of this thesis was to undertake a deeper study of the TDI/AWM software technique performance for the assessment of arterial disease. Individual chapter aims have been described in Section 1.6 and the achievement of these aims, chapter by chapter, is described in the succeeding paragraphs.

The first known *in vivo* reproducibility study of the carotid arteries using the TDI/AWM software technique is presented in Chapter 2. Examination of the TDI cine loops revealed several AWM artefact types and sources of variability. The high inter-loop variability obtained upon 'blind' acquisition of the TDI data emphasises the need for careful review of TDI and AWM data at the time of acquisition. This enables identification of artefacts and allows for repeat acquisitions. In this way, artefact incidence may be minimised, and provide superior AWM index reproducibility to that obtained here.

A detailed assessment of TDI/AWM technique accuracy is provided in Chapter 3. Accuracy was assessed using an in-house validation device based upon a moving plate arrangement. The TDI/AWM software technique systematically underestimated maximum dilation for sinusoidal device motion, increasingly so as AWM amplitude increased. At the same time AWM precision increased. Underestimation of maximum dilation will contribute to the underestimation of the elasticity of the vessel wall *in vivo*. Raw TDI data derived from physiologic motion was found to be affected by an artefact of unknown cause not observed in any other AWM data, *in vivo* or *in vitro*. This rendered AWM data variable to an unacceptable degree for quantitative accuracy assessment. Further investigation is required to remedy this problem.

In order to assess AWM precision upon varying beam vessel geometry, a compliant wall flow phantom was designed and characterised in Chapters 4 and 5. There are no other detailed characterisations of AWM phantoms in the literature. The VMM and TMM employed were characterised mechanically, revealing elastic moduli at the lower end of the *in vivo* range, and acoustically demonstrating good matches with tissue. The resulting phantom provided AWM dilations, velocities and accelerations within the physiological range, satisfying the primary aim of Chapters 4 and 5. Two main limitations in the phantom generated AWM were observed and these provide scope for future work. Firstly, the phantom was unable to generate the AWM rise times observed at the lower extreme of the physiologic range. Secondly, high frequency oscillations in dilation of the order of 25 Hz were observed in phantom generated AWM, which are not observed *in vivo*.

The compliant wall flow phantom was employed to investigate the effects of variations in beam-vessel geometry in Chapter 6. This has not been investigated in the literature. Vessel depth, scan plane-vessel axis coincidence, beam-vessel angle and transducer pressure were all found to have a marked effect on AWM precision. Chapter 2 revealed that deviations from optimum scanning geometry are common on application of the TDI/AWM technique *in vivo*. This is especially so in the case of internal carotid arteries in particular. Therefore, the effects of these variations in technique precision are unavoidable, but must be taken into account when comparing AWM acquired from different arterial segments and even different AWM loops from the same segment, since observer variability can result in variations in geometry between scans.

Potential improvements to the work performed here have been discussed separately in each chapter. In broader terms though, there is scope for further investigations with the TDI/AWM software technique. In this thesis, before any other work, it was necessary to assess the ability of the TDI/AWM software to evaluate maximum dilation of the scanned segment overall, for the special, simplified case of uniform elasticity along the scanned segment. However, this particular AWM technique is set

apart from others in the literature by its ability to measure AWM over a segment of artery rather than a single point. This allows identification of spatial variations in strain and elasticity along the scanned segment, which is of particular value in the investigation of plaque motion relative to the artery wall. Suitable representative indices of relative motion, such as the Mg index defined in Chapter 2, should be identified. It would also be of value to evaluate the accuracy and precision of the TDI/AWM software technique to resolve relative motion of adjacent segments of vessel walls in the laboratory, to give some indicator of *in vivo* efficacy. This could be implemented using non-uniform elasticity VMM segments in the compliant wall flow phantom designed in this thesis.

Appendix A: Measures of arterial stiffness

There are a large number of parameters, of varying complexity which all give some measure of the arteries biomechanical properties. Given the complex nature of the artery wall; its lack of homogeneity, viscoelastic characteristics, and variations in structure with site and age these parameters vary in their ability to accurately express the biomechanical behaviour of the artery. An overview of the range of parameters is provided, while a more comprehensive list is provided by O'Rourke et al⁹⁷.

The most fundamental index of elasticity which may be applied to arteries, Young's modulus (E) is an expression of the strain exhibited by a material, ϵ when subjected to a given stress, σ (Equation A.1). Blood pressure provides the tensile stress in this context.

$$E = \sigma / \epsilon \quad \text{(Equation A.1)}$$

For a material with linear elastic properties, E equals the gradient of the stress-strain curve before the elastic limit is reached. However, vascular tissue does not behave linearly and so the tangent modulus, E_t is a more appropriate measure (Equation A.2). This is also a ratio of stress to strain but applies to a specific strain or stress level and equals the gradient of a tangent to the stress strain curve at that point. Given the viscous characteristics exhibited by the artery; quoted elastic moduli must also be quoted with the applied distension rate.

$$E_t = \left(\delta\sigma / \delta\epsilon \right) \quad \text{Equation A.2}$$

Conventional elasticity measurements involve extension in 1D. However this is not the case for the approximately cylindrical geometry of the artery and one may only be able to measure a change in radius. The definitions of E and E_t can be adapted to take account of this, approximating an artery to an isotropic and applying the definition derived by Love¹⁵² (Equation A.3).

$$E_{inc} = 2(1 - \sigma^2) \left(\frac{\Delta P}{\Delta R_o} \right) \frac{R_i^2 R_o}{(R_o^2 - R_i^2)} \quad (\text{Equation A.3})$$

The previous measures are indicators of material elasticity alone. There are a number of measures which express the overall stiffness, since vessel elasticity is in part dictated by wall thickness and vessel radius. The elastic pressure strain modulus (E_p) was introduced by Peterson et al¹⁵³.

$$E_p = \frac{D \Delta P}{\Delta D} \quad (\text{Equation A.4})$$

Where the pulse pressure ΔP is the difference between systolic and diastolic pressures P_{sys} and P_{dia} . Distensibility (DC) and compliance (CC) are similar in definition⁹⁷. Distension and pressure measurements made *in vitro* then later *in vivo* revealed that the logarithm of P_{sys}/P_{dia} varied linearly with the changes in diameter. In order to have a linear 'stiffness' scale the stiffness parameter β was devised^{154,155}.

$$\beta = \frac{\ln(P_{sys}/P_{dia})}{(D_{sys} - D_{dia})/D_{dia}} \quad (\text{Equation A.5})$$

Another approach in characterising the biomechanical properties of the artery is to consider the wall dilation as a wave propagating along the length of the artery resulting from the fluid pressure wave initiated at the left ventricle of the heart. The speed of the pulse propagation, the pulse wave velocity, c_0 is a function of the artery's 'stiffness' and is given by the equation below.

$$c_0 = \sqrt{\frac{Eh}{2R\rho(1 - \sigma^2)}} \quad (\text{Equation A.6})$$

This is a corrected form of the Moens-Korteweg equation where R is the vessel radius and h is the wall thickness. The corrected form takes into account the fact that artery wall thickness changes with wall distension using the correction factor $(1 - \sigma^2)$ ⁸.

Appendix B: Calculation of probability of significant results upon multiple tests of AWM index agreement.

P(0) - Probability of zero significant results at the 95 % confidence level

P(1) - Probability of one significant result at the 95 % confidence level

P(>2) - Probability of two or more significant results at the 95 % confidence level

Assuming a binomial distribution,

$$P(0) = 0.95^{16} = 0.44$$

$$P(1) = 16 \times 0.95^{15} \times 0.05 = 0.37$$

$$P(>2) = 1 - (P(0) + P(1)) = 1 - 0.81 = 0.19$$

Therefore, there is a probability of 0.19 of obtaining 2 or more significant results at the 95 % confidence level.

Appendix C Preliminary measurements to detect strain rate dependence of tangent modulus of elasticity, E_t in VMM and TMM (Chapter 4)

E_t at 5% strain was compared for sample extension at two strain rates, $0.5 \% s^{-1}$ (5mm/min) and $1.4 \% s^{-1}$ (15mm/min) for 30 day old samples of recipe C TMM. Mean E_t values ± 1 standard error are quoted for each strain rate.

	Parameter	Value
TMM	n	20 @ each strain rate
	Mean $E_t @ 0.5 \% s^{-1} / kPa$	131.1 ± 2
	$E_t @ 1.4 \% s^{-1} / kPa$	131.1 ± 3
	Difference in E_t	0
VMM	n	9 @ each strain rate
	Mean $E_t @ 0.5 \% s^{-1} / kPa$	200.0 ± 9
	$E_t @ 1.4 \% s^{-1} / kPa$	182.1 ± 2
	Difference in E_t	17.9

Table C.1: Comparison of TMM and VMM E_t values obtained at two prospective strain rates.

Appendix D: A qualitative explanation of pressure and flow propagation in the compliant wall phantom

Propagation towards and away from a point of AWM measurement ‘a’ is considered (Figure D.1, Table D.1). Implicit in this explanation is the treatment of the flow-pressure cycles as travelling waves. As a flow-pressure cycle approaches, pressure, flow and the spatial pressure gradient $(P_b - P_a)/(b - a)$ (or dP/dx where the separation, x of the two points is very small) increases, and as the cycle propagates away from ‘a’ the same parameters experience decreases (flow is directly related to the spatial pressure gradient). The variation in pressure will be accompanied by similar changes in dilation, the walls distending as the pressure cycle approaches and contracting as it retreats. Note that these changes do not occur simultaneously, since there are phase differences between velocity and pressure. Furthermore, reflected waves and distortion of the flow and pressure waveforms with propagation are not taken into account here. However, this simplified description will aid in identifying mechanisms by which AWM varies with applied flow.

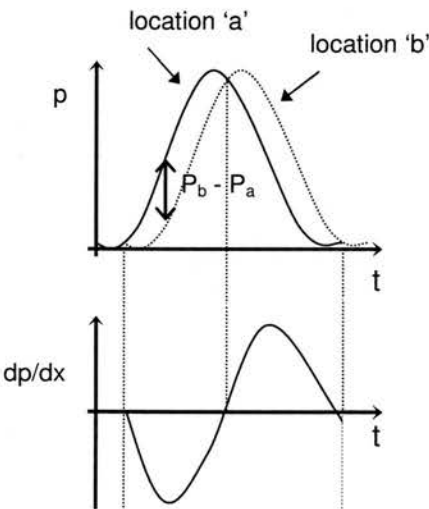


Figure D.1: Schematic plots of pressure at locations ‘a’ and ‘b’ (p_a and p_b), and pressure gradient variations (dp/dx) between the two.

	Q_a	P_a	AWM_a	$(P_b - P_a)$
Flow cycle approaches a	↑	↑	↑	↑
Flow cycle passes a	↓	↓	↓	↓

Table D.1: Variation of flow, Q_a and pressure, p_a at location 'a' in the phantom on the approach and retreat of a single flow cycle transmitted from the pump. p_b represents the pressure a short distance, x downstream from point 'a'. '↑' implies an increase and '↓' implies a decrease.

Reference List

1. World Health Organisation 2005, Strategic priorities of the WHO Cardiovascular Disease programme, Geneva, viewed 31 July 2005, <http://www.who.int/cardiovascular_diseases/priorities/en/>
2. Tegos,T.J., Kalodiki,E., Daskalopoulou,S.S. & Nicolaides,A.N. Stroke: epidemiology, clinical picture, and risk factors--Part I of III. *Angiology* **51**, 793-808 (2000).
3. Tegos,T.J., Kalodiki,E., Sabetai,M.M. & Nicolaides,A.N. The genesis of atherosclerosis and risk factors: a review. *Angiology* **52**, 89-98 (2001).
4. Nichols,W.W. & O'Rourke,M.F. McDonalds blood flow in arteries: Theoretical, experimental and clinical principles., pp. 12-53 (Edward Arnold, London,1990).
5. Warlow,C.P. *et al.* Stroke: A practical guide to management., pp. 223-300 (Blackwell Science Ltd., Oxford,2001).
6. Sandercock,P.A., Warlow,C.P., Jones,L.N. & Starkey,I.R. Predisposing factors for cerebral infarction: the Oxfordshire community stroke project. *British Medical Journal* **298**, 75-80 (1989).
7. Warlow,C.P. *et al.* Stroke: A practical guide to management., pp. 762-784 (Blackwell Science Ltd., Oxford,2001).
8. Nichols,W.W. & O'Rourke,M.F. McDonalds blood flow in arteries: Theoretical, experimental and clinical principles., pp. 77-114 (Edward Arnold, London,1990).
9. Lusis,A.J. Atherosclerosis. *Nature* **407**, 233-241 (2000).
10. Strydom,H.C. *et al.* A definition of initial, fatty streak, and intermediate lesions of atherosclerosis. A report from the Committee on Vascular Lesions of the Council on Arteriosclerosis, American Heart Association. *Circulation* **89**, 2462-2478 (1994).
11. Strydom,H.C. *et al.* A definition of advanced types of atherosclerotic lesions and a histological classification of atherosclerosis. A report from the Committee on Vascular Lesions of the Council on Arteriosclerosis, American Heart Association. *Circulation* **92**, 1355-1374 (1995).
12. Maseri,A. & Fuster,V. Is There a Vulnerable Plaque? *Circulation* **107**, 2068-2071 (2003).

13. European Carotid Surgery Trialists' Collaborative Group. MRC European Carotid Surgery Trial: interim results for symptomatic patients with severe (70-99%) or with mild (0-29%) carotid stenosis. *Lancet* **337**, 1235-1243 (1991).
14. North American Symptomatic Carotid Endarterectomy Trial Collaborators. Beneficial effect of carotid endarterectomy in symptomatic patients with high-grade carotid stenosis. North American Symptomatic Carotid Endarterectomy Trial Collaborators. *New England Journal of Medicine*. **325**, 455-453 (1991).
15. Williams,J. Jerry.Williams@luht.scot.nhs.uk. 05/08/2003. 'X-ray angiography' Email to J.A. Dineley (Judith.Dineley@ed.ac.uk).
16. Warlow,C.P. *et al.* Stroke: A practical guide to management., pp. 28-105 (Blackwell Science Ltd., Oxford,2001).
17. Rapp,J.H. & Saloner,D. Current status of carotid imaging by MRA. *Cardiovascular Surgery* **11**, 445-447 (2003).
18. Yucel,E.K. *et al.* Magnetic Resonance Angiography : Update on Applications for Extracranial Arteries. *Circulation* **100**, 2284-2301 (1999).
19. Culebras,A., Masdeu,J.C. & Kase,C.S. Practise guidelines for the use of imaging in transient ischemic attacks and acute stroke. A report of the stroke council. *Stroke* **28**, 1480-1497 (1997).
20. Cloft,H.J., Murphy,K.J., Prince,M.P. & Brunberg,J.A. 3D gadolinium-enhanced MR angiography of the carotid arteries. *Magnetic Resonance Imaging* **14**, 593-600 (1996).
21. Levy,M.M., Baum,R.A. & Carpenter,J.P. Endovascular surgery based solely on noninvasive preprocedural imaging. *Journal of Vascular Surgery*. **28**, 995-1003 (1998).
22. Hoskins,P.R., Fish,P.R., McDicken,W.N. & Moran,C. Developments in cardiovascular ultrasound. Part 2: Arterial applications. *Medical and biological engineering and computing* **36**, 259-269 (1998).
23. Hoskins,P.R., Loupas,T. & McDicken,W.N. A comparison of the Doppler spectra from human blood and artificial blood used in a flow phantom. *Ultrasound in Medicine & Biology* **16**, 141-147 (1990).
24. Moneta,G.L. *et al.* Correlation of North American Symptomatic Carotid Endarterectomy Trial (NASCET) angiographic definition of 70% to 99% internal carotid artery stenosis with duplex scanning. *Journal of Vascular Surgery* **17**, 152-157 (1993).

25. Hoskins,P.R. Ultrasound techniques for measurement of blood flow and tissue motion. *Biorheology* **39**, 451-459 (2002).
26. Mathiesen,E.B., Joakimsen,O. & Bonaa,K.H. Intersonographer reproducibility and intermethod variability of ultrasound measurements of carotid artery stenosis: The Tromso study. *Cerebrovascular Diseases* **10**, 207-213 (2000).
27. Howard,G. *et al.* An Approach for the Use of Doppler Ultrasound as a Screening Tool for Hemodynamically Significant Stenosis (Despite Heterogeneity of Doppler Performance): A Multicenter Experience. *Stroke* **27**, 1951 (1996).
28. Howard,G. *et al.* Carotid artery intimal-medial thickness distribution in general populations as evaluated by B-mode ultrasound. ARIC Investigators. *Stroke* **24**, 1297 (1993).
29. Chambless,L.E. *et al.* Carotid wall thickness is predictive of incident clinical stroke: the Atherosclerosis Risk in Communities (ARIC) study. *Am. J. Epidemiol.* **151**, 478 (2000).
30. Riley,W.A., Barnes,R., Evans,G.W. & Burke,G.L. Ultrasonic measurement of the elastic modulus of the common carotid artery. *Stroke* **23**, 952-956 (1992).
31. Simon,A., Gariepy,J., Chironi,G., Megnien,J.L. & Levenson,J. Intima-media thickness: a new tool for diagnosis and treatment of cardiovascular risk. *Journal of Hypertension.* **20**, 159-169 (2002).
32. Renemann,R.S., Hoeks,A.P.G. & Westerhof,N. Non-invasive assessment of artery wall properties in humans- methods and interpretations. *Journal of vascular investigation* **2**, 53-64 (1996).
33. Labropoulos,N. *et al.* Viscoelastic properties of normal and atherosclerotic carotid arteries. *European Journal of Vascular and Endovascular Surgery* **19**, 221-225 (2000).
34. Van Bortel,L.M. *et al.* Does B-mode common carotid artery intima-media thickness differ from M-mode? *Ultrasound in Medicine & Biology* **27**, 1333-1336 (2001).
35. Selzer,R.H., Mack,W.J., Lee,P.L., Kwong-Fu,H. & Hodis,H.N. Improved common carotid elasticity and intima-media thickness measurements from computer analysis of sequential ultrasound frames. *Atherosclerosis* **154**, 185-193 (2001).
36. Hoskins,P.R., Fish,P.R., McDicken,W.N. & Moran,C. Developments in cardiovascular ultrasound. Part 2: Arterial applications. *Medical and biological engineering and computing* **36**, 259-269 (1998).

37. van Swijndregt, M.A.D. *et al.* An in vitro evaluation of the line pattern of the near and far walls of carotid arteries using B-mode ultrasound. *Ultrasound in Medicine & Biology* **22**, 1007-1015 (1996).
38. Fayad, Z.A. & Fuster, V. Clinical imaging of the high risk or vulnerable atherosclerotic plaque. *Circ Res* **89**, 305-316 (2001).
39. Trivedi, R.A. *et al.* Multi-sequence In vivo MRI can Quantify Fibrous Cap and Lipid Core Components in Human Carotid Atherosclerotic Plaques. *European Journal of Vascular and Endovascular Surgery* **28**, 207-213 (2004).
40. Viles-Gonzalez, J.F. *et al.* In Vivo 16-Slice, Multidetector-Row Computed Tomography for the Assessment of Experimental Atherosclerosis: Comparison With Magnetic Resonance Imaging and Histopathology. *Circulation* **110**, 1467-1472 (2004).
41. Rumberger, J.A., Simons, D.B., Fitzpatrick, L.A., Sheedy, P.F. & Schwarz, R.S. Coronary Artery Calcium Area by Electron-Beam Computed Tomography and Coronary Atherosclerotic Plaque Area : A Histopathologic Correlative Study. *Circulation* **92**, 2157 (1995).
42. Gray-Weale, A.C., Graham, J.C., Burnett, J.R., Byrne, K. & Lusby, R.J. Carotid artery atheroma: Comparison of preoperative B-mode ultrasound appearance with carotid endarterectomy specimen pathology. *Journal of cardiovascular surgery* **29**, 676-681 (1988).
43. Langsfeld, M., Gray-Weale, A.C. & Lusby, R.J. The role of plaque morphology and diameter reduction in the development of new symptoms in asymptomatic carotid arteries. *Journal of Vascular Surgery* **9**, 548-557 (1989).
44. de Bray, J.M. *et al.* Reproducibility in ultrasonic characterisation of carotid plaques. *Cerebrovascular diseases* **8**, 273-277 (1998).
45. European Carotid Plaque Study Group. Carotid artery plaque composition: relationship to clinical presentation and ultrasound B-mode imaging. *European Journal of Vascular and Endovascular Surgery* **10**, 23-30 (1995).
46. Moore, M.P. *et al.* Characterisation of coronary atherosclerotic morphology by spectral analysis of radiofrequency signal: in vitro intravascular ultrasound study with histological and radiological validation. *Heart* **79**, 459-467 (1998).
47. Tegos, T.J. *et al.* Echomorphologic and histopathologic characteristics of unstable carotid plaques. *American Journal of Neuroradiology* **21**, 1937-1944 (2000).

48. Zhao,S.Z., Xu,X.Y. & Collins,M.W. The numerical analysis of fluid-solid interactions for blood flow in arterial structures, Part 1: a review of models for arterial wall behaviour. *Proceedings of the institution of mechanical engineers part H- Journal of engineering in medicine* **212**, 229-240 (1998).
49. Humphrey,J.D. & Na,S. Elastodynamics and arterial wall stress. *Annals of Biomedical Engineering*. **30**, 509-523 (2002).
50. Cox,R.H. Passive mechanics and connective tissue of canine arteries. *American Journal of Physiology* **234**, H533-H541 (1978).
51. Armentano,R.L., Barra,J.G., Levenson,J., Simon,A. & Pichel,R.H. Arterial Wall Mechanics in Conscious Dogs : Assessment of Viscous, Inertial, and Elastic Moduli to Characterize Aortic Wall Behavior. *Circ Res* **76**, 468 (1995).
52. Bank,A.J., Kaiser,D.R., Rajala,S. & Cheng,A. In Vivo Human Brachial Artery Elastic Mechanics : Effects of Smooth Muscle Relaxation. *Circulation* **100**, 41 (1999).
53. Bergel,D.H. The dynamic elastic properties of the arterial wall. *Journal of Physiology* **156**, 458-469 (1961).
54. Lee,R.T., Grodzinsky,A.J., Frank,E.H., Kamm,R.D. & Schoen,F.J. Structure-dependent dynamic mechanical behavior of fibrous caps from human atherosclerotic plaques. *Circulation* **83**, 1764-1770 (1991).
55. Loree,H.M. *et al.* Mechanical-Properties of Model Atherosclerotic Lesion Lipid Pools. *Arteriosclerosis and Thrombosis* **14**, 230-234 (1994).
56. Latham,R.D. *et al.* Regional wave travel and reflections along the human aorta: a study with six simultaneous micromanometric pressures. *Circulation* **72**, 1257 (1985).
57. Bank,A.J. & Kaiser D.R. Smooth muscle relaxation: Effects on arterial compliance, distensibility, elastic modulus and pulse wave velocity. *Hypertension* **32**, 356-359 (1998).
58. Isnard,R.N. *et al.* Pulsatile diameter and elastic modulus of the aortic arch inessential hypertension:a non-invasive study. *Journal of the American College of Cardiology* **13**, 399-405 (1989).
59. Roach,M.R. & Burton,A.C. The reason for the shape of the distensibility curves of arteries. *Canadian Journal of Biochemistry and Physiology* **35**, 681-690 (1957).
60. Safar,M.E., London,G.M., Asmar,R.G., Hugues,C.J. & Laurent,S.A. An indirect approach for the study of the elastic modulus of the brachial artery in patients with essential hypertension. *Cardiovascular Research* **20**, 563-567 (1986).

61. Bergel,D.H. The static elastic properties of the arterial wall. *Journal of Physiology* **156**, 445-447 (1961).
62. Burton,A.C. Relation of structure to function of the tissues of the wall of blood vessels. *Physiological Reviews* **34**, 619-642 (1954).
63. Bank,A.J. *et al.* Contribution of Collagen, Elastin, and Smooth Muscle to In Vivo Human Brachial Artery Wall Stress and Elastic Modulus. *Circulation* **94**, 3263 (1996).
64. Bank,A.J. *et al.* Direct Effects of Smooth Muscle Relaxation and Contraction on In Vivo Human Brachial Artery Elastic Properties. *Circ Res* **77**, 1008 (1995).
65. Riley,W.A., Evans,G.W., Sharrett,A.R., Burke,G.L. & Barnes,R.W. Variation of common carotid artery elasticity with intimal-medial thickness: the arie study. *Ultrasound in Medicine & Biology* **23**, 157-164 (1997).
66. Nichols,W.W. & O'Rourke,M.F. McDonalds blood flow in arteries: Theoretical, experimental and clinical principles., pp. 398-420 (Edward Arnold, London,1990).
67. Hansen,F., Mangell,P., Sonesson,B. & Lanne,T. Diameter and compliance in the human common carotid artery - variations with age and sex. *Ultrasound in Medicine & Biology* **21**, 1-9 (1995).
68. Ahlgren,A.R., Hansen,F., Sonesson,B. & Lanne,T. Stiffness and diameter of the common carotid artery and abdominal aorta in women. *Ultrasound in Medicine & Biology* **23**, 983-988 (1997).
69. Schmidt-Trucksass,A. *et al.* Assessment of carotid wall motion and stiffness with tissue doppler imaging. *Ultrasound in Medicine & Biology* **24**, 639-646 (1998).
70. Nagai,Y. *et al.* Carotid arterial stiffness as a surrogate for aortic stiffness: relationship between carotid artery pressure-strain elastic modulus and aortic pulse wave velocity. *Ultrasound in Medicine & Biology* **25**, 181-188 (1999).
71. Richardson,P.D. Biomechanics of plaque rupture: Progress, problems, and new frontiers. *Annals of Biomedical Engineering* **30**, 524-536 (2002).
72. Topoleski,L.D.T., Salunke,N.V., Humphrey,J.D. & Mergner,W.J. Composition- and history-dependent radial compressive behavior of human atherosclerotic plaque. *Journal of Biomedical Materials Research* **35**, 117-127 (1997).
73. Salunke,N.V., Topoleski,L.D.T., Humphrey,J.D. & Mergner,W.J. Compressive stress-relaxation of human atherosclerotic plaque. *Journal of Biomedical Materials Research* **55**, 236-241 (2001).

74. Cheng,G.C., Loree,H.M., Kamm,R.D., Fishbein,M.C. & Lee,R.T. Distribution of circumferential stress in ruptured and stable atherosclerotic lesions. A structural analysis with histopathological correlation. *Circulation* **87**, 1179-1187 (1993).
75. Lee,R.T., Loree,H.M. & Fishbein,M.C. High stress regions in saphenous vein bypass graft atherosclerotic lesions. *Journal of the American College of Cardiology*. **24**, 1639-1644 (1994).
76. Lendon,C.L., Davies,M.J., Born,G.V.R. & Richardson,P.D. Atherosclerotic Plaque Caps Are Locally Weakened When Macrophages Density Is Increased. *Atherosclerosis* **87**, 87-90 (1991).
77. Burleigh,M.C. *et al.* Collagen Type-I and Type-Iii, Collagen Content, Gags and Mechanical Strength of Human Atherosclerotic Plaque Caps - Span-Wise Variations. *Atherosclerosis* **96**, 71-81 (1992).
78. Richardson,P.D., Davies,M.J. & Born,G.V.R. Influence of Plaque Configuration and Stress-Distribution on Fissuring of Coronary Atherosclerotic Plaques. *Lancet* **2**, 941-944 (1989).
79. Loree,H.M. *et al.* Mechanical-Properties of Model Atherosclerotic Lesion Lipid Pools. *Arteriosclerosis and Thrombosis* **14**, 230-234 (1994).
80. Lee,R.T., Schoen,F.J., Loree,H.M., Lark,M.W. & Libby,P. Circumferential Stress and Matrix Metalloproteinase 1 in Human Coronary Atherosclerosis: Implications for Plaque Rupture. *Arterioscler Thromb Vasc Biol* **16**, 1070-1073 (1996).
81. Hayashi,K. & Imai,Y. Tensile property of atheromatous plaque and an analysis of stress in atherosclerotic wall. *Journal of Biomechanics*. **30**, 573-579 (1997).
82. Kilpatrick,D. *et al.* Effect of plaque composition on fibrous cap stress in carotid endarterectomy specimens. *Journal of biomechanical engineering* **123**, 635-638 (2001).
83. Loree,H.M., Kamm,R.D., Stringfellow,R.G. & Lee,R.T. Effects of fibrous cap thickness on peak circumferential stress in model atherosclerotic vessels. *Circulation Research*. **71**, 850-858 (1992).
84. Huang,H. *et al.* The Impact of Calcification on the Biomechanical Stability of Atherosclerotic Plaques. *Circulation* **103**, 1051 (2001).
85. Williamson,S.D. *et al.* On the sensitivity of wall stresses in diseased arteries to variable material properties. *Journal of biomechanical engineering* **125**, 147-155 (2003).

86. Pannier,B.M., Avolio,A.P., Hoeks,A., Mancia,G. & Takazawa,K. Methods and devices for measuring arterial compliance in humans. *American Journal of Hypertension* **15**, 743-753 (2002).
87. Wilkinson,I.B. *et al.* Heart rate dependency of pulse pressure amplification and arterial stiffness. *American Journal of Hypertension* **15**, 24-30 (2002).
88. Takazawa,K. *et al.* Assessment of Vasoactive Agents and Vascular Aging by the Second Derivative of Photoplethysmogram Waveform. *Hypertension* **32**, 365 (1998).
89. Breithaupt-Grogler,K., Ling,M., Boudoulos,H. & Belz,G.G. Protective effect of chronic garlic intake on elastic properties of aorta in the elderly. *Circulation* **96**, 2649-2655 (1997).
90. Bleasdale,R.A., Parker,K.H. & Jones,C.J.L. Chasing the wave. Unfashionable but important new concepts in arterial wave travel. *American journal of heart circulation and physiology* **284**, H1879-H1885 (2003).
91. Eriksson,A., Greiff,E., Loupas,T., Persson,M. & Pesque,P. Arterial pulse wave velocity with Tissue Doppler Imaging. *Ultrasound in Medicine & Biology* **28**, 571-580 (2002).
92. Anderson,T. & McDicken,W.N. Measurement of tissue motion. *Proceedings of the institution of mechanical engineers, Part H Journal of engineering in Medicine* **213**, 181-191 (1999).
93. Meinders,J.M., Brands,P.J., Willigers,J.M., Kornet,L. & Hoeks,A.P.G. Assessment of the spatial homogeneity of artery dimension parameters with high frame rate 2D B-mode. *Ultrasound in Medicine & Biology* **27**, 785-794 (2001).
94. Graf,S. *et al.* Experimental and clinical validation of arterial diameter waveform and intimal medial waveform obtained from B-mode ultrasound image processing. *Ultrasound in Medicine & Biology* **25**, 1353-1363 (1999).
95. Golemati,S. *et al.* Carotid artery wall motion from B-mode ultrasound using region tracking and block matching. *Ultrasound in Medicine & Biology* **29**, 387-399 (2003).
96. Bonnefous,O. Arterial wall motion imaging: A new approach for vascular characterisation. *BMUS Bulletin* **8**, 19-23 (2000).
97. O'Rourke,M.F., Staessen,J.A., Vlachopoulos,C., Duprez,D. & Plante,G. Clinical applications of arterial stiffness; definitions and reference values. *American Journal of Hypertension* **15**, 426-444 (2002).
98. Gao,L., Parker,K.J., Lerner,R.M. & Levinson,S.F. Imaging of the elastic properties of tissue- a review. *Ultrasound in Medicine & Biology* **22**, 959-977 (1996).

99. de Korte,C.L., Woutman,H.A., van der Steen,A.F.W., Pasterkamp,G. & Bom,N. Characterisation of plaque components with intravascular ultrasound elastography: a validation study in vitro. *Circulation* **102**, 617-623 (2000).
100. Ophir,J., Cespedes,E.I., Ponnekati,H., Yazdi,Y. & Li,X. Elastography: A method for imaging the elasticity in biological tissues. *Ultrasonic Imaging* **13**, 111-134 (1991).
101. van der Steen,A.F.W. *et al.* Recent developments in IVUS. *BMUS Bulletin* **8**, 24-27 (2000).
102. Kanai,H., Hasegawa,H., Ichiki,M., Tezuka,F. & Koiwa,Y. Elasticity imaging of atheroma with transcutaneous ultrasound: Preliminary study. *Circulation* **107**, 3018-3021 (2003).
103. Steinman,D.A. Image-based computational fluid dynamics modeling in realistic arterial geometries. *Ann. Biomed. Eng* **30**, 483-497 (2002).
104. Bonnefous,O., Criton,A., Germond,L. & Denis,E. New TDI developments for vascular and cardiac applications, 2000 IEEE Ultrasonics Symposium. 1285-1290. 2000.
105. Germond,L., Bonnefous,O. & Loupas,T. Quantitative assessment of the artery dilation measurements with an arterial phantom, 2001 IEEE Ultrasonics symposium. 1413-1416. 2001.
106. Long,A., Rouet,L., Bissery,A., Goeau-Brissonniere,O. & Sapoval,M. Aortic compliance in healthy subjects: Evaluation of tissue Doppler imaging. *Ultrasound in Medicine & Biology* **30**, 753-759 (2004).
107. Bland,J.M. & Altman,D.G. Statistical-Methods for Assessing Agreement Between 2 Methods of Clinical Measurement. *Lancet* **1**, 307-310 (1986).
108. van Swijndregt,M.A.D., De Lange,E.E., De Groot,E. & Ackerstaff,R.G.A. An in vivo evaluation of the reproducibility of intima-media thickness measurements of the carotid artery segments using B-mode ultrasound. *Ultrasound in Medicine & Biology* **25**, 323-330 (1999).
109. Madsen,E.L., Zagzebski,J.A., Banjavie,R.A. & Jutila,R.E. Tissue mimicking materials for ultrasound phantoms. *Medical Physics*. **5**(5):391-4, -Oct (1978).
110. Madsen,E.L. *et al.* Interlaboratory Comparison of Ultrasonic-Attenuation and Speed Measurements. *Journal of Ultrasound in Medicine* **5**, 569-576 (1986).
111. Teirlinck,C.J.P.M. *et al.* Development of an example flow test object and comparison of five of these test objects, constructed in various laboratories. *Ultrasonics* **36**, 653-660 (1998).

112. de Korte, C.L., Cespedes, E.I., van der Steen, A.F., Norder, B. & te, N.K. Elastic and acoustic properties of vessel mimicking material for elasticity imaging. *Ultrasonic Imaging*. 112-126 (1997).
113. Ryan, L.K. & Foster, F.S. Tissue equivalent vessel phantoms for intravascular ultrasound. *Ultrasound in Medicine and Biology* **23**, 261-273 (1997).
114. Pythoud, F., Stergiopoulos, N. & Meister, J.J. Modeling of the Wave Transmission Properties of Large Arteries Using Nonlinear Elastic Tubes. *Journal of Biomechanics* **27**, 1379-1381 (1994).
115. Chu, K.C. & Rutt, B.K. Polyvinyl alcohol cryogel: An ideal phantom material for MR studies of arterial flow and elasticity. *Magnetic Resonance in Medicine* **37**, 314-319 (1997).
116. Fromageau, J., Brusseau, E., Vray, D., Gimenez, G. & Delachartre, P. Characterization of PVA cryogel for intravascular ultrasound elasticity imaging. *Ieee Transactions on Ultrasonics Ferroelectrics and Frequency Control* **50**, 1318-1324 (2003).
117. Papageorgiou, G.L. & Jones, N.B. Physical Modeling of the Arterial-Wall .1. Testing of Tubes of Various Materials. *Journal of Biomedical Engineering* **9**, 153-156 (1987).
118. Rickey, D.W., Picot, P.A., Christopher, D.A. & Fenster, A. A wall-less vessel phantom for Doppler ultrasound studies. *Ultrasound in Medicine & Biology* **21**, 1163-1176 (1995).
119. Walker, R.D., Smith, R.E., Sherriff S.B. & Wood, R.F.M. Latex vessels with customized compliance for use in arterial flow models. *Physiological Measurement* **20**, 277-286 (1999).
120. Duck, F.A. Physical Properties of Tissue, A Comprehensive Reference book. Academic Press, London & New York (1990).
121. Drangova, M. *et al.* Elasticity and geometry measurements of vascular specimens using a high-resolution laboratory CT scanner. *Physiological Measurement* 277-290 (1993).
122. Greenleaf, J.F., Duck, F.A., Samayoa, W.F. & Johnson, S.A. Ultrasonic Data Acquisition and Processing System for Atherosclerotic Tissue Characterization. *Ieee Transactions on Sonics and Ultrasonics* **SU22**, 218 (1975).
123. Liao, D. *et al.* Arterial Stiffness and the Development of Hypertension : The ARIC Study. *Hypertension* **34**, 201-206 (1999).
124. Loree, H.M. *et al.* Mechanical-Properties of Model Atherosclerotic Lesion Lipid Pools. *Arteriosclerosis and Thrombosis* **14**, 230-234 (1994).

125. Krouskop, T.A., Wheeler, T.M., Kallel, F., Garra, B.S. & Hall, T. Elastic moduli of breast and prostate tissues under compression. *Ultrasonic Imaging*. 260-274 (1990).
126. Bullen, B.A., Quaade, F., Olesen, E. & Lund, S.A. Ultrasonic Reflections Used for Measuring Subcutaneous Fat in Humans. *Human Biology* **37**, 375-& (1965).
127. Errabolu, R.L., Sehgal, C.M., Bahn, R.C. & Greenleaf, J.F. Measurement of ultrasonic nonlinear parameter in excised fat tissues. *Ultrasound in Medicine & Biology*. *14*(2):137-46, (1988).
128. Madsen, E.L. Tissue Characterization with Ultrasound. Greenleaf, J.F. (ed.), pp. 165-181 (CRC Press Inc., Boca Raton, Florida, 1986).
129. Hall, T.J. Elasticity imaging phantoms. *Ultrasound in Medicine & Biology* **29**, S207-S208 (2003).
130. Hall, T.J., Bilgen, M., Insana, M.F. & Krouskop, T.A. Phantom materials for elastography. *Ieee Transactions on Ultrasonics Ferroelectrics and Frequency Control* **44**, 1355-1365 (1997).
131. Surry, K.J.M., Austin, H.J.B., Fenster, A. & Peters, T.M. Poly(vinyl alcohol) cryogel phantoms for use in ultrasound and MR imaging. *Physics in Medicine and Biology* 5529-5546 (2004).
132. Hoskins, P.R. Testing of doppler ultrasound equipment. Hoskins, P.R., Sherriff, S.B. & Evans, J.A. (eds.), pp. 12-29 (Institute of Physics & Engineering in Medicine, York, 1994).
133. Thompson, R.S., Aldis, G.K. & Linnett, I.W. Doppler ultrasound spectral power-density distribution - measurement artifacts in steady flow. *Medical & Biological Engineering & Computing* **28**, 60-66 (1990).
134. Hoskins, P.R. & Ramnarine, K.V. Doppler Ultrasound: Physics, Instrumentation and Clinical Applications. Evans, D.H. & McDicken, W.N. (eds.), pp. 382-404 (John Wiley & Sons Inc, 1990).
135. Tortoli, P., Berti, P., Guidi, F., Thompson, R.S. & Aldis, G.K. Flow imaging with pulsed Doppler ultrasound: refraction artefacts and dual mode propagation. Schneider, S. C., Levy, M., and McAvoy, B. R. 2, 1269-1272. 5-10-1997. Piscataway, New Jersey, IEEE. Proceedings of the 1997 IEEE Ultrasonics Symposium, 1997. 5-8-1997.
136. Thompson, R.S. & Aldis, G.K. Effect of a cylindrical refracting interface on ultrasound intensity and the CW Doppler spectrum. *IEEE Transactions on Biomedical Engineering* **43**, 451-459 (1996).

137. Ramnarine,K.V., Anderson,T. & Hoskins,P.R. Construction and geometric stability of physiological flow rate wall-less stenosis phantoms. *Ultrasound in Medicine and Biology* **27**, 245-250 (2001).
138. Ramnarine,K.V., Hoskins,P.R., Routh,H.F. & Davidson,F. Doppler backscatter properties of a blood-mimicking fluid for Doppler performance assessment. *Ultrasound in Medicine & Biology* **25**, 105-110 (1999).
139. Burlew,M.M., Madsen,E.L., Zagzebski,J.A., Banjavic,R.A. & Sum,S.W. New Ultrasound Tissue-Equivalent Material. *Radiology* **134**, 517-520 (1980).
140. te Nijenhuis,K. Investigation into the ageing process in gels of gelatin/water systems by the measurement of their dynamic moduli, Part I - Phenomenology. *Colloid & Polymer Science* **259**, 522-535 (1981).
141. Dunn,F. & Goss,S.A. Tissue Characterization with Ultrasound. Greenleaf,J.F. (ed.), pp. 1-13 (CRC Press Inc., Boca Raton, Florida,1986).
142. Browne,J.E., Ramnarine,K.V., Watson,A.J. & Hoskins,P.R. Assessment of the acoustic properties of common tissue-mimicking test phantoms. *Ultrasound in Medicine & Biology* **29**, 1053-1060 (2003).
143. Fleming,A.D., McDicken,W.N., Sutherland,G.R. & Hoskins,P.R. Assessment of colour doppler tissue imaging using test-phantoms. *Ultrasound in Medicine & Biology* **20**, 937-951 (1994).
144. Nowicki,A., Olszewski,R., Etienne,J., Karlowicz,P. & Adamus,J. Assessment of wall velocity gradient imaging using a test phantom. *Ultrasound in Medicine & Biology* **22**, 1255-1260 (1996).
145. Mijovic,B. & Liepsch,D. Experimental flow studies in an elastic Y-model. *Technology and health care* **11**, 115-141 (2003).
146. Mai,J.J. & Insana,M.F. Strain imaging of internal deformation. *Ultrasound in Medicine & Biology* **28**, 1475-1484 (2002).
147. Ramnarine,K.V., Nassiri,D.K., Hoskins,P.R. & Lubbers,J. Validation of a New Blood-Mimicking Fluid for Use in Doppler Flow Test Objects. *Ultrasound in Medicine & Biology* **24**, 451-459 (1998).
148. Learoyd,B.M. & Taylor,M.G. Alterations with Age in Viscoelastic Properties of Human Arterial Walls. *Circulation Research* **18**, 278-292 (1966).
149. Nichols,W.W. & O'Rourke,M.F. McDonalds blood flow in arteries: Theoretical, experimental and clinical principles., pp. 125-142 (Edward Arnold, London,1990).
150. Nichols,W.W. & O'Rourke,M.F. McDonalds blood flow in arteries: Theoretical, experimental and clinical principles., pp. 283-329 (Edward Arnold, London,1990).

151. Holdsworth,D.W., Norley,C.J.D., Frayne,R., Steinman,D.A. & Rutt,B.K. Characterization of common carotid artery blood-flow waveforms in normal human subjects. *Physiological Measurement* **20**, 219-240 (1999).
152. Love,A.E.H. A treatise on the mathematical theory of elasticity. Dover publications, New York (1944).
153. Peterson,L.H., Jensen,R.E. & Parnell,J. Mechanical properties of arteries in vivo. *Circ Res* **8**, 622-639 (1960).
154. Hayashi,K., Handa,H., Nagasawa,S., Okumura,A. & Moritake,K. Stiffness and elastic behavior of human intracranial and extracranial arteries. *Journal of Biomechanics* **13**, 175-184 (1980).
155. Kawasaki,T., Sasayama,S., Yagi,S., Asakawa,T. & Hirai,T. Noninvasive Assessment of the Age-Related-Changes in Stiffness of Major Branches of the Human Arteries. *Cardiovascular Research* **21**, 678-687 (1987).